Resource Allocation Techniques for Spectral and Energy-Efficient Next Generation Wireless Networks

by

©Quang Nhat Le

A dissertation submitted to the School of Graduate Studies
in partial fulfillment of the requirements for the degree of

Doctor of Philosophy

Faculty of Engineering and Applied Science
Memorial University

May 2024

St. John's, Newfoundland

Abstract

Efficient utilization of wireless resources is mandated to fulfill the requirements of the sixth-generation (6G) wireless networks, such as high data rates, low latency, and ubiquitous connectivity. The word "resource" implies quantities such as bandwidth, power, and time. Efficiently allocating such limited resources is an effective means to enhance the wireless systems' performance. Specifically, resource allocation intends to assign limited resources to users, maximizing the utilization of these resources, and attaining the best system performance. In this line, in this dissertation, low-complexity and efficient resource allocation strategies in networks assisted by various technologies, including non-orthogonal multiple access (NOMA), reconfigurable intelligent surface (RIS), full-duplex (FD), cell-free massive multiple-input multiple-output (CFmMIMO), and integrated sensing and communication (ISAC) are developed and investigated. The first part of the dissertation focuses on analyzing the outage and throughput performances, as well as optimizing the sum rate for an FD NOMA-assisted cooperative spectrum-sharing network. The second part develops novel user clustering and resource allocation algorithms to boost the sum spectral efficiency of a CFmMIMO-NOMA system. Besides, novel low-complexity resource allocation algorithms for optimizing the energy efficiency and total transmit power of RIS-aided CF and RIS-enabled federated learning (FL) networks are proposed. The third part examines the application of RIS and FD in ISAC networks to improve the transmission rate and sensing performance. Finally, the last part draws

concluding remarks and discusses several topics for future investigation.

To my family

Acknowledgements

First of all, I would like to express my deepest gratitude to my supervisor, Prof. Octavia A. Dobre, for giving me a great opportunity to study at Memorial University and work as part of the Advanced Wireless and Optical Communications Laboratory. Prof. Dobre was always available for discussions, provided significant constructive feedback, continuously encouraged and supported me not only in my research work but also in my daily life. Without her conscientious and whole-hearted guidance, I could not obtain good research results and accomplish my research goals.

Secondly, I could not have accomplished this PhD journey without the financial support from my supervisor, the Faculty of Engineering and Applied Science, the School of Graduate Studies, and the Natural Science and Engineering Research Council of Canada.

Thirdly, I would like to extend my sincere thanks to all my laboratory colleagues for their devoted help in my daily life. Their friendship and support have meant a lot to me.

Finally, I would like to thank my parents for their constant love, limitless support, and encouragement throughout my life.

Co-Authorship Statement

I, Quang Nhat Le, hold a principle author status for all the manuscript chapters (Chapters 2-6) in this dissertation. However, each manuscript is co-authored by my supervisor and co-researchers, whose contributions have facilitated the development of this work as described below.

- Paper 1 in Chapter 2: Quang Nhat Le, Animesh Yadav, Nam-Phong Nguyen, Octavia A. Dobre, and Ruiqin Zhao, "Full-duplex non-orthogonal multiple access cooperative overlay spectrum-sharing networks with SWIPT," *IEEE Trans. Green Commun. Netw.,* vol. 5, no. 1, pp. 322-334, Mar. 2021.

  I was the primary author, with authors 2-5 contributing to the development of the idea and refinement of the presentation.

- Paper 2 in Chapter 3: Quang Nhat Le, Van-Dinh Nguyen, Octavia A. Dobre, Nam-Phong Nguyen, Ruiqin Zhao, and Symeon Chatzinotas, "Learning-assisted user clustering in cell-free massive MIMO-NOMA networks," *IEEE Trans. Veh. Technol.,* vol. 70, no. 12, pp. 12872-12887, Oct. 2021.

  I was the primary author, with authors 2-6 contributing to the development of the idea and refinement of the presentation.

- Paper 3 in Chapter 4: Quang Nhat Le, Van-Dinh Nguyen, Octavia A. Dobre, and Ruiqin Zhao, "Energy efficiency maximization in RIS-aided cell-free network with

limited backhaul," *IEEE Commun. Lett.,* vol. 25, no. 6, pp. 1974-1978, June 2021. I was the primary author, with authors 2-4 contributing to the development of the idea and refinement of the presentation.

- Paper 4 in Chapter 5: Quang Nhat Le, Lina Bariah, Octavia A. Dobre, and Sami Muhaidat, "Reconfigurable intelligent surface-enabled federated learning for power-constrained devices," *IEEE Commun. Lett.,* vol. 26, no. 11, pp. 2725-2729, Nov. 2022.

  I was the primary author, with authors 2-4 contributing to the development of the idea and refinement of the presentation.

- Paper 5 in Chapter 6: Quang Nhat Le, Van-Dinh Nguyen, Octavia A. Dobre, and Hyundong Shin, "RIS-assisted full-duplex integrated sensing and communication," *IEEE Wirel. Commun. Lett.,* vol. 12, no. 10, pp. 1677-1681, Oct. 2023.

  I was the primary author, with authors 2-4 contributing to the development of the idea and refinement of the presentation.

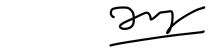

Quang Nhat Le

April 6th, 2024

Date

Table of Contents

Abstract ii

Acknowledgments v

Co-Authorship Statement vii

Table of Contents xiii

List of Tables xiv

List of Figures xvii

List of Abbreviations xviii

1 Introduction and Overview 1

1.1 Background and Motivation 1

1.2 Key 6G Communication Technologies 2

1.2.1 Reconfigurable Intelligent Surface (RIS) 3

1.2.2 Non-Orthogonal Multiple Access (NOMA) 3

1.2.3 Cell-Free Massive Multiple-Input Multiple-Output (CFmMIMO) . . 6

1.2.4 Integrated Sensing and Communication (ISAC) 8

1.2.5 Full-Duplex (FD) 9

1.3 Thesis Contribution 10
1.4 Thesis Organization 11
References 12

2 Outage Analysis and Sum Rate Maximization of Full-Duplex, Simultaneous Wireless Information and Power Transfer, Cooperative NOMA-Aided Overlay Spectrum-Sharing Networks 18

2.1 Abstract 18
2.2 Introduction 19
2.3 System Model 24
2.3.1 System Description 24
2.3.2 Signal Model 25
2.4 Performance Analysis 29
2.4.1 Primary Network 30
2.4.1.1 Outage Probability 30
2.4.1.2 Throughput 32
2.4.2 Secondary Network 32
2.4.2.1 Outage Probability 32
2.4.2.2 Throughput 33
2.5 Sum Rate Maximization 33
2.5.1 Problem Formulation 34
2.5.2 Proposed Solution 36
2.5.3 Convergence and Complexity Analysis 39
2.6 Numerical Results 40
2.6.1 Outage Probability 41
2.6.2 System Throughput 46
2.6.3 Sum Rate 46

2.7 Conclusion . . . 48
Appendix A . . . 49
Appendix B . . . 49
Appendix C . . . 52
Appendix D . . . 54
References . . . 55

3 Efficient User Clustering Approaches and Sum Rate Maximization in NOMA-CFmMIMO Networks 60

3.1 Abstract . . . 60
3.2 Introduction . . . 61
3.2.1 Related Work . . . 62
3.2.2 Motivation and Main Contributions . . . 65
3.2.3 Chapter Organization and Notations . . . 66
3.3 System Model . . . 67
3.3.1 System Description . . . 67
3.3.2 Signal Model and Sum Spectral Efficiency (SSE) . . . 68
3.3.2.1 Uplink Training . . . 68
3.3.2.2 Downlink Data Transmission . . . 70
3.3.2.3 Downlink Performance Analysis . . . 72
3.4 Clustering Cell-Free Massive MIMO-NOMA System . . . 75
3.4.1 The k-means Algorithm . . . 75
3.4.2 Proposed k-means++ Algorithm . . . 79
3.4.3 Proposed Improved k-means++ Algorithm . . . 80
3.5 The SSE Maximization . . . 83
3.6 COmMIMO-NOMA System . . . 88
3.6.1 Performance Analysis . . . 89

3.6.2 Proposed Solution to Problem (3.49) . . . 90
3.7 Numerical Results . . . 92
3.7.1 Simulation Parameters . . . 92
3.7.2 Selection of the Initial Number of Clusters . . . 93
3.7.3 Numerical Results for the Performance Analysis . . . 95
3.7.4 Numerical Results for Optimal Power Allocation . . . 97
3.8 Conclusion . . . 100
Appendix A . . . 101
References . . . 103

4 Energy Efficiency Maximization in RIS-Aided Cell-Free Network with Limited Backhaul 109

4.1 Abstract . . . 109
4.2 Introduction . . . 110
4.3 System Model . . . 111
4.3.1 Transmission Model . . . 112
4.3.1.1 Optimization Problem Formulation . . . 113
4.4 Proposed Alternating Descent-based Iterative Algorithm . . . 115
4.4.1 Beamforming Descent Iteration . . . 115
4.4.2 Phase Descent Iteration . . . 118
4.5 Numerical Results . . . 120
4.6 Conclusion . . . 124
Appendix A . . . 124
References . . . 125

5 Transmit Power Minimization of RIS-Enabled Federated Learning Networks 127

5.1 Abstract . . . 127
5.2 Introduction . . . 128
5.3 System Model . . . 130
5.3.1 Wireless Power Transfer (WPT) Model . . . 131
5.3.2 Distributed Federated Learning (FL) Model . . . 132
5.4 Problem Formulation . . . 134
5.5 Proposed Solution . . . 136
5.5.1 Transmit Power Optimization . . . 136
5.5.2 Aggregation Beamforming Optimization . . . 138
5.5.3 Phase Shift Optimization . . . 138
5.6 Numerical Results . . . 140
5.7 Conclusion . . . 143
References . . . 144

6 Transmission Rate Maximization in RIS-Assisted FD ISAC Networks 147

6.1 Abstract . . . 147
6.2 Introduction . . . 148
6.3 System Model and Problem Formulation . . . 149
6.3.1 System Model . . . 149
6.3.2 Problem Formulation . . . 151
6.4 Proposed Solution . . . 151
6.4.1 Transmit Power and Beamforming Iteration . . . 152
6.4.2 Phase Shift Iteration . . . 153
6.4.3 Sub-Optimal Design based on Maximal Ratio Transmission (MRT) 157
6.5 Numerical Results . . . 159
6.6 Conclusion . . . 162
References . . . 164

7 Conclusions and Future Work **167**

7.1 Conclusions 167

7.2 Possible Directions for Future Research 168

List of Tables

3.1 Simulation Parameters. 93

3.2 Silhouette Score for CFmMIMO-NOMA and COmMIMO-NOMA. 94

4.1 Simulation Parameters. 121

List of Figures

1.1 An illustration of the downlink power-domain NOMA model with two UEs. 4

1.2 An illustration of the uplink power-domain NOMA model with two UEs. . 4

1.3 An illustration of the CFmMIMO system. 6

2.1 Illustration of FD NOMA-supported cooperative overlay CR network. . . . 23

2.2 Block time T for the FD $\mathrm{ST_b}$. 26

2.3 Outage probability of primary and secondary networks operating in FD and HD modes, where $\beta = 0.8$, $N = 5$, and $K = 3$. ana: analytical results; sim: simulation results. 40

2.4 Impact of the number of STs K on the outage performance of primary and secondary networks operating in FD and HD modes, where $\beta = 0.8$, $N = 5$, and $\bar{\gamma} = -9$ dB. 42

2.5 Effect of the number of transmit antennas N on the outage performance of primary and secondary networks operating in FD and HD modes, where $\beta = 0.8$, $K = 3$, and $\bar{\gamma} = -9$ dB. 43

2.6 Impact of the PS β on the outage performance of primary and secondary networks operating in FD and HD modes, where $N = 5$, $K = 3$, and $\bar{\gamma} = -5$ dB. 44

2.7 Impact of ST_b-PR channel mean on the outage probability of primary and secondary networks operating in FD and HD modes, where $\beta = 0.8$, $N = 5$, $K = 3$, $\bar{\gamma} = -5$ dB, $\lambda_{ps} = 5$, and $\lambda_{sr} = 50$. 45
2.8 System throughput of primary and secondary networks operating in FD and HD modes, where $\beta = 0.8$, $N = 5$, and $K = 3$. 45
2.9 Convergence of the proposed sum rate maximization algorithm with different number of SRs M in FD and HD modes, where $\beta = 0.8$, $N = 5$, $K = 3$, and $\bar{\gamma} = -5$ dB. 46
2.10 Effect of ST_b-PR channel mean on the average sum rate of the proposed network in FD and HD modes, where $\beta = 0.8$, $N = 5$, $K = 3$, $\bar{\gamma} = -5$ dB, $\lambda_{ps} = 5$, and $\lambda_{sr} = 50$. 47
2.11 Impact of the PS coefficient β on the average sum rate of the proposed network in FD and HD modes, where $N = 5$, $K = 3$, and $\bar{\gamma} = -5$ dB. . . . 48

3.1 An illustration of the CFmMIMO-NOMA system. 67
3.2 A system topology with $M = 32$ APs and $N = 20$ UEs is used in numerical examples. 94
3.3 The SSE of CFmMIMO-NOMA versus the total power budget of all APs for the k-means, k-means++, and improved k-means++ algorithms. 95
3.4 The SSE of CFmMIMO-NOMA and COmMIMO-NOMA versus the total power budget of all APs. 96
3.5 Convergence behavior of Algorithm 5 with different number of AP antennas, K. 97
3.6 The SSE of different UC algorithms. 98
3.7 SSE of CFmMIMO-NOMA and COmMIMO-NOMA: with and without PA. 99
3.8 The effect of SIC performance coefficient on the SSE of CFmMIMO-NOMA and COmMIMO-NOMA systems. 99

3.9 The joint effect of the numbers of antennas K and APs M on the average SSE of different UC algorithms, for $MK = 512$. 100
3.10 Effect of the number of UEs L on the SSE for the k-means, k-means++, and improved k-means++ algorithms. 101

4.1 Illustration of an RIS-CF network. 112
4.2 System layout with $M = 4$ APs, $N = 4$ RISs, and $L = 8$ UEs. 121
4.3 Convergence of Algorithm 6 with different number of antennas per AP. . . 122
4.4 Average EE vs. the maximum transmit power per AP, $P^{\max}$. 123
4.5 Average EE vs. the maximum backhaul capacity, $C^{\max}$. 123

5.1 System model. 131
5.2 Convergence of Algorithm 7 with different values of Θ_k. 140
5.3 Total transmit power of participating MUs versus the numbers of MUs. . . 141
5.4 Total transmit power of participating MUs versus the number of RIS REs with different values of Θ_k. 142
5.5 Total transmit power of participating MUs versus the number of RIS REs with different numbers of MUs. 142

6.1 The RIS-ISAC system. 149
6.2 Convergence rate of Algorithm 8 with different values of K. 160
6.3 Transmission rate of the UE versus the UE's transmit power. 161
6.4 Transmission rate of the UE versus the BS's receive antennas. 161
6.5 Transmission rate of the UE versus the required sensing power. 162

List of Abbreviations

5G	Fifth Generation
6G	Sixth Generation
AI	Artificial Intelligence
AP	Access Point
AWGN	Additive White Gaussian Noise
BCA	Block Coordinate Ascend
BS	Base Station
CDF	Cumulative Distribution Function
CFmMIMO	Cell-Free Massive Multiple-Input Multiple-Output
CPU	Central Processing Unit
CR	Cognitive Radio
CSI	Channel State Information
DoF	Degree-of-Freedom
EE	Energy Efficiency

EH	Energy Harvesting
eMBB	Enhanced Mobile Broadband
ES	Exhaustive Search
FD	Full-Duplex
FL	Federated Learning
fpZF	full-pilot Zero-Forcing
HD	Half-Duplex
i.i.d	independent and identically distributed
IA	Inner Approximation
ID	Information Decoding
ISAC	Integrated Sensing And Communication
KKT	Karush-Kuhn-Tucker
MIMO	Multiple-Input Multiple-Output
ML	Machine Learning
MMSE	Minimum Mean Square Error
mMTC	Massive Machine Type Communication
MRT	Maximum Ratio Transmission
mRZF	modified Regularized Zero-Forcing
MUs	Mobile Users

NOMA	Non-Orthogonal Multiple Access
PDF	Probability Density Function
PT	Primary Transmitter
PU	Primary User
QoS	Quality-of-Service
RE	Reflecting Element
RF	Radio Frequency
RIS	Reconfigurable Intelligent Surface
SE	Spectral Efficiency
SI	Self-Interference
SIC	Successive Interference Cancellation
SINR	Signal-to-Interference-plus-Noise Ratio
SOCP	Second-Order Cone Programming
SR	Secondary Transmitter
ST	Secondary Transmitter
SU	Secondary User
SWIPT	Simultaneous Wireless Information and Power Transfer
TDD	Time Division Duplex
TDMA	Time Division Multiple Access

UAV	Unmanned Aerial Vehicle
UC	User Clustering
UDN	Ultra-Dense Network
UE	User Equipment
URLLC	Ultra-Reliable and Low Latency Communications
VLC	Visible Light Communication
WPT	Wireless Power Transfer

Chapter 1

Introduction and Overview

1.1 Background and Motivation

Within the last decade, mobile communication systems have significantly evolved to meet the escalating demand for high data rates [1]. Such demand has ever-increased with the recent epidemic of COVID–19 to support remote data sharing and high-quality video conferencing. Fulfilling such high data rates is, however, challenging due to the scarcity of wireless resources, i.e., bandwidth, power, frequency, and time [2]. To cope with this scarcity, diverse resource allocation schemes are provided as an efficient means to enhance the system's performance [3]. Resource allocation strategies intend to assign limited resources to users, maximizing the utilization of these resources, and attaining the best system performance.

In future communication networks, e.g., sixth-generation (6G) wireless, resource allocation techniques have to be integrated with novel emerging communication technologies to help satisfy the demands for emerging services [4]. For instance, 6G networks are expected to reach a 100-fold peak data rate (Tb/s) growth, a 10-fold latency decrease, and a 99.99 % end-to-end reliability requirement compared to the fifth-generation

(5G) networks [5]. These service requirements have stimulated upcoming communication scenarios to replace the conventional 5G enhanced mobile broadband (eMBB), massive machine type communication (mMTC), and ultra-reliable and low latency communications (URLLC) with their improved 6G counterparts: further eMBB, ultra mMTC, and URLLC diverse variants [5]. Further, several technologies including cell-free massive multiple-input multiple-output (CFmMIMO) [6], full-duplex (FD) [1], integrated sensing and communication (ISAC) [7], non-orthogonal multiple access (NOMA) [7], and reconfigurable intelligent surface (RIS) [8] have been proposed to fulfill the increased service requirements of 6G networks. CFmMIMO has the potential to provide all users in a network with uniform quality-of-service (QoS) [6]. FD has the ability to theoretically double the spectral efficiency (SE) by allowing transceivers to simultaneously transmit and receive data in the same frequency band [1]. NOMA ensures that multiple users are served within the same spectrum resources, thus enhancing the SE and user fairness [7]. RIS can improve the capacity and coverage of wireless communication networks by smartly reconfiguring the wireless propagation environment through software-controlled reflections [8]. ISAC enables the combination of sensing and communication systems in order to efficiently utilize resources and make use of their mutual advantages [7]. Reaping the benefits of the above technologies can be further expanded by integration with resource allocation techniques. Motivated by the above, this dissertation aims to optimize resource allocation and propose optimal or low-complexity sub-optimal solutions to enhance the system performance for CFmMIMO, FD, ISAC, NOMA, and RIS-assisted networks.

1.2 Key 6G Communication Technologies

In order to obtain the target 6G performance, enabling technologies such as RIS, NOMA, CFmMIMO, ISAC, and FD have been introduced [9]. Details of such technologies are

presented in the following subsections.

1.2.1 Reconfigurable Intelligent Surface (RIS)

Recently, RIS has been considered as a promising technology to improve the capacity and coverage of wireless communication networks by smartly reconfiguring the wireless propagation environment through software-controlled reflections [10]. Specifically, RIS is a planar array structure that consists of a large number of low-cost passive reflecting elements. These elements, independently adjusted by the RIS controller, cause amplitude and/or phase modifications to the electromagnetic incident signals in order to be coherently added toward specific positions. Hence, RIS can be able to intelligently change the channel conditions between the transmitter and the receiver via controllable and smart signal reflections [10, 11]. Owing to its potential to achieve fine-tuned channel gains, enhanced QoS, and improved coverage range of wireless networks, integrating RIS with other emerging technologies, such as NOMA, CFmMIMO, ISAC, and FD has attracted considerable research attention. For example, RIS can significantly boost the SE for NOMA systems [12, 13], enhance the SE and the energy efficiency (EE) for CFmMIMO systems [12, 14], improve communication, sensing and localization precision for ISAC systems [8, 12], and decrease the effect of self-interference (SI) at the FD systems' receivers [15].

1.2.2 Non-Orthogonal Multiple Access (NOMA)

NOMA has been recognized as a technology which has the potential to enhance the SE and user fairness for 5G and beyond wireless networks [16]. In NOMA, multiple user equipments (UEs) are allowed to simultaneously transmit and receive their signals in the same time-frequency resources by using different signal signatures (i.e., code-domain NOMA) or power levels (i.e., power-domain NOMA). Power-domain NOMA has been

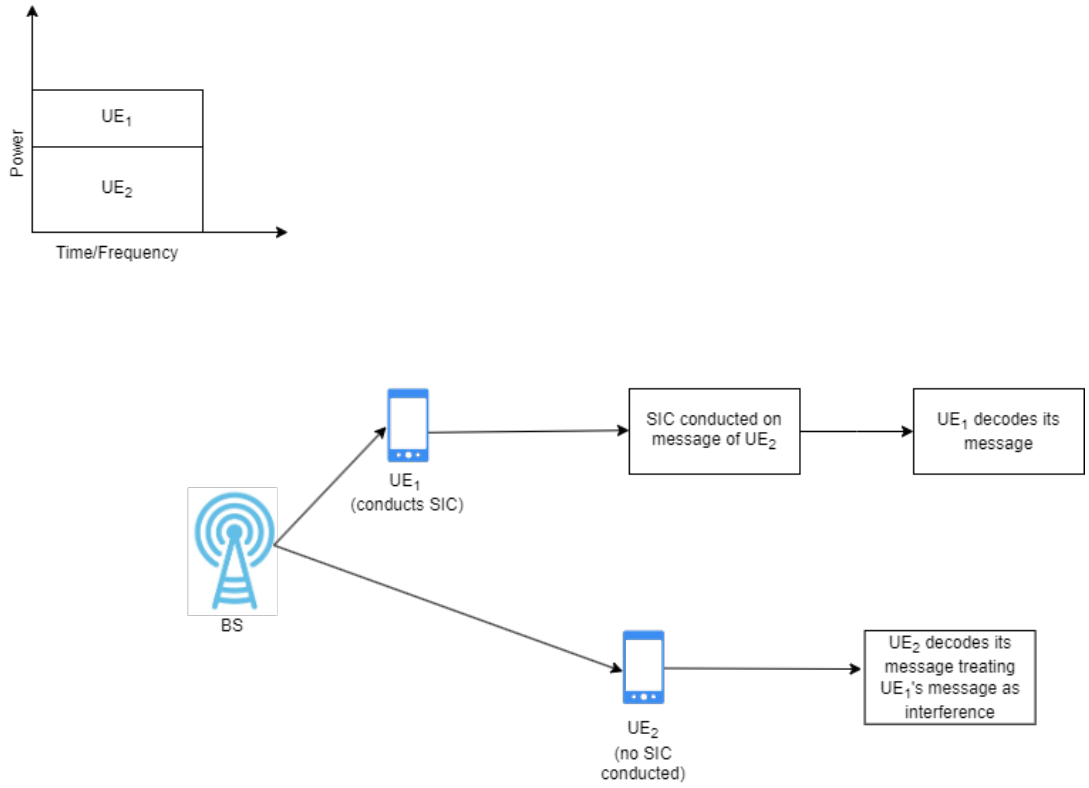

Fig. 1.1: An illustration of the downlink power-domain NOMA model with two UEs.

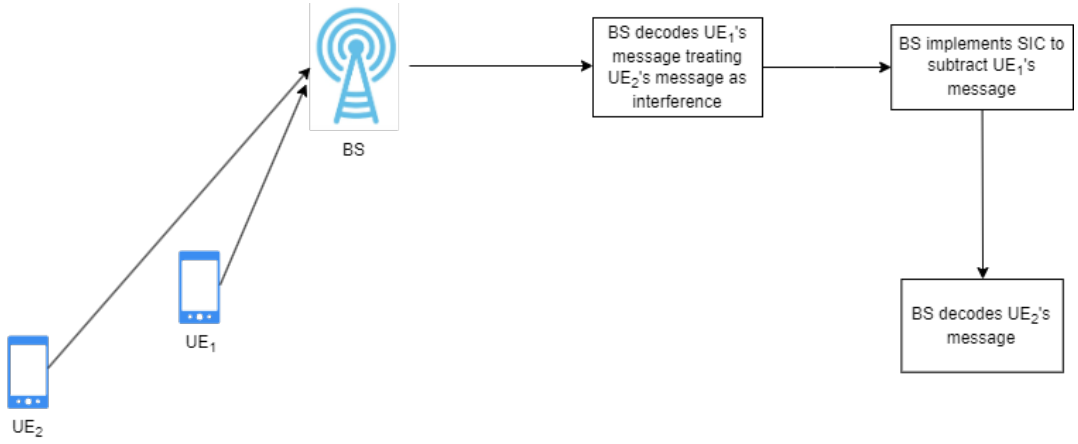

Fig. 1.2: An illustration of the uplink power-domain NOMA model with two UEs.

shown to have the potential to considerably enhance the SE and realize massive connectivity [17]. NOMA[1] has been demonstrated to outperform conventional orthogonal multiple access (OMA) schemes in many aspects, e.g., by providing lower latency, higher spectrum efficiency, and massive connectivity [18].

In downlink NOMA, the key benefit is attributed to the fact that UEs with better channel conditions are able to cancel the interference caused by UEs with poorer channel conditions using the successive interference cancellation (SIC) technique. User fairness is then achieved by allocating a large portion of the total power budget to the weak UEs, which also guarantees SIC's feasibility at the strong UEs. Fig. 1.1 illustrates an example of downlink power-domain NOMA scenario with two UEs. The UE with weak channel conditions, i.e., UE_2, is allocated more power to decode its signal by considering UE_1's signal as noise. By implementing the SIC technique, the UE with strong channel conditions, i.e., UE_1, can decode the UE_2's signal, subtract the UE_2's signal from the superimposed signal, and then decode its own signal.

In uplink NOMA, the base station (BS) conducts successive decoding and cancellation of different UE signals, ranked by their channel strength. Fig. 1.2 illustrates an example of uplink power-domain NOMA scenario with two UEs. The BS firstly decodes the UE_1's signal by considering the UE_2's signal as noise. Secondly, SIC is performed by the BS to subtract the UE_1's signal and then decode the UE_2's signal.

Thus so far, many research works have been performed to solve the resource allocation problems for both downlink and uplink NOMA transmission schemes, and some examples are provided as follows. With regard to downlink NOMA, Si et al. [19] proposed a power allocation algorithm to maximize the strong user's transmission rate in a NOMA system. An energy-efficient power allocation scheme was developed in [20] to maximize the EE of a NOMA system. With regard to uplink NOMA, a joint time switching and power

[1]NOMA refers to power-domain NOMA in the rest of this dissertation.

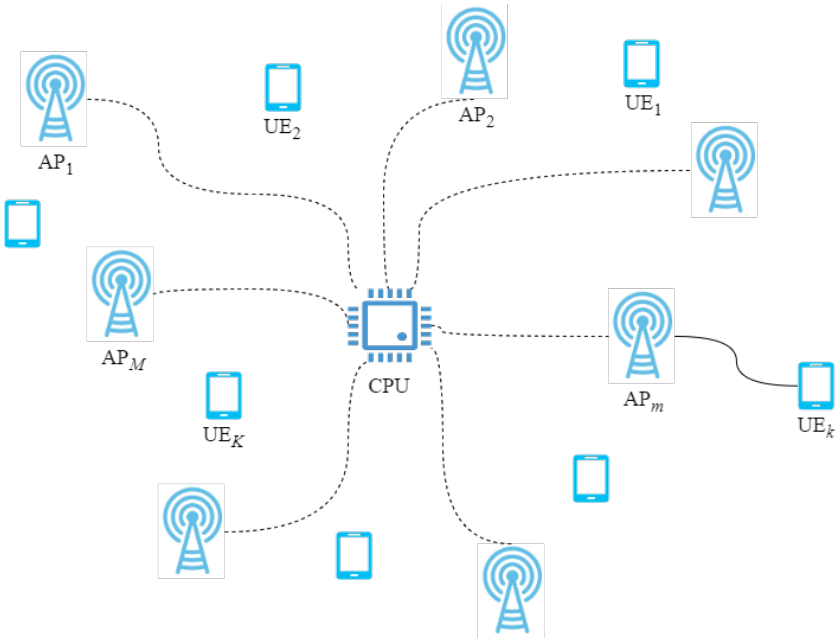

Fig. 1.3: An illustration of the CFmMIMO system.

allocation strategy was proposed in [21] to maximize the uplink data rate for an uplink NOMA system. A three-step resource allocation optimization strategy, including equalizer optimization, power allocation, and RIS beamforming, was developed in [22] to maximize the sum rate for a uplink NOMA system.

1.2.3 Cell-Free Massive Multiple-Input Multiple-Output (CFmMIMO)

CFmMIMO is one of the major technological enablers for 6G wireless networks [6]. As illustrated in Fig. 1.3, a large number of spatially distributed access points (APs) are connected to a central processing unit (CPU) and coherently serve multiple UEs in the same time-frequency resources [23]. The CFmMIMO technology has received increased research attention in recent years due to (i) its potential to offer all UEs in a network with uniform QoS, (ii) the possible compatibility with recent developments in radio-access network, (iii) the great improvement of the network performance in various aspects, such as

superior SE and EE, as compared to the co-located mMIMO and conventional small-cell systems, and (iv) the flexible integration with various emerging technologies for 5G and beyond networks in order to enhance the network performance in different perspectives, such as enhancing the network coverage, SE, EE, and massive connectivity [6, 23]. Thus so far, research works have been carried out to handle the resource allocation problems for CFmMIMO operation with enabling technologies, i.e., NOMA, RIS, and FD. With regard to the CFmMIMO integration with NOMA, UEs are grouped into spatial clusters, and all UEs in each cluster are served on the same time-frequency-spatial resources, while the transmitted data messages to/from different UEs are assigned various power levels [6]. In [24], an optimum power allocation design was proposed to maximize the SE for a NOMA-based CFmMIMO system. The authors in [25] developed an optimal method for user pairing in a RIS-NOMA-assisted CFmMIMO system. By integrating NOMA with CFmMIMO systems, the number of concurrently served UEs becomes higher than that of OMA-assisted CFmMIMO systems. Also, such integration can lead to a significant performance improvement for system models with low path-loss exponents and high AP density. With regard to the CFmMIMO operation with RIS, utilizing RIS can enhance the SE and EE of the CFmMIMO systems due to an extra degree-of-freedom (DoF) provided by RIS. In [26], the sum rate of a RIS-assisted CFmMIMO system is maximized by optimizing the APs' transmit beamforming and RIS coefficients. The authors in [27] considered the EE maximization problem of RIS-assisted CFmMIMO system. Results showed that the RIS-based CFmMIMO systems achieve higher sum data rate and EE than the conventional CFmMIMO systems. With regard to the CFmMIMO integration with FD, APs operating in FD mode can boost the SE of CFmMIMO systems since they are able to serve both downlink and uplink UEs on the same spectrum resource [28, 29]. Also, low-cost and low-power APs are well-suited for short-range transmissions between APs and UEs [30]. In [28], the sum SE of an FD-CFmMIMO system was maximized by

optimizing the AP duplex mode selection. The authors in [29] considered the SE maximization problem of an FD-CFmMIMO system by optimizing the AP selection, power, and subcarrier allocation.

1.2.4 Integrated Sensing and Communication (ISAC)

Sensing is considered an important task of the next-generation cellular networks [31]. Many emerging mobile applications, such as smart manufacturing and industrial Internet-of-Things, not only need high-rate transmission with low latency and high reliability, but also require location information with high accuracy [32]. In order to offer better performance and efficiently utilize the spectrum, energy and hardware resources, integrating sensing and communication functions into a single network has become a favorable approach. By jointly optimizing wireless resources, waveform and signal processing flow, a significant performance gain can be achieved in ISAC networks [31, 32]. Research has been conducted to deal with the resource allocation problems for ISAC integrated with enabling technologies, e.g., RIS, NOMA, and FD. With regard to the ISAC integration with RIS, the latter can be used to simultaneously modify the communication and sensing channels, thus improving both communication and sensing performance [33]. In [34], the sum rate maximization problem of a RIS-assisted ISAC system was addressed by jointly optimizing the transmit beamforming at the BS and the phase shifts of RIS. Simulation results showed that the proposed system considerably decreases the mutual interference between radar and BS, and enhances the sum rate for the communication system. In [35], the minimum beampattern gain was maximized by jointly optimizing transmit beamforming at BS, power allocation coefficients among NOMA UEs, and reflection coefficients at the RIS for a NOMA-assisted RIS-ISAC system. NOMA can be beneficial for the proposed RIS-ISAC system due to i) its potential to offer extra DoFs by multiplexing UEs in the power domain and utilizing SIC to mitigate the inter-user interference, and ii) its

capability to allow more UEs to be served than the conventional OMA. With regard to the ISAC integration with FD, working in the FD mode can allow the transceivers to concurrently transmit a dual-functional signal, receive the echo signal, and remove the SI due to the leakage of the transmit signal to the receiver [36]. In [37], a two-criteria optimization problem, i.e., power consumption minimization and sum rate maximization, was addressed by jointly optimizing the downlink dual-functional transmit signal, the uplink receive beamformers at the BS, and the transmit power at the uplink UEs. Simulation results showed that FD communication-assisted ISAC outperforms the half-duplex (HD) communication-based ISAC in terms of SE and EE.

1.2.5 Full-Duplex (FD)

FD can theoretically double the SE of wireless networks due to its ability to enable simultaneous transmission and reception in the same frequency band. This is in contrast to the traditional HD systems that require the use of distinct orthogonal links for downlink and uplink transmissions. FD systems, however, suffer from the SI, where the received signal is interfered by the transmitted signal. Recent advancements in SI suppression techniques have been introduced to reduce the SI problem and enable FD communication [30]. With proper SI suppression techniques, FD can be a catalyst for boosting other emerging wireless technologies, such as NOMA, CFmMIMO, RIS, and ISAC. These integrated technologies can further enhance the SE and EE, and reduce latency of future wireless networks. Thus so far, research works have been performed to solve the resource allocation problems for FD operation with enabling technologies, i.e., NOMA, CFmMIMO, RIS, and ISAC. With regard to the FD integration with NOMA, using NOMA can help reduce latency and enhance massive connectivity by serving multiple UEs on the given radio resources at the same time [38–40]. In [38], the authors analyzed various FD NOMA-based models, including cooperative, cellular, and cognitive networks, and provided insights on resource

allocation problems. The authors in [39] addressed the resource allocation problem to maximize the sum rate for a RIS-aided FD multi-channel NOMA network. In [40], the total transmit power minimization problem for a RIS-aided FD-NOMA network was formulated and solved by jointly optimizing the power allocation coefficients, the active and the passive beamformings. The authors in [39, 40] showed that incorporating RIS with FD communication-based networks is profitable as it can help increase the SE and EE, and expand the network coverage. With regard to the CFmMIMO and ISAC integration with FD, it is of practical interest to employ FD in CF-mMIMO and ISAC systems in order to reap all their combined benefits for achieving higher SE and EE [28, 29], and enabling sensing and communication simultaneously [30, 36, 37].

1.3 Thesis Contribution

In this thesis, I have identified and investigated the following research points:

1. I have studied the application of FD, simultaneous wireless information and power transfer (SWIPT), and NOMA in cooperative spectrum-sharing networks. The outage probability and throughput have been derived in tight closed-form approximated expressions and used to evaluate the system performance. The power allocation problem has been formulated and solved by a proposed rapid convergent iterative algorithm to maximize the sum rate of the primary and secondary networks [41].

2. I have devised novel and efficient unsupervised machine learning-based user clustering (UC) algorithms to effectively cluster UEs into disjoint clusters for a CFmMIMO-NOMA system. The sum SE maximization problem, taking into account power constraints at APs, necessary conditions for implementing SIC, and required SE constraints at UEs, has been formulated and solved by a proposed simple yet efficient iterative algorithm [42].

3. I have investigated the integration of RIS in a cell-free (CF) network. The EE maximization problem, considering a joint design of transmit beamformers at APs and reflecting coefficients at RISs of RIS-CF network, has been formulated and addressed by a proposed simple yet efficient alternating algorithm [43].

4. I have developed a framework that applies RIS-aided wireless power transfer (WPT) in a federated learning (FL) network. The participating mobile users' total transmit power minimization problem, taking into account a joint design of the transmission time, power control, and the RIS's phase shifts, has been formulated and solved by a proposed simple yet efficient iterative algorithm [44].

5. I have explored the application of RIS in an ISAC network. The optimization problem, involving a joint design of the BS's transmit beamforming, UE's transmit power, and RIS's phase shifts, has been formulated and addressed by a proposed block coordinate ascend (BCA)-based iterative algorithm to maximize the UE's transmission rate [45].

1.4 Thesis Organization

In the remainder of this dissertation, each of the above-mentioned research contributions is discussed as follows. Chapter 2 develops an outage analysis and an optimization algorithm for sum rate maximization of FD, SWIPT, and NOMA-assisted spectrum sharing networks. Chapter 3 introduces efficient UC approaches and proposes an optimization framework for sum rate maximization of NOMA-based CFmMIMO networks. Chapter 4 focuses on RIS-assisted CF networks and presents an optimization framework to maximize the EE performance. Chapter 5 considers RIS-enabled FL networks and develops an optimization algorithm to minimize the total transmit power of MUs. Chapter 6 introduces RIS-assisted FD ISAC networks and proposes an optimization algorithm to maximize the

transmission rate of UE. Finally, Chapter 7 draws conclusions and presents the directions for future research.

References

[1] A. Yadav and O. A. Dobre, "All technologies work together for good: A glance to future mobile networks," *IEEE Wireless Commun.*, vol. 25, no. 4, pp. 10–16, Aug. 2018.

[2] Y. Xu, G. Gui, H. Gacanin, and F. Adachi, "A survey on resource allocation for 5G heterogeneous networks: Current research, future trends, and challenges," *IEEE Commun. Surveys Tuts.*, vol. 23, no. 2, pp. 668–695, 2nd Quart. 2021.

[3] B. Su, *Resource Allocation Optimization for Future Wireless Communication Systems.* Ph.D dissertation, School of Comput. and Commun., Lancaster Univ., Lancaster, UK, 2020. [Online]. Available: https://eprints.lancs.ac.uk/id/eprint/148097/1/Resource_Allocation_Optimization_for_Future_Wireless_Communication_Systems.pdf

[4] X. You *et al.*, "Toward 6G TKμ extreme connectivity: Architecture, key technologies and experiments," *IEEE Wireless Commun.*, vol. 30, no. 3, pp. 86–95, June 2023.

[5] Z. Wang *et al.*, "A tutorial on extremely large-scale MIMO for 6G: Fundamentals, signal processing, and applications," *arXiv preprint arXiv:2307.07340v1*, July 2023.

[6] S. Elhoushy, M. Ibrahim, and W. Hamouda, "Cell-free massive MIMO: A survey," *IEEE Commun. Surveys Tuts.*, vol. 24, no. 1, pp. 492–523, 1st Quart. 2022.

[7] X. Mu, Z. Wang, and Y. Liu, "NOMA for integrating sensing and communications towards 6G: A multiple access perspective," *IEEE Wireless Commun.*, pp. 1–8, early access, Jan. 2023.

[8] R. Liu *et al.*, "Integrated sensing and communication with reconfigurable intelligent surfaces: Opportunities, applications, and future directions," *IEEE Wireless Commun.*, vol. 30, no. 1, pp. 50–57, Feb. 2023.

[9] C.-X. Wang *et al.*, "On the road to 6G: Visions, requirements, key technologies, and testbeds," *IEEE Commun. Surveys Tuts.*, vol. 25, no. 2, pp. 905–974, 2nd Quart. 2023.

[10] Y. Liu *et al.*, "Reconfigurable intelligent surfaces: Principles and opportunities," *IEEE Commun. Surveys Tuts.*, vol. 23, no. 3, pp. 1546–1577, 3rd Quart. 2021.

[11] H. Zhang and B. Di, "Intelligent omni-surfaces: Simultaneous refraction and reflection for full-dimensional wireless communications," *IEEE Commun. Surveys Tuts.*, vol. 24, no. 4, pp. 1997–2028, 4th Quart. 2022.

[12] O. Maraqa *et al.*, "A survey of rate-optimal power domain NOMA with enabling technologies of future wireless networks," *IEEE Commun. Surveys Tuts.*, vol. 22, no. 4, pp. 2192–2235, 4th Quart. 2020.

[13] X. Li *et al.*, "Sum rate maximization for RIS-aided NOMA with direct links," *IEEE Netw. Lett.*, vol. 4, no. 2, pp. 55–58, June 2022.

[14] T. V. Chien *et al.*, "Phase shift design for RIS-aided cell-free massive MIMO with improved differential evolution," *IEEE Wireless Commun. Lett.*, vol. 12, no. 9, pp. 1499–1503, Sep. 2023.

[15] P. K. Sharma and P. Garg, "Intelligent reflecting surfaces to achieve the full-duplex wireless communication," *IEEE Commun. Lett.*, vol. 25, no. 2, pp. 622–626, Feb. 2021.

[16] Y. Liu *et al.*, "Developing NOMA to next generation multiple access: Future vision and research opportunities," *IEEE Wireless Commun.*, vol. 29, no. 6, pp. 120–127, Dec. 2022.

[17] M. Zeng, W. Hao, O. A. Dobre, and Z. Ding, "Cooperative NOMA: State of the art, key techniques, and open challenges," *IEEE Netw.*, vol. 34, no. 5, pp. 205–211, Sep./Oct. 2020.

[18] Y. Yuan *et al.*, "NOMA for next-generation massive IoT: Performance potential and technology directions," *IEEE Commun. Mag.*, vol. 59, no. 7, pp. 115–121, July 2021.

[19] Q. Si *et al.*, "Cooperative SM-based NOMA scheme with SWIPT," *IEEE Trans. Veh. Technol.*, vol. 70, no. 6, pp. 6195–6199, June 2021.

[20] H. Cui, X. Ye, and F. You, "Energy-efficient resource allocation for heterogeneous SWIPT-NOMA systems," *IEEE Access*, vol. 10, pp. 79 281–79 288, July 2022.

[21] M. B. Goktas and Z. Ding, "A wireless power transfer assisted NOMA transmission scheme for 5G and beyond mMTC," *IEEE Wireless Commun. Lett.*, vol. 11, no. 6, pp. 1239–1242, June 2022.

[22] X. Yang, H. Wang, and Y. Feng, "Sum rate maximization for active RIS-aided uplink multi-antenna NOMA systems," *IEEE Wireless Commun. Lett.*, vol. 12, no. 7, pp. 1149–1153, July 2023.

[23] H. A. Ammar *et al.*, "User-centric cell-free massive MIMO networks: A survey of opportunities, challenges and solutions," *IEEE Commun. Surveys Tuts.*, vol. 24, no. 1, pp. 611–652, 1st Quart. 2022.

[24] J. Zhang *et al.*, "Performance analysis and optimization of NOMA-based cell-free massive MIMO for IoT," *IEEE Internet Things J.*, vol. 9, no. 12, pp. 9625–9639, June 2022.

[25] X.-T. Dang *et al.*, "Optimal user pairing approach for NOMA-based cell-free massive MIMO systems," *IEEE Trans. Veh. Technol.*, vol. 4, no. 72, pp. 4751–4765, Apr. 2023.

[26] Y. Zhang *et al.*, "Reconfigurable intelligent surface aided cell-free MIMO communications," *IEEE Wireless Commun. Lett.*, vol. 10, no. 4, pp. 775–779, Apr. 2021.

[27] ——, "Beyond cell-free MIMO: Energy efficient reconfigurable intelligent surface aided cell-free MIMO communications," *IEEE Trans. Cogn. Commun. Netw.*, vol. 7, no. 2, pp. 412–426, June 2021.

[28] Y. Zhu *et al.*, "Optimization of duplex mode selection for network-assisted full-duplex cell-free massive MIMO systems," *IEEE Commun. Lett.*, vol. 25, no. 11, pp. 3649–3653, Nov. 2021.

[29] B. Li *et al.*, "Spectral-efficiency of cell-free massive MIMO with multicarrier-division duplex," *IEEE Trans. Veh. Technol.*, vol. 72, no. 3, pp. 3404–3418, Mar. 2023.

[30] M. Mohammadi, Z. Mobini, D. Galappaththige, and C. Tellambura, "A comprehensive survey on full-duplex communication: Current solutions, future trends, and open issues," *IEEE Commun. Surveys Tuts.*, vol. 25, no. 4, pp. 2190–2244, 4th Quart. 2023.

[31] J. A. Zhang *et al.*, "Enabling joint communication and radar sensing in mobile networks—a survey," *IEEE Commun. Surveys Tuts.*, vol. 24, no. 1, pp. 306–345, 1st Quart. 2022.

[32] A. Liu *et al.*, "A survey on fundamental limits of integrated sensing and communication," *IEEE Commun. Surveys Tuts.*, vol. 24, no. 2, pp. 994–1034, 2nd Quart. 2022.

[33] S. P. Chepuri *et al.*, "Integrated sensing and communications with reconfigurable intelligent surfaces: From signal modeling to processing," *IEEE Signal Process. Mag.*, vol. 40, no. 6, pp. 41–62, Sep. 2023.

[34] E. Shtaiwi *et al.*, "Sum-rate maximization for RIS-assisted integrated sensing and communication systems with manifold optimization," *IEEE Trans. Commun.*, vol. 71, no. 8, pp. 4909–4923, Aug. 2023.

[35] J. Zuo *et al.*, "Exploiting NOMA and RIS in integrated sensing and communication," *IEEE Trans. Veh. Technol.*, vol. 72, no. 10, pp. 12 941–12 955, Oct. 2023.

[36] Z. Liu, S. Aditya, H. Li, and B. Clerckx, "Joint transmit and receive beamforming design in full-duplex integrated sensing and communications," *IEEE J. Sel. Areas Commun.*, vol. 41, no. 9, pp. 2907–2919, Sep. 2023.

[37] Z. He *et al.*, "Full-duplex communication for ISAC: Joint beamforming and power optimization," *IEEE J. Sel. Areas Commun.*, vol. 41, no. 9, pp. 2920–2936, Sep. 2023.

[38] M. Mohammadi *et al.*, "Full-duplex non-orthogonal multiple access for next generation wireless systems," *IEEE Commun. Mag.*, vol. 57, no. 5, pp. 110–116, May 2019.

[39] M. Forouzanmehr and S. Akhlaghi, "Sum-rate maximization for RIS-aided full-duplex non-orthogonal multiple access networks: Joint passive beamforming and resource allocation," *IEEE Trans. Green Commun. Netw.*, vol. 1, no. 1, pp. 1–13, Aug. 2023.

[40] Q. Wang *et al.*, "Transmit power minimization for STAR-RIS aided FD-NOMA networks," *IEEE Trans. Veh. Technol.*, pp. 1–6, Oct. 2023.

[41] Q. N. Le, A. Yadav, N.-P. Nguyen, O. A. Dobre, and R. Zhao, "Full-duplex non-orthogonal multiple access cooperative overlay spectrum-sharing networks with SWIPT," *IEEE Trans. Green Commun. Netw.*, vol. 5, no. 1, pp. 322–334, Mar. 2021.

[42] Q. N. Le, V.-D. Nguyen, O. A. Dobre, N.-P. Nguyen, R. Zhao, and S. Chatzinotas, "Learning-assisted user clustering in cell-free massive MIMO-NOMA networks," *IEEE Trans. Veh. Technol.*, vol. 70, no. 12, pp. 12 872–12 887, Oct. 2021.

[43] Q. N. Le, V.-D. Nguyen, O. A. Dobre, and R. Zhao, "Energy efficiency maximization in RIS-aided cell-free network with limited backhaul," *IEEE Commun. Lett.*, vol. 25, no. 6, pp. 1974–1978, Feb. 2021.

[44] Q. N. Le, L. Bariah, O. A. Dobre, and S. Muhaidat, "Reconfigurable intelligent surface-enabled federated learning for power-constrained devices," *IEEE Commun. Lett.*, vol. 26, no. 11, pp. 2725–2729, Aug. 2022.

[45] Q. N. Le, V.-D. Nguyen, O. A. Dobre, and H. Shin, "RIS-assisted full-duplex integrated sensing and communication," *IEEE Wirel. Commun. Lett.*, vol. 12, no. 10, pp. 1677–1681, Oct. 2023.

Chapter 2

Outage Analysis and Sum Rate Maximization of Full-Duplex, Simultaneous Wireless Information and Power Transfer, Cooperative NOMA-Aided Overlay Spectrum-Sharing Networks

2.1 Abstract

This chapter proposes a novel NOMA assisted cooperative spectrum-sharing network, in which one of the FD secondary transmitters (STs) is chosen among many for forwarding the primary transmitter's and its own information to primary receiver and secondary receivers, respectively, using NOMA technique. To stimulate the ST to conduct cooperative

transmission and sustain its operations, the SWIPT technique is utilized by the ST to harvest the primary signal's energy. In order to evaluate the proposed system's performance, the outage probability and system throughput for the primary and secondary networks are derived in tight closed-form approximations. Further, the sum rate optimization problem is formulated for the proposed cooperative network and a rapid convergent iterative algorithm is proposed to obtain the optimized power allocation coefficients. Numerical results show that FD, SWIPT, and NOMA techniques greatly boost the performance of cooperative spectrum-sharing network in terms of outage probability, system throughput, and sum rate compared to that of half-duplex NOMA and the conventional orthogonal multiple access-time division multiple access networks.

2.2 Introduction

NOMA has been recognized as a potential SE improving technique for the fifth-generation (5G) and beyond wireless networks [1–4]. Its underlying principle enables multiple users to concurrently access and transmit their signals in the same spectrum resource block (i.e., time/frequency/code domain) by using different signal signatures for the case of code-domain NOMA (CD-NOMA) or power levels for the case of power-domain NOMA (PD-NOMA). Message passing algorithm and successive interference cancellation (SIC) are used to separate the superimposed signals for CD-NOMA and PD-NOMA, respectively. Since NOMA can enhance the SE, user fairness, and realize massive connectivity compared to the conventional OMA scheme, it can greatly enhance the performance of wireless networks [1, 5]. In [5], a cooperative relaying system in a device-to-device-NOMA was proposed and its performance was evaluated in terms of scaled system capacity. The proposed system achieved much higher ergodic capacity compared to the conventional OMA system.

For 5G and beyond networks, in addition to the prerequisite of high SE, providing energy-efficient communications is also an important goal. Further, since wireless users are battery-operated, it is more likely that performing cooperative transmisison task will lead to rapid energy exhaustion of their batteries. In order to help mobile users maintain their operations, SWIPT [6, 7] has come out as an efficient way to provide energy and extend the lifetime of energy-constrained wireless devices. In [6], the authors proposed a SWIPT-based NOMA network in which near users being close to the source acted as energy scavenging relays to help the source forward the data to far users. Closed-form expressions for the outage probability and system throughput were obtained to assess the system performance. The authors in [7] developed the system model where the relay user scavenged energy from the base station (BS)'s NOMA signal and used harvested power to forward the information to the destination. The outage probability was used as a performance metric to evaluate their proposed system's performance. However, the work in [5–7] considered half-duplex (HD) relaying mode, where relay nodes cannot simultaneously receive and transmit information in the same frequency band.

With the advancement in antenna and signal processing technologies, FD communication mode has attracted much research interest due to its ability in doubling the spectral efficiency by allowing users to simultaneously receive and transmit data in the same frequency band [8–10]. In [11], the authors proposed the user-assisted cooperative NOMA system in which the strong user operating in FD or HD mode forwarded the information message to the weak user. By analysing the system outage probability and ergodic sum rate, the authors concluded that FD NOMA was superior to HD NOMA in the low signal-to-noise ratio (SNR) region. In [12], the authors considered SWIPT in a cooperative FD NOMA system where the near user relayed the message to the far user by harvesting the radio frequency (RF) energy. The result showed that the effect of self-interference (SI) signal in FD communications was mitigated thanks to SWIPT since additional gain could

be achieved. Besides, cognitive radio (CR) is another potential technology that significantly improves the spectrum efficiency by allowing unauthorized secondary users (SUs) to access authorized primary users's (PUs) spectrum. Hence, integrating NOMA to CR networks has a highly conceivable possibility to provide an efficient spectrum use, so that the requirements of 5G and beyond wireless networks, i.e., high spectral efficiency, low latency, and massive connectivity, can be readily achieved [13, 14]. Considering multiple-input multiple-output (MIMO) CR-NOMA system, the authors in [15] proposed a novel joint antenna selection algorithm to further enhance the system performance. In [16], a cooperative multicast for CR-NOMA scheme was developed to improve the outage probability of PU. In order to maximize the harvested energy of SUs and based on a practical non-linear energy harvesting (EH) model, the authors in [17] proposed an optimal resource allocation strategy in a SWIPT-CR-NOMA network, where SUs shared the licensed spectrum with PUs under the condition that the interference caused by SUs was acceptable. In [18], the cooperative NOMA relay-supported CR network was investigated where SU helped PU by acting as relays and exploited NOMA technique to transmit the PU's and its own messages together to the destination using the licensed spectrum band. Under the same system model as in [18], [19] focused on user scheduling schemes to improve the outage performance for both primary and secondary systems.

Unlike the existing works [15–17], [20] which considered NOMA underlay CR networks, this chapter proposes a novel FD NOMA assisted cooperative overlay spectrum-sharing system with SWIPT that encourages the cooperation between primary and secondary networks. Given that FD, SWIPT, and NOMA are potential spectral and energy efficiency improving technologies for the beyond 5G wireless networks, applying such technologies will not only boost the system performance, but also showcase that they can be operated in tandem in future networks. Although there exist a few works [18, 19] which also considered the application of NOMA to overlay CR network, the major differences of our

work compared with the existing ones are as follows. Firstly, besides spectrum sharing to secondary transmitters (STs), in order to stimulate STs to perform cooperative relaying functions and sustain their operations in terms of energy, SWIPT is applied in our proposed system where STs can harvest RF energy from the primary transmitter (PT)'s signal and use it for their relaying operations. Secondly, STs operate in FD mode, which allows them to concurrently receive and transmit signals in the same transmission time. As a result, significant increase in the spectral and energy efficiencies of the system is readily achieved. Thirdly, the effect of STs scheduling on the system performance is considered, where the best ST is selected to maximize the harvested power and improve the reception quality of primary and secondary networks. The main contributions of this chapter are summarized as follows:

- This chapter proposes an opportunistic ST selection method to choose one best FD ST, which has the best channel connection to the PT, among multiple ones. Besides, this is the first work considering the application of FD, SWIPT, and NOMA in cooperative spectrum-sharing networks.

- This chapter characterizes the performance of primary and secondary networks in terms of outage probability and system throughput over Rayleigh fading channels. To this end, the tight closed-form approximation expressions are obtained for outage probability and system throughput of both primary and secondary networks. Through numerical results, it is shown that the application of FD, SWIPT, and NOMA techniques significantly improve the proposed system performance compared to HD and the conventional OMA-time division multiple access (OMA-TDMA) schemes.

- This chapter proposes an efficient algorithm which solves the power allocation problem to maximize the sum rate of primary and secondary networks. The obtained

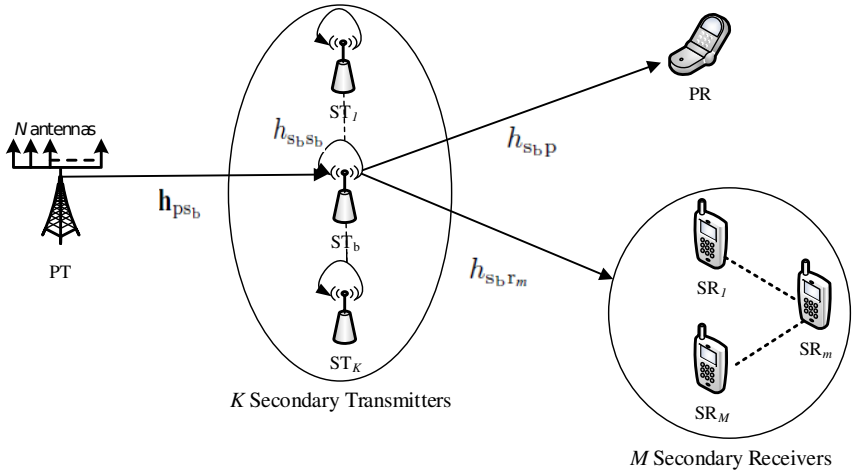

Fig. 2.1: Illustration of FD NOMA-supported cooperative overlay CR network.

results show the superior performance of FD compared to its HD counterpart.

The remainder of this chapter is organized as follows. Section 2.3 describes the system model. In Section 2.4, the outage probability and system throughput for both primary and secondary networks are successfully derived. In Section 2.5, a novel power allocation optimization algorithm is proposed to maximize the sum rate of primary and secondary networks. Numerical results and discussions are shown in Section 2.6. Finally, the chapter is concluded in Section 2.7.

Notations: Bold lowercase letters denote vectors and lowercase characters stand for scalars. $||\cdot||$, $(\cdot)^H$ and $|\cdot|$ correspond to the Euclidean norm, the Hermitian operator, and the absolute value, respectively. $\mathbb{E}[\cdot]$ represents the expectation operation, $\Pr(\cdot)$ denotes probability, and $\mathbb{C}$ is the set of complex-valued numbers.

2.3 System Model

2.3.1 System Description

As illustrated in Fig. 2.1, this chapter considers a cooperative overlay spectrum-sharing system consisting of one pair of primary transceivers denoted by PT and PR, K STs denoted by ST_k, $k = 1, 2, \ldots, K$, and M secondary receivers (SRs) denoted by SR_m, $m = 1, 2, \ldots, M$. All STs operate in FD mode and others operate in HD mode. The PT is equipped with N antennas, $n = 1, 2, \ldots, N$, while the PR and M SRs are equipped with one transmitting/receiving antenna. Each ST has two antennas, one for receiving and the other one for transmitting [12, 21]. The direct link between the PT and the PR does not exist since the PR is far away from the PT [19, 22, 23]. Hence, in order to establish communication between PT and PR, we consider an overlay spectrum-sharing scenario where the PT allows STs to access its spectrum resources as a reward for improving the primary reception by cooperative relaying. The best ST (denoted henceforth by $\mathrm{ST_b}$) is selected among K STs to concurrently transmit the primary information together with its own data to the PR and M SRs by employing the NOMA technique. The aim of selecting the $\mathrm{ST_b}$ is to obtain the best primary and secondary outage performances. Besides, in order to further encourage the $\mathrm{ST_b}$ to conduct the cooperative relaying function, SWIPT is utilized in the model where the $\mathrm{ST_b}$ can harvest energy from the PT signal and use it for relaying purpose [22].

The transmission time is partitioned into equal transmission time slots of duration T. All wireless channels undergo Rayleigh block fading with coherence time of T. The channel coefficients are independent and identically distributed (i.i.d.) from one slot to the next. The channel coefficients from the $\mathrm{ST_b}$ to the PR and the SR_m are denoted by complex scalars $h_{\mathrm{s_b p}}$ and $h_{\mathrm{s_b r}_m}$, respectively. Under Rayleigh fading model, the channel gains $|h_{\mathrm{s_b p}}|^2$ and $|h_{\mathrm{s_b r}_m}|^2$ are exponential random variables (RVs) with mean $\mathbb{E}[|h_{\mathrm{s_b p}}|^2] = \lambda_{\mathrm{sp}}$

and $\mathbb{E}[|h_{\mathrm{s_b r}_m}|^2] = \lambda_{\mathrm{sr}}$, respectively. The channel vector from the PT to the ST_k is denoted by $\mathbf{h}_{\mathrm{ps}_k} \in \mathbb{C}^{N\times 1}$, where each element follows the Rayleigh distribution. Therefore, the channel gain $||\mathbf{h}_{\mathrm{ps}_k}||^2$ follows the Gamma distribution with parameter (N, λ_{ps}), where λ_{ps} denotes the mean. Transmit beamforming is used for PT-$\mathrm{ST_b}$ link to enhance the reception quality of the $\mathrm{ST_b}$. The noise at each receiver is modeled as additive white Gaussian noise (AWGN) with zero mean and variance σ_n [18, 19]. Further, all nodes are assumed to have perfect channel state information (CSI) to other nodes [18, 19, 22, 23].

2.3.2 Signal Model

At the start of the transmission time slot T, the $\mathrm{ST_b}$ is selected by the PT according to the following selection criterion:

$$\mathrm{ST_b} = \underset{k=1,2,\ldots,K}{\arg\max}\, ||\mathbf{h}_{\mathrm{ps}_k}||^2. \tag{2.1}$$

Practically, the PT can obtain the CSIs from the K STs by first sending the pilot signals to STs, then STs will estimate and feedback their CSIs to the PT. Thereafter, the PT will select a ST ($\mathrm{ST_b}$) which has the best connection to it.

After choosing the $\mathrm{ST_b}$, the PT beamforms its signal to the $\mathrm{ST_b}$. The received RF signal sent by the PT at the $\mathrm{ST_b}$ is given by

$$y_{\mathrm{p,s_b}} = \mathbf{h}_{\mathrm{ps_b}}^H \mathbf{w}_{\mathrm{p}} \sqrt{P_{\mathrm{s}}} x_0 + h_{\mathrm{s_b s_b}} \sqrt{P_{\mathrm{s_b}}} x_s + n_{\mathrm{s_b}}, \tag{2.2}$$

where $\mathbf{w}_{\mathrm{p}} = \mathbf{h}_{\mathrm{ps_b}}/||\mathbf{h}_{\mathrm{ps_b}}||$ denotes the transmit beamforming vector, x_0 is the PT's information signal with $\mathbb{E}[|x_0|^2] = 1$, x_s is the composite transmit signal[1] of the $\mathrm{ST_b}$ including signals of the PR and M SRs with $\mathbb{E}[|x_s|^2] = 1$. $P_{\mathrm{s_b}}$ denotes the transmit power of the

[1]This chapter assumes that the FD STs decode the received signal without any delay, and hence, the decoded PT's signal x_0 is included in x_s.

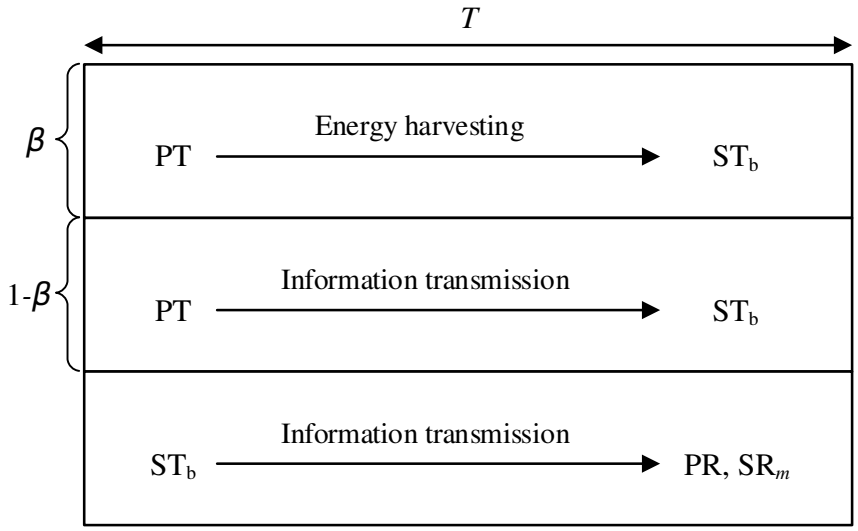

Fig. 2.2: Block time T for the FD $\mathrm{ST_b}$.

$\mathrm{ST_b}$, $h_{\mathrm{s_b s_b}}$ represents the SI channel, and $n_{\mathrm{s_b}}$ is the AWGN antenna noise at the $\mathrm{ST_b}$.

Fig. 2.2 describes the transmission time slot T at the $\mathrm{ST_b}$, where the fraction β ($0 < \beta < 1$) of the received RF signal power from the PT is used for EH and the remaining (1-β) fraction of the received RF signal energy for information decoding (ID). Thus, according to (2.2), the harvested power at the $\mathrm{ST_b}$ is given by [24, 25]

$$P_{\mathrm{H}} = \eta\beta\Big(\underbrace{P_{\mathrm{s}}||\mathbf{h}_{\mathrm{ps_b}}||^2}_{\text{RF EH}} + \underbrace{P_{\mathrm{s_b}}|h_{\mathrm{s_b s_b}}|^2}_{\text{Self-EH}} \Big), \tag{2.3}$$

where η denotes the energy conversion efficiency, $0 < \eta \leq 1$. The $\mathrm{ST_b}$ harvests both the dedicated energy from the PT and its own energy from the SI channel [25, 26].

From (2.3), since the energy harvested from the PT is much larger than that of the receiver noise, this chapter ignores the negligible energy harvested from the receiver noise [24]. Next, the transmit power and the harvested power of the $\mathrm{ST_b}$ should satisfy $P_{\mathrm{s_b}} = \xi\psi P_{\mathrm{H}}$ [24], where $P_{\mathrm{s_b}}$ refers to the transmit power of the $\mathrm{ST_b}$, ξ denotes the portion of the harvested power consumed by the power amplifier of the $\mathrm{ST_b}$, and ψ is the energy utilization efficiency, $0 \leq \xi \leq 1$ and $0 < \psi < 1$. Thus, the available transmit power of the

$\mathrm{ST_b}$ is expressed as:

$$\begin{aligned} P_{\mathrm{s_b}} &= \xi\psi P_{\mathrm{H}} \\ &= \eta\beta\xi\psi\Big(P_{\mathrm{s}}||\mathbf{h}_{\mathrm{ps_b}}||^2 + P_{\mathrm{s_b}}|h_{\mathrm{s_b s_b}}|^2\Big) \\ &= \rho P_{\mathrm{s}}||\mathbf{h}_{\mathrm{ps_b}}||^2, \end{aligned} \tag{2.4}$$

where $\rho = \frac{\eta\beta\xi\psi}{1-\eta\beta\xi\psi|h_{\mathrm{s_b s_b}}|^2}$.

The sampled baseband signal at the $\mathrm{ST_b}$ is shown as:

$$y^{\mathrm{ID}}_{\mathrm{p,s_b}} = \mathbf{h}^H_{\mathrm{ps_b}}\mathbf{w}_{\mathrm{p}}\sqrt{(1-\beta)P_{\mathrm{s}}}x_0 + h_{\mathrm{s_b s_b}}\sqrt{(1-\beta)P_{\mathrm{s_b}}}x_s + \sqrt{(1-\beta)}n_{\mathrm{s_b}} + n_{c,\mathrm{s_b}}, \tag{2.5}$$

where $n_{c,\mathrm{s_b}}$ denotes the AWGN circuit noise due to RF to baseband signal conversion. We ignore the antenna noise $n_{\mathrm{s_b}}$ since its strength is much lower than that of the circuit processing noise $n_{c,\mathrm{s_b}}$ [24]. Hence, (2.5) can be rewritten as:

$$y^{\mathrm{ID}}_{\mathrm{p,s_b}} = \mathbf{h}^H_{\mathrm{ps_b}}\mathbf{w}_{\mathrm{p}}\sqrt{(1-\beta)P_{\mathrm{s}}}x_0 + h_{\mathrm{s_b s_b}}\sqrt{(1-\beta)P_{\mathrm{s_b}}}x_s + n_{c,\mathrm{s_b}}. \tag{2.6}$$

From (2.4) and (2.6), the achievable data rate at the $\mathrm{ST_b}$ to decode x_0 is given by

$$R_{\mathrm{s_b},x_0} = \log_2\left(1 + \frac{(1-\beta)\bar{\gamma}||\mathbf{h}_{\mathrm{ps_b}}||^2}{(1-\beta)\rho\bar{\gamma}|h_{\mathrm{s_b s_b}}|^2||\mathbf{h}_{\mathrm{ps_b}}||^2 + 1}\right), \tag{2.7}$$

where $\bar{\gamma} = P_{\mathrm{s}}/\sigma_n$ denotes the transmit SNR.

The $\mathrm{ST_b}$ first decodes x_0. If x_0 is successfully decoded, the $\mathrm{ST_b}$ superimposes x_0 with x_i, $i = 1, 2, \ldots, M$, according to the NOMA principle and broadcasts the composite signal $x_s = \sum_{i=0}^{M}\sqrt{\alpha_i P_{\mathrm{s_b}}}x_i$ to all $M+1$ receivers, where x_i denotes the information signal intended to the PR ($i = 0$) and SR_i ($i = 1, \ldots, M$), and α_i denotes the corresponding power allocation coefficient with condition $\sum_{i=0}^{M}\alpha_i = 1$. Accordingly, the composite received

signal at the receiver r_i, $0 \leq i \leq M$, from the $\mathrm{ST_b}$ can be expressed as:

$$y_{\mathrm{s_b},\mathrm{r}_i} = \sum_{i=0}^{M} \sqrt{\alpha_i P_{\mathrm{s_b}}} h_{\mathrm{s_b r}_i} x_i + n_{\mathrm{r}_i}, \tag{2.8}$$

where $h_{\mathrm{s_b r}_0}$ is also denoted as $h_{\mathrm{s_b p}}$.

This chapter considers the pessimistic case when the PR is grouped with M SRs whose channel gains are stronger.[2] Hence, the channel gain of the $\mathrm{ST_b}$-PR link is always smaller than the channel gains of the $\mathrm{ST_b}$-SR_m links. Henceforth, we assume that channel gains are sorted as $|h_{\mathrm{s_b p}}|^2 \leq |h_{\mathrm{s_b r}_1}|^2 \leq \ldots \leq |h_{\mathrm{s_b r}_M}|^2$ at the $\mathrm{ST_b}$ [18, 19]. Based on the NOMA principle, the power allocation coefficients used at the $\mathrm{ST_b}$ should fulfil the following condition $\alpha_0 \geq \ldots \geq \alpha_M$ [18, 19].

Each SR_m performs SIC to distinguish the superimposed signals. The SR_m first decodes x_0 followed by $x_1, \ldots, x_m$ according to the order of the $\mathrm{ST_b}$-SR_m channel gains. Using (2.4) and (2.8), the achievable data rate at the SR_m to decode x_m is expressed as:

$$R_{\mathrm{r}_m} = R_{\mathrm{r}_m, x_m} = \log_2 \left(1 + \mathrm{SINR}_{\mathrm{r}_m, x_m}\right), \tag{2.9}$$

where SINR represents signal-to-interference-plus-noise ratio.

The rate (2.9) is achievable provided that the condition $R_{\mathrm{r}_v, x_m} \geq \bar{R}_m$, $\forall v > m$, $v = m+1, \ldots, M$, is met, where $\bar{R}_m$ denotes the predefined target data rate set for SR_m, and R_{r_v, x_m} is the achievable data rate at the SR_v to decode x_m with $v > m$, which is expressed as:

$$R_{\mathrm{r}_v, x_m} = \log_2 \left(1 + \mathrm{SINR}_{\mathrm{r}_v, x_m}\right), \tag{2.10}$$

[2]Note that this is a worst case for PR in terms of outage probability, system throughput, and sum transmission rate. This will be showed later in this chapter. For the other cases when the channel gain of the PR is stronger than M SRs, the analysis of these cases can be similarly obtained.

where

$$\mathrm{SINR}_{\mathrm{r}_v,x_m} = \log_2\left(1 + \frac{\alpha_m \rho\bar{\gamma}||\mathbf{h}_{\mathrm{ps_b}}||^2|h_{\mathrm{s_br}_v}|^2}{\sum\limits_{i=m+1}^{M} \alpha_i \rho\bar{\gamma}||\mathbf{h}_{\mathrm{ps_b}}||^2|h_{\mathrm{s_br}_v}|^2 + 1}\right). \tag{2.11}$$

The SR_v then successfully subtracts x_m from the received composite signal. The SIC process will last until its own signal x_v is successfully decoded. Similarly, the achievable data rate at the PR to decode x_0 is expressed as:

$$R_{\mathrm{p}} = R_{\mathrm{r}_0,x_0} = \log_2\left(1 + \frac{\alpha_0 \rho\bar{\gamma}||\mathbf{h}_{\mathrm{ps_b}}||^2|h_{\mathrm{s_bp}}|^2}{\sum\limits_{i=1}^{M} \alpha_i \rho\bar{\gamma}||\mathbf{h}_{\mathrm{ps_b}}||^2|h_{\mathrm{s_bp}}|^2 + 1}\right), \tag{2.12}$$

where $h_{\mathrm{s_bp}} = h_{\mathrm{s_br}_0}$, and the achievable data rate at the SR_M to decode x_M is expressed as:

$$R_{\mathrm{r}_M} = R_{\mathrm{r}_M,x_M} = \log_2\left(1 + \alpha_M \rho\bar{\gamma}||\mathbf{h}_{\mathrm{ps_b}}||^2|h_{\mathrm{s_br}_M}|^2\right). \tag{2.13}$$

Note that if $\mathrm{ST_b}$ fails to decode x_0, it will not transmit any signals. This can be explained by the sole purpose that PT grants $\mathrm{ST_b}$ the permission to access primary spectrum only if $\mathrm{ST_b}$ is able to help it send its message to the PR. Thus, the achievable data rates at the PR and the SR_m in both cases are shown as:

$$R_{\mathrm{p}} = R_{\mathrm{r}_m} = 0. \tag{2.14}$$

2.4 Performance Analysis

This section will provide the performance analysis for primary and secondary networks in terms of outage probability and system throughput for the proposed system. The outage

analysis is useful for practical purposes, as it offers information about the minimum data rate over which a wireless link or a communications system can operate as desired.

2.4.1 Primary Network

2.4.1.1 Outage Probability

In order to calculate the outage probability for the primary network, this section needs to obtain the cumulative distribution function (CDF) and probability density function (PDF) of $||\mathbf{h}_{\mathrm{ps_b}}||^2$, which are given in Lemma 2.1.

Lemma 2.1. *The* CDF *and* PDF *of* $||\mathbf{h}_{\mathrm{ps_b}}||^2$ *are derived as:*

$$F_{||\mathbf{h}_{\mathrm{ps_b}}||^2}(x) = \sum_{l=0}^{K} \binom{K}{l} (-1)^l \exp\left(-\frac{lx}{\lambda_{\mathrm{ps}}}\right) \sum_{j=0}^{l(N-1)} \frac{C_j x^j}{{\lambda_{\mathrm{ps}}}^j}, \tag{2.15}$$

$$f_{||\mathbf{h}_{\mathrm{ps_b}}||^2}(x) = \sum_{l=1}^{K} \binom{K}{l} (-1)^l \exp\left(-\frac{lx}{\lambda_{\mathrm{ps}}}\right) \sum_{j=0}^{l(N-1)} \frac{C_j}{{\lambda_{\mathrm{ps}}}^j} \left(j x^{j-1} - \frac{l}{\lambda_{\mathrm{ps}}} x^j\right). \tag{2.16}$$

Proof: See Appendix A. ■

Next, this section derives the outage probability for the primary network, where the outage event occurs under two circumstances. The first situation is when the $\mathrm{ST_b}$ can not successfully decode x_0. The second one occurs when the PR can not decode x_0 provided that the $\mathrm{ST_b}$ is able to decode x_0. Accordingly, the outage probability of the primary network is expressed as:

$$P_{\mathrm{p}} = \Pr\left(R_{\mathrm{s_b},x_0} < \bar{R}_0\right) + \Pr\left(R_{\mathrm{s_b},x_0} \geq \bar{R}_0, R_{\mathrm{p}} < \bar{R}_0\right), \tag{2.17}$$

where $\bar{R}_0$ is the target data rate of the primary signal x_0.

Remark. *Recalling* (2.4) *and* (2.7)*, it is obvious that when the power splitting (PS) coefficient* β *increases, the transmit power* ($P_{\mathrm{s_b}}$) *and the achievable data rate* ($R_{\mathrm{s_b},x_0}$) *of the* $\mathrm{ST_b}$ *readily rise. It is also straightforward to see that the achievable data rates of the* PR *and* SRs*, which are illustrated in* (2.12) *and* (2.13)*, go up with the increase in* β*. Thus, the increase in* $R_{\mathrm{s_b},x_0}$ *leads to the decrease in outage probability of the primary network in* (2.17) *and the secondary network in* (2.20)*. However, when* β *reaches the optimal value at which the lowest outage probability of primary and secondary networks is obtained, and if* β *continues increasing to 1, the achievable data rate of* $\mathrm{ST_b}$ *in* (2.7) *decreases and reaches to 0. This is due to the fact that less power is left for the* $\mathrm{ST_b}$ *to decode* x_0*; hence, the outage probability of both networks, as given in* (2.17) *and* (2.20)*, increases and attains 1, which results in the worst performance. This result is also corroborated in* Fig. 2.6.

Theorem 2.1. *The outage probability of the primary network can be approximated as:*

$$P_{\mathrm{p}} \approx \sum_{l=0}^{K} \binom{K}{l} (-1)^l \exp\left(-\frac{l\mu}{\lambda_{\mathrm{ps}}\bar{\gamma}}\right) \sum_{j=0}^{l(N-1)} C_j \left(\frac{\mu}{\lambda_{\mathrm{ps}}\bar{\gamma}}\right)^j + \iota_q \widetilde{\sum}\Big(\sim\Big) \frac{(-1)^{c+n+l}}{q+c} \frac{C_j}{l^j} \times \left[\left(j + \frac{n\Theta_0 l}{\lambda_{\mathrm{sp}}\lambda_{\mathrm{ps}}\bar{\gamma}}\right)\Gamma\left(j, \frac{l\mu}{\lambda_{\mathrm{ps}}\bar{\gamma}}\right) - \Gamma\left(j+1, \frac{l\mu}{\lambda_{\mathrm{ps}}\bar{\gamma}}\right) - \frac{n\Theta_0 jl}{\lambda_{\mathrm{sp}}\lambda_{\mathrm{ps}}\bar{\gamma}}\Gamma\left(j-1, \frac{l\mu}{\lambda_{\mathrm{ps}}\bar{\gamma}}\right)\right], \tag{2.18}$$

where $\iota_q = \frac{Q!}{(q-1)!(Q-q)!}$, $Q = M+1$, $\widetilde{\sum} = \sum_{c=0}^{Q-q} \sum_{n=0}^{q+c} \sum_{l=1}^{K} \sum_{j=0}^{l(N-1)}$, *and* $\Big(\sim\Big) = \binom{Q-q}{c}\binom{q+c}{n}\binom{K}{l}$. $\gamma_0 = 2^{\bar{R}_0} - 1$, $|h_{\mathrm{s_b s_b}}|^2 = I_{\mathrm{SI}}$, $\mu = \frac{\gamma_0}{(1-\beta)(1-\gamma_0\rho I_{\mathrm{SI}})}$, $\Theta_0 = \frac{\gamma_0}{\rho\left(\alpha_0 - \sum_{i=1}^{M}\alpha_i\gamma_0\right)}$, *and* $\Gamma(\cdot,\cdot)$ *is the incomplete gamma function [28, Eq. (8.350.2)]. Note that* $q = 1$ *for the* PR *and* $q = m+1$ *for the* SR_m*.* P_{p} *is derived in* (2.18) *when* $\gamma_0 < \min\left[1/(\rho I_{\mathrm{SI}}), \alpha_0/\left(\sum_{i=1}^{M}\alpha_i\right)\right]$*, otherwise* $P_{\mathrm{p}} = 1$*.*

Proof: See Appendix B. ■

2.4.1.2 Throughput

Given that the $\mathrm{ST_b}$ transmits information to the PR at a constant rate $\bar{R}_0$ bps/Hz, the throughput of the primary network in the delay-limited transmission mode is computed as [11]:

$$\nu_{\mathrm{p}} = (1 - P_{\mathrm{p}})\, \bar{R}_0, \tag{2.19}$$

where P_{p} is shown in (2.18).

Remark. *From* (2.19)*, since* P_{p} *is smaller than or equals to 1 and as the transmit* SNR $\bar{\gamma}$ *increases, the outage performance of the primary network greatly improves (*P_{p} *decreases as shown in* Fig. 2.3*). Hence, the throughput of the primary network* ν_{p} *goes up with the rise in the transmit* SNR $\bar{\gamma}$ *and converges to a throughput floor which equals to* $\bar{R}_0$ *at high* $\bar{\gamma}$*. Note that the throughput of the secondary network* ν_{s} *given in* (2.22) *also enhances with the increase in the transmit* SNR $\bar{\gamma}$ *and attains a throughput floor which equals to* $\sum_{m=1}^{M} \bar{R}_m$ *at the high* $\bar{\gamma}$*. These results are also verified in* Fig. 2.8.

2.4.2 Secondary Network

2.4.2.1 Outage Probability

This section derives the outage probability for the secondary network. The outage event of the SR_m occurs either when the $\mathrm{ST_b}$ can not successfully decode x_0 or when the SR_m fails to decode any $x_{m'}$, $0 \leq m' \leq m$, as long as $\mathrm{ST_b}$ successfully decodes x_0. Based on this, the outage probability of the SR_m is shown as:

$$P_{\mathrm{r}_m} = \Pr\left(R_{\mathrm{s_b},x_0} < \bar{R}_0\right) + \Pr\left(R_{\mathrm{s_b},x_0} \geq \bar{R}_0, \overline{P}_{\mathrm{r}_m}\right), \tag{2.20}$$

where $\overline{P}_{\mathrm{r}_m}$ denotes the outage probability that the SR_m fails to decode any $x_{m'}$, $0 \leq m' \leq m$.

Theorem 2.2. *The outage probability of the* SR_m *can be approximated as:*

$$P_{\mathrm{r}_m} \approx \sum_{l=0}^{K} \binom{K}{l} (-1)^l \exp\left(-\frac{l\mu}{\lambda_{\mathrm{ps}}\bar{\gamma}}\right) \sum_{j=0}^{l(N-1)} C_j \left(\frac{\mu}{\lambda_{\mathrm{ps}}\bar{\gamma}}\right)^j + \iota_q \widetilde{\sum}\Big(\sim\Big) \frac{(-1)^{c+n+l}}{q+c} \frac{C_j}{l^j} \times \left[\left(j + \frac{n\Theta l}{\lambda_{\mathrm{sr}}\lambda_{\mathrm{ps}}\bar{\gamma}}\right)\Gamma\left(j, \frac{l\mu}{\lambda_{\mathrm{ps}}\bar{\gamma}}\right) - \Gamma\left(j+1, \frac{l\mu}{\lambda_{\mathrm{ps}}\bar{\gamma}}\right) - \frac{n\Theta jl}{\lambda_{\mathrm{sr}}\lambda_{\mathrm{ps}}\bar{\gamma}}\Gamma\left(j-1, \frac{l\mu}{\lambda_{\mathrm{ps}}\bar{\gamma}}\right)\right], \tag{2.21}$$

where $\gamma_{m'} = 2^{\bar{R}_{m'}} - 1$, $\bar{R}_{m'}$ *denotes the target data rate of* $x_{m'}$, $\Theta = \max(\Theta_0, \ldots, \Theta_m)$, $\Theta_{m'} = \frac{\gamma_{m'}}{\rho\left(\alpha_{m'} - \sum_{i=m'+1}^{M} \alpha_i \gamma_{m'}\right)}$, $0 \le m' \le m$. *Note that,* $q = m+1$ *for* SR_m.

Proof: See Appendix C. ■

2.4.2.2 Throughput

The system throughput of the secondary network is given by:

$$\nu_{\mathrm{s}} = \sum_{m=1}^{M} (1 - P_{\mathrm{r}_m}) \bar{R}_m, \tag{2.22}$$

where P_{r_m} is obtained from (2.21).

2.5 Sum Rate Maximization

In the previous section, the power allocation coefficients were kept fixed, which are not optimal. Thus, to further improve the performance of the system, this section formulates the sum rate maximization problem to obtain the optimal power allocation coefficients at the ST_{b} and develop a solution method and algorithm.

2.5.1 Problem Formulation

Recalling (2.9) and the condition $R_{\mathrm{r}_v,x_m} \geq \bar{R}_m$, $\forall v > m$, $v = m+1, \ldots, M$, the achievable data rate to decode x_m at the SR_m is expressed as:

$$R_{x_m} = \log_2 \left(1 + \min \left(\mathrm{SINR}_{\mathrm{r}_m,x_m}, \ldots, \mathrm{SINR}_{\mathrm{r}_M,x_m}\right)\right). \tag{2.23}$$

Lemma 2.2. *From* (2.23)*, the achievable data rate to decode* x_m *by the* SR_m *is rewritten as*

$$R_{x_m} = \log_2 \left(1 + \mathrm{SINR}_{\mathrm{r}_m,x_m}\right). \tag{2.24}$$

Proof: It is proved by contradiction. Let us first assume that $\mathrm{SINR}_{\mathrm{r}_0,x_0} \geq \mathrm{SINR}_{\mathrm{r}_1,x_0}$. Then, we have

$$\begin{aligned}
&\mathrm{SINR}_{\mathrm{r}_0,x_0} \geq \mathrm{SINR}_{\mathrm{r}_1,x_0} \\
&\Leftrightarrow \frac{\alpha_0 \rho \bar{\gamma} ||\mathbf{h}_{\mathrm{ps_b}}||^2 |h_{\mathrm{s_bp}}|^2}{\sum\limits_{i=1}^{M} \alpha_i \rho \bar{\gamma} ||\mathbf{h}_{\mathrm{ps_b}}||^2 |h_{\mathrm{s_bp}}|^2 + 1} \geq \frac{\alpha_0 \rho \bar{\gamma} ||\mathbf{h}_{\mathrm{ps_b}}||^2 |h_{\mathrm{s_br}_1}|^2}{\sum\limits_{i=1}^{M} \alpha_i \rho \bar{\gamma} ||\mathbf{h}_{\mathrm{ps_b}}||^2 |h_{\mathrm{s_br}_1}|^2 + 1} \\
&\Leftrightarrow \alpha_0 \sum_{i=1}^{M} \alpha_i \left(\rho \bar{\gamma} ||\mathbf{h}_{\mathrm{ps_b}}||^2\right)^2 |h_{\mathrm{s_bp}}|^2 |h_{\mathrm{s_br}_1}|^2 + \alpha_0 \rho \bar{\gamma} ||\mathbf{h}_{\mathrm{ps_b}}||^2 |h_{\mathrm{s_bp}}|^2 \\
&\geq \alpha_0 \sum_{i=1}^{M} \alpha_i \left(\rho \bar{\gamma} ||\mathbf{h}_{\mathrm{ps_b}}||^2\right)^2 |h_{\mathrm{s_bp}}|^2 |h_{\mathrm{s_br}_1}|^2 + \alpha_0 \rho \bar{\gamma} ||\mathbf{h}_{\mathrm{ps_b}}||^2 |h_{\mathrm{s_br}_1}|^2 \\
&\Leftrightarrow |h_{\mathrm{s_bp}}|^2 \geq |h_{\mathrm{s_br}_1}|^2.
\end{aligned}$$

The above result violates the condition of channel gain order that is set earlier. Hence, $\mathrm{SINR}_{\mathrm{r}_0,x_0} \leq \mathrm{SINR}_{\mathrm{r}_1,x_0}$. Following similar derivation steps as previously mentioned, $\mathrm{SINR}_{\mathrm{r}_0,x_0} \leq \mathrm{SINR}_{\mathrm{r}_m,x_0}, \forall m$. Thus, $\min \left(\mathrm{SINR}_{\mathrm{r}_0,x_0}, \mathrm{SINR}_{\mathrm{r}_1,x_0}, \ldots, \mathrm{SINR}_{\mathrm{r}_M,x_0}\right) = \mathrm{SINR}_{\mathrm{r}_0,x_0}$.

By generalizing the above result, the achievable data rate to decode the SR_m's data

x_m, $1 \leq m \leq M$, by all $\mathrm{SR}_{m'}$, $m \leq m' \leq M$, is given by

$$\begin{aligned} R_{x_m} &= \log_2\left(1 + \min(\mathrm{SINR}_{\mathrm{r}_m,x_m}, \ldots, \mathrm{SINR}_{\mathrm{r}_M,x_m})\right) \\ &= \log_2\left(1 + \mathrm{SINR}_{\mathrm{r}_m,x_m}\right). \end{aligned} \tag{2.25}$$

■

Using Lemma 2.2, the sum rate maximization problem is formulated as follows:

$$\underset{\boldsymbol{\alpha}}{\text{maximize}} \quad R_{x_0} + \sum_{m'=1}^{M-1} R_{x_{m'}} + R_{x_M} \tag{2.26a}$$

$$\text{s.t.} \quad R_{x_i} \geq \bar{R}_i, 0 \leq i \leq M, \tag{2.26b}$$

$$\alpha_0 \geq \ldots \geq \alpha_i \geq \ldots \geq \alpha_M, \tag{2.26c}$$

$$\sum_{i=0}^{M} \alpha_i \leq 1, \tag{2.26d}$$

where $\boldsymbol{\alpha} = [\alpha_0, \alpha_1, \ldots, \alpha_M]$ denotes the power allocation coefficients vector. The constraint (2.26b) ensures that the QoS requirement $\bar{R}_i$ of each link is guaranteed, the constraint in (2.26c) represents the necessary conditions related to fairness among the users, and the constraint in (2.26d) puts limit on the total transmit power at the ST_b.

It can be observed that the original problem (2.26) is non-convex because of the objective function, and it is difficult to solve it quickly to obtain a global solution. Instead, this section aims to solve it for suboptimal solution with faster convergence. To this end, this section invokes several useful steps, such as its equivalent transformation and approximation, as described in the next subsection, to solve (2.26).

2.5.2 Proposed Solution

By noting that the logarithmic function is a monotonically non-decreasing function, (2.26) is equivalently written as:

$$\underset{\boldsymbol{\alpha}}{\text{maximize}}\left\{ \prod_{i=0}^{M}(1+\text{SINR}_{\text{r}_i,x_i}) \mid (2.26\text{b}), (2.26\text{c}), \text{ and } (2.26\text{d}) \right\}. \tag{2.27}$$

By introducing a new vector of slack variables $\mathbf{t} = [t_0, \ldots, t_M]$, the problem (2.27) can be equivalently recast as:

$$\begin{aligned}
\underset{\boldsymbol{\alpha},\mathbf{t}}{\text{maximize}} \quad & \prod_{i=0}^{M} t_i && (2.28\text{a})\\
\text{s.t.} \quad & \text{SINR}_{r_0,x_0} \geq t_0 - 1, && (2.28\text{b})\\
& \text{SINR}_{r_{m'},x_{m'}} \geq t_{m'} - 1, 1 \leq m' \leq M-1, && (2.28\text{c})\\
& \text{SINR}_{r_M,x_M} \geq t_M - 1, && (2.28\text{d})\\
& \alpha_0 \rho\bar{\gamma}||\mathbf{h}_{\text{ps}_\text{b}}||^2 |h_{\text{s}_\text{b}\text{p}}|^2 \geq \left(2^{\bar{R}_0}-1\right)\left(\sum_{i=1}^{M}\alpha_i\rho\bar{\gamma}||\mathbf{h}_{\text{ps}_\text{b}}||^2|h_{\text{s}_\text{b}\text{p}}|^2+1\right), && (2.28\text{e})\\
& \alpha_{m'}\rho\bar{\gamma}||\mathbf{h}_{\text{ps}_\text{b}}||^2 |h_{\text{s}_\text{b}\text{r}_{m'}}|^2 \geq \left(2^{\bar{R}_{m'}}-1\right)\left(\sum_{i=m'+1}^{M}\alpha_i\rho\bar{\gamma}||\mathbf{h}_{\text{ps}_\text{b}}||^2|h_{\text{s}_\text{b}\text{r}_{m'}}|^2+1\right)\\
& , 1 \leq m' \leq M-1, && (2.28\text{f})\\
& \alpha_M \rho\bar{\gamma}||\mathbf{h}_{\text{ps}_\text{b}}||^2 |h_{\text{s}_\text{b}\text{r}_M}|^2 \geq \left(2^{\bar{R}_M}-1\right), && (2.28\text{g})\\
& (2.26\text{c}) \ \& \ (2.26\text{d}). && (2.28\text{h})
\end{aligned}$$

By noting that the constraints (2.28b)-(2.28d) are active at optimality, then (2.28) is the equivalent formulation of (2.27). Further, note that the objective function (2.28a) is the product of optimization variables $t_i, \forall i$, and hence, admits a second-order cone (SOC) representation. However, (2.28) is still intractable because of the non-convexity involved in constraints (2.28b) and (2.28c). Next, the constraints (2.28b) and (2.28c) are

considered and reformulated as follows:

$$(2.28b) \Leftrightarrow \begin{cases} \sum_{i=1}^{M} \alpha_i \rho \bar{\gamma} ||\mathbf{h}_{\mathrm{ps_b}}||^2 |h_{\mathrm{s_b p}}|^2 + 1 \leq z_0, & (2.29a) \\ \alpha_0 \rho \bar{\gamma} ||\mathbf{h}_{\mathrm{ps_b}}||^2 |h_{\mathrm{s_b p}}|^2 \geq z_0 t_0 - z_0, & (2.29b) \end{cases}$$

$$(2.28c) \Leftrightarrow \begin{cases} \sum_{i=m'+1}^{M} \alpha_i \rho \bar{\gamma} ||\mathbf{h}_{\mathrm{ps_b}}||^2 |h_{\mathrm{s_b r}_{m'}}|^2 + 1 \leq z_{m'}, & (2.30a) \\ \alpha_{m'} \rho \bar{\gamma} ||\mathbf{h}_{\mathrm{ps_b}}||^2 |h_{\mathrm{s_b r}_{m'}}|^2 \geq z_{m'} t_{m'} - z_{m'}, & (2.30b) \end{cases}$$

where $1 \leq m' \leq M-1$ and $\mathbf{z} = [z_0, z_1, \ldots, z_{M-1}]$ represent newly introduced variables. After replacing (2.28b) and (2.28c) with (2.29a) and (2.29b), and (2.30a) and (2.30b), respectively, we get an equivalent formulation of (2.28). However, this is still non-convex because of (2.29b) and (2.30b). To this end, this section approximates them by using the first-order Taylor series expansion. Firstly, this section considers (2.29b) and rewrites the multiplicative terms $z_0 t_0$ in the form of the difference of convex (d.c.) functions as follows:

$$z_0 t_0 = \frac{1}{4} \left[(z_0 + t_0)^2 - (z_0 - t_0)^2 \right]. \tag{2.31}$$

Then, approximating $(z_0 - t_0)^2$ by using the first-order Taylor series around the point $(z_0^{(\tau)}, t_0^{(\tau)})$, which is obtained at the τth iteration, (2.29b) can be replaced with the following convex constraint:

$$\alpha_0 \rho \bar{\gamma} ||\mathbf{h}_{\mathrm{ps_b}}||^2 |h_{\mathrm{s_b p}}|^2 \geq 0.25 (z_0 + t_0)^2 - z_0 - 0.25 \Bigg[\left(z_0^{(\tau)} - t_0^{(\tau)} \right)^2 + 2 \left(z_0^{(\tau)} - t_0^{(\tau)} \right) \times \left(z_0 - z_0^{(\tau)} - t_0 + t_0^{(\tau)} \right) \Bigg]. \tag{2.32}$$

Similarly, (2.30b) can be replaced with the following convex constraint:

$$\alpha_{m'}\rho\bar{\gamma}||\mathbf{h}_{\mathrm{ps_b}}||^2|h_{\mathrm{s_br}_{m'}}|^2 \geq 0.25\left(z_{m'}+t_{m'}\right)^2 - z_{m'} - 0.25\Bigg[\left(z_{m'}^{(\tau)}-t_{m'}^{(\tau)}\right)^2 + 2\left(z_{m'}^{(\tau)}-t_{m'}^{(\tau)}\right) \times \left(z_{m'}-z_{m'}^{(\tau)}-t_{m'}+t_{m'}^{(\tau)}\right)\Bigg]. \tag{2.33}$$

Finally, the convex problem to be solved at the τth iteration can be written as:

$$\underset{\boldsymbol{\alpha},\mathbf{t},\mathbf{z}}{\text{maximize}} \quad \prod_{i=0}^{M} t_i \tag{2.34a}$$

$$\text{s.t.} \quad \begin{cases} \sum\limits_{i=1}^{M} \alpha_i\rho\bar{\gamma}||\mathbf{h}_{\mathrm{ps_b}}||^2|h_{\mathrm{s_bp}}|^2 + 1 \leq z_0, \\ (2.32), \end{cases}, \tag{2.34b}$$

$$\begin{cases} \sum\limits_{i=m'+1}^{M} \alpha_i\rho\bar{\gamma}||\mathbf{h}_{\mathrm{ps_b}}||^2|h_{\mathrm{s_br}_{m'}}|^2 + 1 \leq z_{m'}, \\ (2.33), \end{cases}, 1 \leq m' \leq M-1, \tag{2.34c}$$

$$\alpha_M\rho\bar{\gamma}||\mathbf{h}_{\mathrm{ps_b}}||^2|h_{\mathrm{s_br}_M}|^2 \geq t_M - 1, \tag{2.34d}$$

$$(2.28\mathrm{e}) - (2.28\mathrm{h}). \tag{2.34e}$$

After solving (2.34), the involved optimization variables are updated and the procedure is repeated until convergence. The proposed algorithm is summarized in Algorithm 1.

Algorithm 1 Proposed iterative algorithm to solve (2.26).

Initialization: Set $\tau = 0$ and generate an initial feasible point $(t_i^{(0)}, z_{m'}^{(0)}), 0 \leq i \leq M, 0 \leq m' \leq M-1$.

1: **repeat**
2: Solve the convex program (2.34) to obtain the optimal solution: $(t_i^{(\tau),\star}, z_{m'}^{(\tau),\star}), 0 \leq i \leq M, 0 \leq m' \leq M-1$.
3: Update $(t_i^{(\tau+1)}, z_{m'}^{(\tau+1)}) := (t_i^{(\tau),\star}, z_{m'}^{(\tau),\star}), 0 \leq i \leq M, 0 \leq m' \leq M-1$.
4: Set $\tau = \tau + 1$.
5: **until** Convergence

2.5.3 Convergence and Complexity Analysis

The proposed algorithm begins with a random initial feasible point for the updated variables $(t_i^{(0)}, z_{m'}^{(0)}), 0 \leq i \leq M, 0 \leq m' \leq M-1$. In each iteration, the convex program (2.34) is solved to produce the next feasible point $(t_i^{(\tau+1)}, z_{m'}^{(\tau+1)}), 0 \leq i \leq M, 0 \leq m' \leq M-1$. This procedure is successively repeated until convergence, which is stated in the following proposition.

Proposition 1. *Initialized from a feasible point* $(t_i^{(0)}, z_{m'}^{(0)}), 0 \leq i \leq M, 0 \leq m' \leq M-1$, *Algorithm 1 produces a sequence* $(t_i^{(\tau)}, z_{m'}^{(\tau)}), 0 \leq i \leq M, 0 \leq m' \leq M-1$, *of improved solutions to problem* (2.34), *which satisfy the Karush-Kuhn-Tucker (KKT) conditions. The sequence* $\left\{\prod_{i=0}^{M} t_i^{(\tau)}\right\}_{\tau=1}^{\infty}$ *is monotonically increasing and converges after a finite number of iterations for a given error tolerance* $\epsilon > 0$.

Proof: See Appendix D. ■

An SOC programming (SOCP) is solved in each iteration of the procedure illustrated in Algorithm 1. Hence, the worst case of the complexity is regulated by the SOCP in each run. To assess the complexity estimate, the worst case complexity of the SOCP in (2.34) is estimated. As shown in [29], for general interior-point methods, the complexity of the SOCP relies on the number of constraints, variables, and the dimension of each SOC constraint. The total number of constraints in (2.34) is $3M + 4 + a$, where a is a non-negative integer constant and denotes the SOC constraints with different M. This is because the objective function in (2.34) represents the equivalent SOC of the geometric mean [29]. Hence, the number of iterations required to decrease the duality gap to a small constant is upper bounded by $\mathcal{O}\left(\sqrt{3M+4+a}\right)$ [29]. The per iteration worst case complexity estimate of the interior-point method is $\mathcal{O}\left((3M+2+a)^2(3M)\right)$, where $3M+2+a$ and $3M$ represent the number of optimization variables and the dimension of the SOC constraints in (2.34), respectively.

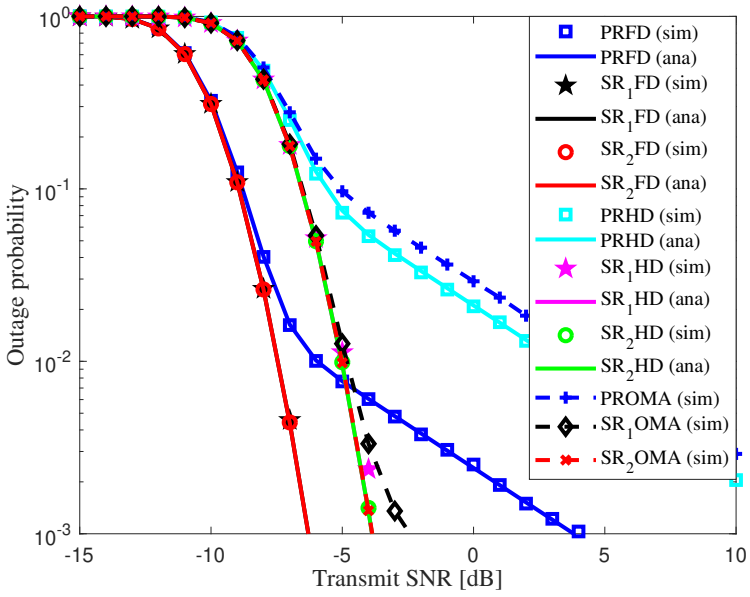

Fig. 2.3: Outage probability of primary and secondary networks operating in FD and HD modes, where $\beta = 0.8$, $N = 5$, and $K = 3$. ana: analytical results; sim: simulation results.

2.6 Numerical Results

In this section, simulation results are presented to verify the findings presented in Sections 2.4 and 2.5. Without loss of generality, we set $M = 2$, $\lambda_{\rm ps} = 5$, and $\lambda_{\rm sp} = \lambda_{\rm sr} = 50$.[3] The target data rates of primary and secondary signals are $\bar{R}_0 = \bar{R}_1 = \bar{R}_2 = 0.5$ bps/Hz. The residual SI channel $h_{\rm s_b s_b}$ is modeled as described in [30, 31], and its variance is set to $|h_{\rm s_b s_b}|^2 = I_{\rm SI} = \sqrt{\zeta}$, where ζ = -1 dB [30]. The energy conversion efficiency is set to be $\eta = 0.75$, $\xi = 1$, and $\psi = 0.75$ [24]. For the results corresponding to the outage probability analysis, the power allocation coefficients are set as $\alpha_0 = 0.6$, $\alpha_1 = 0.3$, and $\alpha_2 = 0.1$.

2.6.1 Outage Probability

Fig. 2.3 compares the outage probability performance between primary and secondary networks operating in FD and HD modes. The conventional OMA-TDMA scheme is considered as a benchmark. In OMA-TDMA scheme, the first κ fraction of the block time T, where κ denotes the time allocation parameter, is used for the transmission from the PT to the $\mathrm{ST_b}$, whereas the remaining (1-κ) fraction of T is equally divided into (M+1) time slots for the transmission from the $\mathrm{ST_b}$ to the PR and M SRs. In this figure, the block time allocation parameter κ is set to 1/2. Further, PRFD, $\mathrm{SR_1}$FD, and $\mathrm{SR_2}$FD curves denote the outage performance of the PR, the $\mathrm{SR_1}$, and the $\mathrm{SR_2}$ when the $\mathrm{ST_b}$ operates in FD mode, respectively. PRHD, $\mathrm{SR_1}$HD, and $\mathrm{SR_2}$HD curves represent the outage performance of the PR, the $\mathrm{SR_1}$, and the $\mathrm{SR_2}$ when the $\mathrm{ST_b}$ operates in HD mode, respectively, while PROMA, $\mathrm{SR_1}$OMA, and $\mathrm{SR_2}$OMA curves are the outage performance of the PR, the $\mathrm{SR_1}$, and the $\mathrm{SR_2}$ in OMA-TDMA scheme, respectively. As can be seen from Fig. 2.3, for both FD and HD cases, the outage performance of the primary network is worse than that of the secondary network[4]. This can be explained that even though the PR is assigned larger power allocation coefficient compared to the $\mathrm{SR_1}$ and the $\mathrm{SR_2}$, the quality of $\mathrm{ST_b}$-PR channel is worst compared to that of $\mathrm{ST_b}$-$\mathrm{SR_1}$ and $\mathrm{ST_b}$-$\mathrm{SR_2}$ channels and since the PR suffers interference from SRs when it decodes its information, which lets the achievable data rate of the PR in (2.12) be smaller than that of SRs in (2.9). Hence, outage probability obtained at the PR is higher than that at SRs. In addition, it can be seen that outage probability of both networks in FD case is much smaller than that in HD mode, confirming the benefit of FD compared with HD technique. This makes sense since with FD, the $\mathrm{ST_b}$ can simultaneously receive the signal from the PT and

[3]This chapter considers the network scenario where STs are located near the PR and SRs, but they are far from PT.

[4]Note that, if the PR is grouped with SRs whose channel gains are weaker, the outage performance of the PR and SRs will swap.

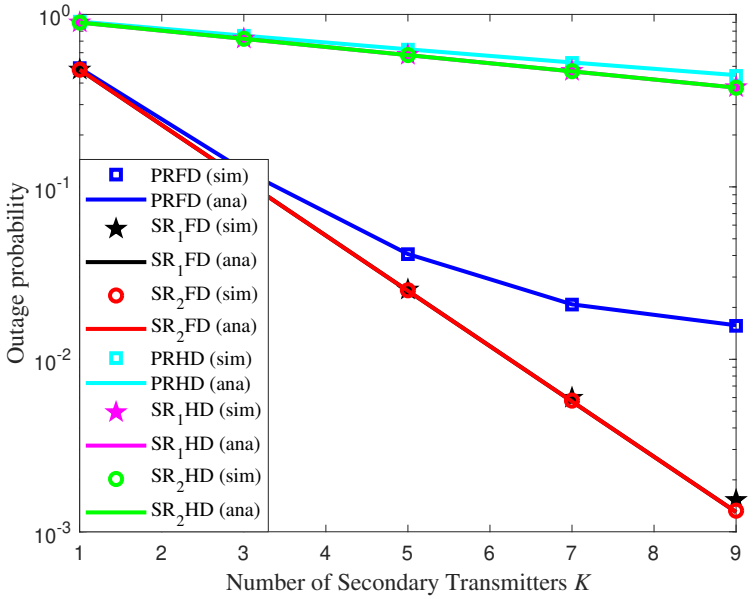

Fig. 2.4: Impact of the number of STs K on the outage performance of primary and secondary networks operating in FD and HD modes, where $\beta = 0.8$, $N = 5$, and $\bar{\gamma} = -9$ dB.

forward its signal to the PR and SRs, whereas with the HD technique the $\mathrm{ST_b}$ has to separate the time used for receiving the PT's signal and the time for its transmission to the PR and SRs. Furthermore, the performance of the proposed FD-NOMA scheme is obviously better than OMA-TDMA scheme for both primary and secondary networks since the proposed scheme enhances the use of primary spectrum resource, i.e., the PR and SRs are concurrently served in the same resource block, while the OMA-TDMA scheme requires separated resource blocks. From Fig. 2.3, it can be seen that the tight closed-form approximate expression curves, which are shown in (2.18) and (2.21), match well with simulation results. Hence, this verifies the correctness of the mathematical analysis.

Fig. 2.4 shows the impact of the number of STs K on the outage probability of primary and secondary networks operating in FD and HD modes. It can be observed that when K increases, the outage performance of both primary and secondary networks in FD and HD modes is greatly improved. This is because the growth in the number of STs increases

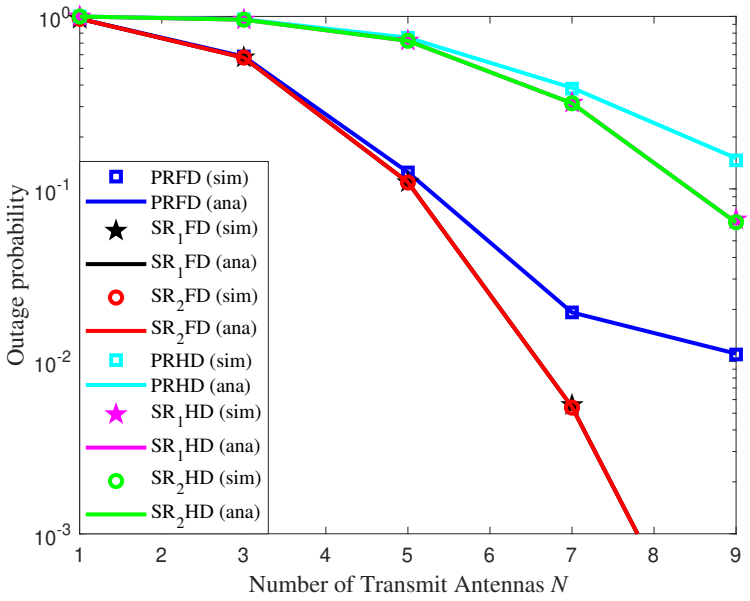

Fig. 2.5: Effect of the number of transmit antennas N on the outage performance of primary and secondary networks operating in FD and HD modes, where $\beta = 0.8$, $K = 3$, and $\bar{\gamma} = -9$ dB.

the probability of choosing the optimal $\mathrm{ST_b}$.

Next, the effect of the number of transmit antennas N on the outage probability of primary and secondary networks operating in FD and HD modes is shown in Fig. 2.5. It can be seen that for both FD and HD cases, the larger the number of transmit antennas at the PT, the better the outage performance can be obtained. The reason is that a larger number of antennas provide higher spatial diversity, which in turn leads to improved signal reception quality at the $\mathrm{ST_b}$.

Fig. 2.6 depicts the impact of PS ratio β on the outage performance of the FD and HD primary and secondary networks. As β increases, the outage probability of both networks significantly reduces and attains the minimal values. The reason is that the growth in β allows the $\mathrm{ST_b}$ to harvest more energy and in turn enhances the $\mathrm{ST_b}$'s transmit power and the achievable data rate at the $\mathrm{ST_b}$ as shown in (2.4) and (2.7), respectively, which improves the information reception at the PR and SRs. Nevertheless, as β continues

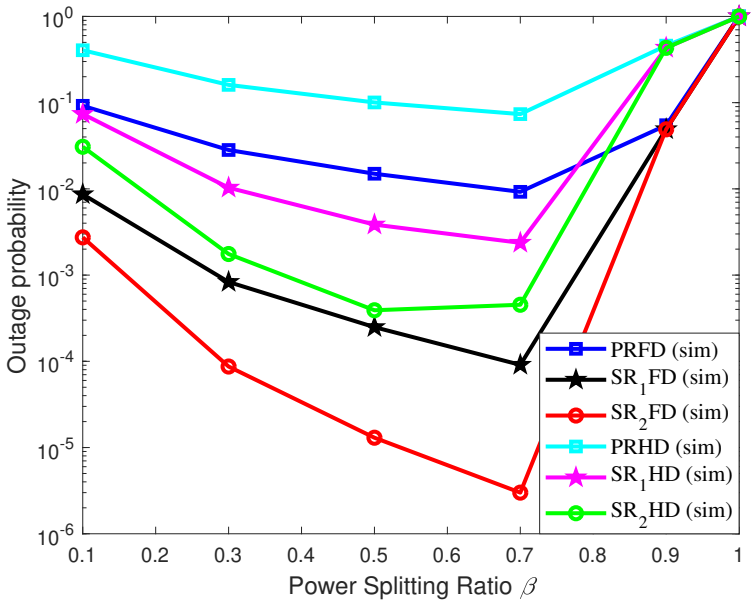

Fig. 2.6: Impact of the PS β on the outage performance of primary and secondary networks operating in FD and HD modes, where $N = 5$, $K = 3$, and $\bar{\gamma} = -5$ dB.

increasing and reaches 1, the outage probability of both networks goes up and attains 1 since more power is given for energy harvesting and less power is left for the $\mathrm{ST_b}$ to decode x_0. Hence, outage occurs since the $\mathrm{ST_b}$ is unable to decode the PT's signal.

Fig. 2.7 illustrates the outage performance of primary and secondary networks in the FD and HD modes when the mean of $\mathrm{ST_b}$-PR (λ_{sp}) channel varies, respectively. It is clear that the outage performance of primary and secondary networks greatly improves for better channel quality (higher channel mean) of $\mathrm{ST_b}$-PR link for both FD and HD modes. Note that similar results of the outage performance of primary and secondary networks in FD and HD modes are obtained with the increase in the mean of PT-$\mathrm{ST_b}$ (λ_{ps}) or $\mathrm{ST_b}$-SRs (λ_{sr}) channels as a result of the improvement in channel quality.

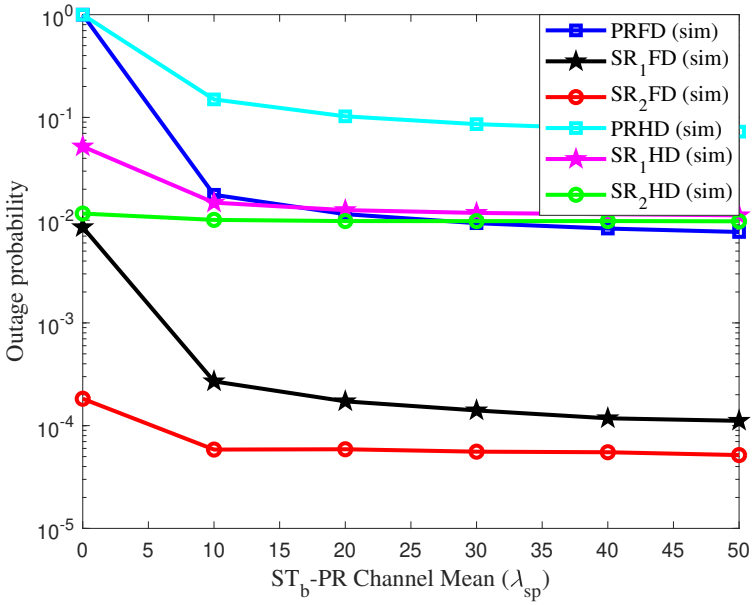

Fig. 2.7: Impact of $\mathrm{ST_b}$-PR channel mean on the outage probability of primary and secondary networks operating in FD and HD modes, where $\beta = 0.8$, $N = 5$, $K = 3$, $\bar{\gamma} = -5$ dB, $\lambda_{\mathrm{ps}} = 5$, and $\lambda_{\mathrm{sr}} = 50$.

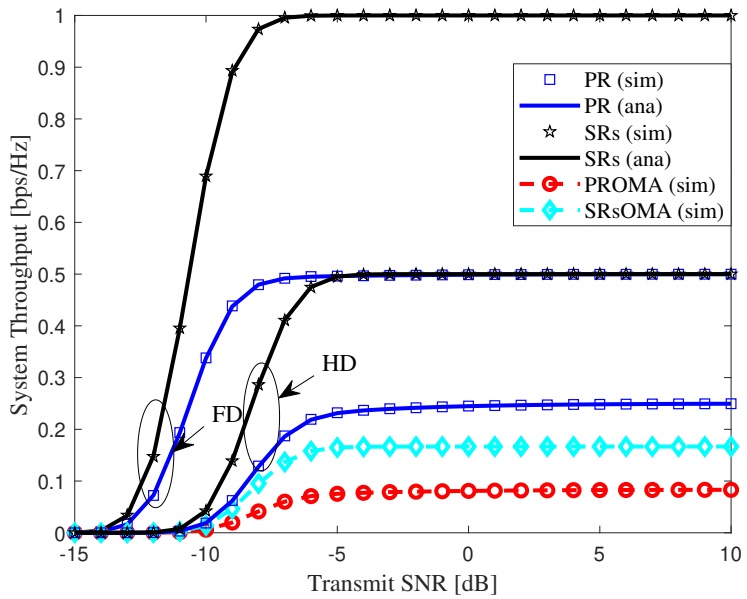

Fig. 2.8: System throughput of primary and secondary networks operating in FD and HD modes, where $\beta = 0.8$, $N = 5$, and $K = 3$.

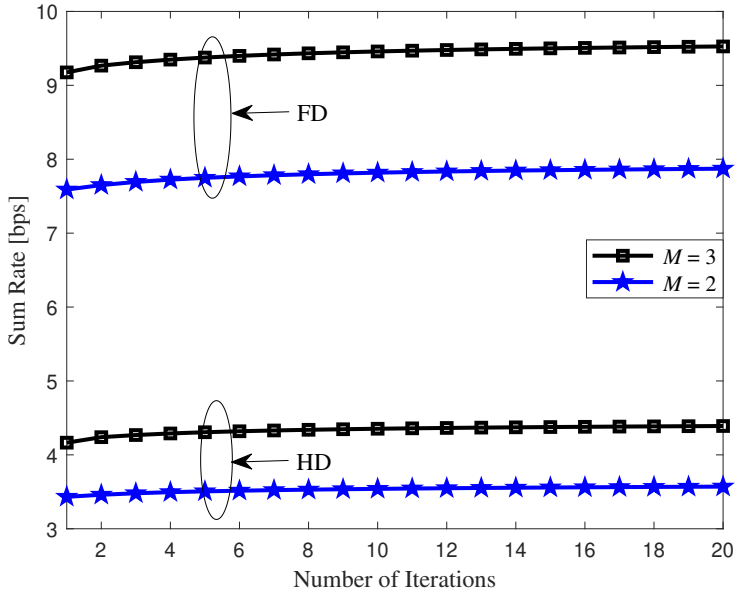

Fig. 2.9: Convergence of the proposed sum rate maximization algorithm with different number of SRs M in FD and HD modes, where $\beta = 0.8$, $N = 5$, $K = 3$, and $\bar{\gamma} = -5$ dB.

2.6.2 System Throughput

The system throughput of primary and secondary networks in FD and HD modes is illustrated in Fig. 2.8. It is clear that the proposed scheme obtains much higher system throughput than HD and the conventional OMA-TDMA schemes due to its lower outage probability. Besides, for all schemes, as the transmit SNR increases, the system throughput of primary and secondary networks goes up and reaches the system throughput floor, as presented in Remark 2.4.1.2.

2.6.3 Sum Rate

Fig. 2.9 illustrates the convergence behavior of our proposed sum rate maximization algorithm for the network when the $\mathrm{ST_b}$ operates in FD and HD modes, respectively. It can be observed that the proposed sum rate maximization algorithm only requires a small number of iterations to converge in both modes. Besides, increasing the number of SRs

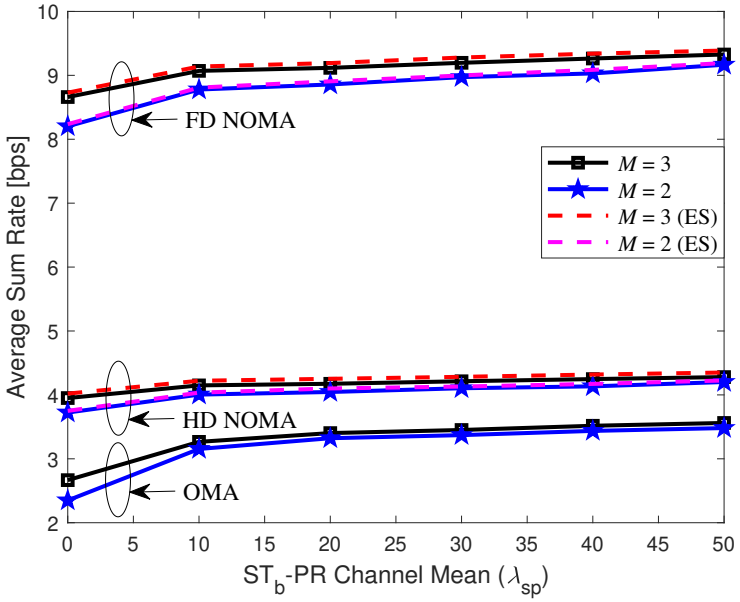

Fig. 2.10: Effect of $\mathrm{ST_b}$-PR channel mean on the average sum rate of the proposed network in FD and HD modes, where $\beta = 0.8$, $N = 5$, $K = 3$, $\bar{\gamma} = -5$ dB, $\lambda_{\mathrm{ps}} = 5$, and $\lambda_{\mathrm{sr}} = 50$.

M can significantly augment the sum rate of the proposed network in both modes.

Fig. 2.10 demonstrates the impact of $\mathrm{ST_b}$-PR (λ_{sp}) channel mean on the average sum rate of the network when the FD and HD operation modes are used, respectively. It is obvious that the average sum rate greatly enhances with better channel quality (higher channel mean) of the $\mathrm{ST_b}$-PR link for both modes. Note that similar results of the average sum rate in FD and HD modes are obtained with the increase in the mean of PT-$\mathrm{ST_b}$ (λ_{ps}) or $\mathrm{ST_b}$-SRs (λ_{sr}) channels as a result of the enhancement in the channel quality. Furthermore, the average sum rate achieved by the proposed system using NOMA is higher than that in OMA-TDMA scheme. Moreover, this figure also compares the performance of Algorithm 1 with the exhaustive search (ES), which is the method to find the globally optimal solution by searching all possible combinations of power allocation values. It can be seen that the average sum rate achieved by Algorithm 1 is very close to the globally optimal solution found by the ES method. Therefore, the proposed iterative algorithm is able to achieve near-optimal performance with low complexity.

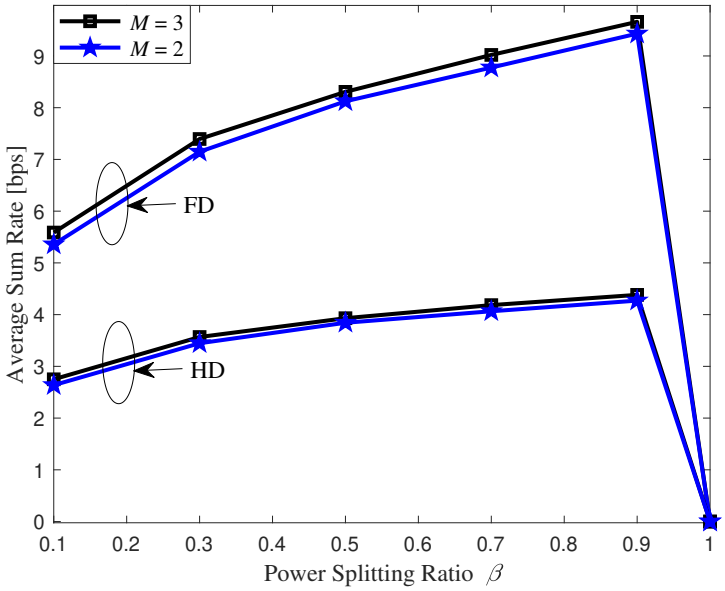

Fig. 2.11: Impact of the PS coefficient β on the average sum rate of the proposed network in FD and HD modes, where $N = 5$, $K = 3$, and $\bar{\gamma} = -5$ dB.

Next, the effect of the PS coefficient β on the average sum rate in the FD and HD cases is examined in Fig. 2.11. It is seen that as β increases, the average sum rate of the network operating in both FD and HD modes considerably grows for different number of SRs. The achieved results are reasonable since the rise in β enables the $\mathrm{ST_b}$ to scavenge more energy and in turn improves the transmit power of the $\mathrm{ST_b}$, and hence, enhances the achievable data rates of the PR and SRs. However, when β reaches 1, all RF power is harvested and no power is available for the PT to the $\mathrm{ST_b}$ information processing. Hence, the sum transmission rate of primary and secondary networks equals to 0 as the $\mathrm{ST_b}$ is unable to decode the PT's signal.

2.7 Conclusion

In this chapter, a novel NOMA assisted cooperative spectrum-sharing network has been proposed to encourage the collaboration between primary and secondary networks. In

particular, the PT needs the help from the $\mathrm{ST_b}$ to relay its information and as an incentive, the $\mathrm{ST_b}$ has access to primary network's spectrum and uses it to transmit primary and secondary messages concurrently by using NOMA. The outage probability of primary and secondary networks has been derived in tight closed-form approximate expressions, and used to evaluate the system performance. Besides, the power allocation coefficients at $\mathrm{ST_b}$ have been optimized to maximize the sum transmission rate of the primary and secondary networks. Numerical results have showed the superior performance of the FD-NOMA system compared to the HD-NOMA and the conventional OMA-TDMA systems. Furthermore, it has been seen that several system design parameters, i.e., number of ST transmit antennas N, number of STs K, number of SRs M, the power allocation coefficients α, power splitting ratio β, which have high impact on the system performance, should be carefully chosen in order to optimize the performance of the FD-SWIPT-NOMA cooperative spectrum-sharing network when applied in practice.

Appendix A: Proof of Lemma 2.1

By using that $||\mathbf{h}_{\mathrm{ps}_k}||^2$ has the Gamma distribution and the PT-ST_k links are independent, the CDF of $||\mathbf{h}_{\mathrm{ps_b}}||^2 = \max\limits_{k=1,2,\ldots,K} ||\mathbf{h}_{\mathrm{ps}_k}||^2$ can be derived as in (2.15), where $C_j = 1$ for $j = 0$, $C_j = l$ for $j = 1$, and $C_j = \frac{1}{j}\sum\limits_{p=1}^{q} \frac{pl-j+p}{p!} C_{j-p}$ for $2 \leq j \leq l(N-1)$. $q = \min(j, N-1)$. By differentiating (2.15), the PDF of $||\mathbf{h}_{\mathrm{ps_b}}||^2$ can be obtained as in (2.16).

Appendix B: Proof of Theorem 2.1

By denoting the first term $\Pr\left(R_{\mathrm{s_b},x_0} < \bar{R}_0\right)$ and the second term $\Pr\left(R_{\mathrm{s_b},x_0} \geq \bar{R}_0, R_{\mathrm{p}} < \bar{R}_0\right)$ in (2.17) as Φ_1 and Φ_2, respectively, and substituting (2.7) and (2.15) into Φ_1, Φ_1 can be

rewritten as:

$$\begin{aligned}\Phi_1 &= \Pr\left[\frac{(1-\beta)\bar{\gamma}||\mathbf{h}_{\mathrm{ps_b}}||^2}{(1-\beta)\rho\bar{\gamma}I_{\mathrm{SI}}||\mathbf{h}_{\mathrm{ps_b}}||^2+1} < \gamma_0\right] \\ &= \Pr\left[||\mathbf{h}_{\mathrm{ps_b}}||^2 < \frac{\gamma_0}{\bar{\gamma}\left(1-\beta\right)\left(1-\gamma_0\rho I_{\mathrm{SI}}\right)}\right] \\ &= \Pr\left(||\mathbf{h}_{\mathrm{ps_b}}||^2 < \frac{\mu}{\bar{\gamma}}\right) \\ &= \sum_{l=0}^{K}\begin{pmatrix} K \\ l \end{pmatrix}(-1)^l \exp\left(-\frac{l\mu}{\lambda_{\mathrm{ps}}\bar{\gamma}}\right)\sum_{j=0}^{l(N-1)} C_j \left(\frac{\mu}{\lambda_{\mathrm{ps}}\bar{\gamma}}\right)^j, \end{aligned} \tag{2.35}$$

where $\gamma_0 < 1/(\rho I_{\mathrm{SI}})$; otherwise $\Phi_1 = 1$, which leads to Φ_2 in (2.17) equalling to 0 and hence $P_{\mathrm{p}} = 1$.

Next, this appendix derives the term Φ_2 in (2.17). Substituting (2.7) and (2.12) into (2.17), Φ_2 can be rewritten as:

$$\begin{aligned}\Phi_2 &= \Pr\left[||\mathbf{h}_{\mathrm{ps_b}}||^2 \geq \frac{\gamma_0}{\bar{\gamma}\left(1-\beta\right)\left(1-\gamma_0\rho I_{\mathrm{SI}}\right)}, ||\mathbf{h}_{\mathrm{ps_b}}||^2|h_{\mathrm{s_bp}}|^2 < \frac{\gamma_0}{\bar{\gamma}\rho\Big(\alpha_0 - \sum\limits_{i=1}^{M}\alpha_i\gamma_0\Big)}\right] \\ &= \Pr\left(||\mathbf{h}_{\mathrm{ps_b}}||^2 \geq \frac{\mu}{\bar{\gamma}}, ||\mathbf{h}_{\mathrm{ps_b}}||^2|h_{\mathrm{s_bp}}|^2 < \frac{\Theta_0}{\bar{\gamma}}\right), \end{aligned} \tag{2.36}$$

where $\gamma_0 < \min\left[1/(\rho I_{\mathrm{SI}}), \alpha_0/\left(\sum\limits_{i=1}^{M}\alpha_i\right)\right]$. If $\gamma_0 > \alpha_0/\left(\sum\limits_{i=1}^{M}\alpha_i\right)$, $P_{\mathrm{p}} = 1$.

With the use of the binomial theorem [27, Eq. (1.111)] and order statistics [18], the CDF of $|h_{\mathrm{s_bp}}|^2$ is shown as follows:

$$\begin{aligned}F_{|h_{\mathrm{s_bp}}|^2}(x) &= \iota_q \sum_{c=0}^{Q-q}\begin{pmatrix} Q-q \\ c \end{pmatrix}\frac{(-1)^c}{q+c}\left[F_{|\bar{h}_{\mathrm{s_bp}}|^2}(x)\right]^{q+c} \\ &= \iota_q \sum_{c=0}^{Q-q}\begin{pmatrix} Q-q \\ c \end{pmatrix}\frac{(-1)^c}{q+c}\sum_{n=0}^{q+c}\begin{pmatrix} q+c \\ n \end{pmatrix}(-1)^n \exp\left(-\frac{nx}{\lambda_{\mathrm{sp}}}\right), \end{aligned} \tag{2.37}$$

where $|\bar{h}_{\mathrm{s_b p}}|^2$ is the unsorted channel gain of $\mathrm{ST_b}$-PR link and $F_{|\bar{h}_{\mathrm{s_b p}}|^2}(x) = 1 - \exp\left(-\frac{x}{\lambda_{\mathrm{sp}}}\right)$. Besides, $q = 1$ for PR and $q = m + 1$ for SR_m.

In the case that $\gamma_0 < \min\left[1/(\rho I_{\mathrm{SI}}), \alpha_0 / \left(\sum_{i=1}^{M} \alpha_i\right)\right]$ and using (2.16) and (2.37), (2.36) can be further derived as:

$$\begin{aligned}
\Phi_2 &= \int_{\mu/\bar{\gamma}}^{\infty} \Pr\left(|h_{\mathrm{s_b p}}|^2 < \frac{\Theta_0}{\bar{\gamma} x}\right) f_{||\mathbf{h}_{\mathrm{ps_b}}||^2}(x) dx \\
&= \int_{\mu/\bar{\gamma}}^{\infty} \iota_q \sum_{c=0}^{Q-q} \sum_{n=0}^{q+c} \binom{Q-q}{c} \binom{q+c}{n} \frac{(-1)^{c+n}}{q+c} \exp\left(-\frac{n\Theta_0}{\lambda_{\mathrm{sp}} \bar{\gamma} x}\right) \sum_{l=1}^{K} \binom{K}{l} (-1)^l \\
&\times \exp\left(-\frac{lx}{\lambda_{\mathrm{ps}}}\right) \sum_{j=0}^{l(N-1)} \frac{C_j}{{\lambda_{\mathrm{ps}}}^j} \left(j x^{j-1} - \frac{l}{\lambda_{\mathrm{ps}}} x^j\right) dx \\
&= \int_{\mu/\bar{\gamma}}^{\infty} \iota_q \widetilde{\sum}\Big(\sim\Big) \frac{(-1)^{c+n+l}}{q+c} \exp\left(-\frac{n\Theta_0}{\lambda_{\mathrm{sp}} \bar{\gamma} x}\right) \exp\left(-\frac{lx}{\lambda_{\mathrm{ps}}}\right) \frac{C_j}{{\lambda_{\mathrm{ps}}}^j} \left(j x^{j-1} - \frac{l}{\lambda_{\mathrm{ps}}} x^j\right) dx,
\end{aligned} \tag{2.38}$$

where $\widetilde{\sum} = \sum_{c=0}^{Q-q} \sum_{n=0}^{q+c} \sum_{l=1}^{K} \sum_{j=0}^{l(N-1)}$ and $\Big(\sim\Big) = \binom{Q-q}{c} \binom{q+c}{n} \binom{K}{l}$.

Since the integral in (2.38) can not be further simplified, this appendix uses the following approximation $e^{-\alpha/x} \approx 1 - \alpha/x$ for large values of $|x|$ [26]. Hence, (2.38) can be further given by

$$\begin{aligned}
\Phi_2 \approx &\int_{\mu/\bar{\gamma}}^{\infty} \iota_q \widetilde{\sum}\Big(\sim\Big) \frac{(-1)^{c+n+l}}{q+c} \exp\left(-\frac{lx}{\lambda_{\mathrm{ps}}}\right) \frac{C_j}{{\lambda_{\mathrm{ps}}}^j} \left(j x^{j-1} - \frac{l}{\lambda_{\mathrm{ps}}} x^j\right) dx \\
&- \int_{\mu/\bar{\gamma}}^{\infty} \iota_q \widetilde{\sum}\Big(\sim\Big) \frac{(-1)^{c+n+l}}{q+c} \frac{n\Theta_0}{\lambda_{\mathrm{sp}} \bar{\gamma} x} \exp\left(-\frac{lx}{\lambda_{\mathrm{ps}}}\right) \frac{C_j}{{\lambda_{\mathrm{ps}}}^j} \left(j x^{j-1} - \frac{l}{\lambda_{\mathrm{ps}}} x^j\right) dx.
\end{aligned} \tag{2.39}$$

With the help of [27, Eq. (3.381.3)] and after some manipulation steps, (2.39) can be

further solved as:

$$\begin{aligned}\Phi_2 &\approx \iota_q \widetilde{\sum}(\sim) \frac{(-1)^{c+n+l}}{q+c} \frac{C_j}{{\lambda_{\rm ps}}^j} \left[j \left(\frac{l}{\lambda_{\rm ps}} \right)^{-j} \Gamma\left(j, \frac{l\mu}{\lambda_{\rm ps}\bar{\gamma}} \right) - \left(\frac{l}{\lambda_{\rm ps}} \right)^{-j} \Gamma\left(j+1, \frac{l\mu}{\lambda_{\rm ps}\bar{\gamma}} \right) \right] \\ &- \iota_q \widetilde{\sum}(\sim) \frac{(-1)^{c+n+l}}{q+c} \frac{n\Theta_0}{\lambda_{\rm sp}\bar{\gamma}} \frac{C_j}{{\lambda_{\rm ps}}^j} \left[j \left(\frac{l}{\lambda_{\rm ps}} \right)^{-j+1} \Gamma\left(j-1, \frac{l\mu}{\lambda_{\rm ps}\bar{\gamma}} \right) - \left(\frac{l}{\lambda_{\rm ps}} \right)^{-j+1} \Gamma\left(j, \frac{l\mu}{\lambda_{\rm ps}\bar{\gamma}} \right) \right] \\ &\approx \iota_q \widetilde{\sum}(\sim) \frac{(-1)^{c+n+l}}{q+c} \frac{C_j}{l^j} \left[\left(j + \frac{n\Theta_0 l}{\lambda_{\rm sp}\lambda_{\rm ps}\bar{\gamma}} \right) \Gamma\left(j, \frac{l\mu}{\lambda_{\rm ps}\bar{\gamma}} \right) - \Gamma\left(j+1, \frac{l\mu}{\lambda_{\rm ps}\bar{\gamma}} \right) \right. \\ &\left. - \frac{n\Theta_0 jl}{\lambda_{\rm sp}\lambda_{\rm ps}\bar{\gamma}} \Gamma\left(j-1, \frac{l\mu}{\lambda_{\rm ps}\bar{\gamma}} \right) \right]. \end{aligned} \tag{2.40}$$

Finally, substituting (2.35) and (2.40) into (2.17), this appendix obtains the desired result as in (2.18).

Appendix C: Proof of Theorem 2.2

Denote the second term $\Pr\left(R_{{\rm s_b},x_0} \geq R_0, \overline{P}_{{\rm r}_m}\right)$ in (2.20) as Υ. Since the first term in (2.20) is already derived in (2.35), we will derive the second term Υ. $\overline{P}_{{\rm r}_m}$ in Υ can be written as:

$$\overline{P}_{{\rm r}_m} = 1 - \Pr\left({\rm E}^c_{{\rm r}_m,0} \cap \ldots \cap {\rm E}^c_{{\rm r}_m,m} \right), \tag{2.41}$$

where $\mathrm{E}^{c}_{\mathrm{r}_m,m'} = R_{\mathrm{r}_m,x_{m'}} \geq \bar{R}_{m'}$, $0 \leq m' \leq m$, denotes the event that SR_m successfully decodes $x_{m'}$. From (2.9) and (2.10), $\Pr\left(\mathrm{E}^{c}_{\mathrm{r}_m,m'}\right)$ is expressed as:

$$\begin{aligned}
&\Pr\left(\mathrm{E}^{c}_{\mathrm{r}_m,m'}\right) \\
&= \Pr\left[\frac{\alpha_{m'}\rho\bar{\gamma}||\mathbf{h}_{\mathrm{ps_b}}||^2|h_{\mathrm{s_br}_m}|^2}{\sum\limits_{i=m'+1}^{M}\alpha_i\rho\bar{\gamma}||\mathbf{h}_{\mathrm{ps_b}}||^2|h_{\mathrm{s_br}_m}|^2+1} \geq \gamma_{m'}\right] \\
&= \Pr\left[||\mathbf{h}_{\mathrm{ps_b}}||^2|h_{\mathrm{s_br}_m}|^2 \geq \frac{\gamma_{m'}}{\bar{\gamma}\rho\left(\alpha_{m'}-\sum\limits_{i=m'+1}^{M}\alpha_i\gamma_{m'}\right)}\right] \\
&= \Pr\left(||\mathbf{h}_{\mathrm{ps_b}}||^2|h_{\mathrm{s_br}_m}|^2 \geq \frac{\Theta_{m'}}{\bar{\gamma}}\right), \qquad (2.42)
\end{aligned}$$

when $\gamma_{m'} \leq \alpha_{m'}/\left(\sum\limits_{i=m'+1}^{M}\alpha_i\right)$; otherwise, SR_m suffers from the outage. According to (2.41) and (2.42), $\overline{P}_{\mathrm{r}_m}$ is revised as:

$$\begin{aligned}
\overline{P}_{\mathrm{r}_m} &= 1-\Pr\left[||\mathbf{h}_{\mathrm{ps_b}}||^2|h_{\mathrm{s_br}_m}|^2 \geq \frac{\max\left(\Theta_0,\Theta_1,\ldots,\Theta_m\right)}{\bar{\gamma}}\right] \\
&= \Pr\left(||\mathbf{h}_{\mathrm{ps_b}}||^2|h_{\mathrm{s_br}_m}|^2 \leq \frac{\Theta}{\bar{\gamma}}\right). \qquad (2.43)
\end{aligned}$$

Next, substituting (2.43) into Υ in (2.20), Υ is rewritten as:

$$\Upsilon = \Pr\left(||\mathbf{h}_{\mathrm{ps_b}}||^2 \geq \frac{\mu}{\bar{\gamma}}, ||\mathbf{h}_{\mathrm{ps_b}}||^2|h_{\mathrm{s_br}_m}|^2 \leq \frac{\Theta}{\bar{\gamma}}\right). \qquad (2.44)$$

Following the same steps to derive Φ_2 in Appendix B, Υ is lastly obtained as follows:

$$\begin{aligned}
\Upsilon \approx \iota_q\widetilde{\sum}\Big(\sim\Big)\frac{(-1)^{c+n+l}}{q+c}\frac{C_j}{l^j}\Bigg[&\left(j+\frac{n\Theta l}{\lambda_{\mathrm{sr}}\lambda_{\mathrm{ps}}\bar{\gamma}}\right)\Gamma\left(j,\frac{l\mu}{\lambda_{\mathrm{ps}}\bar{\gamma}}\right)-\Gamma\left(j+1,\frac{l\mu}{\lambda_{\mathrm{ps}}\bar{\gamma}}\right) \\
&-\frac{n\Theta jl}{\lambda_{\mathrm{sr}}\lambda_{\mathrm{ps}}\bar{\gamma}}\Gamma\left(j-1,\frac{l\mu}{\lambda_{\mathrm{ps}}\bar{\gamma}}\right)\Bigg]. \qquad (2.45)
\end{aligned}$$

Finally, substituting (2.35) and (2.45) into (2.20), the final result is obtained as in (2.21).

Appendix D: Proof of Proposition 1

Let define $\mathcal{F}(\mathbf{t}) \triangleq \prod_{i=0}^{M} t_i$. Note that $\mathcal{F}(\mathbf{t}) \geq \mathcal{F}^{(\tau)}(\mathbf{t}), \forall \mathbf{t}$, and $\mathcal{F}(\mathbf{t}^{(\tau)}) = \mathcal{F}^{(\tau)}(\mathbf{t}^{(\tau)})$. Further, $\mathcal{F}^{(\tau)}(\mathbf{t}^{(\tau+1)}) > \mathcal{F}^{(\tau)}(\mathbf{t}^{(\tau)})$ whenever $(\mathbf{t}^{(\tau+1)}) \neq (\mathbf{t}^{(\tau)})$ since the former and the latter are the optimal solution and a feasible point for (2.34), respectively. Hence, $\mathcal{F}(\mathbf{t}^{(\tau+1)}) \geq \mathcal{F}^{(\tau)}(\mathbf{t}^{(\tau+1)}) > \mathcal{F}^{(\tau)}(\mathbf{t}^{(\tau)}) = \mathcal{F}(\mathbf{t}^{(\tau)})$, presenting that $(\mathbf{t}^{(\tau+1)})$ is a better feasible point than $(\mathbf{t}^{(\tau)})$ for problem (2.28). The sequence $(\mathbf{t}^{(\tau)})$ of improved feasible points for (2.28) thus converges at least to a locally optimal solution which satisfies the KKT conditions [28]. As a result, the objective value of (2.34) is monotonically increasing, i.e., $\prod_{i=0}^{M} t_i^{(\tau)} \geq \prod_{i=0}^{M} t_i^{(\tau-1)}$.

References

[1] S. M. R. Islam, N. Avazov, O. A. Dobre, and K.-S. Kwak, "Power-domain non-orthogonal multiple access (NOMA) in 5G systems: Potentials and challenges," *IEEE Commun. Surveys Tuts.,* vol. 19, no. 2, pp. 721-742, 2nd Quart. 2017.

[2] D. Wan, M. Wen, F. Ji, H. Yu, and F. Chen, "Non-orthogonal multiple access for cooperative communications: Challenges, opportunities, and trends," *IEEE Wireless Commun.,* vol. 25, no. 2, pp. 109-117, Apr. 2018.

[3] S. M. R. Islam, M. Zeng, O. A. Dobre, and K. Kwak, *Non-Orthogonal Multiple Access (NOMA): How It Meets 5G and Beyond.* New Jersey, USA: Wiley 5G Ref, 2019.

[4] A. Yadav and O. A. Dobre, "All technologies work together for good: A glance to future mobile networks," *IEEE Wireless Commun.,* vol. 25, no. 4, pp. 10-16, Aug. 2018.

[5] J.-B. Kim, I.-H. Lee, and J. Lee, "Capacity scaling for D2D aided cooperative relaying systems using NOMA," *IEEE Wireless Commun. Lett.,* vol. 7, no. 1, pp. 42-45, Feb. 2018.

[6] Y. Liu, Z. Ding, M. Elkashlan, and H. V. Poor, "Cooperative non-orthogonal multiple access with simultaneous wireless information and power transfer," *IEEE J. Sel. Areas Commun.,* vol. 34, no. 4, pp. 938-953, Apr. 2016.

[7] M. Ashraf, A. Shahid, J. W. Jang, and K.-G. Lee, "Energy harvesting non-orthogonal multiple access system with multi-antenna relay and base station," *IEEE Access,* vol. 5, pp. 17660-17670, Sep. 2017.

[8] G. I. Tsiropolous, A. Yadav, M. Zeng, and O. A. Dobre, "Cooperation in 5G HetNets: Advanced spectrum access and D2D assisted communications," *IEEE Wireless Commun.,* vol. 24, no. 5, pp. 110-117, Oct. 2017.

[9] A. Yadav, G. I. Tsiropolous, and O. A. Dobre, "Full-duplex communications: Performance in ultradense mm-wave small-cell wireless networks," *IEEE Vehic. Tech. Mag,* vol. 13, no. 2, pp. 40-47, Apr. 2018.

[10] B. V. Nguyen, H. Jung and K. Kim, "Physical layer security schemes for full-duplex cooperative systems: State of the art and beyond," *IEEE Commun. Mag.,* vol. 56, no. 11, pp. 131-137, Nov. 2018.

[11] X. Yue, Y. Liu, S. Kang, A. Nallanathan, and Z. Ding, "Exploiting full/half-duplex user relaying in NOMA systems," *IEEE Trans. Commun.,* vol. 66, no. 2, pp. 560-575, Feb. 2018.

[12] Y. Alsaba, C. Y. Leow, and S. K. A. Rahim, "Full-duplex cooperative non-orthogonal multiple access with beamforming and energy harvesting," *IEEE Access,* vol. 6, pp. 19726-19738, Apr. 2018.

[13] L. Lv, J. Chen, Q. Ni, Z. Ding, and H. Jiang, "Cognitive non-orthogonal multiple access with cooperative relaying: A new wireless frontier for 5G spectrum sharing," *IEEE Commun. Mag.,* vol. 56, no. 4, pp. 188-195, Apr. 2018.

[14] F. Zhou, Y. Wu, Y.-C. Liang, Z. Li, Y. Wang, and K.-K. Wong, "State of the art, taxonomy, and open issues on cognitive radio networks with NOMA," *IEEE Wireless Commun.,* vol. 25, no. 2, pp. 100-108, Apr. 2018.

[15] Y. Yu, H. Chen, Y. Li, Z. Ding, and L. Zhuo, "Antenna selection in MIMO cognitive radio-inspired NOMA systems," *IEEE Commun. Lett.,* vol. 21, no. 12, pp. 2658-2661, Dec. 2017.

[16] L. Lv, J. Chen, Q. Ni and Z. Ding, "Design of cooperative non-orthogonal multicast cognitive multiple access for 5G systems: User scheduling and performance analysis," *IEEE Trans. Commun.,* vol. 65, no. 6, pp. 2641-2656, June 2017.

[17] Y. Wang, Y. Wu, F. Zhou, Z. Chu, Y. Wu, and F. Yuan, "Multi-objective resource allocation in a NOMA cognitive radio network with a practical non-linear energy harvesting model," *IEEE Access,* vol. 6, pp. 12973-12982, Dec. 2017.

[18] L. Lv, Q. Ni, Z. Ding, and J. Chen, "Application of non-orthogonal multiple access in cooperative spectrum-sharing networks over Nakagami-m fading channels," *IEEE Trans. Veh. Technol.,* vol. 66, no. 6, pp. 5506-5511, June 2017.

[19] L. Lv, L. Yang, H. Jiang, T. H. Luan, and J. Chen, "When NOMA meets multiuser cognitive radio: Opportunistic cooperation and user scheduling," *IEEE Trans. Veh. Technol.,* vol. 67, no. 7, pp. 6679-6684, July 2018.

[20] S. Lee, T. Q. Duong, D. B. da Costa, D.-B. Ha, and S. Q. Nguyen, "Underlay cognitive radio networks with cooperative non-orthogonal multiple access," *IET Commun.,* vol. 12, no. 3, pp. 359-366, Feb. 2018.

[21] M. F. Kader, S. Y. Shin, and V. C. M. Leung, "Full-duplex non-orthogonal multiple access in cooperative relay sharing for 5G systems," *IEEE Trans. Veh. Technol.,* vol. 67, no. 7, pp. 5831-5840, July 2018.

[22] H. Xing, X. Kang, K.-K. Wong, and A. Nallanathan, "Optimizing DF cognitive radio networks with full-duplex-enabled energy access points," *IEEE Trans. Wireless Commun.,* vol. 16, no. 7, pp. 4683-4697, July 2017.

[23] B. Cai, Y. Chen, Y. Chen, Y. Cao, N. Zhao, and Z. Ding, "A novel spectrum sharing scheme assisted by secondary NOMA relay," *IEEE Wireless Commun. Lett.,* vol. 7, no. 5, pp. 732–735, Oct. 2018.

[24] L. Zhao, X. Wang, and T. Riihonen, "Transmission rate optimization of full-duplex relay systems powered by wireless energy transfer," *IEEE Trans. Wireless Commun.,* vol. 16, no. 10, pp. 6438-6450, Oct. 2017.

[25] A. Yadav, O. A. Dobre, and H. V. Poor, "Is self-interference in full-duplex communications a foe or a friend?," *IEEE Signal Process. Lett.,* vol. 25, no. 7, pp. 951-955, July 2018.

[26] Q. N. Le, V. N. Q. Bao, and B. An, "Full-duplex distributed switch-and-stay energy harvesting selection relaying networks with imperfect CSI: Design and outage analysis," *J. Commun. Netw.,* vol. 20, no. 1, pp. 29-46, Feb. 2018.

[27] I. S. Gradshteyn and I. M. Ryzhik, "Table of integrals, series, and products," New York, NY, USA, Elsevier, 2007.

[28] B. R. Marks and G. P. Wright, "A general inner approximation algorithm for nonconvex mathematical programs," *Operations Research*, vol. 26, no. 4, pp. 681-683, July 1978.

[29] M. F. Hanif, Z. Ding, T. Ratnarajah, and G. K. Karagiannidis, "A minorization-maximization method for optimizing sum rate in the downlink of non-orthogonal multiple access systems," *IEEE Trans. Signal Process.,* vol. 64, no. 1, pp. 76-88, Jan. 2016.

[30] Y. Zeng and R. Zhang, "Full-duplex wireless-powered relay with self-energy recycling," *IEEE Wireless Commun. Lett.,* vol. 4, no. 2, pp. 201-204, Apr. 2015.

[31] Z. Hu, C. Yuan, F. Zhu, and F. Gao, "Weighted sum transmit power minimization for full-duplex system with SWIPT and self-energy recycling," *IEEE Access,* vol. 4, pp. 4874-4881, July 2016.

Chapter 3

Efficient User Clustering Approaches and Sum Rate Maximization in NOMA-CFmMIMO Networks

3.1 Abstract

The superior SE and user fairness feature of NOMA systems are achieved by exploiting UC more efficiently. However, a random UC certainly results in a suboptimal solution while an exhaustive search method comes at the cost of high complexity, especially for systems of medium-to-large size. To address this problem, this chapter develops two efficient unsupervised machine learning based UC algorithms, namely k-means++ and improved k-means++, to effectively cluster users into disjoint clusters in CFmMIMO system. Adopting full-pilot zero-forcing at APs to comprehensively assess the system performance, we formulate the sum SE optimization problem taking into account power constraints at APs, necessary conditions for implementing successive interference cancellation, and required SE constraints at UEs. The formulated optimization problem is highly

non-convex, and thus, it is difficult to obtain the global optimal solution. Therefore, this chapter develops a simple yet efficient iterative algorithm for its solution. In addition, the performance of collocated massive MIMO-NOMA (COmMIMO-NOMA) system is also characterized. Numerical results are provided to show the superior performance of the proposed UC algorithms compared to baseline schemes. The effectiveness of applying NOMA in CFmMIMO and COmMIMO systems is also validated.

3.2 Introduction

The tremendous growth in the number of emerging applications will certainly pose enormous traffic demands with ultra-high connection density for next-generation wireless networks. It is approximated that more than 20 billion devices were connected to the Internet in 2020, and this number is predicted to exceed 35 billion devices by 2025 [1]. The global data traffic of mobile devices is expected to reach 226 exabytes per month by 2026 [2], and will further increase over the next decade. However, traditional OMA techniques seem to reach their fundamental limits in the near future, and therefore are no longer suitable to meet these requirements. Consequently, it calls for innovative techniques that utilize radio resources more efficiently to attain the optimal performance.

NOMA has been envisaged as a key enabling technology that significantly enhances SE and user fairness of traditional wireless communication systems [3–5]. In NOMA, multiple UEs are allowed to simultaneously transmit and receive their signals in the same time-frequency resource by using different signal signatures (i.e., code-domain NOMA) or power levels (i.e., power-domain NOMA) [6–8][1]. In particular, in a downlink system the key benefit of NOMA is attributed to the fact that UEs with better channel conditions are able to cancel the interference caused by UEs with poorer channel conditions using

[1]This chapter will focus on power-domain NOMA; henceforth, it is referred to NOMA.

the SIC technique. User fairness is then achieved by allocating a large portion of the total power budget to weak UEs, which also guarantees the SIC's feasibility at strong UEs.

Recently, CFmMIMO, which is a scalable version of massive MIMO networks, has been introduced to overcome the large propagation losses as well as provide better quality-of-experience services for cell-edge UEs [9–11]. CFmMIMO comprises a large number of APs that are spatially distributed over a wide area to coherently serve multiple UEs in the same time-frequency resources. All APs are coordinated by a CPU through fronthaul links. Each AP performs beamforming based on its local CSI only, and this feature thus greatly reduces the complexity in terms of the fronthaul overhead. Since each UE is coherently served by all APs, the effect of cell boundaries can be effectively removed. It was shown in [9] and [12] that CFmMIMO is superior to small-cell and COmMIMO in terms of SE and EE, respectively. However, the key advantages of favorable propagation and channel hardening properties to multiplex numerous UEs are only achieved in the case of multiple antennas at APs and/or low propagation losses [13]. For the aforementioned reasons, it is of pivotal interest to study the combination of NOMA and CFmMIMO to reap all their benefits, towards fulfilling the conflicting demands on high SE, massive connectivity with low latency, and high reliability with user fairness of future wireless networks [14].

3.2.1 Related Work

Despite its potential, there are only a few research works investigating the benefit of NOMA in CFmMIMO systems in the literature. NOMA for downlink CFmMIMO was first studied in [15], where the closed-form expression of the achievable sum rate was derived. Numerical results showed the superior performance of NOMA compared to OMA. The authors in [16] investigated the impact of NOMA in the uplink CFmMIMO system and derived a closed-form approximation for the sum SE (SSE). Simulation re-

sults demonstrated that CFmMIMO-NOMA is capable of utilizing the scarce spectrum more efficiently. In [17], different types of precoding techniques such as maximum ratio transmission (MRT), full-pilot zero-forcing (fpZF), and modified regularized ZF (mRZF) at APs were considered in downlink CFmMIMO-NOMA. It was shown that downlink CFmMIMO-NOMA with mRZF and fpZF precoders significantly outperforms the OMA with MRT in terms of the achievable sum rate. These existing works mainly focused on characterizing the performance analysis in CFmMIMO-NOMA, but did not show how UEs are paired/grouped.

To be spectrally-efficient, it is crucial to group a sufficiently large number of UEs with distinct channel conditions that performs NOMA jointly [3–5, 18]. In the context of CFmMIMO-NOMA, the authors in [19] proposed three distance-based pairing schemes including near pairing, far pairing, and random pairing to group UEs into disjoint clusters. It is not surprising to see that the close pairing, where two UEs with the smallest distance between them are paired, provides the worst performance, which is also aligned with the NOMA principle [3, 4]. Another interesting study is to group a large number of UEs into one cluster [20], referred to as UC, in which a low complexity suboptimal method based on the Jaccard distance coefficient was developed to find the most dissimilar UEs in the CFmMIMO-NOMA system. Nevertheless, the UC algorithms in the above-cited works were developed based on the distances among UEs only, without considering any learning features.

Recently, unsupervised machine learning (ML) techniques have been considered as an effective means for different optimization targets, which exploit adaptive learning features. In this regard, the authors in [21] proposed a kernel-power-density based algorithm to cluster multipath components of MIMO channels into disjoint groups. A cluster-based geometrical dynamic stochastic model was introduced in [22], where scattered nodes were grouped into different clusters according to the density of nodes in MIMO scenarios.

In [23], a clustered sparse Bayesian learning algorithm was developed for channel estimation in a hybrid analog-digital massive MIMO system by using the sparsity characteristic of angular domain channel. The authors in [24] proposed a clustering scheme for machine-to-machine communications in a hybrid time-division multiple access-NOMA system in order to increase the battery lifetime of machines, using the popular k-means algorithm [25]. This work was extended in [26] to improve the network sum throughput by considering an enhanced k-means algorithm. Further, the k-means algorithm was used to cluster UEs in mmwave-NOMA [27] and CFmMIMO [28]. Although these works demonstrated the effectiveness of applying unsupervised ML to clustering tasks for various wireless communication systems, its application for UC in CFmMIMO-NOMA has not been previously studied.

On the other hand, the k-means has also been considered as the most well-known data clustering algorithm due to its simple implementation, that allows to provide more insight into the underlying nature and structure of the data. There are several variants of the k-means algorithm based on choosing different representative points for the clusters, including the k-medoids [29], k-medians [30], k-modes [31], and employing feature transformation techniques, including weighted k-means [32] and kernel k-means [33]. Different from the k-means algorithm where the representative point for each cluster is the mean of all the points within each cluster, the representative point for each cluster in the k-medoids, k-medians, and k-modes algorithms is the actual data point inside each cluster, the median of each cluster, and the mode of each cluster, respectively. Although the k-medoids and k-medians are more robust to outliers than the k-means, their computational complexity is much higher and therefore not suitable for large datasets. Moreover, the k-modes is designed to handle categorical data, and thus not appropriate for numerical data. Given that the k-means algorithm considers all features equally important, the weighted k-means introduces a feature weighting mechanism, where different features are

assigned different weights [32]. In [33], the kernel functions are applied in the k-means in order to find non-linearly separable clusters. However, both the weighted and kernel k-means algorithms are computationally more expensive than the k-means.

3.2.2 Motivation and Main Contributions

In CFmMIMO-NOMA systems, the effect of network interference is increasingly abnormal and acute as the APs become denser. Most existing works on CFmMIMO-NOMA systems [15–17] focused on the performance analysis while they neglect the importance of UC, which has been shown to significantly improve the performance of NOMA-based systems [3,4,34]. A direct application of random UC schemes [4,18] to CFmMIMO-NOMA systems would result in poor performance, even worse than the traditional linear beamforming without NOMA. In addition, a joint UC and beamforming design [5], which clusters UEs by means of the tensor model, is not very practical for CFmMIMO-NOMA due to excessively high complexity in terms of computational and signalling overhead. Although the k-means algorithm has been widely adopted for different clustering tasks [24–28], its main drawback is sensitivity to the initialization of centroids.

Taking into account all these issues, this chapter devises novel UC algorithms along with an efficient transmission strategy such that the SSE of CFmMIMO-NOMA systems is remarkably enhanced. In particular, our main contributions are summarized as follows:

- This chapter proposes two efficient unsupervised ML-based UC algorithms, including k-means++ and improved k-means++, to effectively cluster UEs into disjoint clusters in CFmMIMO-NOMA. The proposed k-means++ algorithms further address the limitation of k-means due to the randomness of initial centroids. In addition, they are able to ensure the maximum number of UEs per cluster, which can not be achieved by the conventional k-means.

- By adopting the fpZF precoding at APs, this chapter formulates optimization problems for both CFmMIMO-NOMA and COmMIMO-NOMA systems by incorporating power constraints at APs, necessary conditions for implementing SIC at UEs, and the minimum SE requirement at UEs; these belong to the difficult class of non-convex optimization problems. Towards appealing applications, two low-complexity iterative algorithms based on the inner approximation (IA) method [35] are developed for their solutions, which are guaranteed to converge to at least a locally optimal solution.

- Extensive numerical results are provided to confirm the effectiveness of the proposed UC algorithms on the SSE performance over the current state-of-the-art approaches, i.e., close-, far- and random-pairing schemes [19], and Jaccard-based UC scheme [20]. They also show the significantly achieved SSE gains of CFmMIMO-NOMA over COmMIMO-NOMA.

3.2.3 Chapter Organization and Notations

The remainder of this chapter is organized as follows. Section 3.3 describes the system model. In Section 3.4, two unsupervised ML-based UC algorithms are presented. The proposed iterative algorithms for CFmMIMO-NOMA and COmMIMO-NOMA are introduced in Sections 3.5 and 3.6, respectively. Numerical results are given in Section 3.7, while Section 3.8 concludes the chapter.

Notations: Bold uppercase letters, bold lowercase letters, and lowercase characters stand for matrixes, vectors, and scalars, respectively. $|\cdot|$, $(\cdot)^H$, $(\cdot)^T$, $(\cdot)^*$, and $||\cdot||_2$ correspond to the cardinality, the Hermitian transpose, the transpose, the conjugate, and the $l2-$norm operators, respectively. $\mathbb{E}[\cdot]$ represents the expectation operation. $\mathcal{CN}(\mu, \sigma^2)$ stands for circularly symmetric complex Gaussian random variable (RV) with mean μ and

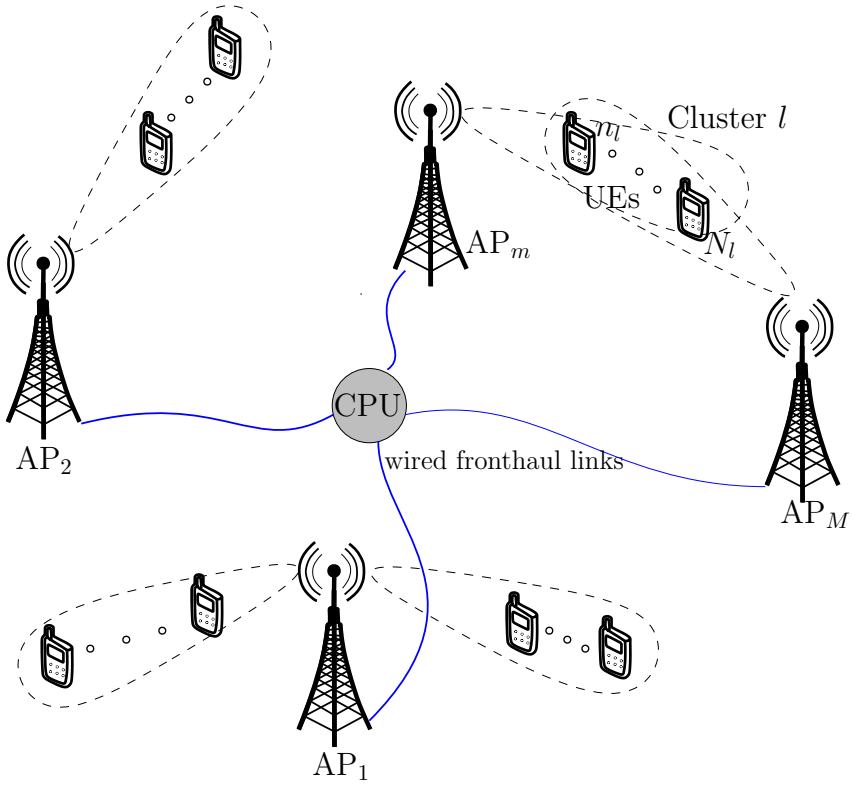

Fig. 3.1: An illustration of the CFmMIMO-NOMA system.

variance σ^2.

3.3 System Model

3.3.1 System Description

This chapter considers an CFmMIMO-NOMA system, where the set $\mathcal{M} \triangleq \{1, 2, \cdots, M\}$ of M APs is connected to the CPU through perfect wired fronthaul links to serve the set $\mathcal{N} \triangleq \{1, 2, \cdots, N\}$ of N UEs via a shared wireless medium, as shown in Fig. 3.1. Each AP is equipped with K antennas, while each UE has a single antenna. APs and UEs are assumed to be randomly distributed in a wide coverage area. The communication between APs and UEs follows the time division duplex (TDD) mode. Each coherence interval, denoted by τ_c, includes two phases: uplink training τ_p ($\tau_p < \tau_c$) and downlink

data transmission ($\tau_c - \tau_p$). The total N UEs are grouped into L clusters and each UE belongs to one cluster only. We denote the set of L clusters by $\mathcal{L} \triangleq \{1, 2, \cdots L\}$. The set of UEs in the l-th cluster is defined as $\mathcal{N}_l \triangleq \{1_l, \cdots, n_l, \cdots, N_l\}$ with $|\mathcal{N}_l| = N_l$, where $\bigcup_{l \in \mathcal{L}} |\mathcal{N}_l| = N$ and $\mathcal{N}_l \bigcap \mathcal{N}_{l'} = \emptyset$ for $l \neq l'$.

3.3.2 Signal Model and Sum Spectral Efficiency (SSE)

3.3.2.1 Uplink Training

In the uplink training phase, all UEs send their training pilots to APs for channel estimation. Then, downlink channels are achieved by leveraging the channel reciprocity property of the TDD mode. With the aim of minimizing the channel estimation overhead in CFmMIMO-NOMA, UEs in the same cluster share the same pilot sequence, and the pilot sequences among different clusters are pairwisely orthogonal [15, 19] which requires $\tau_p \geq L$. This chapter assumes that $\tau_p = L$. Let denote the pilot sequence sent from the UEs in the l-th cluster by $\boldsymbol{\phi}_l \in \mathbb{C}^{\tau_p \times 1}$ with $l \in \{1, 2, \ldots, \tau_p\}$, satisfying the orthogonality, i.e., $\|\boldsymbol{\phi}_l\|_2^2 = \tau_p$ and $\boldsymbol{\phi}_l^H \boldsymbol{\phi}_{l'} = 0$ if $l \neq l'$. The channel vector from UE n_l to AP$_m$ is defined as $\mathbf{h}_{m,n_l} \in \mathbb{C}^{K \times 1}$. This chapter focuses on slowly time-varying channels, and assumes that the channel coefficients are static during the τ_c interval. The channel $\mathbf{h}_{m,n_l}$ is generally modeled as follows:

$$\mathbf{h}_{m,n_l} = \sqrt{\beta_{m,n_l}} \bar{\mathbf{h}}_{m,n_l}, \tag{3.1}$$

where β_{m,n_l} represents the large-scale fading coefficient accounting for path loss and shadowing, and $\bar{\mathbf{h}}_{m,n_l} \in \mathbb{C}^{K \times 1}$ is the small-scale fading vector in which the components are independent and identically distributed (i.i.d.) $\mathcal{CN}(0, 1)$ RVs. The training signals re-

ceived at AP_m can be written as follows:

$$\mathbf{Y}_m^p = \sum_{l \in \mathcal{L}} \sum_{n_l \in \mathcal{N}_l} \sqrt{\rho_{n_l}} \mathbf{h}_{m,n_l} \boldsymbol{\phi}_l^H + \mathbf{W}_m^p, \tag{3.2}$$

where ρ_{n_l} and $\mathbf{W}_m^p \in \mathbb{C}^{K \times \tau_p}$ are the normalized transmit power of UE n_l and the additive noise matrix at AP_m whose elements follow $\mathcal{CN}(0,1)$, respectively.

Given $\mathbf{Y}_m^p$, AP_m estimates $\mathbf{h}_{m,n_l}$ using the minimum mean square error (MMSE) criterion. The projection $\hat{\mathbf{y}}_m^p \in \mathbb{C}^{K \times 1}$ of $\mathbf{Y}_m^p$ at AP_m onto $\boldsymbol{\phi}_l$ can be derived as follows:

$$\hat{\mathbf{y}}_m^p = \mathbf{Y}_m^p \boldsymbol{\phi}_l = \tau_p \sum_{n_l \in \mathcal{N}_l} \sqrt{\rho_{n_l}} \mathbf{h}_{m,n_l} + \mathbf{W}_m^p \boldsymbol{\phi}_l. \tag{3.3}$$

Hence, the MMSE estimate of $\mathbf{h}_{m,n_l}$ is given as

$$\begin{aligned} \hat{\mathbf{h}}_{m,n_l} &= \mathbb{E}\{\mathbf{h}_{m,n_l} (\hat{\mathbf{y}}_m^p)^H\} \left(\mathbb{E}\{\hat{\mathbf{y}}_m^p (\hat{\mathbf{y}}_m^p)^H\}\right)^{-1} \hat{\mathbf{y}}_m^p \\ &= \upsilon_{m,n_l} \hat{\mathbf{y}}_m^p, \end{aligned} \tag{3.4}$$

where $\upsilon_{m,n_l} = \frac{\sqrt{\rho_{n_l}} \beta_{m,n_l}}{\tau_p \sum\limits_{n'_l \in \mathcal{N}_l} \rho_{n'_l} \beta_{m,n'_l} + 1}$. The estimation error vector of $\mathbf{h}_{m,n_l}$ is given as

$$\mathbf{e}_{m,n_l} = \mathbf{h}_{m,n_l} - \hat{\mathbf{h}}_{m,n_l}, \tag{3.5}$$

where the elements of $\mathbf{e}_{m,n_l}$ and $\hat{\mathbf{h}}_{m,n_l}$ are i.i.d. RVs distributed as $\mathcal{CN}\left(\mathbf{0}, \left(\beta_{m,n_l} - \gamma_{m,n_l}\right) \mathbf{I}_K\right)$ and $\mathcal{CN}\left(\mathbf{0}, \gamma_{m,n_l} \mathbf{I}_K\right)$, respectively, with $\gamma_{m,n_l} = \frac{\tau_p \rho_{n_l} \beta_{m,n_l}^2}{\tau_p \sum\limits_{n'_l \in \mathcal{N}_l} \rho_{n'_l} \beta_{m,n'_l} + 1}$. Note that there is no cooperation among APs to exchange the channel estimate information.

Remark. *The so-called pilot contamination exists when APs estimate the channels of UEs belonging to the same cluster. The relationship of channel estimates of UE n_l and*

UE n'_l in the l-th cluster with $n_l \neq n'_l$ and $n_l, n'_l \in \mathcal{N}_l$, at AP_m is expressed as follows:

$$\hat{\boldsymbol{h}}_{m,n_l} = \frac{\sqrt{\rho_{n_l}}\beta_{m,n_l}}{\sqrt{\rho_{n'_l}}\beta_{m,n'_l}}\hat{\boldsymbol{h}}_{m,n'_l}. \tag{3.6}$$

3.3.2.2 Downlink Data Transmission

Under TDD operation, this chapter considers the channel reciprocity to acquire CSI to precode the transmit signals in the downlink [9, 12]. This chapter adopts the fpZF precoding [36] to cancel inter-cluster interference, but still take into account intra-cluster interference. Compared with the pure ZF [37], each AP computes fpZF precoding using its local CSI only, leading to a distributed implementable algorithm. From (3.2), the full-rank matrix $\tilde{\mathbf{H}}_m \in \mathbb{C}^{K\times\tau_p}$ of fpZF precoder at AP_m is given by [36]

$$\tilde{\mathbf{H}}_m = \mathbf{Y}_m^p\boldsymbol{\phi}, \tag{3.7}$$

where $\boldsymbol{\phi} = [\boldsymbol{\phi}_1, \boldsymbol{\phi}_2, \cdots, \boldsymbol{\phi}_{\tau_p}] \in \mathbb{C}^{\tau_p\times\tau_p}$ denotes the collection of τ_p orthogonal pilot sequences. Hence, from (3.4) and (3.7), the channel estimate $\hat{\mathbf{h}}_{m,n_l}$ is rewritten as

$$\hat{\mathbf{h}}_{m,n_l} = \upsilon_{m,n_l}\tilde{\mathbf{H}}_m\boldsymbol{\varphi}_l, \tag{3.8}$$

where $\boldsymbol{\varphi}_l$ is the l-th column of the identity matrix $\mathbf{I}_{\tau_p}$. From (3.7) and (3.8), the beamforming vector $\boldsymbol{w}_{m,l} \in \mathbb{C}^{K\times 1}$ oriented to the l-th cluster at AP_m can be expressed as follows:

$$\boldsymbol{w}_{m,l} = \frac{\tilde{\mathbf{H}}_m\left(\tilde{\mathbf{H}}_m^H\tilde{\mathbf{H}}_m\right)^{-1}\boldsymbol{\varphi}_l}{\sqrt{\mathbb{E}\left\{\left\|\tilde{\mathbf{H}}_m\left(\tilde{\mathbf{H}}_m^H\tilde{\mathbf{H}}_m\right)^{-1}\boldsymbol{\varphi}_l\right\|_2^2\right\}}}. \tag{3.9}$$

The transmitted signal $\boldsymbol{x}_m \in \mathbb{C}^{K\times 1}$ from AP_m is given by

$$\boldsymbol{x}_m = \sum_{l\in\mathcal{L}} \sum_{n_l\in\mathcal{N}_l} \sqrt{\rho_{n_l}^m}\boldsymbol{w}_{m,l} x_{n_l}, \tag{3.10}$$

where x_{n_l} is the symbol intended for UE n_l, and $\rho_{n_l}^m$ is the normalized transmit power (normalized by the noise power at AP_m) allocated to UE n_l at AP_m. Besides, x_{n_l} and $x_{n'_{l'}}$ for $l, l' \in \mathcal{L}$ and $n_l, n'_{l'} \in \mathcal{N}$ must satisfy the following condition

$$\mathbb{E}\Big\{x_{n_l}(x_{n'_{l'}})^*\Big\} = \begin{cases} 1, & \text{if } \ l = l' \ \text{ and } \ n = n', \\ 0, & \text{otherwise.} \end{cases} \tag{3.11}$$

Then, the received signal at UE n_l in the l-th cluster can be written as

$$\begin{aligned} y_{n_l} &= \sum_{m\in\mathcal{M}} \mathbf{h}_{m,n_l}^H \boldsymbol{x}_m + z_{n_l} \\ &= \underbrace{\sum_{m\in\mathcal{M}} \sqrt{\rho_{n_l}^m}\mathbf{h}_{m,n_l}^H \boldsymbol{w}_{m,l} x_{n_l}}_{\text{Desired signal}} + \underbrace{\sum_{m\in\mathcal{M}} \sum_{n'_l\in\mathcal{N}_l\setminus\{n_l\}} \sqrt{\rho_{n'_l}^m}\mathbf{h}_{m,n_l}^H \boldsymbol{w}_{m,l} x_{n'_l}}_{\text{Intra-cluster interference before SIC}} \\ &\quad + \underbrace{\sum_{m\in\mathcal{M}} \sum_{l'\in\mathcal{L}\setminus\{l\}} \sum_{n_{l'}\in\mathcal{N}_{l'}} \sqrt{\rho_{n_{l'}}^m}\mathbf{h}_{m,n_l}^H \boldsymbol{w}_{m,l'} x_{n_{l'}}}_{\text{Inter-cluster interference}} + z_{n_l}, \end{aligned} \tag{3.12}$$

where $z_{n_l} \sim \mathcal{CN}(0,1)$ is the additive white Gaussian noise (AWGN) at UE n_l.

Without loss of generality, in the l-th cluster this chapter considers a descending order of channel gain, i.e., UEs 1_l and N_l are the users with strongest and weakest channel gains, respectively. By NOMA principle [3, 4], UE n_l in the l-th cluster first decodes the signals of UEs $n'_l > n_l$ with poorer channel conditions, and then its own signal is successively decoded after removing the interference from those UEs. Denote by $\mathrm{SINR}_{n_l}^{n'_l}$ and $\mathrm{SINR}_{n'_l}^{n'_l}$ the signal-to-interference-plus-noise ratios (SINRs) in decoding the signal of UE n'_l by UE n_l and itself, respectively. Towards an efficient and implementable SIC, the following

necessary condition is considered [19]

$$\mathbb{E}\left\{\log_2\left(1+\mathrm{SINR}_{n_l}^{n'_l}\right)\right\} \geq \mathbb{E}\left\{\log_2\left(1+\mathrm{SINR}_{n'_l}^{n'_l}\right)\right\}, \tag{3.13}$$

$\forall n_l < n'_l, \forall l \in \mathcal{L}$.

Remark. *We note that perfect SIC is practically unattainable owing to the effects of intra-cluster pilot contamination and channel estimation errors. Consequently, the received signal at UE n_l in the l-th cluster after SIC processing can be written as follows:*

$$\begin{aligned}\bar{y}_{n_l} = &\underbrace{\sum_{m\in\mathcal{M}} \sqrt{\rho_{n_l}^m}\boldsymbol{h}_{m,n_l}^H \boldsymbol{w}_{m,l} x_{n_l}}_{\textit{Desired signal}} + \underbrace{\sum_{m\in\mathcal{M}} \sum_{n'_l=1}^{n_l-1} \sqrt{\rho_{n'_l}^m}\boldsymbol{h}_{m,n_l}^H \boldsymbol{w}_{m,l} x_{n'_l}}_{\textit{Intra-cluster interference after SIC}} \\ &+ \underbrace{\sqrt{\zeta_{n_l}} \sum_{m\in\mathcal{M}} \sum_{n''_l=n_l+1}^{N_l} \sqrt{\rho_{n''_l}^m}\boldsymbol{h}_{m,n_l}^H \boldsymbol{w}_{m,l} x_{n''_l}}_{\textit{Intra-cluster interference due to imperfect SIC}} \\ &+ \underbrace{\sum_{m\in\mathcal{M}} \sum_{l'\in\mathcal{L}\setminus\{l\}} \sum_{n_{l'}\in\mathcal{N}_{l'}} \sqrt{\rho_{n_{l'}}^m}\boldsymbol{h}_{m,n_l}^H \boldsymbol{w}_{m,l'} x_{n_{l'}}}_{\textit{Inter-cluster interference}} + z_{n_l},\end{aligned} \tag{3.14}$$

where ζ_{n_l} is a general SIC performance coefficient at UE n_l in the l-th cluster. In particular, $\zeta_{n_l} = 1$ ($\zeta_{n_l} = 0$) indicates no SIC (perfect SIC), while $0 < \zeta_{n_l} < 1$ means imperfect SIC.

3.3.2.3 Downlink Performance Analysis

Given the UC algorithms that will be introduced in Section 3.4, we first derive the SSE of CFmMIMO-NOMA. From (3.14), the SINR of UE n_l in the l-th cluster is given by

$$\mathrm{SINR}_{n_l} = \frac{|\mathrm{DS}|^2}{\mathbb{E}\left\{|\mathrm{BU}|^2\right\} + \sum\limits_{n'_l=1}^{n_l-1} \mathbb{E}\left\{|\mathrm{ICI}|^2\right\} + \sum\limits_{n''_l=n_l+1}^{N_l} \mathbb{E}\left\{|\mathrm{RICI}|^2\right\} + \sum\limits_{l'\in\mathcal{L}\setminus\{l\}} \sum\limits_{n_{l'}\in\mathcal{N}_{l'}} \mathbb{E}\left\{|\mathrm{UI}|^2\right\} + 1}, \tag{3.15}$$

where $\text{DS} = \mathbb{E}\Big\{\sum\limits_{m\in\mathcal{M}}\sqrt{\rho_{n_l}^m}\mathbf{h}_{m,n_l}^H\boldsymbol{w}_{m,l}\Big\}$, $\text{BU} = \Big(\sum\limits_{m\in\mathcal{M}}\sqrt{\rho_{n_l}^m}\mathbf{h}_{m,n_l}^H\boldsymbol{w}_{m,l} - \mathbb{E}\Big\{\sum\limits_{m\in\mathcal{M}}\sqrt{\rho_{n_l}^m}\mathbf{h}_{m,n_l}^H\boldsymbol{w}_{m,l}\Big\}\Big)$, $\text{ICI} = \sum\limits_{m\in\mathcal{M}}\sqrt{\rho_{n'_l}^m}\mathbf{h}_{m,n_l}^H\boldsymbol{w}_{m,l}$, $\text{RICI} = \sqrt{\zeta_{n_l}}\sum\limits_{m\in\mathcal{M}}\sqrt{\rho_{n''_l}^m}\mathbf{h}_{m,n_l}^H\boldsymbol{w}_{m,l}$, and $\text{UI} = \sum\limits_{m\in\mathcal{M}}\sqrt{\rho_{n_{l'}}^m}\mathbf{h}_{m,n_l}^H\boldsymbol{w}_{m,l'}$ are the coherent beamforming gain (desired signal), beamforming gain uncertainty, intra-cluster interference after SIC, residual interference due to imperfect SIC, and inter-cluster interference, respectively.

To simplify (3.15), we first compute the expectation term in the denominator of (3.9) [38]:

$$\mathbb{E}\left\{\left\|\tilde{\mathbf{H}}_m\left(\tilde{\mathbf{H}}_m^H\tilde{\mathbf{H}}_m\right)^{-1}\boldsymbol{\varphi}_l\right\|_2^2\right\} = \frac{\upsilon_{m,n_l}^2}{\gamma_{m,n_l}(K-\tau_p)},\ \forall n_l \in \mathcal{N}_l. \tag{3.16}$$

From (3.8), (3.9), and (3.16), we have

$$\begin{aligned}\hat{\mathbf{h}}_{m,n_i}^H\boldsymbol{w}_{m,l} &= \frac{\upsilon_{m,n_i}}{\upsilon_{m,n_l}}\boldsymbol{\varphi}_i^H\boldsymbol{\varphi}_l\sqrt{\gamma_{m,n_l}(K-\tau_p)} \\ &= \begin{cases}\sqrt{\gamma_{m,n_l}(K-\tau_p)}, & \text{if } i=l,\\ 0, & \text{if } i\neq l.\end{cases}\end{aligned} \tag{3.17}$$

Lemma 3.1. *The closed-form expression for the SE of UE n_l in the l-th cluster is given by*

$$\begin{aligned}R_{n_l} &= \left(1-\frac{\tau_p}{\tau_c}\right)\log_2\Big(1+\text{SINR}_{n_l}\Big) \\ &= \left(1-\frac{\tau_p}{\tau_c}\right)\log_2\Big(1+\min_{n'_l=1,\ldots,n_l}\text{SINR}_{n'_l}^{n_l}\Big),\ \forall n_l.\end{aligned} \tag{3.18}$$

With $\boldsymbol{\rho} \triangleq \{\rho_{n_l}^m\}_{m\in\mathcal{M},n_l\in\mathcal{N}_l,l\in\mathcal{L}}$, $\text{SINR}_{n_l}^{n_l}$ and $\text{SINR}_{n'_l}^{n_l}$, $\forall n'_l < n_l$, are derived as follows:

$$\text{SINR}_{n_l}^{n_l} = \frac{(K-\tau_p)\Big(\sum\limits_{m\in\mathcal{M}}\sqrt{\rho_{n_l}^m\gamma_{m,n_l}}\Big)^2}{\mathcal{I}_{n_l}^{n_l}(\boldsymbol{\rho})+1}, \tag{3.19}$$

$$\mathrm{SINR}_{n'_l}^{n_l} = \frac{(K-\tau_p)\Big(\sum\limits_{m\in\mathcal{M}}\sqrt{\rho_{n_l}^m\gamma_{m,n'_l}}\Big)^2}{\mathcal{I}_{n'_l}^{n_l}(\boldsymbol{\rho})+1}, \tag{3.20}$$

where $\mathcal{I}_{n_l}^{n_l}(\boldsymbol{\rho})$ *and* $\mathcal{I}_{n'_l}^{n_l}(\boldsymbol{\rho})$ *are defined as*

$$\begin{aligned}
\mathcal{I}_{n_l}^{n_l}(\boldsymbol{\rho}) &\triangleq \sum_{n''_l\in\mathcal{N}_l\setminus\{n_l\}} \eta_{n''_{l'}}(K-\tau_p)\Big(\sum_{m\in\mathcal{M}}\sqrt{\rho_{n''_l}^m\gamma_{m,n_l}}\Big)^2 \\
&\quad + \sum_{l'\in\mathcal{L}}\sum_{n''_{l'}\in\mathcal{N}_{l'}}\sum_{m\in\mathcal{M}} \eta_{n''_{l'}}\rho_{n''_{l'}}^m\left(\beta_{m,n_l}-\gamma_{m,n_l}\right), \\
\mathcal{I}_{n'_l}^{n_l}(\boldsymbol{\rho}) &\triangleq \sum_{n''_l\in\mathcal{N}_l\setminus\{n_l\}} \eta_{n''_{l'}}(K-\tau_p)\Big(\sum_{m\in\mathcal{M}}\sqrt{\rho_{n''_l}^m\gamma_{m,n'_l}}\Big)^2 \\
&\quad + \sum_{l'\in\mathcal{L}}\sum_{n''_{l'}\in\mathcal{N}_{l'}}\sum_{m\in\mathcal{M}} \eta_{n''_{l'}}\rho_{n''_{l'}}^m\left(\beta_{m,n'_l}-\gamma_{m,n'_l}\right),
\end{aligned}$$

with

$$\eta_{n''_{l'}} = \begin{cases} 1, & \text{if } l' \neq l \text{ or } l' = l \text{ and } n''_l \leq n_l, \\ \zeta_{n_l}, & \text{otherwise.} \end{cases}$$

Proof. We follow similar steps as in [17] to derive (3.19) and (3.20), by taking into account the residual interference due to imperfect SIC. □

We define the virtual channel of UE n_l in the l-th cluster as $\mathbf{h}_{n_l} = [\gamma_{1,n_l},\ldots,\gamma_{M,n_l}]^T$, $\forall n_l \in \mathcal{N}_l$. We assume that UEs in the l-th cluster are sorted based on their virtual channels, such as $\|\mathbf{h}_{1_l}\|_2 \geq \|\mathbf{h}_{2_l}\|_2 \geq \ldots \geq \|\mathbf{h}_{N_l}\|_2$, $\forall l \in \mathcal{L}$. From (3.18), the SSE of CFmMIMO-NOMA is expressed as

$$\begin{aligned}
R_\Sigma &= \sum_{l\in\mathcal{L}}\sum_{n_l\in\mathcal{N}_l} R_{n_l} \\
&= \Big(1-\frac{\tau_p}{\tau_c}\Big)\sum_{l\in\mathcal{L}}\sum_{n_l\in\mathcal{N}_l}\log_2\Big(1+\mathrm{SINR}_{n_l}\Big).
\end{aligned} \tag{3.21}$$

3.4 Clustering Cell-Free Massive MIMO-NOMA System

In CFmMIMO systems, a large number of APs are deployed in the area, which leads to the heterogeneous locations between UEs and different APs. In this section, we propose two unsupervised ML-based UC algorithms to effectively divide all UEs into separate clusters, which are implemented at the CPU by exploiting the large-scale fading coefficients and considering all the APs. Similar to [19] and [28], large-scale fading coefficients of UEs are assumed to be collected and shared with the CPU before performing the UC algorithm. We note that it is only necessary to estimate the large-scale fading coefficients once every 40 τ_c intervals [15], and thus, conveying these coefficients via the fronthaul links occurs much less frequently than data transmission. Denote by $\boldsymbol{\beta}_n \triangleq [\beta_{1,n}, \beta_{2,n}, \ldots, \beta_{M,n}]^T \in \mathbb{R}^{M\times 1}$ the set of large-scale fading coefficients from all APs associated to UE $n, \forall n \in \mathcal{N}$. The vector $\boldsymbol{\beta}_n$ can be considered as an effective feature-vector denoting the location of UE n.

3.4.1 The k-means Algorithm

The k-means algorithm for UC studied in [27] and [28] is one of the simplest unsupervised ML algorithms to partition UEs in the coverage area into separate groups. The key idea is to find a user-specified number of clusters L, which are represented by L centroids, one for each cluster. The number of clusters L in the k-means algorithm is predetermined. The principle of k-means algorithm is given as follows. Firstly, L initial centroids are randomly selected. Secondly, each point is assigned to the nearest centroid, and each mass of points assigned to the same centroid creates a cluster. Then, the centroid of each cluster is updated according to the points associated to the cluster. The assignment and update processes of centroids are repeated until either there is no change in the clusters

or centroids remain similarly.

In the context of NOMA systems, it should be noted that the k-means algorithm studied in [27] results in clusters that have unlimited number of UEs, which may not be applicable to NOMA systems because of the increase in SIC computational complexity and the degradation of the decoding performance. As the number of UEs per group increases, it also becomes more challenging to achieve suitable receive power ratios among NOMA UEs, especially under practical setups where the SIC is imperfect and error propagation can be significant. Hence, this chapter imposes a constraint to limit the number of UEs per cluster. In the context of CFmMIMO-NOMA, the procedure of k-means can be summarized as follows:

- Step 1: L initial centroids are randomly selected from N UEs, where L is a predefined number. The set of L cluster centroids is defined as follows:

$$\mathcal{C} = \{c_l, l \in \mathcal{L}\}, \tag{3.22}$$

  where c_l represents the centroid of the l-th cluster.

- Step 2: Each UE $n \in \mathcal{N}$ is grouped to the nearest centroid, and hence, UEs assigned to the same centroid creates a cluster:

$$l' = \underset{\forall l \in \mathcal{L}}{\arg\min}\, f_d\left(\boldsymbol{\beta}_n, \boldsymbol{\beta}_{c_l}\right), \tag{3.23}$$

  where $f_d\left(\boldsymbol{\beta}_n, \boldsymbol{\beta}_{c_l}\right) = \left\|\boldsymbol{\beta}_n - \boldsymbol{\beta}_{c_l}\right\|_2$ represents the Euclidean distance from UE n to centroid c_l [27]. As shown in (3.23), UE n is grouped to l'-th cluster (denoted by centroid $c_{l'}$) since the distance from UE n to centroid $c_{l'}$ is nearest.

- Step 3: The centroid of each cluster is recalculated under given UEs assigned to this

cluster:

$$\boldsymbol{\beta}_{c_l} = \frac{1}{|\mathcal{N}_l|} \sum_{n \in \mathcal{N}_l} \boldsymbol{\beta}_n, \forall l \in \mathcal{L}, \tag{3.24}$$

where $\boldsymbol{\beta}_{c_l}$ represents the updated centroid for the l-th cluster, which can be calculated by the mean of all UEs belonging to the l-th cluster.

- Step 4: Steps 2-3 are repeated until convergence, i.e., there is no change in the clusters or the centroids remain the same.

- Step 5: If $\exists l'' \in \mathcal{L}$ such that $|\mathcal{N}_{l''}| > \iota$, where ι denotes the maximum number of UEs in each cluster, and with $\mathcal{L}''$ denoting the set of clusters with size exceeding ι, i.e., $\mathcal{L}'' = \{l'', l'' \in \mathcal{L} \text{ with } |\mathcal{N}_{l''}| > \iota\}$, the UEs from the oversized clusters in $\mathcal{L}''$ are pooled as:

$$\mathcal{N}' = \bigcup_{\forall l'' \in \mathcal{L} \text{ with } |\mathcal{N}_{l''}| > \iota} \mathcal{N}_{l''}. \tag{3.25}$$

  Repeat Steps 1-4 to $\mathcal{N}'$ targeting $|\mathcal{L}''| + 1$ clusters.

  Update the number of clusters $\mathcal{L} \leftarrow \mathcal{L} + 1$.

- Step 6: Step 5 is repeated until $|\mathcal{N}_l| \leq \iota$, $\forall l \in \mathcal{L}$.

Note that Steps 5-6 are performed iteratively to ensure that all clusters are bounded above. The k-means algorithm for UC in CFmMIMO-NOMA is given in Algorithm 2. Note that k-means is a greedy algorithm, which can converge to a local minimum since its performance highly depends on the predefined number of clusters L and the centroid initialization process, i.e., how to select L initial centroids.

Algorithm 2 The k-means Algorithm for UC in CFmMIMO-NOMA

Input: L and $\boldsymbol{\beta}_n, \forall n \in \mathcal{N}$.
*//**Identify L cluster centroids at random c_l, $\forall l \in \mathcal{L}$ (Step 1)**//*
Set $\mathcal{C} = \emptyset$ and $l = 1$, where $\mathcal{C}$ denotes the set of cluster centroids.
while $l \leq L$ **do**
  $c_l = \mathsf{generateRandom}[1, N]$;
  if $c_l \notin \mathcal{C}$ **then**
    $\mathcal{C} \leftarrow c_l$;
    $l = l + 1$;
  end if
end while
*//**Main process (Steps 2-4)**//*
while $\mathcal{C}$ changes **do**
  *//**Identify $\mathcal{N}_{l'}$, $\forall l' \in \mathcal{L}$, containing the subset of UEs that are closer to $c_{l'}$ than c_l, with $l' \neq l$ (Step 2)**//*
  for $n \in \mathcal{N} \backslash \mathcal{C}$ **do**
    $l' = \arg\min_{\forall l \in \mathcal{L}} f_d\left(\boldsymbol{\beta}_n, \boldsymbol{\beta}_{c_l}\right)$, where $f_d\left(\boldsymbol{\beta}_n, \boldsymbol{\beta}_{c_l}\right) = ||\boldsymbol{\beta}_n - \boldsymbol{\beta}_{c_l}||_2$;
    $\mathcal{N}_{l'} \leftarrow n$;
  end for
  *//**Recalculate c_l of cluster $\mathcal{N}_l$, $\forall l \in \mathcal{L}$ (Step 3)**//*
  for $l = 1 : L$ **do**
    $\boldsymbol{\beta}_{c_l} = \frac{1}{|\mathcal{N}_l|} \sum_{n \in \mathcal{N}_l} \boldsymbol{\beta}_n$;
  end for
end while
*//**Ensure $|\mathcal{N}_l| \leq \iota$, $\forall l \in \mathcal{L}$ (Steps 5-6)**//*
$\mathcal{L}'' = \{l'', l'' \in \mathcal{L}$ with $|\mathcal{N}_{l''}| > \iota\}$;
$\mathcal{L} = \mathcal{L} \setminus \mathcal{L}''$;
while $\mathcal{L}'' \neq \emptyset$ **do**
  $\mathcal{N}' = \bigcup_{\forall l'' \in \mathcal{L}''} \mathcal{N}_{l''}$;
  Repeat Steps 2-22 to $\mathcal{N}'$ with $|\mathcal{L}'''| = |\mathcal{L}''| + 1$ clusters, where $\mathcal{L}'''$ denotes the set of $|\mathcal{L}''| + 1$ clusters;
  $\mathcal{L} = \mathcal{L} \cup \{l'', l'' \in \mathcal{L}'''$ with $|\mathcal{N}_{l''}| \leq \iota\}$;
  $\mathcal{L}'' = \{l'', l'' \in \mathcal{L}'''$ with $|\mathcal{N}_{l''}| > \iota\}$;
end while
Output: $\mathcal{N}_l$ and c_l, $\forall l \in \mathcal{L}$.

3.4.2 Proposed k-means++ Algorithm

One drawback of the k-means algorithm is that it is sensitive to the initialization of the centroids [39,40]. If an initial centroid is a far point, it might not associate with any other points. Equivalently, more than one initial centroids might be created into the same cluster which leads to poor grouping. In this section, the k-means++ algorithm is developed to resolve this issue. It aims at providing a clever initialization of the centroids that improves the quality of the grouping process. Besides, the proposed k-means++ algorithm is able to control the maximum number of UEs per cluster. Except for the improvement in the centroid initialization process, the remainder of k-means++ algorithm is the same as in the k-means. In the context of CFmMIMO-NOMA, the proposed k-means++ can be summarized as follows:

- Step 1: The first initial centroid c_1 is randomly selected from N UEs.
- Step 2: For each UE n (with $n \in \mathcal{N}$ and $n \notin \mathcal{C}$), its distance from the nearest centroid is calculated as follows:

$$f_d\left(\boldsymbol{\beta}_n, \boldsymbol{\beta}_{c_t}\right) = \left\|\boldsymbol{\beta}_n - \boldsymbol{\beta}_{c_t}\right\|_2, \tag{3.26}$$

  where $c_t = \underset{\forall c_l \in \mathcal{C}}{\arg\min}\, f_d\left(\boldsymbol{\beta}_n, \boldsymbol{\beta}_{c_l}\right)$.

- Step 3: The next centroid is selected from UEs ($\forall n \in \mathcal{N} \backslash \mathcal{C}$) such that the probability of selecting a UE as a centroid is in direct proportion to its distance from the nearest and previously selected centroid, i.e., the UE having the maximum distance from the nearest centroid is virtually to be chosen next as a centroid:

$$c_l = \underset{\forall n \in \mathcal{N} \backslash \mathcal{C}}{\arg\max}\, f_d\left(\boldsymbol{\beta}_n, \boldsymbol{\beta}_{c_t}\right). \tag{3.27}$$

- Step 4: Steps 2-3 are repeated until $L-1$ centroids are selected.
- Step 5: The process continues following Steps 2-6 in the k-means algorithm.

The centroid initialization process of the proposed k-means++ (from step 1 to step 4) ensures that chosen centroids are far away from each other. This increases the opportunity of initially selecting centroids that are located in different clusters. The proposed k-means++ algorithm for UC in CFmMIMO-NOMA is described in Algorithm 3.

3.4.3 Proposed Improved k-means++ Algorithm

As shown in Sections 3.4.1 and 3.4.2, the performance of the k-means algorithm can be enhanced by selecting the L initial centroids more effectively. Based on the characteristics of CFmMIMO-NOMA, we propose the improved k-means++ algorithm which includes a new approach to cleverly select L initial centroids. Since initial centroids are chosen as UEs that have highest large scale fading coefficients to the largest number of APs, the resulting clusters are served by more APs with better signal quality. The procedure of improved k-means++ is summarized as follows:

- Step 1: Each AP identifies an associated UE, denoted by Λ_m, which has the best connection, i.e., highest large-scale fading coefficient $\beta_{m,n}$:

$$\Lambda_m = \underset{\forall n \in \mathcal{N}}{\arg\max}\, \beta_{m,n}, \forall m \in \mathcal{M}. \tag{3.28}$$

- Step 2: The CPU then selects a subset of APs, denoted by Υ_n, which have best connections to UE n:

$$\Upsilon_n = \{\text{AP}_m : \text{UE } n == \Lambda_m\}, \forall n \in \mathcal{N}. \tag{3.29}$$

Algorithm 3 The k-means++ Algorithm for UC in CFmMIMO-NOMA

Input: L and $\boldsymbol{\beta}_n$, $\forall n \in \mathcal{N}$.
*//**Identify the first cluster centroid c_l (Step 1)**//*
Set $\mathcal{C} = \emptyset$ and $c_1 = \mathsf{generateRandom}[1, N]$;
$\mathcal{C} \leftarrow c_1$ and set $f = 0$;
*//**Identify $L-1$ cluster centroids, c_l, $l = 2, \ldots, L$ (Steps 2-4)**//*
for $l = 2 : L$ **do**
  for $n = 1 : N$ **do**
    for $t = 1 : l-1$ **do**
      if $n \neq c_t$ **then**
        $dis\,(1,t) = f_d\left(\boldsymbol{\beta}_n, \boldsymbol{\beta}_{c_t}\right)$, where $f_d\left(\boldsymbol{\beta}_n, \boldsymbol{\beta}_{c_t}\right) = \|\boldsymbol{\beta}_n - \boldsymbol{\beta}_{c_t}\|_2$;
      else
        $dis\,(1,t) = \text{NaN}$;
        $f = f + 1$;
      end if
    end for
    if $f == 0$ **then**
      $dist\,(1,n) = \max\ dis$;
    else
      $dist\,(1,n) = \text{NaN}$;
      $f = 0$;
    end if
  end for
  $c_l = \underset{\forall n \in \mathcal{N} \setminus \mathcal{C}}{\arg\max}\ dist$;
  $\mathcal{C} \leftarrow c_l$;
end for
*//**Main process (Step 5)**//*
while $\mathcal{C}$ changes **do**
  for $n \in \mathcal{N} \setminus \mathcal{C}$ **do**
    $l' = \underset{\forall l \in \mathcal{L}}{\arg\min}\ f_d\left(\boldsymbol{\beta}_n, \boldsymbol{\beta}_{c_l}\right)$, where $f_d\left(\boldsymbol{\beta}_n, \boldsymbol{\beta}_{c_l}\right) = \|\boldsymbol{\beta}_n - \boldsymbol{\beta}_{c_l}\|_2$;
    $\mathcal{N}_{l'} \leftarrow n$;
  end for
  for $l = 1 : L$ **do**
    $\boldsymbol{\beta}_{c_l} = \frac{1}{|\mathcal{N}_l|} \sum\limits_{n \in \mathcal{N}_l} \boldsymbol{\beta}_n$;
  end for
end while
*//**Ensure $|\mathcal{N}_l| \leq \iota$, $\forall l \in \mathcal{L}$ (Step 5)**//*
$\mathcal{L}'' = \{l'', l'' \in \mathcal{L}$ with $|\mathcal{N}_{l''}| > \iota\}$;
$\mathcal{L} = \mathcal{L} \setminus \mathcal{L}''$;
while $\mathcal{L}'' \neq \emptyset$ **do**
  $\mathcal{N}' = \bigcup\limits_{\forall l'' \in \mathcal{L}''} \mathcal{N}_{l''}$;
  Repeat Steps 2-35 to $\mathcal{N}'$ with $|\mathcal{L}'''| = |\mathcal{L}''| + 1$ clusters, where $\mathcal{L}'''$ denotes the set of $|\mathcal{L}''| + 1$ clusters;
  $\mathcal{L} = \mathcal{L} \cup \{l'', l'' \in \mathcal{L}'''$ with $|\mathcal{N}_{l''}| \leq \iota\}$;
  $\mathcal{L}'' = \{l'', l'' \in \mathcal{L}'''$ with $|\mathcal{N}_{l''}| > \iota\}$;
end while
Output: $\mathcal{N}_l$ and c_l, $\forall l \in \mathcal{L}$.

- Step 3: The CPU selects a UE having the highest number of serving APs as a centroid:

$$c_l = \underset{\forall n \in \mathcal{N} \setminus \mathcal{C}}{\arg\max} |\Upsilon_n|, \tag{3.30}$$

  where $|\Upsilon_n|$ denotes the cardinality of Υ_n.

- Step 4: Step 3 is repeated until L centroids are chosen.

- Step 5: The process continues following Steps 2-6 in the k-means algorithm.

The centroid initialization process of the improved k-means++ for UC in CFmMIMO-NOMA (Steps 1-4 above) is described in Algorithm 4.

Algorithm 4 Centroid Initialization Process of the Improved k-means++ Algorithm for UC in CFmMIMO-NOMA

Input: L and $\boldsymbol{\beta}_n, \forall n \in \mathcal{N}$.
*//**Identify UE that has the best connection to each AP (Step 1)**//*
for $m = 1 : M$ **do**
  $\Lambda_m = \underset{\forall n \in \mathcal{N}}{\arg\max}\, \beta_{m,n}$;
end for
*//**Identify the subset of APs that have best connections to each UE (Step 2)**//*
for $n = 1 : N$ **do**
  for $m = 1 : M$ **do**
    if $n == \Lambda_m$ **then**
      $\Upsilon_n \leftarrow m$;
    end if
  end for
end for
*//**Identify L cluster centroids, c_l, $\forall l \in \mathcal{L}$, that have large number of serving APs (Steps 3-4)**//*
$\mathcal{C} = \emptyset$, where $\mathcal{C}$ denotes the set of cluster centroids.
for $l = 1 : L$ **do**
  $c_l = \underset{\forall n \in \mathcal{N} \setminus \mathcal{C}}{\arg\max} |\Upsilon_n|$;
  $\mathcal{C} \leftarrow c_l$;
end for
Output: $\mathcal{C}$.

3.5 The SSE Maximization

From (3.19) and (3.20), it is clear that the SSE of CFmMIMO-NOMA highly depends on the power allocation (PA) at all APs. Thus, it is necessary to optimize the transmit power at APs so that the SSE of CFmMIMO-NOMA can be enhanced. In this section, we aim at optimizing the normalized transmit power $\boldsymbol{\rho} \triangleq \{\rho_{n_l}^m\}_{m,n_l,l}$ to maximize the SSE under the constraints of the transmit power budget at the APs, SIC conditions, and minimum required SE at UEs. The optimization problem can be mathematically expressed as

$$\max_{\boldsymbol{\rho}} \quad \Big(1-\frac{\tau_p}{\tau_c}\Big)\sum_{l\in\mathcal{L}}\sum_{n_l\in\mathcal{N}_l}\log_2\Big(1+\mathrm{SINR}_{n_l}\Big) \tag{3.31a}$$

$$\text{s.t.} \quad \sum_{l\in\mathcal{L}}\sum_{n_l\in\mathcal{N}_l}\rho_{n_l}^m \le P_{\max}^m, \forall m\in\mathcal{M}, \tag{3.31b}$$

$$\rho_{n_l}^m \le \rho_{n_l+1}^m, n_l\in[1,N_l-1], \forall m\in\mathcal{M}, l\in\mathcal{L}, \tag{3.31c}$$

$$\Big(1-\frac{\tau_p}{\tau_c}\Big)\log_2\Big(1+\mathrm{SINR}_{n_l}\Big)\ge \bar{R}_{n_l}, \forall n_l. \tag{3.31d}$$

Herein, constraint (3.31b) indicates that the total transmit power at AP_m is limited by the normalized maximum power $P_{\max}^m$, constraint (3.31c) is the necessary condition to implement SIC in the l-th cluster, $\forall l\in\mathcal{L}$, and constraint (3.31d) denotes the minimum SE requirement $\bar{R}_{n_l}$ of UE n_l, $\forall n_l$. We note that SINR_{n_l} in (3.31a) is a nonconvex and nonsmooth function with respect to $\boldsymbol{\rho}$, making problem (3.31) intractable. Therefore, it may not be possible to solve the problem directly. In addition, the globally optimal solution (e.g., exhaustive search) comes at the cost of high computational complexity, and may not be suitable for practical implementation. In what follows, we develop newly approximated functions using the IA framework [35,41], and then propose a fast converging and low-complexity algorithm.

Equivalent Optimization Problem: To apply the IA method, several transformations are necessary to make (3.31) tractable. To do so, we introduce the auxiliary variables

$\mathbf{r} \triangleq \left\{r_{n_l}\right\}_{\forall n_l}$ and $\boldsymbol{\varphi} \triangleq \left\{\varphi_{n_l}\right\}_{\forall n_l}$ to rewrite (3.31) equivalently as

$$\max_{\boldsymbol{\rho},\mathbf{r},\boldsymbol{\varphi}} \quad \left(1-\frac{\tau_p}{\tau_c}\right)\sum_{l\in\mathcal{L}}\sum_{n_l\in\mathcal{N}_l} r_{n_l} \tag{3.32a}$$

$$\text{s.t.} \quad \ln\left(1+\varphi_{n_l}\right) \geq r_{n_l}\ln 2,\ \forall n_l \in \mathcal{N}_l, \tag{3.32b}$$

$$\text{SINR}_{n'_l}^{n_l} \geq \varphi_{n_l},\ \forall n'_l < n_l,\ \forall n_l \in \mathcal{N}_l, \tag{3.32c}$$

$$\text{SINR}_{n_l}^{n_l} \geq \varphi_{n_l},\ \forall n_l \in \mathcal{N}_l, \tag{3.32d}$$

$$\left(1-\frac{\tau_p}{\tau_c}\right) r_{n_l} \geq \bar{R}_{n_l}, \forall n_l, \tag{3.32e}$$

$$(3.31\text{b}), (3.31\text{c}). \tag{3.32f}$$

It is clear that the objective function becomes linear. The equivalence between (3.31) and (3.32) is verified by the following lemma.

Lemma 3.2. *Problems* (3.31) *and* (3.32) *share the same optimal solution set and the same optimal objective value. In particular, let* $(\boldsymbol{\rho}^\star, \mathbf{r}^\star, \boldsymbol{\varphi}^\star)$ *be the optimal solution to problem* (3.32)*, then* $\boldsymbol{\rho}^\star$ *is also the optimal solution to problem* (3.31) *and vice versa.*

Proof. The proof is done by showing the fact that constraints (3.32b)-(3.32d) will hold with equality at the optimum. This statement is proved by contradiction. Suppose that constraints (3.32c) and (3.32d) are inactive at the optimum for some users, i.e., there exists $\varphi'_{n_l} > 0$ such as $\min\left(\text{SINR}_{n'_l}^{n_l}, \text{SINR}_{n_l}^{n_l}\right) = \varphi'_{n_l} > \varphi^\star_{n_l}$. It is clear that φ'_{n_l} is also a feasible point to (3.32b), and $r'_{n_l} = \ln\left(1+\varphi'_{n_l}\right)/\ln 2 > \ln\left(1+\varphi^\star_{n_l}\right)/\ln 2 = r^\star_{n_l}$. As a consequence, this results in a strictly larger objective value, i.e., $\left(1-\frac{\tau_p}{\tau_c}\right)\sum_{l\in\mathcal{L}}\sum_{n_l\in\mathcal{N}_l} r'_{n_l} > \left(1-\frac{\tau_p}{\tau_c}\right)\sum_{l\in\mathcal{L}}\sum_{n_l\in\mathcal{N}_l} r^\star_{n_l}$, which contradicts the assumption that $(\boldsymbol{\rho}^\star, \mathbf{r}^\star, \boldsymbol{\varphi}^\star)$ represents the optimal solution to problem (3.32). □

Inner Approximation (IA) for Problem (3.32)*:* The nonconvex parts include (3.32c) and (3.32d). The direct application of IA method is still not possible due to the com-

plication of $\mathrm{SINR}_{n'_l}^{n_l}$ and $\mathrm{SINR}_{n_l}^{n_l}$. In the following, the change of variable is made as $\rho_{n_l}^m = (\hat{\rho}_{n_l}^m)^2, \forall n_l \in \mathcal{N}_l$. Firstly, (3.32c) can be handled by rewriting $\mathrm{SINR}_{n'_l}^{n_l}$ as

$$\mathrm{SINR}_{n'_l}^{n_l} = \frac{(K-\tau_p)\Big(\sum\limits_{m\in\mathcal{M}} \hat{\rho}_{n_l}^m \sqrt{\gamma_{m,n'_l}}\Big)^2}{\mathcal{I}_{n'_l}^{n_l}(\hat{\boldsymbol{\rho}}) + 1}, \tag{3.33}$$

where $\hat{\boldsymbol{\rho}} \triangleq \{\hat{\rho}_{n_l}^m\}_{\forall n_l}$ and

$$\begin{aligned}\mathcal{I}_{n'_l}^{n_l}(\hat{\boldsymbol{\rho}}) \triangleq & \sum_{n''_l \in \mathcal{N}_l \setminus \{n_l\}} \eta_{n''_{l'}} (K-\tau_p)\Big(\sum_{m\in\mathcal{M}} \hat{\rho}_{n''_l}^m \sqrt{\gamma_{m,n'_l}}\Big)^2 \\ & + \sum_{l'\in\mathcal{L}} \sum_{n''_{l'}\in\mathcal{N}_{l'}} \sum_{m\in\mathcal{M}} \eta_{n''_{l'}} \left(\hat{\rho}_{n''_{l'}}^m\right)^2 \left(\beta_{m,n'_l} - \gamma_{m,n'_l}\right).\end{aligned} \tag{3.34}$$

By introducing the slack variables $\boldsymbol{\varpi} \triangleq \{\varpi_{n'_l}^{n_l}\}_{\forall n_l}, \boldsymbol{\tau} \triangleq \{\tau_{n''_l}^{n'_l}\}_{\forall n_l}$, and $\boldsymbol{\theta} \triangleq \{\theta_{n'_l}^{n_l}\}_{\forall n_l}$, constraint (3.32c) can be equivalently rewritten as

$$(3.32c) \Leftrightarrow \begin{cases} \sum\limits_{m\in\mathcal{M}} \hat{\rho}_{n_l}^m \sqrt{\gamma_{m,n'_l}} \geq \varpi_{n'_l}^{n_l}, \ \forall n'_l < n_l, \forall n_l \in \mathcal{N}_l, & \text{(3.35a)} \\ \sum\limits_{m\in\mathcal{M}} \hat{\rho}_{n''_l}^m \sqrt{\gamma_{m,n'_l}} \leq \tau_{n''_l}^{n'_l}, \ \forall n'_l < n_l, \ \forall n_l \in \mathcal{N}_l, & \text{(3.35b)} \\ \mathcal{I}_{n'_l}^{n_l}(\hat{\boldsymbol{\rho}}, \boldsymbol{\tau}) \leq \theta_{n'_l}^{n_l}, \ \forall n'_l < n_l, \ \forall n_l \in \mathcal{N}_l, & \text{(3.35c)} \\ (K-\tau_p)\dfrac{\left(\varpi_{n'_l}^{n_l}\right)^2}{\theta_{n'_l}^{n_l}+1} \geq \varphi_{n_l}, \ \forall n'_l < n_l, \ \forall n_l \in \mathcal{N}_l, & \text{(3.35d)} \end{cases}$$

where

$$\mathcal{I}_{n'_l}^{n_l}(\hat{\boldsymbol{\rho}}, \boldsymbol{\tau}) \triangleq \sum_{n''_l \in \mathcal{N}_l \setminus \{n_l\}} \eta_{n''_{l'}} (K-\tau_p)\left(\tau_{n''_l}^{n'_l}\right)^2 + \sum_{l'\in\mathcal{L}} \sum_{n''_{l'}\in\mathcal{N}_{l'}} \sum_{m\in\mathcal{M}} \eta_{n''_{l'}} \left(\hat{\rho}_{n''_{l'}}^m\right)^2 \left(\beta_{m,n'_l} - \gamma_{m,n'_l}\right) \tag{3.36}$$

is a quadratic function. Here, constraint (3.35d) remains nonconvex. We note that $(\varpi_{n'_l}^{n_l})^2/(\theta_{n'_l}^{n_l}+1)$ is the quadratic-over-linear function, which is convex with respect to $(\varpi_{n'_l}^{n_l}, \theta_{n'_l}^{n_l})$. Let $(\varpi_{n'_l}^{n_l,(\kappa)}, \theta_{n'_l}^{n_l,(\kappa)})$ be a feasible point of $(\varpi_{n'_l}^{n_l}, \theta_{n'_l}^{n_l})$ at the κ-th iteration of

an iterative algorithm and by the IA principle, constraint (3.35d) can be convexified as

$$(K-\tau_p)\Big(\frac{2\varpi_{n'_l}^{n_l,(\kappa)}}{\theta_{n'_l}^{n_l,(\kappa)}+1}\varpi_{n'_l}^{n_l}-\frac{\left(\varpi_{n'_l}^{n_l,(\kappa)}\right)^2}{\left(\theta_{n'_l}^{n_l,(\kappa)}+1\right)^2}(\theta_{n'_l}^{n_l}+1)\Big)\geq\varphi_{n_l}, \tag{3.37}$$

$\forall n'_l < n_l,\ \forall n_l \in \mathcal{N}_l$. Similarly, constraint (3.32d) can be iteratively approximated as

$$(3.32\text{d}) \Leftrightarrow \begin{cases} \sum\limits_{m\in\mathcal{M}} \hat{\rho}_{n_l}^m \sqrt{\gamma_{m,n_l}} \geq \varpi_{n_l}^{n_l},\ \forall n_l \in \mathcal{N}_l, & (3.38\text{a}) \\ \sum\limits_{m\in\mathcal{M}} \hat{\rho}_{n''_l}^m \sqrt{\gamma_{m,n_l}} \leq \tau_{n''_l}^{n_l},\ \forall n_l \in \mathcal{N}_l, & (3.38\text{b}) \\ \mathcal{I}_{n_l}^{n_l}(\hat{\boldsymbol{\rho}},\boldsymbol{\tau}) \leq \theta_{n_l}^{n_l},\ \forall n_l \in \mathcal{N}_l, & (3.38\text{c}) \\ (K-\tau_p)\Big(\frac{2\varpi_{n_l}^{n_l,(\kappa)}}{\theta_{n_l}^{n_l,(\kappa)}+1}\varpi_{n_l}^{n_l}-\frac{\left(\varpi_{n_l}^{n_l,(\kappa)}\right)^2}{\left(\theta_{n_l}^{n_l,(\kappa)}+1\right)^2}(\theta_{n_l}^{n_l}+1)\Big)\geq\varphi_{n_l},\ \forall n_l \in \mathcal{N}_l, & (3.38\text{d}) \end{cases}$$

where

$$\mathcal{I}_{n_l}^{n_l}(\hat{\boldsymbol{\rho}},\boldsymbol{\tau}) \triangleq \sum_{n''_l\in\mathcal{N}_l\setminus\{n_l\}} \eta_{n''_l}(K-\tau_p)\left(\tau_{n''_l}^{n_l}\right)^2 + \sum_{l'\in\mathcal{L}}\sum_{n''_{l'}\in\mathcal{N}_{l'}}\sum_{m\in\mathcal{M}} \eta_{n''_{l'}}\left(\hat{\rho}_{n''_{l'}}^m\right)^2(\beta_{m,n_l}-\gamma_{m,n_l}).$$

In summary, the convex approximate program of (3.32) solved at iteration $\kappa+1$ is given as

$$\max_{\hat{\boldsymbol{\rho}},\mathbf{r},\boldsymbol{\varphi},\boldsymbol{\varpi},\boldsymbol{\tau},\boldsymbol{\theta}} \quad \Big(1-\frac{\tau_p}{\tau_c}\Big)\sum_{l\in\mathcal{L}}\sum_{n_l\in\mathcal{N}_l} r_{n_l} \tag{3.39a}$$

$$\text{s.t.} \quad (3.32\text{b}), (3.32\text{e}), (3.35\text{a})-(3.35\text{c}), (3.37), (3.38\text{a})-(3.38\text{d}), \tag{3.39b}$$

$$\sum_{l\in\mathcal{L}}\sum_{n_l\in\mathcal{N}_l}(\hat{\rho}_{n_l}^m)^2 \leq P_{\max}^m, \forall m\in\mathcal{M}, \tag{3.39c}$$

$$\hat{\rho}_{n_l}^m \leq \hat{\rho}_{n_l+1}^m, n_l \in [1, N_l-1], \forall m\in\mathcal{M}, l\in\mathcal{L}. \tag{3.39d}$$

Conic Quadratic Program: Problem (3.39) is a mix of exponential and quadratic constraints, resulting in a generic convex program. The major complexity in solving such

a program is due to the logarithm function in (3.32b), making the use of convex solvers (e.g., SeDuMi [42] and MOSEK [43]) inefficient. To bypass this issue, we use a lower bound of $\ln\Big(1+\varphi_{n_l}\Big)$ as [4, Eq. (66)]

$$\ln\Big(1+\varphi_{n_l}\Big) \geq \ln(1+\varphi_{n_l}^{(\kappa)}) + \frac{\varphi_{n_l}^{(\kappa)}}{\varphi_{n_l}^{(\kappa)}+1} - \frac{(\varphi_{n_l}^{(\kappa)})^2}{\varphi_{n_l}^{(\kappa)}+1}\frac{1}{\varphi_{n_l}}, \tag{3.40}$$

$\forall \varphi_{n_l}^{(\kappa)} > 0, \varphi_{n_l} > 0$, which is a concave function. We note that (3.40) holds with equality at the optimum, i.e., $\varphi_{n_l}^{(\kappa)} = \varphi_{n_l}^{(\kappa+1)}$. Next, by introducing new variables $\bar{\boldsymbol{\varphi}} \triangleq \{\bar{\varphi}_{n_l}\}_{\forall n_l}$, the conic quadratic approximate program of (3.39) is given as

$$\max_{\hat{\boldsymbol{\rho}},\mathbf{r},\boldsymbol{\varphi},\bar{\boldsymbol{\varphi}},\boldsymbol{\varpi},\boldsymbol{\tau},\boldsymbol{\theta}} \quad \Big(1-\frac{\tau_p}{\tau_c}\Big)\sum_{l\in\mathcal{L}}\sum_{n_l\in\mathcal{N}_l} r_{n_l} \tag{3.41a}$$

$$\text{s.t. } (3.32\text{e}), (3.35\text{a})-(3.35\text{c}), (3.37), (3.38\text{a})-(3.38\text{d}), (3.39\text{c}), (3.39\text{d}), \tag{3.41b}$$

$$\mathcal{F}^{(\kappa)}(\varphi_{n_l}^{(\kappa)}, \bar{\varphi}_{n_l}) \geq r_{n_l}\ln 2,\ \forall n_l \in \mathcal{N}_l, \tag{3.41c}$$

$$0.25\left(\varphi_{n_l}+\bar{\varphi}_{n_l}\right)^2 \geq 0.25\left(\varphi_{n_l}-\bar{\varphi}_{n_l}\right)^2 + 1,\ \forall n_l \in \mathcal{N}_l, \tag{3.41d}$$

where $\mathcal{F}^{(\kappa)}(\varphi_{n_l}^{(\kappa)}, \bar{\varphi}_{n_l}) \triangleq \ln(1+\varphi_{n_l}^{(\kappa)}) + \frac{\varphi_{n_l}^{(\kappa)}}{\varphi_{n_l}^{(\kappa)}+1} - \frac{(\varphi_{n_l}^{(\kappa)})^2}{\varphi_{n_l}^{(\kappa)}+1}\bar{\varphi}_{n_l}$. We note that (3.41d) is a second-order cone constraint and must hold with equality at the optimum. The proposed IA-based iterative algorithm is summarized in Algorithm 5.

Algorithm 5 Proposed IA-based Iterative Algorithm to Solve Problem (3.31)

Initialization: Set $\kappa := 0$ and generate an initial feasible point $(\boldsymbol{\varpi}^{(0)}, \boldsymbol{\theta}^{(0)}, \boldsymbol{\varphi}^{(0)})$.

1: **repeat**
2: Solve the conic quadratic approximate program (3.41) to obtain the optimal solution, denoted by $(\hat{\boldsymbol{\rho}}^\star, \mathbf{r}^\star, \boldsymbol{\varphi}^\star, \bar{\boldsymbol{\varphi}}^\star, \boldsymbol{\varpi}^\star, \boldsymbol{\tau}^\star, \boldsymbol{\theta}^\star)$;
3: Update $(\boldsymbol{\varphi}^{(\kappa+1)}, \boldsymbol{\varpi}^{(\kappa+1)}, \boldsymbol{\theta}^{(\kappa+1)}) := (\boldsymbol{\varphi}^\star, \boldsymbol{\varpi}^\star, \boldsymbol{\theta}^\star)$;
4: Set $\kappa := \kappa + 1$;
5: **until** Convergence, i.e., $\Big(\sum_{l\in\mathcal{L}}\sum_{n_l\in\mathcal{N}_l} r_{n_l}^{(\kappa)} - \sum_{l\in\mathcal{L}}\sum_{n_l\in\mathcal{N}_l} r_{n_l}^{(\kappa-1)}\Big)\Big/\sum_{l\in\mathcal{L}}\sum_{n_l\in\mathcal{N}_l} r_{n_l}^{(\kappa-1)} < \epsilon$
6: **Ouput**: $\boldsymbol{\rho}^\star$ with $\rho_{n_l}^{m,(\star)} = (\hat{\rho}_{n_l}^{m,(\star)})^2, \forall n_l \in \mathcal{N}_l$.

Convergence and Complexity Analysis: The proposed algorithm starts by randomly

generating an initial feasible point for the updated variables $(\boldsymbol{\varpi}^{(0)}, \boldsymbol{\theta}^{(0)}, \boldsymbol{\varphi}^{(0)})$. In each iteration, we solve the convex program (3.41) to produce the next feasible point $(\boldsymbol{\varphi}^{(\kappa+1)}, \boldsymbol{\varpi}^{(\kappa+1)}, \boldsymbol{\theta}^{(\kappa+1)})$. This procedure is successively repeated until convergence, which is stated in the following proposition.

Proposition 2. *Initialized from a feasible point* $(\boldsymbol{\varpi}^{(0)}, \boldsymbol{\theta}^{(0)}, \boldsymbol{\varphi}^{(0)})$*, Algorithm 5 produces a sequence* $\{\boldsymbol{\varphi}^{(\kappa)}, \boldsymbol{\varpi}^{(\kappa)}, \boldsymbol{\theta}^{(\kappa)}\}$ *of improved solutions to problem* (3.41)*, which satisfy the Karush-Kuhn-Tucker (KKT) conditions. In light of the IA principles, the sequence* $\left\{\left(1-\frac{\tau_p}{\tau_c}\right)\sum_{l\in\mathcal{L}}\sum_{n_l\in\mathcal{N}_l} r_{n_l}^{(\kappa)}\right\}_{\kappa=1}^{\infty}$ *is monotonically increasing and converges after a finite number of iterations for a given error tolerance* $\epsilon > 0$*.*

Proof. Please see Appendix A. □

The computational complexity of Algorithm 5 mainly depends on solving the approximate problem (3.41), which is polynomial in the number of constraints and optimization variables. Problem (3.41) has $v = NM + 3N + 3\sum_{l=1}^{L} \frac{N_l(N_l-1)}{2}$ scalar real variables and $c = 8\sum_{l=1}^{L}\left(\frac{N_l(N_l-1)}{2} + M(N_l-1)\right)+M$ quadratic and linear constraints. As a result, the worst-case computational cost of Algorithm 8 in each iteration is $\mathcal{O}(v^2c^{2.5} + c^{3.5})$ [44].

3.6 COmMIMO-NOMA System

This section considers a COmMIMO-NOMA system, which serves as a benchmark for CFmMIMO-NOMA. The main differences between CFmMIMO-NOMA and COmMIMO-NOMA systems are as follows: *i*) in CFmMIMO-NOMA, in general $\beta_{m,n_l} \neq \beta_{m',n_l}$, for $m \neq m'$, whereas in COmMIMO-NOMA, $\beta_{m,n_l} = \beta_{m',n_l}$; and *ii*) in CFmMIMO-NOMA, a power constraint is applied at each AP individually, whereas in COmMIMO-NOMA, a total power constraint is applied at the collocated AP equipped with MK antennas. Unless otherwise specified, all notations and symbols given in the previous sections will be reused in this section.

3.6.1 Performance Analysis

Similar to Lemma 3.1, the closed-form expression for the SE of UE n_l in the l-th cluster is given by

$$\begin{aligned} R_{n_l} &= \Big(1-\frac{\tau_p}{\tau_c}\Big)\log_2\Big(1+\mathrm{SINR}_{n_l}\Big) \\ &= \Big(1-\frac{\tau_p}{\tau_c}\Big)\log_2\Big(1+\min_{n'_l=1,\ldots,n_l}\mathrm{SINR}_{n'_l}^{n_l,}\Big),\ \forall n_l\in\mathcal{N}_l. \end{aligned} \tag{3.42}$$

By replacing $\rho_{n_l}^m$ with $\rho_{n_l}, \forall n_l$, $\mathrm{SINR}_{n_l}^{n_l,}$ and $\mathrm{SINR}_{n'_l}^{n_l,}$, $\forall n'_l < n_l$, are derived as follows:

$$\mathrm{SINR}_{n_l}^{n_l,} = \frac{(K-\tau_p)\rho_{n_l}\gamma_{n_l}}{\mathcal{I}_{n_l}^{n_l}(\boldsymbol{\rho})+1}, \tag{3.43}$$

$$\mathrm{SINR}_{n'_l}^{n_l,} = \frac{(K-\tau_p)\rho_{n_l}\gamma_{n'_l}}{\mathcal{I}_{n'_l}^{n_l}(\boldsymbol{\rho})+1}, \tag{3.44}$$

where

$$\mathcal{I}_{n_l}^{n_l}(\boldsymbol{\rho}) \triangleq \sum_{n''_l\in\mathcal{N}_l\setminus\{n_l\}}\eta_{n''_{l'}}(K-\tau_p)\rho_{n''_l}\gamma_{n_l} + \sum_{l'\in\mathcal{L}}\sum_{n''_{l'}\in\mathcal{N}_{l'}}\eta_{n''_{l'}}\rho_{n''_{l'}}\left(\beta_{n_l}-\gamma_{n_l}\right), \tag{3.45}$$

$$\mathcal{I}_{n'_l}^{n_l}(\boldsymbol{\rho}) \triangleq \sum_{n''_l\in\mathcal{N}_l\setminus\{n_l\}}\eta_{n''_{l'}}(K-\tau_p)\rho_{n''_l}\gamma_{n'_l} + \sum_{l'\in\mathcal{L}}\sum_{n''_{l'}\in\mathcal{N}_{l'}}\eta_{n''_{l'}}\rho_{n''_{l'}}\left(\beta_{n'_l}-\gamma_{n'_l}\right), \tag{3.46}$$

and $\gamma_{n_l} = \frac{\tau_p\rho_{n_l}\beta_{n_l}^2}{\tau_p\sum_{n'_l\in\mathcal{N}_l}\rho_{n'_l}\beta_{n'_l}+1}$; $\eta_{n''_{l'}}$ is defined as

$$\eta_{n''_{l'}} = \begin{cases} 1, & \text{if } l'\neq l \text{ or } l'=l \text{ and } n''_l \leq n_l, \\ \zeta_{n_l}, & \text{otherwise.} \end{cases} \tag{3.47}$$

The SSE of the COmMIMO-NOMA system is expressed as follows:

$$R_{\Sigma} = \sum_{l \in \mathcal{L}} \sum_{n_l \in \mathcal{N}_l} R_{n_l} = \Big(1 - \frac{\tau_p}{\tau_c}\Big) \log_2\Big(1 + \mathrm{SINR}_{n_l}\Big). \tag{3.48}$$

The SSE maximization problem for COmMIMO-NOMA is stated as

$$\max_{\boldsymbol{\rho}} \quad \Big(1 - \frac{\tau_p}{\tau_c}\Big) \sum_{l \in \mathcal{L}} \sum_{n_l \in \mathcal{N}_l} \log_2\Big(1 + \mathrm{SINR}_{n_l}\Big) \tag{3.49a}$$

$$\text{s.t.} \quad \sum_{l \in \mathcal{L}} \sum_{n_l \in \mathcal{N}_l} \rho_{n_l} \leq P_{\max}, \tag{3.49b}$$

$$\rho_{n_l} \leq \rho_{n_l+1}, n_l \in [1, N_l - 1], \forall l \in \mathcal{L}, \tag{3.49c}$$

$$\Big(1 - \frac{\tau_p}{\tau_c}\Big) \log_2\Big(1 + \mathrm{SINR}_{n_l}\Big) \geq \bar{R}_{n_l}, \forall n_l. \tag{3.49d}$$

3.6.2 Proposed Solution to Problem (3.49)

By making the change of variable as $\rho_{n_l} = (\hat{\rho}_{n_l})^2, \forall n_l \in \mathcal{N}_l$ and following similar steps from (3.32) to (3.39), problem (3.49) is equivalently transformed to the following tractable

form

$$\max_{\hat{\boldsymbol{\rho}},\mathbf{r},\boldsymbol{\varphi},\boldsymbol{\theta}} \quad \left(1-\frac{\tau_p}{\tau_c}\right)\sum_{l\in\mathcal{L}}\sum_{n_l\in\mathcal{N}_l} r_{n_l} \tag{3.50a}$$

$$\text{s.t.} \quad \ln\left(1+\varphi_{n_l}\right) \geq r_{n_l}\ln 2,\ \forall n_l\in\mathcal{N}_l, \tag{3.50b}$$

$$\mathcal{I}_{n'_l}^{n_l}(\hat{\boldsymbol{\rho}}) \leq \theta_{n'_l}^{n_l},\ \forall {n'}_l < n_l,\ \forall n_l\in\mathcal{N}_l, \tag{3.50c}$$

$$\mathcal{I}_{n_l}^{n_l}(\hat{\boldsymbol{\rho}}) \leq \theta_{n_l}^{n_l},\ \forall n_l\in\mathcal{N}_l, \tag{3.50d}$$

$$\frac{(K-\tau_p)(\hat{\rho}_{n_l})^2\gamma_{n'_l}}{\theta_{n'_l}^{n_l}+1} \geq \varphi_{n_l},\ \forall {n'}_l < n_l,\ \forall n_l\in\mathcal{N}_l, \tag{3.50e}$$

$$\frac{(K-\tau_p)(\hat{\rho}_{n_l})^2\gamma_{n_l}}{\theta_{n_l}^{n_l}+1} \geq \varphi_{n_l},\ \forall n_l\in\mathcal{N}_l, \tag{3.50f}$$

$$\sum_{l\in\mathcal{L}}\sum_{n_l\in\mathcal{N}_l}(\hat{\rho}_{n_l})^2 \leq P_{\max}, \tag{3.50g}$$

$$\hat{\rho}_{n_l} \leq \hat{\rho}_{n_l+1}, n_l\in[1,N_l-1], \forall l\in\mathcal{L}, \tag{3.50h}$$

$$\left(1-\frac{\tau_p}{\tau_c}\right)r_{n_l} \geq \bar{R}_{n_l}, \forall n_l, \tag{3.50i}$$

where

$$\mathcal{I}_{n'_l}^{n_l}(\hat{\boldsymbol{\rho}}) \triangleq \sum_{n''_l\in\mathcal{N}_l\setminus\{n_l\}}\eta_{n''_{l'}}(K-\tau_p)(\hat{\rho}_{n''_l})^2\gamma_{n'_l} + \sum_{l'\in\mathcal{L}}\sum_{n''_{l'}\in\mathcal{N}_{l'}}\eta_{n''_{l'}}(\hat{\rho}_{n''_{l'}})^2\left(\beta_{n'_l}-\gamma_{n'_l}\right), \tag{3.51}$$

$$\mathcal{I}_{n_l}^{n_l}(\hat{\boldsymbol{\rho}}) \triangleq \sum_{n''_l\in\mathcal{N}_l\setminus\{n_l\}}\eta_{n''_{l'}}(K-\tau_p)(\hat{\rho}_{n''_l})^2\gamma_{n_l} + \sum_{l'\in\mathcal{L}}\sum_{n''_{l'}\in\mathcal{N}_{l'}}\eta_{n''_{l'}}(\hat{\rho}_{n''_{l'}})^2\left(\beta_{n_l}-\gamma_{n_l}\right). \tag{3.52}$$

The nonconvex constraints are (3.50e) and (3.50f). Let $(\hat{\rho}_{n_l}^{(\kappa)}, \theta_{n_l}^{n_l,(\kappa)})$ be a feasible point of $(\hat{\rho}_{n_l}, \theta_{n_l}^{n_l})$ at iteration κ. By (3.40), the conic quadratic approximate program for solving

(3.50) is given as

$$\max_{\hat{\boldsymbol{\rho}},\mathbf{r},\boldsymbol{\varphi},\bar{\boldsymbol{\varphi}},\boldsymbol{\theta}} \quad \left(1-\frac{\tau_p}{\tau_c}\right)\sum_{l\in\mathcal{L}}\sum_{n_l\in\mathcal{N}_l} r_{n_l} \tag{3.53a}$$

$$\text{s.t.} \quad (3.41\text{c}), (3.41\text{d}), (3.50\text{c}), (3.50\text{d}), (3.50\text{g})-(3.50\text{i}), \tag{3.53b}$$

$$(K-\tau_p)\gamma_{n'_l}\mathcal{G}^{(\kappa)}(\hat{\rho}_{n_l},\theta^{n_l}_{n'_l}) \geq \varphi_{n_l},$$

$$\forall n'_l < n_l,\ \forall n_l \in \mathcal{N}_l, \tag{3.53c}$$

$$(K-\tau_p)\gamma_{n_l}\mathcal{G}^{(\kappa)}(\hat{\rho}_{n_l},\theta^{n_l}_{n_l}) \geq \varphi_{n_l},\ \forall n_l \in \mathcal{N}_l, \tag{3.53d}$$

where $\mathcal{G}^{(\kappa)}(\hat{\rho}_{n_l},\theta^{n_l}_{n'_l}) \triangleq \frac{2\hat{\rho}^{(\kappa)}_{n_l}}{\theta^{n_l,(\kappa)}_{n'_l}+1}\hat{\rho}_{n_l} - \frac{\left(\hat{\rho}^{(\kappa)}_{n_l}\right)^2}{\left(\theta^{n_l,(\kappa)}_{n'_l}+1\right)^2}(\theta^{n_l}_{n'_l}+1)$ and $\mathcal{G}^{(\kappa)}(\hat{\rho}_{n_l},\theta^{n_l}_{n_l}) \triangleq \frac{2\hat{\rho}^{(\kappa)}_{n_l}}{\theta^{n_l,(\kappa)}_{n_l}+1}\hat{\rho}_{n_l} - \frac{\left(\hat{\rho}^{(\kappa)}_{n_l}\right)^2}{\left(\theta^{n_l,(\kappa)}_{n_l}+1\right)^2}(\theta^{n_l}_{n_l}+1)$. The solution to problem (3.49) can be found by using Algorithm 5, in which we replace problem (3.41) by problem (3.53) in Step 2. The worst-case computational complexity of solving (3.53) in each iteration is $\mathcal{O}(\bar{v}^2\bar{c}^{2.5}+\bar{c}^{3.5})$ [44], where $\bar{v} = 4N+\sum_{l=1}^{L}\frac{N_l(N_l-1)}{2}$ and $\bar{c} = \sum_{l=1}^{L}\left(N_l(N_l-1)+\frac{(N_l-1)^2}{2}\right)+2N+1$ are scalar real variables and constraints, respectively.

3.7 Numerical Results

This section quantitatively assesses the performance of the proposed unsupervised ML-based UC algorithms in CFmMIMO-NOMA system.

3.7.1 Simulation Parameters

A CFmMIMO-NOMA system including $M = 32$ APs and $N = 20$ UEs is considered as shown in Fig. 3.2, where all APs and UEs are uniformly distributed within a circular region with a radius of 1 km. The large-scale fading coefficient of all channels is modeled

Table 3.1: Simulation Parameters.

Parameter	Value
System bandwidth (B)	20 MHz
Number of APs (M)	32
Number of UEs (N)	20
Number of antennas per AP (K)	16
Total power budget for all APs	40 dBm
Power budget at UEs	23 dBm
Noise power at receivers	-104 dBm
SIC performance coefficient at UEs	0.05
Maximum number of UEs in each cluster (ι)	2
Minimum SE requirement of UE n_l ($\bar{R}_{n_l}$)	0.5 bps/Hz

as [9] $\beta_{m,n_l} = 10^{\frac{\text{PL}(d_{m,n_l})+\sigma_{sh}z}{10}}$, $\forall m \in \mathcal{M}$, $n_l \in \mathcal{N}_l$, where d_{m,n_l} is the distance from AP_m to UE n_l. The shadow fading is modeled as an RV z, which follows $\mathcal{CN}(0,1)$ with standard deviation $\sigma_{sh} = 8$ dB. The path loss $\text{PL}(d_{m,n_l})$ is calculated based on the three-slope path loss model in [9,37,45]. Unless otherwise stated, other key parameters are shown in Table 3.1, where all APs are assumed to have the same power budget [9, 37]. The used convex solver is SeDuMi [42] in the MATLAB environment.

3.7.2 Selection of the Initial Number of Clusters

The performance of the k-means based UC algorithms is highly affected by the initial value of number of clusters L [27, 28]. Thus, it is essential to investigate the particular feature of the UEs' distribution in CFmMIMO-NOMA system to choose a proper number of clusters, such that the SSE is maximized. A reliable and precise approach to validate the initial optimal number of clusters L is the silhouette score [46], which is the mean silhouette coefficient of all UEs. The silhouette coefficient of an UE is calculated as $\frac{c-b}{\max(c,b)}$, where b denotes the mean distance to other UEs in the same cluster (so-called the mean intra-cluster distance), and c represents the mean distance to UEs of the next closest cluster which is the one that minimizes b, excluding the UE's own cluster (so-called

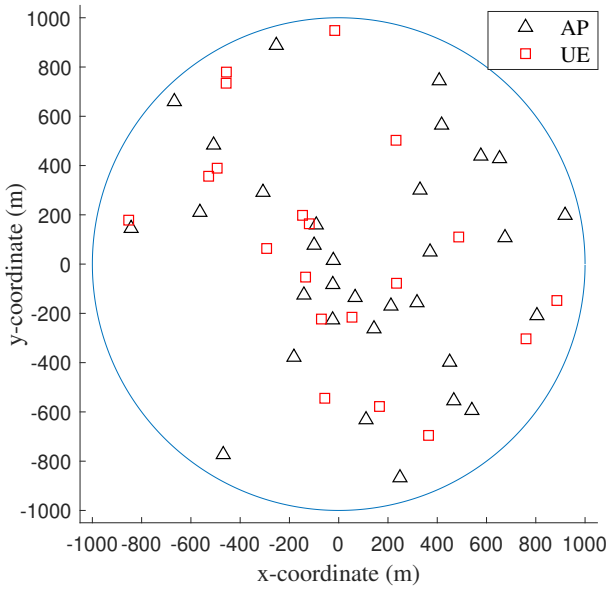

Fig. 3.2: A system topology with $M = 32$ APs and $N = 20$ UEs is used in numerical examples.

Table 3.2: Silhouette Score for CFmMIMO-NOMA and COmMIMO-NOMA.

Number of clusters L		2	3	4	5	6	7	8	9	10	11	12	13	14	15
Silhouette Score	CFmMIMO-NOMA	0.72	0.15	0.23	0.31	0.35	0.37	0.63	0.78	**0.99**	0.25	0.40	0.47	0.53	0.64
	COmMIMO-NOMA	0.75	0.06	0.17	0.30	0.39	0.47	0.64	0.85	**0.98**	0.30	0.38	0.50	0.56	0.58

mean nearest-cluster distance). The value of the silhouette coefficient ranges from -1 to +1. A coefficient close to +1 means that the UE is well matched to its own cluster and far from other clusters. A coefficient close to 0 indicates that the UE is near a cluster boundary, whereas a coefficient close to -1 implies that the UE is assigned to the wrong cluster. Table 3.2 shows the silhouette score versus the number of clusters L. It is observed that the inital optimal number of clusters for this setting is $L^\star = 10$. Note that this is the initial value of the number of clusters to execute the modified k-means and k-means based UC algorithms, and not the total number of clusters obtained after implementing the corresponding algorithms.

In what follows, $L = 10$ is set to verify the performance analysis in Section 3.7.3 and to evaluate the performance of the proposed algorithms in Section 3.7.4.

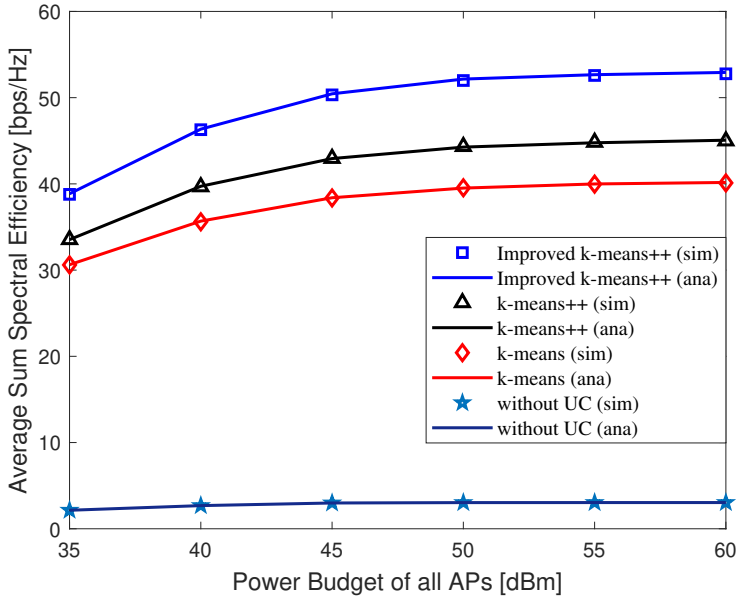

Fig. 3.3: The SSE of CFmMIMO-NOMA versus the total power budget of all APs for the k-means, k-means++, and improved k-means++ algorithms.

3.7.3 Numerical Results for the Performance Analysis

We now investigate the performance of the two proposed unsupervised ML-based UC algorithms with fixed PA. The transmit power at each AP allocated to a specific UE follows the fixed PA scheme. Each AP allocates equal power to each cluster, and then, the fractional transmit PA [47] is used to allocate the power to a specific UE in each cluster based on the virtual channel gains presented in subsection 3.3.2.3. As a benchmark, we also consider the COmMIMO-NOMA system, which is presented in Section 3.6.

Fig. 3.3 illustrates the SSE performance of CFmMIMO-NOMA versus the total power budget of all APs for different UC algorithms. For comparison, the performance of the k-means algorithm and the CFmMIMO-NOMA without UC is also plotted. For the CFmMIMO-NOMA without UC, SIC is implemented at all UEs. It can be seen that the proposed UC algorithms significantly outperform the conventional k-means algorithm and without UC. This confirms the effectiveness of UC in CFmMIMO-NOMA systems.

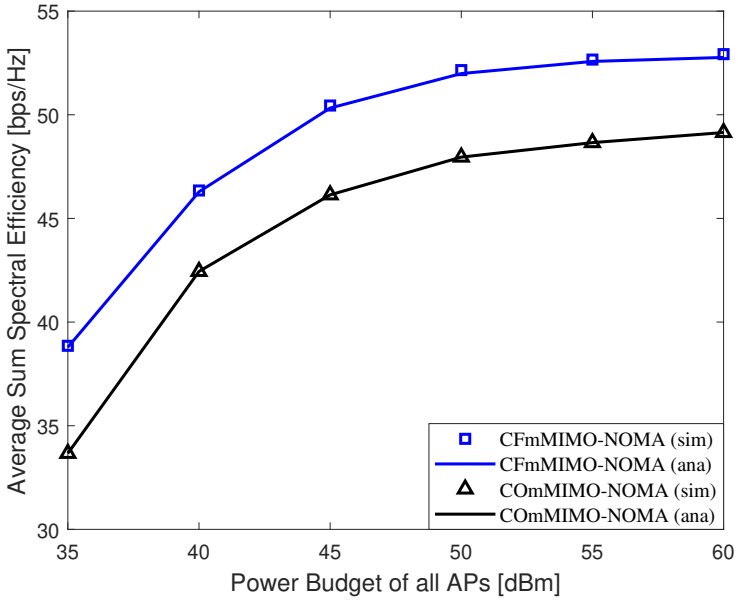

Fig. 3.4: The SSE of CFmMIMO-NOMA and COmMIMO-NOMA versus the total power budget of all APs.

Furthermore, the improved k-means++ achieves the best SSE among all algorithms, which can be attributed to the fact that the effective initialization of centroids is capable of improving the quality of the clustering process, and thus, of NOMA for CFmMIMO.

Next, the SSE performance of the CFmMIMO-NOMA and COmMIMO-NOMA systems using the improved k-means++ algorithm versus the total power budget of all APs is shown in Fig. 3.4. It can be observed that the performance of the CFmMIMO-NOMA system is better than that of COmMIMO-NOMA. This is attributed to the fact that CFmMIMO with many distributed APs brings the service antennas closer to UEs which not only reduces path losses but also provides higher degree of macro-diversity, compared to COmMIMO. In the following numerical results, unless otherwise specified, the improved k-means++ algorithm is used for UC.

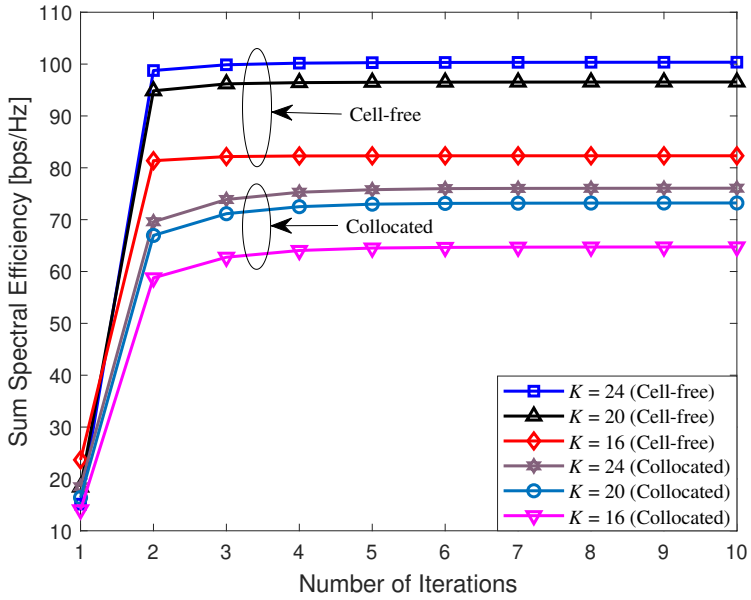

Fig. 3.5: Convergence behavior of Algorithm 5 with different number of AP antennas, K.

3.7.4 Numerical Results for Optimal Power Allocation

Fig. 3.5 evaluates the convergence speed of Algorithm 5 for CFmMIMO-NOMA and COmMIMO-NOMA with different values of K. The proposed algorithm converges within three iterations and the convergence speed of both systems is not sensitive to the number of AP antennas, K. As expected, the SSE is monotonically increasing after each iteration. Compared to the results in Figs. 3.3 and 3.4 with fixed PA at the power budget of 40 dBm, Algorithm 5 yields a significantly better performance in terms of SSE.

Fig. 3.6 shows the impact of the proposed k-means++ and improved k-means++ algorithms on the system performance of CFmMIMO-NOMA. For comparison, we also plot the SSE of the k-means (i.e., Algorithm 2) and the recently proposed UC approaches, including near pairing, far pairing, random pairing [19], and the Jaccard-based UC [20]. The main result observed from the figure is that the proposed unsupervised ML-based UC algorithms achieve better SSE performance compared to the baseline ones, and the performance gaps are wider when $P_{\max}$ increases. This implies that the two proposed

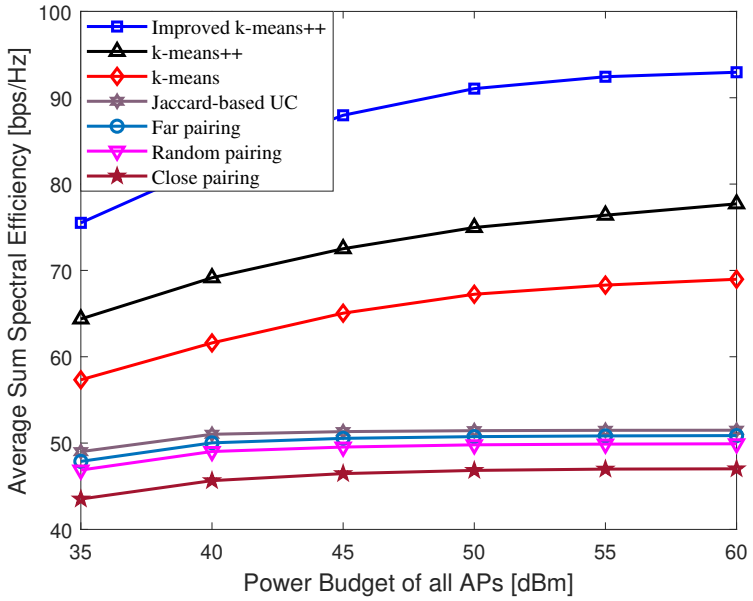

Fig. 3.6: The SSE of different UC algorithms.

UC schemes are capable of exploiting UC more effectively, so that the SSE is remarkably enhanced.

Fig. 3.7 demonstrates the benefit of optimizing PA for CFmMIMO-NOMA and COmMIMO-NOMA systems. The SSE of both systems is significantly enhanced with optimal PA compared to the fixed PA (FPA) scheme. Hence, this shows the necessity of optimizing PA for both systems, especially for CFmMIMO-NOMA.

Next, the effect of the SIC performance coefficient ζ_{n_l} on the SSE of CFmMIMO-NOMA and COmMIMO-NOMA is examined in Fig. 3.8. It is noted that $\zeta_{n_l} = 1$ ($\zeta_{n_l} = 0$) indicates no SIC (perfect SIC), while $0 < \zeta_{n_l} < 1$ means imperfect SIC. The system performance without NOMA/SIC is plotted. It is clear that the SSE of CFmMIMO-NOMA degrades when $\zeta_{n_l}, \forall n_l$ increases. It implies that the SIC performance coefficient is required to be small enough to exploit the full potential of NOMA in CFmMIMO. Nevertheless, the SSE achieved by CFmMIMO-NOMA and COmMIMO-NOMA systems is much higher than their counterparts without NOMA/SIC.

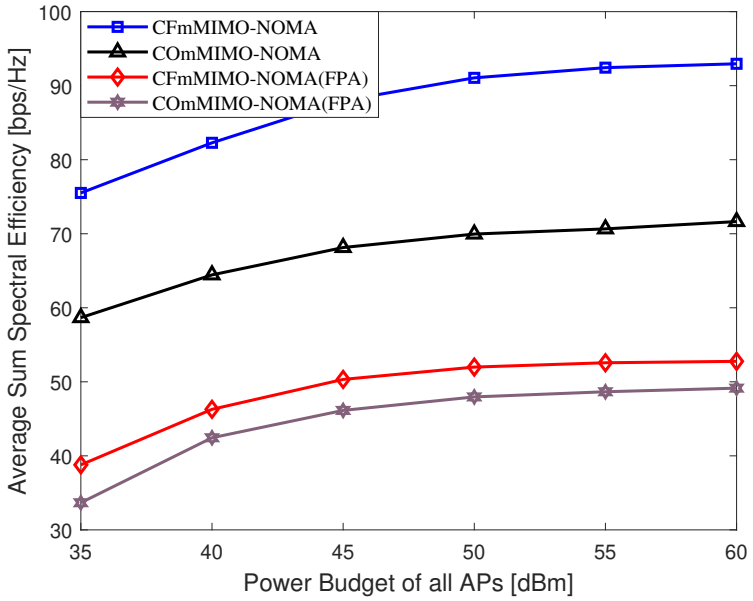

Fig. 3.7: SSE of CFmMIMO-NOMA and COmMIMO-NOMA: with and without PA.

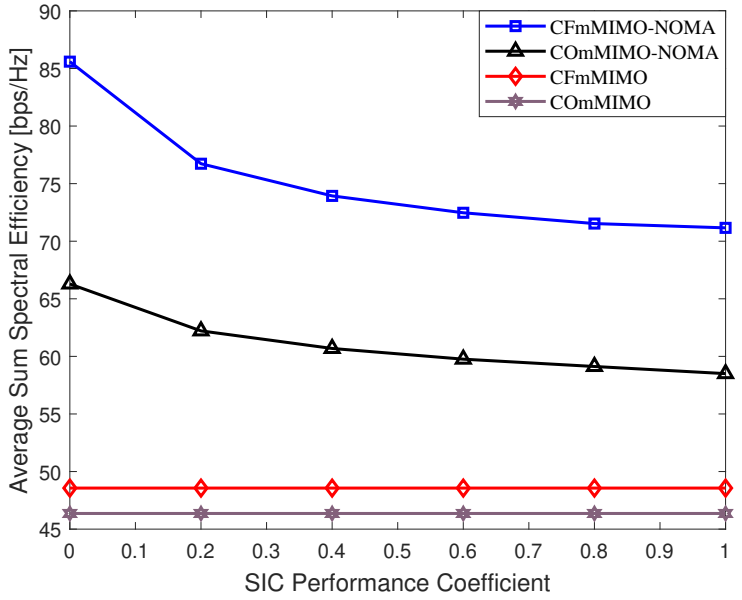

Fig. 3.8: The effect of SIC performance coefficient on the SSE of CFmMIMO-NOMA and COmMIMO-NOMA systems.

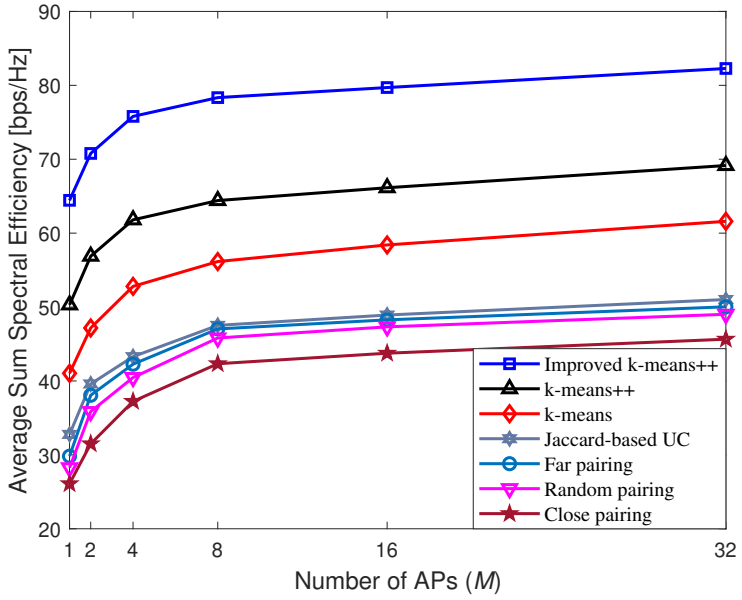

Fig. 3.9: The joint effect of the numbers of antennas K and APs M on the average SSE of different UC algorithms, for $MK = 512$.

Fig. 3.9 shows the joint effect of the numbers of antennas K and APs M on the average SSE of different UC algorithms. $MK = 512$ is fixed and M is selected from the set $M \in [1, 2, 4, 8, 16, 32]$. When $M = 1$, then $K = 512$, which represents COmMIMO-NOMA. From the figure, it can be seen that the SSE increases with the increase in M, which translates into a lower number of AP antennas, K. As such, this not only reduces path losses, but also increases the degree of macro-diversity.

Lastly, the impact of the number of UEs on the SSE of the proposed k-means++ and improved k-means++ algorithms in CFmMIMO-NOMA system is illustrated in Fig. 3.10. It can be observed that the SSE significantly increases with the number of UEs.

3.8 Conclusion

This chapter has investigated a downlink CFmMIMO-NOMA system, for which two efficient unsupervised ML-based UC algorithms have been proposed to effectively cluster

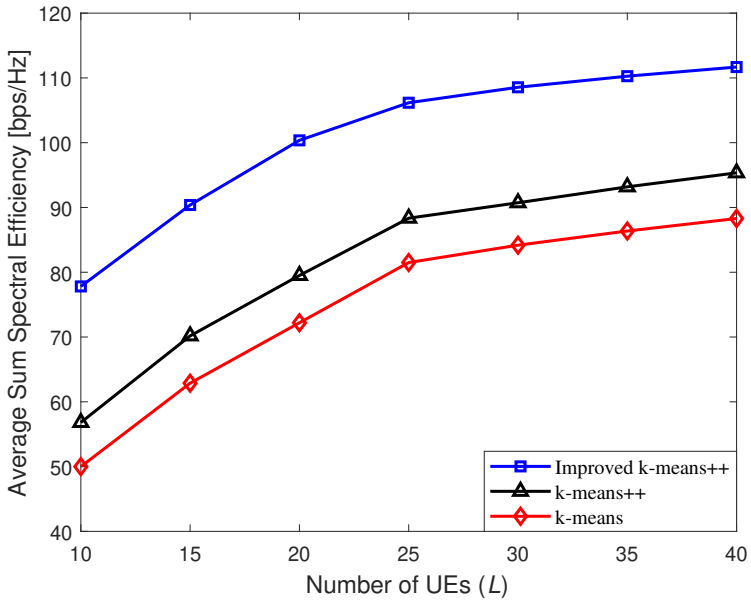

Fig. 3.10: Effect of the number of UEs L on the SSE for the k-means, k-means++, and improved k-means++ algorithms.

the users. Using the fpZF precoding at APs, this chapter has considered the problem of power allocation to maximize SSE. Since the formulated problem is intractable, this chapter has developed a low-complexity iterative algorithm based on the IA framework for its solution. Numerical results have confirmed the effectiveness of the proposed UC algorithms, and show their superior performance compared to the baseline schemes. The proposed PA algorithm converges fast, and significantly outperforms CFmMIMO-NOMA without optimizing PA and COmMIMO-NOMA in terms of SSE.

Appendix A: Proof of Proposition 2

By contradiction and IA principles, we can easily prove that constraints (3.35a)-(3.35c), (3.37), (3.38a)-(3.38d) and (3.41d) must hold with equality at optimum. Let us define

$\mathcal{F}(\varphi_{n_l}) \triangleq \ln(1+\varphi_{n_l})$. From (3.40), we have

$$\mathcal{F}(\varphi_{n_l}) \geq \mathcal{F}^{(\kappa)}(\varphi^{(\kappa)}, \bar{\varphi}_{n_l}), \tag{3.54}$$

and

$$\mathcal{F}(\varphi_{n_l}^{(\kappa)}) = \mathcal{F}^{(\kappa)}(\varphi^{(\kappa)}, \bar{\varphi}_{n_l}). \tag{3.55}$$

Thus, it is true that

$$\begin{aligned}\mathcal{F}(\varphi_{n_l}^{(\kappa)}) &\geq \mathcal{F}^{(\kappa-1)}(\varphi^{(\kappa)}, \bar{\varphi}_{n_l}) \\ &\geq \mathcal{F}^{(\kappa-1)}(\varphi^{(\kappa-1)}, \bar{\varphi}_{n_l}) = \mathcal{F}(\varphi_{n_l}^{(\kappa-1)}).\end{aligned} \tag{3.56}$$

These results imply that $(\boldsymbol{\varpi}^{(\kappa)}, \boldsymbol{\theta}^{(\kappa)}, \boldsymbol{\varphi}^{(\kappa)})$ is an improved solution to problem (3.41), compared to $(\boldsymbol{\varpi}^{(\kappa-1)}, \boldsymbol{\theta}^{(\kappa-1)}, \boldsymbol{\varphi}^{(\kappa-1)})$. By [35, Theorem 1], the sequence $\{\boldsymbol{\varpi}^{(\kappa)}, \boldsymbol{\theta}^{(\kappa)}, \boldsymbol{\varphi}^{(\kappa)}\}$ converges to at least local optima which satisfy the KKT conditions. As a result, the objective value of problem (3.41) is monotonically increasing, i.e., $\left(1-\frac{\tau_p}{\tau_c}\right)\sum_{l\in\mathcal{L}}\sum_{n_l\in\mathcal{N}_l} r_{n_l}^{(\kappa)} \geq \left(1-\frac{\tau_p}{\tau_c}\right)\sum_{l\in\mathcal{L}}\sum_{n_l\in\mathcal{N}_l} r_{n_l}^{(\kappa-1)}$. In addition, the sequence of the objective values is upper bounded due to power constraints (3.39c), which completes the proof.

References

[1] Iot-analytics.com, *State of the IoT 2020: 12 billion IoT Connections, Surpassing non-IoT for the First Time*, Nov. 2020. [Online]. Available: https://iot-analytics.com/state-of-the-iot-2020-12-billion-iot-connections-surpassing-non-iot-for-the-first-time

[2] *Ericsson Mobility Report*, Nov. 2020. [Online]. Available: https://ericsson.com/4adc87/assets/local/mobility-report/documents/2020/november-2020-ericsson-mobility-report.pdf

[3] S. M. R. Islam, N. Avazov, O. A. Dobre, and K.-S. Kwak, "Power-domain non-orthogonal multiple access (NOMA) in 5G systems: Potentials and challenges," *IEEE Commun. Surveys Tuts.*, vol. 19, no. 2, pp. 721–742, 2nd Quart. 2017.

[4] V.-D. Nguyen, H. D. Tuan, T. Q. Duong, H. V. Poor, and O.-S. Shin, "Precoder design for signal superposition in MIMO-NOMA multicell networks," *IEEE J. Select. Areas Commun.*, vol. 35, no. 12, pp. 2681–2695, Dec. 2017.

[5] H. V. Nguyen, V.-D. Nguyen, O. A. Dobre, D. N. Nguyen, E. Dutkiewicz, and O.-S. Shin, "Joint power control and user association for NOMA-based full-duplex systems," *IEEE Trans. Commun.*, vol. 67, no. 11, pp. 8037–8055, Nov. 2019.

[6] Z. Shi, W. Gao, S. Zhang, J. Liu, and N. Kato, "AI-enhanced cooperative spectrum sensing for non-orthogonal multiple access," *IEEE Wirel. Commun.*, vol. 27, no. 2, pp. 173–179, Apr. 2020.

[7] ——, "Machine learning-enabled cooperative spectrum sensing for non-orthogonal multiple access," *IEEE Trans. Wireless Commun.*, vol. 19, no. 9, pp. 5692–5702, Sep. 2020.

[8] T. K. Nguyen, H. H. Nguyen, and H. D. Tuan, "Max-min QoS power control in generalized cell-free massive MIMO-NOMA with optimal backhaul combining," *IEEE Trans. Veh. Technol.*, vol. 69, no. 10, pp. 10 949–10 964, Oct. 2020.

[9] H. Q. Ngo, A. Ashikhmin, H. Yang, E. G. Larsson, and T. L. Marzetta, "Cell-free massive MIMO versus small cells," *IEEE Trans. Wireless Commun.*, vol. 16, no. 3, pp. 1834–1850, Mar. 2017.

[10] E. Nayebi, A. Ashikhmin, T. L. Marzetta, H. Yang, and B. D. Rao, "Precoding and power optimization in cell-free massive MIMO systems," *IEEE Trans. Wireless Commun.*, vol. 16, no. 7, pp. 4445–4459, July 2017.

[11] M. Bashar, K. Cumanan, A. G. Burr, M. Debbah, and H. Q. Ngo, "On the uplink max–min SINR of cell-free massive MIMO systems," *IEEE Trans. Wireless Commun.*, vol. 18, no. 4, pp. 2021–2036, Apr. 2019.

[12] H. Q. Ngo, L.-N. Tran, T. Q. Duong, M. Matthaiou, and E. G. Larsson, "On the total energy efficiency of cell-free massive MIMO," *IEEE Trans. Green Commun. Netw.*, vol. 2, no. 1, pp. 25–39, Mar. 2018.

[13] Z. Chen and E. Björnson, "Channel hardening and favorable propagation in cell-free massive MIMO with stochastic geometry," *IEEE Trans. Commun.*, vol. 66, no. 11, pp. 5205–5219, Nov. 2018.

[14] X. Chen, D. W. K. Ng, W. Yu, E. G. Larsson, N. Al-Dhahir, and R. Schober, "Massive access for 5G and beyond," *IEEE J. Select. Areas Commun.*, vol. 39, no. 3, pp. 615–637, Mar. 2021.

[15] Y. Li and G. A. A. Baduge, "NOMA-aided cell-free massive MIMO systems," *IEEE Wireless Commun. Lett.*, vol. 7, no. 6, pp. 950–953, Dec. 2018.

[16] Y. Zhang, H. Cao, M. Zhou, and L. Yang, "Spectral efficiency maximization for uplink cell-free massive MIMO-NOMA networks," in *Proc. IEEE Inter. Conf. Commun. Works.*, May 2019, pp. 1–6.

[17] F. Rezaei, C. Tellambura, A. A. Tadaion, and A. R. Heidarpour, "Rate analysis of cell-free massive MIMO-NOMA with three linear precoders," *IEEE Trans. Commun.*, vol. 68, no. 6, pp. 3480–3494, June 2020.

[18] S. M. R. Islam, M. Zeng, O. A. Dobre, and K.-S. Kwak, "Resource allocation for downlink NOMA systems: Key techniques and open issues," *IEEE Wireless Commun.*, vol. 25, no. 2, pp. 40–47, Apr. 2018.

[19] M. Bashar, K. Cumanan, A. G. Burr, H. Q. Ngo, L. Hanzo, and P. Xiao, "On the performance of cell-free massive MIMO relying on adaptive NOMA/OMA mode-switching," *IEEE Trans. Commun.*, vol. 68, no. 2, pp. 792–810, Feb. 2020.

[20] F. Rezaei, A. R. Heidarpour, C. Tellambura, and A. A. Tadaion, "Underlaid spectrum sharing for cell-free massive MIMO-NOMA," *IEEE Commun. Lett.*, vol. 24, no. 4, pp. 907–911, Apr. 2020.

[21] R. He, Q. Li, B. Ai, Y. L.-A. Geng, A. F. Molisch, V. Kristem, Z. Zhong, and J. Yu, "A kernel-power-density-based algorithm for channel multipath components clustering," *IEEE Trans. Wireless Commun.*, vol. 16, no. 11, pp. 7138–7151, Nov. 2017.

[22] X. Xie, Z. Zhang, H. Jiang, J. Dang, and L. Wu, "Cluster-based geometrical dynamic stochastic model for MIMO scattering channels," in *Proc. Inter. Conf. Wireless Commun. and Signal Process. (WCSP)*, Oct. 2017, pp. 1–5.

[23] Y. Wang, A. Liu, X. Xia, and K. Xu, "Exploiting the clustered sparsity for channel estimation in hybrid analog-digital massive MIMO systems," *IEEE Access*, vol. 7, pp. 4989–5000, Dec. 2018.

[24] A. B. Rozario and M. F. Hossain, "An architecture for M2M communications over cellular networks using clustering and hybrid TDMA-NOMA," in *Proc. Inter. Conf. Infor. and Commun. Tech. (ICoICT)*, May 2018, pp. 18–23.

[25] A. K. Jain, "Data clustering: 50 years beyond k-means," *Pattern Recognition Lett.*, vol. 31, no. 8, pp. 651–666, June 2010.

[26] E. Cabrera and R. Vesilo, "An enhanced k-means clustering algorithm with non-orthogonal multiple access (NOMA) for MMC networks," in *Proc. Inter. Telecommun Net. and App. Conf. (ITNAC)*, Nov. 2018, pp. 1–8.

[27] J. Cui, Z. Ding, P. Fan, and N. Al-Dhahir, "Unsupervised machine learning-based user clustering in millimeter-wave-NOMA systems," *IEEE Trans. Wireless Commun.*, vol. 17, no. 11, pp. 7425–7440, Sep. 2018.

[28] F. Riera-Palou, G. Femenias, A. G. Armada, and A. Pérez-Neira, "Clustered cell-free massive MIMO," in *Proc. IEEE Globecom Workshops*, Dec. 2018, pp. 1–6.

[29] H.-S. Park and C.-H. Jun, "A simple and fast algorithm for k-medoids clustering," *Expert Syst. Appl.*, vol. 36, no. 2, pp. 3336–3341, Mar. 2009.

[30] C. Whelan, G. Harrell, and J. Wang, "Understanding the k-medians problem," in *Proc. Int. Conf. Sci. Comput.*, 2015, pp. 219–222.

[31] F. Cao, J. Liang, D. Li, L. Bai, and C. Dang, "A dissimilarity measure for the k-modes clustering algorithm," *Knowl. Based Syst.*, vol. 26, pp. 120–127, Feb. 2012.

[32] H. Liu, J. Wu, T. Liu, D. Tao, and Y. Fu, "Spectral ensemble clustering via weighted k-means: Theoretical and practical evidence," *IEEE Trans. Knowl. Data Eng.*, vol. 29, no. 5, pp. 1129–1143, May 2017.

[33] S. Yu, L. Tranchevent, X. Liu, W. Glanzel, J. A. K. Suykens, B. D. Moor, and Y. Moreau, "Optimized data fusion for kernel k-means clustering," *IEEE Trans. Pattern Anal. Mach. Intell.*, vol. 34, no. 5, pp. 1031–1039, May 2012.

[34] M. Morales-Céspedes, O. A. Dobre, and A. García-Armada, "Semi-blind interference aligned NOMA for downlink MU-MISO systems," *IEEE Trans. Commun.*, vol. 68, no. 3, pp. 1852–1865, Mar. 2020.

[35] B. R. Marks and G. P. Wright, "A general inner approximation algorithm for non-convex mathematical programs," *Oper. Res.*, vol. 26, no. 4, pp. 681–683, July-Aug. 1978.

[36] G. Interdonato, M. Karlsson, E. Bjornson, and E. G. Larsson, "Downlink spectral efficiency of cell-free massive MIMO with full-pilot zero-forcing," in *Proc. IEEE Global Conf. Signal and Infor. Process. (GlobalSIP)*, Nov. 2018, pp. 1003–1007.

[37] H. V. Nguyen, V.-D. Nguyen, O. A. Dobre, S. K. Sharma, S. Chatzinotas, B. Ottersten, and O.-S. Shin, "On the spectral and energy efficiencies of full-duplex cell-free massive MIMO," *IEEE J. Select. Areas Commun.*, vol. 38, no. 8, pp. 1698–1718, Aug. 2020.

[38] A. M. Tulino and S. Verdú, "Random matrix theory and wireless communications," *Commun. Inf. Theory*, vol. 1, no. 1, pp. 1–182, June 2004.

[39] D. Arthur and S. Vassilvitskii, "K-means++: The advantages of careful seeding," in *Proc. Symp. Discrete Algorithms*, Jan. 2007, pp. 1027–1035.

[40] P. Fränti and S. Sieranoja, "How much can k-means be improved by using better initialization and repeats?" *Pattern Recognit.*, vol. 93, pp. 95–112, Sep. 2019.

[41] A. Beck, A. Ben-Tal, and L. Tetruashvili, "A sequential parametric convex approximation method with applications to nonconvex truss topology design problems," *J. Global Optim.*, vol. 47, no. 1, pp. 29–51, May 2010.

[42] J. F. Sturm, "Using SeDuMi 1.02, a MATLAB toolbox for optimization over symmetric cones," *Optimiz. Methods and Softw.*, vol. 11-12, pp. 625–653, Sep. 1999.

[43] "I. MOSEK aps," 2014. [Online]. Available: http://www.mosek.com

[44] D. Peaucelle, D. Henrion, and Y. Labit, "Users guide for SeDuMi interface 1.04," 2002. [Online]. Available: http://homepages.laas.fr/peaucell/software/sdmguide.pdf

[45] A. Tang, J. Sun, and K. Gong, "Mobile propagation loss with a low base station antenna for NLOS street microcells in urban area," in *Proc. IEEE Veh. Tech. Conf. (VTC Spring)*, May 2001, pp. 333–336.

[46] A. Geron, *Hands-on Machine Learning with Scikit-learn and Tensorflow: Concepts, Tools, and Techniques to Build Intelligent Systems.* O'Reilly Media Inc., Sep. 2019.

[47] A. Benjebbour, A. Li, Y. Kishiyama, H. Jiang, and T. Nakamura, "System-level performance of downlink NOMA combined with SUMIMO for future LTE enhancements," in *Proc. IEEE Globecom Workshops*, Dec. 2014, pp. 706–710.

Chapter 4

Energy Efficiency Maximization in RIS-Aided Cell-Free Network with Limited Backhaul

4.1 Abstract

Integrating the RIS in a cell-free (RIS-CF) network is an effective solution to improve the capacity and coverage of future wireless systems with low cost and power consumption. The reflecting coefficients of RISs can be programmed to enhance signals received at users. This chapter addresses a joint design of transmit beamformers at access points and reflecting coefficients at RISs to maximize the EE of RIS-CF networks, taking into account the limited backhaul capacity constraints. Due to a very computationally challenging nonconvex problem, this chapter develops a simple yet efficient alternating descent algorithm for its solution. Numerical results verify that the EE of RIS-CF networks is greatly improved, showing the benefit of using RISs.

4.2 Introduction

Ultra-dense networks (UDNs) have been advocated as a key enabler for beyond fifth-generation wireless networks to further increase network capacity [1]. The underlying principle of UDN is to densely deploy a large number of APs and small cells in cellular networks. However, the high density of APs and small cells comes at a cost of severe inter-cell interference [2].

In order to address this bottleneck, CF networks have been recently proposed as a promising technology to effectively resolve the interference issues in existing cellular networks [3, 4]. Since each UE in the network is coherently served by a large number of APs coordinated by a CPU with no cell boundaries, inter-cell interference can be efficiently reduced, and thus the network capacity can be enhanced accordingly [4]. Nonetheless, the performance of CF networks is heavily constrained by the limited backhaul capacity between APs and CPU [5,6]. Further, the dense deployment of APs in CF networks results in an increase in the network energy consumption [7]. Therefore, an efficient scheme to improve the network EE, which will be considered as a major figure-of-merit in the design of future networks, is of crucial importance.

Fortunately, the new revolutionary technology called RIS has been identified as a spectral efficient solution with low cost and power consumption [8]. An RIS consists of a large number of low-cost passive elements, where each element can be adjusted with an independent phase shift to reflect the electromagnetic incident signals, to be added coherently at UEs. It is not too far-fetched to envision a wireless system integrating RIS in a CF network, referred to as RIS-CF, reaping all key advantages of these two technologies. Despite its potential, only some attempts have been made to characterize the performance of RIS-CF in the literature [9, 10]. Unlike these works, which are mainly focusing on maximizing the sum-rate with infinite backhaul capacity links, our goal is to achieve an optimal tradeoff between the total sum-rate and power consumption, taking

into account the impact of limited backhaul capacity.

Naturally, the beamformers at APs and RIS reflecting coefficients need to be jointly optimized to maximize the EE of RIS-CF, which results in a computationally intractable problem since the optimization variables are strongly coupled. To efficiently solve this problem, the alternating descent-based iterative algorithm is proposed, which converges at least to a locally optimal solution. In each iteration of alternating optimization, new approximate functions are developed to tackle the nonconvex parts by leveraging the IA framework [11] and introducing a novel penalty function. Simulation results confirm that the proposed algorithm greatly improves the EE of CF networks over the existing approaches.

Notation: $\mathbf{X}^T$ and $\mathbf{X}^H$ are the transpose and Hermitian transpose of a matrix $\mathbf{X}$, respectively. $\|\cdot\|$ and $|\cdot|$ denote the Euclidean norm of a vector and the absolute value of a complex scalar, respectively. $\Re\{\cdot\}$ returns the real part of an argument.

4.3 System Model

This chapter considers an RIS-CF network as illustrated in Fig. 4.1, where the sets $\mathcal{M} \triangleq \{1, 2, \cdots, M\}$ of M APs and $\mathcal{N} \triangleq \{1, 2, \cdots, N\}$ of N RISs are distributedly deployed to coherently serve the set $\mathcal{L} \triangleq \{1, 2, \cdots, L\}$ of L single-antenna UEs. Each AP is equipped with K antennas, and each RIS is composed of the set $\mathcal{R} \triangleq \{1, 2, \cdots, R\}$ of R passive reflecting elements. A CPU is deployed for control and planning purposes, to which all APs are connected by wired limited-capacity backhaul links. The backhaul link between AP_m and CPU has the predetermined maximum capacity $C_m^{\max}$, $\forall m \in \mathcal{M}$. All RISs are controlled by the CPU or APs by wired or wireless links.

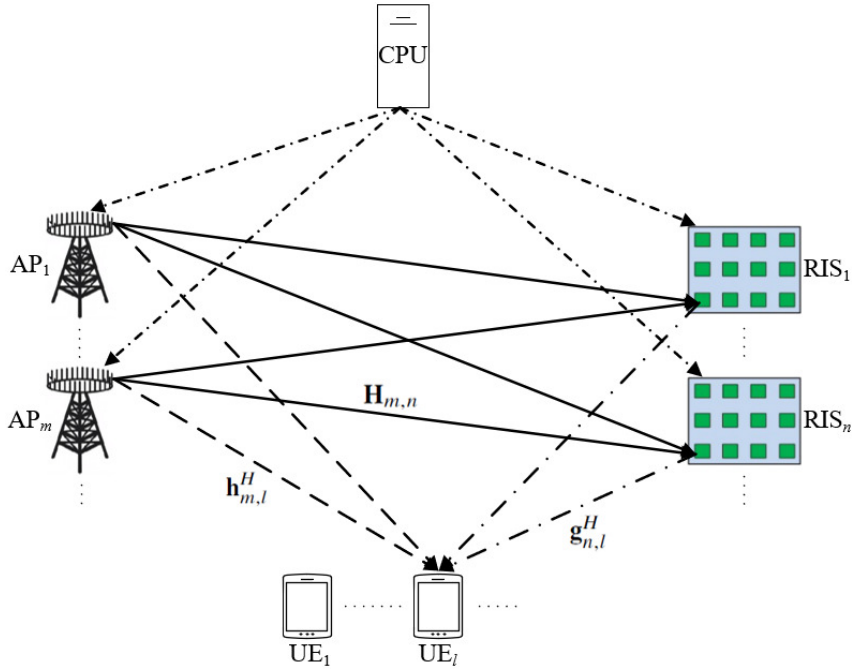

Fig. 4.1: Illustration of an RIS-CF network.

4.3.1 Transmission Model

The transmitted complex baseband signal $\boldsymbol{x}_m \in \mathbb{C}^{K\times 1}$ at AP$_m$ can be written as $\boldsymbol{x}_m = \sum_{l\in\mathcal{L}} \boldsymbol{w}_{m,l} s_l$, where s_l with $\mathbb{E}\{|s_l|^2\} = 1$ and $\boldsymbol{w}_{m,l} \in \mathbb{C}^{K\times 1}$ are the transmitted symbol and beamforming vector intended for UE l, respectively. Due to the directional reflection supported by N RISs, the channel between an AP and a UE includes two parts: the AP-UE (direct) link and N AP-RIS-UE (reflected) links. The equivalent channel $\hat{\mathbf{h}}_{m,l}^H \in \mathbb{C}^{1\times K}$ from AP$_m$ to UE l can be expressed as

$$\begin{aligned}\hat{\mathbf{h}}_{m,l}^H(\boldsymbol{\psi}) &= \mathbf{h}_{m,l}^H + \sum\nolimits_{n\in\mathcal{N}} \mathbf{g}_{n,l}^H \boldsymbol{\Phi}_n \mathbf{H}_{m,n} \\ &= \mathbf{h}_{m,l}^H + \sum\nolimits_{n\in\mathcal{N}} \boldsymbol{\psi}_n^T \left(\mathbf{g}_{n,l}^H\right) \mathbf{H}_{m,n} \end{aligned} \tag{4.1}$$

where $\mathbf{h}_{m,l}^H \in \mathbb{C}^{1\times K}$, $\mathbf{H}_{m,n} \in \mathbb{C}^{R\times K}$, and $\mathbf{g}_{n,l}^H \in \mathbb{C}^{1\times R}$ denote the channels from AP$_m$ to UE l, from AP$_m$ to RIS$_n$, and from RIS$_n$ to UE l, respectively. $\boldsymbol{\Phi}_n \in \mathbb{C}^{R\times R}$ represents the phase shift matrix of RIS$_n$, which can be written as [8]: $\boldsymbol{\Phi}_n \triangleq (e^{j\theta_{n,1}}, e^{j\theta_{n,2}}, \ldots, e^{j\theta_{n,R}})$,

where $\theta_{n,r} \in [0, 2\pi)$ denotes the phase shift of the r-th reflecting element on the RIS$_n$. Further, $\boldsymbol{\Phi}_n$ can be rewritten as $\boldsymbol{\Phi}_n = (\psi_{n,1}, \psi_{n,2}, \ldots, \psi_{n,R})$, with $|\psi_{n,r}| = 1$, $\forall n \in \mathcal{N}$, $r \in \mathcal{R}$. Let define $\boldsymbol{\psi} \triangleq \{\boldsymbol{\psi}_n\}_{\forall n}$ with $\boldsymbol{\psi}_n = \Big[\psi_{n,1}, \psi_{n,2}, \ldots, \psi_{n,R}\Big]^T$.

The signal received at UE l can be expressed as

$$y_l = \sum\nolimits_{m \in \mathcal{M}} \hat{\mathbf{h}}_{m,l}^H \boldsymbol{x}_m + n_l \tag{4.2}$$

where $n_l \sim \mathcal{CN}(0, \sigma^2)$ is the additive white Gaussian noise (AWGN) at UE l. The achievable data rate (nats/s/Hz) of UE l is given as

$$\begin{aligned} R_l(\boldsymbol{w}, \boldsymbol{\psi}) &= \ln\left(1 + \gamma_l(\boldsymbol{w}, \boldsymbol{\psi})\right) \\ &= \ln\left(1 + \frac{\left|\sum_{m \in \mathcal{M}} \hat{\mathbf{h}}_{m,l}^H(\boldsymbol{\psi}) \boldsymbol{w}_{m,l}\right|^2}{\sum_{j \in \mathcal{L} \setminus l} \left|\sum_{m \in \mathcal{M}} \hat{\mathbf{h}}_{m,l}^H(\boldsymbol{\psi}) \boldsymbol{w}_{m,j}\right|^2 + \sigma^2}\right) \\ &= \ln\left(1 + \frac{\left|\hat{\mathbf{h}}_l^H(\boldsymbol{\psi}) \boldsymbol{w}_l\right|^2}{\sum_{j \in \mathcal{L} \setminus l} \left|\hat{\mathbf{h}}_l^H(\boldsymbol{\psi}) \boldsymbol{w}_j\right|^2 + \sigma^2}\right) \end{aligned} \tag{4.3}$$

where $\boldsymbol{w} \triangleq \{\boldsymbol{w}_{m,l}\}_{\forall m,l}$, $\hat{\mathbf{h}}_l = \left[\hat{\mathbf{h}}_{1,l}^H, \hat{\mathbf{h}}_{2,l}^H, \ldots, \hat{\mathbf{h}}_{M,l}^H\right]^H$, and $\boldsymbol{w}_l = \Big[\boldsymbol{w}_{1,l}^H, \boldsymbol{w}_{2,l}^H, \ldots, \boldsymbol{w}_{M,l}^H\Big]^H$.

4.3.1.1 Optimization Problem Formulation

Power consumption model: The total power consumption of the proposed RIS-CF network is modeled as

$$\begin{aligned} P_\Sigma(\boldsymbol{w}) = &\sum\nolimits_{m \in \mathcal{M}} \xi_m \sum\nolimits_{l \in \mathcal{L}} \|\boldsymbol{w}_{m,l}\|^2 + \sum\nolimits_{m \in \mathcal{M}} P_m + \sum\nolimits_{l \in \mathcal{L}} P_l + \sum\nolimits_{n \in \mathcal{N}, r \in \mathcal{R}} P_{n,r} \\ &+ \sum\nolimits_{m \in \mathcal{M}, l \in \mathcal{L}} P_{m,l}^{\mathrm{BH}} \end{aligned} \tag{4.4}$$

where P_m and P_l denote the circuit power consumption of AP$_m$ and UE l, respectively. ξ_m regulates the ineffectiveness of the power amplifier at AP$_m$, and $P_{n,r}$ represents the

low-power consumption of the r-th reflecting element in the n-th RIS [12]. The power consumption for conveying the data and beamformers related to the transmission from AP_m to UE l via backhaul transmission is represented by $P_{m,l}^{\text{BH}}$.

Backhaul constraint: The data rate transmitted by the m-th backhaul link should be ω_m times greater than or equal to the total achievable rate at AP_m, with $\omega_m \geq 1$, $\forall m \in \mathcal{M}$ [5,6]. Then, the per-backhaul capacity constraints can be expressed as:

$$\sum\nolimits_{l\in\mathcal{L}} R_l(\boldsymbol{w},\boldsymbol{\psi}) \leq \frac{C_m^{\max}}{\omega_m},\ \forall m \in \mathcal{M}. \tag{4.5}$$

Our goal is to maximize the EE of the RIS-CF network by jointly optimizing the beamformers at APs $\boldsymbol{w}$ and the reflecting coefficients of RISs $\boldsymbol{\psi}$, stated as

$$\max_{\boldsymbol{w},\boldsymbol{\psi}} \quad \mathcal{E}(\boldsymbol{w},\boldsymbol{\psi}) \triangleq \frac{B\sum_{l\in\mathcal{L}} R_l(\boldsymbol{w},\boldsymbol{\psi})}{P_\Sigma(\boldsymbol{w})} \tag{4.6a}$$

$$\text{s. t.} \quad \sum\nolimits_{l\in\mathcal{L}} \|\boldsymbol{w}_{m,l}\|^2 \leq P_m^{\max}, \forall m \in \mathcal{M}, \tag{4.6b}$$

$$R_l(\boldsymbol{w},\boldsymbol{\psi}) \geq R_l^{\min}, \forall l \in \mathcal{L}, \tag{4.6c}$$

$$\sum\nolimits_{l\in\mathcal{L}} R_l(\boldsymbol{w},\boldsymbol{\psi}) \leq \frac{C_m^{\max}}{\omega_m}, \forall m \in \mathcal{M}, \tag{4.6d}$$

$$|\psi_{n,r}| = 1, \forall n \in \mathcal{N}, r \in \mathcal{R} \tag{4.6e}$$

where (4.6b) indicates the power constraint at AP_m with the maximum transmit power $P_m^{\max}$ and constraint (4.6c) is imposed to guarantee the minimum achievable rate requirement $R_l^{\min}$ of UE l. Problem (4.6) is nonconvex since the objective is nonconcave and constraints (4.6c)-(4.6e) are nonconvex. The complex rate function in (4.3) and the nonconvex constraint on the reflecting coefficients (4.6e) make this problem even more challenging to solve jointly.

4.4 Proposed Alternating Descent-based Iterative Algorithm

In an iterative algorithm based on the IA framework [11], let $(\boldsymbol{\psi}^{(\kappa)}, \boldsymbol{w}^{(\kappa)})$ be the feasible point of (4.6) obtained at the $(\kappa-1)$-th iteration. In this section, an alternating descent algorithm with low complexity is proposed to solve (4.6), i.e. at iteration $\kappa+1$ solving (4.6) to find the optimal solution $\boldsymbol{w}^\star := \boldsymbol{w}^{(\kappa+1)}$ for given $\boldsymbol{\psi}^{(\kappa)}$, and then solving (4.6) to find the optimal solution $\boldsymbol{\psi}^\star := \boldsymbol{\psi}^{(\kappa+1)}$ for given $\boldsymbol{w}^{(\kappa+1)}$.

4.4.1 Beamforming Descent Iteration

At iteration $\kappa+1$, problem (4.6) for given $\boldsymbol{\psi}^{(\kappa)}$ can be expressed as

$$\max_{\boldsymbol{w},\rho} \quad \mathcal{F}(\boldsymbol{w}, \boldsymbol{\psi}^{(\kappa)}) \triangleq \frac{B\sum_{l\in\mathcal{L}} R_l(\boldsymbol{w}|\boldsymbol{\psi}^{(\kappa)})}{\rho} \tag{4.7a}$$

$$\text{s. t.} \quad P_\Sigma(\boldsymbol{w}) \le \rho, \tag{4.7b}$$

$$R_l(\boldsymbol{w}|\boldsymbol{\psi}^{(\kappa)}) \ge R_l^{\min}, \forall l \in \mathcal{L}, \tag{4.7c}$$

$$\sum\nolimits_{l\in\mathcal{L}} R_l(\boldsymbol{w}|\boldsymbol{\psi}^{(\kappa)}) \le \frac{C_m^{\max}}{\omega_m}, \forall m \in \mathcal{M}, \tag{4.7d}$$

$$(4.6b) \tag{4.7e}$$

where ρ is a slack variable to represent the soft power consumption of RIS-CF. The objective (4.7a) is nonconcave, and constraints (4.7c) and (4.7d) are nonconvex in $\boldsymbol{w}$. To tackle the nonconcavity of (4.7a), following inequality is used:

$$\frac{1}{z}\ln\Big(1+x^2/y\Big) \ge \mathcal{A}^{(\kappa)} - \mathcal{B}^{(\kappa)}\frac{y}{x^2} - \mathcal{C}^{(\kappa)}z, \ \forall x,y,z\in\mathbb{R}_+ \tag{4.8}$$

where $\mathcal{A}^{(\kappa)} \triangleq 2\frac{\ln\Big(1+(x^{(\kappa)})^2/y^{(\kappa)}\Big)}{z^{(\kappa)}} + \frac{(x^{(\kappa)})^2/y^{(\kappa)}}{z^{(\kappa)}(1+(x^{(\kappa)})^2/y^{(\kappa)})}$, $\mathcal{B}^{(\kappa)} \triangleq \frac{\Big((x^{(\kappa)})^2/y^{(\kappa)}\Big)^2}{z^{(\kappa)}(1+(x^{(\kappa)})^2/y^{(\kappa)})}$, and $\mathcal{C}^{(\kappa)} \triangleq \frac{\ln\Big(1+(x^{(\kappa)})^2/y^{(\kappa)}\Big)}{(z^{(\kappa)})^2}$. The proof of (4.8) is given in Appendix A. For $\bar{\boldsymbol{w}}_l = e^{-j\arg(\hat{\mathbf{h}}_l^H(\boldsymbol{\psi}^{(\kappa)})\boldsymbol{w}_l)}\boldsymbol{w}_l$

with $j = \sqrt{-1}$, it follows that $|\hat{\mathbf{h}}_l^H(\boldsymbol{\psi}^{(\kappa)})\boldsymbol{w}_l| = \hat{\mathbf{h}}_l^H(\boldsymbol{\psi}^{(\kappa)})\bar{\boldsymbol{w}}_l = \Re\{\hat{\mathbf{h}}_l^H(\boldsymbol{\psi}^{(\kappa)})\bar{\boldsymbol{w}}_l\} \geq 0$ and $|\hat{\mathbf{h}}_l^H(\boldsymbol{\psi}^{(\kappa)})\boldsymbol{w}_{l'}| = \hat{\mathbf{h}}_l^H(\boldsymbol{\psi}^{(\kappa)})\bar{\boldsymbol{w}}_{l'}$ for all $l' \neq l$. Thus, $R_l(\boldsymbol{w}, \boldsymbol{\psi}^{(\kappa)})$ can be rewritten as

$$R_l(\boldsymbol{w}|\boldsymbol{\psi}^{(\kappa)}) = \ln\Big(1 + \frac{\Big(\Re\{\hat{\mathbf{h}}_l^H(\boldsymbol{\psi}^{(\kappa)})\boldsymbol{w}_l\}\Big)^2}{\varphi_l(\boldsymbol{w}|\boldsymbol{\psi}^{(\kappa)})}\Big) \tag{4.9}$$

under the condition that $\Re\{\hat{\mathbf{h}}_l^H(\boldsymbol{\psi}^{(\kappa)})\boldsymbol{w}_l\} \geq 0$, where $\varphi_l(\boldsymbol{w}|\boldsymbol{\psi}^{(\kappa)}) \triangleq \sum_{j\in\mathcal{L}\setminus l} |\hat{\mathbf{h}}_l^H(\boldsymbol{\psi}^{(\kappa)})\boldsymbol{w}_j|^2 + \sigma^2$. Applying inequality (4.8), we obtain

$$\frac{R_l(\boldsymbol{w}|\boldsymbol{\psi}^{(\kappa)})}{\rho} \geq \mathcal{A}_l^{(\kappa)} - \mathcal{B}_l^{(\kappa)} \frac{\varphi_l(\boldsymbol{w}|\boldsymbol{\psi}^{(\kappa)})}{\Big(\Re\{\hat{\mathbf{h}}_l^H(\boldsymbol{\psi}^{(\kappa)})\boldsymbol{w}_l\}\Big)^2} - \mathcal{C}_l^{(\kappa)}\rho \tag{4.10}$$

where $\mathcal{A}_l^{(\kappa)} \triangleq 2\ln\Big(1+\Gamma_l^{(\kappa)}\Big)/\rho^{(\kappa)} + \Gamma_l^{(\kappa)}/\Big(\rho^{(\kappa)}(1+\Gamma_l^{(\kappa)})\Big)$, $\mathcal{B}_l^{(\kappa)} \triangleq (\Gamma_l^{(\kappa)})^2/\Big(\rho^{(\kappa)}(1+\Gamma_l^{(\kappa)})\Big)$, $\mathcal{C}_l^{(\kappa)} \triangleq \ln\Big(1+\Gamma_l^{(\kappa)}\Big)/(\rho^{(\kappa)})^2$, and $\Gamma_l^{(\kappa)} = \Big(\Re\{\hat{\mathbf{h}}_l^H(\boldsymbol{\psi}^{(\kappa)})\boldsymbol{w}_l^{(\kappa)}\}\Big)^2/\varphi_l(\boldsymbol{w}^{(\kappa)}|\boldsymbol{\psi}^{(\kappa)})$. As a result, the concave lower bound of $R_l(\boldsymbol{w}, \boldsymbol{\psi}^{(\kappa)})/\rho$ is found as

$$\mathcal{F}_l^{(\kappa)}(\boldsymbol{w}, \rho|\boldsymbol{\psi}^{(\kappa)}) := \mathcal{A}_l^{(\kappa)} - \mathcal{B}_l^{(\kappa)} \frac{\varphi_l(\boldsymbol{w}|\boldsymbol{\psi}^{(\kappa)})}{\Omega_l^{(\kappa)}(\boldsymbol{w}|\boldsymbol{\psi}^{(\kappa)})} - \mathcal{C}_l^{(\kappa)}\rho \tag{4.11}$$

with the condition $\Omega_l^{(\kappa)}(\boldsymbol{w}|\boldsymbol{\psi}^{(\kappa)}) \triangleq 2\Re\{\hat{\mathbf{h}}_l^H(\boldsymbol{\psi}^{(\kappa)})\boldsymbol{w}_l^{(\kappa)}\}\,\Re\{\hat{\mathbf{h}}_l^H(\boldsymbol{\psi}^{(\kappa)})\boldsymbol{w}_l\} - \Big(\Re\{\hat{\mathbf{h}}_l^H(\boldsymbol{\psi}^{(\kappa)})\boldsymbol{w}_l^{(\kappa)}\}\Big)^2 > 0$. We note that $\mathcal{F}_l^{(\kappa)}(\boldsymbol{w}, \rho|\boldsymbol{\psi}^{(\kappa)})$ is a concave lower bound of $R_l(\boldsymbol{w}|\boldsymbol{\psi}^{(\kappa)})/\rho$, satisfying $\mathcal{F}_l^{(\kappa)}(\boldsymbol{w}^{(\kappa)}, \rho^{(\kappa)}, \boldsymbol{\psi}^{(\kappa)}) = R_l(\boldsymbol{w}^{(\kappa)}, \boldsymbol{\psi}^{(\kappa)})/\rho^{(\kappa)}$.

Following the steps (4.9)-(4.11) with $\rho = 1$, constraint (4.7c) can be directly convexified by

$$\mathcal{R}_l^{(\kappa)}(\boldsymbol{w}|\boldsymbol{\psi}^{(\kappa)}) \geq R_l^{\min}, \forall l \in \mathcal{L} \tag{4.12}$$

where $\mathcal{R}_l^{(\kappa)}(\boldsymbol{w}|\boldsymbol{\psi}^{(\kappa)}) \triangleq \bar{\mathcal{A}}_l^{(\kappa)} - \bar{\mathcal{B}}_l^{(\kappa)} \frac{\varphi_l(\boldsymbol{w}|\boldsymbol{\psi}^{(\kappa)})}{\Omega_l^{(\kappa)}(\boldsymbol{w}|\boldsymbol{\psi}^{(\kappa)})}$, with $\bar{\mathcal{A}}_l^{(\kappa)} \triangleq \ln\Big(1+\Gamma_l^{(\kappa)}\Big) + \Gamma_l^{(\kappa)}/(1+\Gamma_l^{(\kappa)})$ and $\bar{\mathcal{B}}_l^{(\kappa)} \triangleq (\Gamma_l^{(\kappa)})^2/(1+\Gamma_l^{(\kappa)})$.

Finally, (4.7d) is rewritten as

$$(4.7\text{d}) \Leftrightarrow \begin{cases} \sum_{l\in\mathcal{L}} \ln(1+r_l) \leq \dfrac{C_m^{\max}}{\omega_m}, \forall m \in \mathcal{M}, & (4.13\text{a}) \\ \dfrac{\left(\Re\{\hat{\mathbf{h}}_l^H(\boldsymbol{\psi}^{(\kappa)})\boldsymbol{w}_l\}\right)^2}{r_l} \leq \varphi_l(\boldsymbol{w}|\boldsymbol{\psi}^{(\kappa)}),\ \forall l \in \mathcal{L} & (4.13\text{b}) \end{cases}$$

where $\boldsymbol{r} \triangleq \{r_l\}_{l\in\mathcal{L}}$ are newly introduced variables. It is noted that $\ln(1+r_l)$ is a concave function and $\varphi_l(\boldsymbol{w}|\boldsymbol{\psi}^{(\kappa)})$ is a convex function. Following the IA principle, constraints (4.13a) and (4.13b) are innerly convexified as

$$\sum_{l\in\mathcal{L}}\left(\ln(1+r_l^{(\kappa)}) - \frac{r_l^{(\kappa)}}{1+r_l^{(\kappa)}} + \frac{1}{1+r_l^{(\kappa)}} r_l\right) \leq \frac{C_m^{\max}}{\omega_m}, \forall m \in \mathcal{M}, \tag{4.14}$$

$$\frac{\left(\Re\{\hat{\mathbf{h}}_l^H(\boldsymbol{\psi}^{(\kappa)})\boldsymbol{w}_l\}\right)^2}{r_l} \leq \varphi_l^{(\kappa)}(\boldsymbol{w}|\boldsymbol{\psi}^{(\kappa)}),\ \forall l \in \mathcal{L} \tag{4.15}$$

where $\varphi_l^{(\kappa)}(\boldsymbol{w}|\boldsymbol{\psi}^{(\kappa)}) \triangleq \sum_{j\in\mathcal{L}\setminus l}\left(2\Re\{(\boldsymbol{w}_j^{(\kappa)})^H\hat{\mathbf{h}}_l(\boldsymbol{\psi}^{(\kappa)})\hat{\mathbf{h}}_l^H(\boldsymbol{\psi}^{(\kappa)})\boldsymbol{w}_j\} - |\hat{\mathbf{h}}_l^H(\boldsymbol{\psi}^{(\kappa)})\boldsymbol{w}_j^{(\kappa)}|^2\right) + \sigma^2$.

The approximate convex problem of (4.7) solved at iteration $\kappa+1$ is given as

$$\begin{aligned} \max_{\boldsymbol{w},\boldsymbol{r},\rho} \quad & \mathcal{F}^{(\kappa)}(\boldsymbol{w},\boldsymbol{\psi}^{(\kappa)}) \triangleq B\sum\nolimits_{l\in\mathcal{L}} \mathcal{F}_l^{(\kappa)}(\boldsymbol{w},\rho|\boldsymbol{\psi}^{(\kappa)}) && (4.16\text{a}) \\ \text{s. t.} \quad & \Re\{\hat{\mathbf{h}}_l^H(\boldsymbol{\psi}^{(\kappa)})\boldsymbol{w}_l\} \geq 0,\ \forall l \in \mathcal{L}, && (4.16\text{b}) \\ & \Omega_l^{(\kappa)}(\boldsymbol{w}|\boldsymbol{\psi}^{(\kappa)}) \geq 0,\ \forall l \in \mathcal{L}, && (4.16\text{c}) \\ & (4.6\text{b}), (4.7\text{b}), (4.12), (4.14), (4.15). && (4.16\text{d}) \end{aligned}$$

For given $\boldsymbol{\psi}^{(\kappa)}$, the per-iteration computational complexity of solving (4.16) is $\mathcal{O}\Big((4L+M)^{2.5}(L^2(MK+1)^2+4L+M)\Big)$ [13].

4.4.2 Phase Descent Iteration

For given $\boldsymbol{w}^{(\kappa+1)}$, by solving (4.16), the total power consumption $P_{\Sigma}(\boldsymbol{w}^{(\kappa+1)})$ is fixed and then problem (4.6) with regard to $\boldsymbol{\psi}$ can be expressed as

$$\max_{\boldsymbol{\psi}} \quad \mathcal{G}(\boldsymbol{w}^{(\kappa+1)}, \boldsymbol{\psi}) \triangleq B \sum_{l \in \mathcal{L}} R_l(\boldsymbol{\psi}|\boldsymbol{w}^{(\kappa+1)}) \tag{4.17a}$$

$$\text{s. t.} \quad R_l(\boldsymbol{\psi}|\boldsymbol{w}^{(\kappa+1)}) \geq R_l^{\min}, \forall l \in \mathcal{L}, \tag{4.17b}$$

$$\textstyle\sum_{l \in \mathcal{L}} R_l(\boldsymbol{\psi}|\boldsymbol{w}^{(\kappa+1)}) \leq \dfrac{C_m^{\max}}{\omega_m}, \forall m \in \mathcal{M}, \tag{4.17c}$$

$$|\psi_{n,r}| = 1, \forall n \in \mathcal{N}, r \in \mathcal{R}. \tag{4.17d}$$

The main difficulty for solving (4.17) is due to the unit-modulus constraint (4.17d), which is also a nonconvex constraint. To overcome this issue, (4.17d) is relaxed by the following convex constraint:

$$|\psi_{n,r}|^2 \leq 1, \forall n \in \mathcal{N}, r \in \mathcal{R} \tag{4.18}$$

which also implies that $\sum_{n \in \mathcal{N}} \sum_{r \in \mathcal{R}} |\psi_{n,r}|^2 - NR \leq 0$. To ensure that constraint (4.17d) holds true at optimum, the following theorem is introduced.

Theorem 4.1. *The optimality of* (4.17) *is guaranteed by the following penalized optimization problem:*

$$\max_{\boldsymbol{\psi}} \quad B \sum_{l \in \mathcal{L}} R_l(\boldsymbol{\psi}|\boldsymbol{w}^{(\kappa+1)}) + \eta \Big(\sum_{n \in \mathcal{N}} \sum_{r \in \mathcal{R}} |\psi_{n,r}|^2 - NR \Big) \tag{4.19a}$$

$$\text{s. t.} \quad (4.17\text{b}), (4.17\text{c}), (4.18) \tag{4.19b}$$

where $\eta > 0$ is a constant penalty parameter making the objective and penalty terms comparable.

Proof. Due to constraint (4.18), the penalty term $\sum_{n \in \mathcal{N}} \sum_{r \in \mathcal{R}} |\psi_{n,r}|^2 - NR$ is always

negative. This allows the uncertainties of the unit-modulus constraint to be penalized, which ensures $\psi_{n,r} = 1$ at optimum. For a sufficiently large value of η, problems (4.17) and (4.19) share the same optimal solution. A detailed proof can be found in [14, Appendix C]. □

It can be seen that the developments presented in Section III-A are very useful to approximate $R_l(\boldsymbol{\psi}|\boldsymbol{w}^{(\kappa+1)})$ in the objective (4.19a) and constraints (4.17b) and (4.17c). It is also noticed that $\sum_{n\in\mathcal{N}}\sum_{r\in\mathcal{R}}|\psi_{n,r}|^2$ is the sum of quadratic functions, which can be convexified by directly applying the IA method. As a result, the following approximate convex problem of (4.17) is solved at iteration $\kappa+1$:

$$\begin{aligned}
\max_{\boldsymbol{\psi},\boldsymbol{r}} \quad & \mathcal{G}^{(\kappa)}(\boldsymbol{w}^{(\kappa+1)},\boldsymbol{\psi}) \triangleq \\
& B\sum\nolimits_{l\in\mathcal{L}}\mathcal{R}_l^{(\kappa)}(\boldsymbol{\psi}|\boldsymbol{w}^{(\kappa+1)}) + \eta\Big(\mathcal{P}^{(\kappa)}(\boldsymbol{\psi}) - NR\Big) && \text{(4.20a)}\\
\text{s. t.} \quad & \mathcal{R}_l^{(\kappa)}(\boldsymbol{\psi}|\boldsymbol{w}^{(\kappa+1)}) \geq R_l^{\min}, \forall l\in\mathcal{L}, && \text{(4.20b)}\\
& \frac{|\hat{\mathbf{h}}_l^H(\boldsymbol{\psi})\boldsymbol{w}_l^{(\kappa+1)}|^2}{r_l} \leq \varphi_l^{(\kappa)}(\boldsymbol{\psi}|\boldsymbol{w}^{(\kappa+1)}),\ \forall l\in\mathcal{L}, && \text{(4.20c)}\\
& (4.14), (4.18) && \text{(4.20d)}
\end{aligned}$$

where $\mathcal{P}^{(\kappa)}(\boldsymbol{\psi}) \triangleq \sum_{n\in\mathcal{N}}\sum_{r\in\mathcal{R}}\Big(2\Re\{\Big(\psi_{n,r}^{(\kappa)}\Big)^*\psi_{n,r}\} - |\psi_{n,r}^{(\kappa)}|^2\Big)$ and $\varphi_l^{(\kappa)}(\boldsymbol{\psi}|\boldsymbol{w}^{(\kappa+1)}) \triangleq \sum_{j\in\mathcal{L}\setminus l}\Big(2\Re\{(\boldsymbol{w}_j^{(\kappa+1)})^H\hat{\mathbf{h}}_l(\boldsymbol{\psi}^{(\kappa)})\hat{\mathbf{h}}_l^H(\boldsymbol{\psi})\,\boldsymbol{w}_j^{(\kappa+1)}\} - |\hat{\mathbf{h}}_l^H(\boldsymbol{\psi}^{(\kappa)})\boldsymbol{w}_j^{(\kappa+1)}|^2\Big) + \sigma^2$. The per-iteration computational complexity of solving (4.20) is $\mathcal{O}\Big((2L+NR+M)^{2.5}((L+NR)^2+2L+NR+M)\Big)$.

The proposed alternating descent-based iterative algorithm for solving problem (4.6) is summarized in Algorithm 6.

Convergence analysis: From (4.16), it is clear that $\mathcal{F}(\boldsymbol{w}^{(\kappa+1)},\boldsymbol{\psi}^{(\kappa)}) \geq \mathcal{F}^{(\kappa)}(\boldsymbol{w}^{(\kappa+1)},\boldsymbol{\psi}^{(\kappa)}) \geq \mathcal{F}^{(\kappa)}(\boldsymbol{w}^{(\kappa)},\boldsymbol{\psi}^{(\kappa)}) = \mathcal{F}(\boldsymbol{w}^{(\kappa)},\boldsymbol{\psi}^{(\kappa)})$. Similar to (4.20), we have $\mathcal{G}(\boldsymbol{w}^{(\kappa+1)},\boldsymbol{\psi}^{(\kappa+1)}) \geq \mathcal{G}^{(\kappa)}(\boldsymbol{w}^{(\kappa+1)},\boldsymbol{\psi}^{(\kappa+1)}) \geq \mathcal{G}^{(\kappa)}(\boldsymbol{w}^{(\kappa+1)},\boldsymbol{\psi}^{(\kappa)}) = \mathcal{G}(\boldsymbol{w}^{(\kappa+1)},\boldsymbol{\psi}^{(\kappa)})$. As a result, it is true that $\mathcal{E}(\boldsymbol{w}^{(\kappa+1)},\boldsymbol{\psi}^{(\kappa+1)}) \geq \mathcal{E}(\boldsymbol{w}^{(\kappa)},\boldsymbol{\psi}^{(\kappa)})$. In other words, Algorithm 6 generates a sequence

Algorithm 6 Proposed Alternating Descent-based Iterative Algorithm to Solve Problem (4.6)

Initialization: Set $\kappa := 0$ and generate an initial feasible point $(\boldsymbol{\psi}^{(0)}, \boldsymbol{w}^{(0)})$
  repeat
    Given $\boldsymbol{\psi}^{(\kappa)}$, solve the convex problem (4.16) to find the optimal solution $\boldsymbol{w}^{\star}$ and update $\boldsymbol{w}^{(\kappa+1)} := \boldsymbol{w}^{\star}$
    Given $\boldsymbol{w}^{(\kappa+1)}$, solve the convex problem (4.20) to find the optimal solution $\boldsymbol{\psi}^{\star}$ and update $\boldsymbol{\psi}^{(\kappa+1)} := \boldsymbol{\psi}^{\star}$
    Set $\kappa := \kappa + 1$
  until Convergence
  Ouput: $(\boldsymbol{\psi}^{(\kappa)}, \boldsymbol{w}^{(\kappa)})$

$\{(\boldsymbol{w}^{(\kappa)}, \boldsymbol{\psi}^{(\kappa)})\}$ of improved points that converges at least to a locally optimal solution [11].

Choice of η: In practice, a very small η does not make much difference, leading to a slow convergence. A very large η results in an early convergence of Algorithm 6 and a suboptimal solution $\boldsymbol{\psi}^{*}$. Given the simulation setup in Section 4.5, it is numerically observed that $\eta = 10^3$ ensures the convergence of Algorithm 6 with the highest performance.

4.5 Numerical Results

An RIS-CF network including $M = 4$ APs, $N = 4$ RISs, and $L = 8$ UEs is considered as illustrated in Fig. 4.2, where all APs, RISs, and UEs are uniformly distributed within a circular region with 1 km radius. The large-scale fading of all channels is modeled as [4]: $\beta_{a,b} = 10^{\frac{\mathrm{PL}(d_{a,b})+\sigma_{sh}z}{10}}$, where $a = \{m, n\}$, $b = \{n, l\}$, $\forall m \in \mathcal{M}$, $n \in \mathcal{N}$, $l \in \mathcal{L}$, and $d_{a,b}$ is the distance (in km) from a to b. The shadow fading is modeled as a random variable z, which follows $\mathcal{CN}(0, 1)$ with standard deviation $\sigma_{sh} = 8$ dB. The three-slope path loss model (in dB) is considered as [4]: $\mathrm{PL}(d_{a,b}) = -140.7 - 35\log_{10}(d_{a,b}) + 20a_0\log_{10}\Big(d_{a,b}/d_0\Big) + 15a_1\log_{10}\Big(d_{a,b}/d_1\Big)$, where d_j, with $j = \{0, 1\}$, represents the reference distance and $a_j = \max\Big\{0, \frac{d_i - d_{a,b}}{|d_i - d_{a,b}|}\Big\}$. Unless otherwise stated, the key parameters are provided in Table 4.1, following studies in [3, 5, 12]. The used convex solver is SeDuMi [13] in the MATLAB

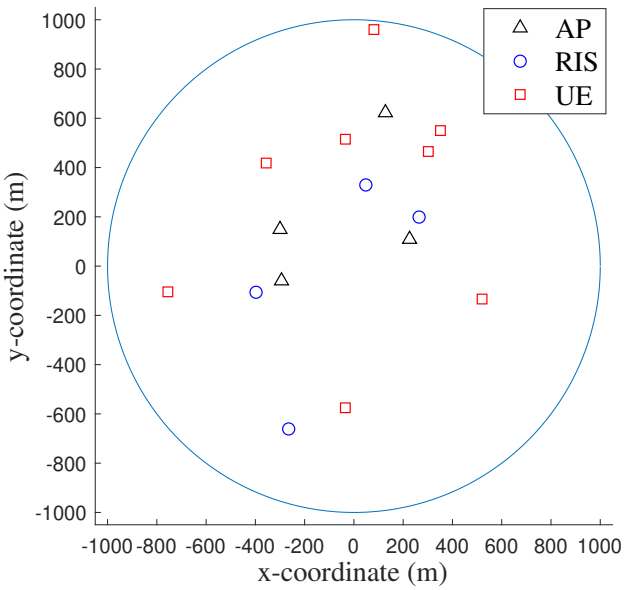

Fig. 4.2: System layout with $M = 4$ APs, $N = 4$ RISs, and $L = 8$ UEs.

Table 4.1: Simulation Parameters.

Parameter	Value	Parameter	Value
$P_{m,l}^{\mathrm{BH}}$	0 dBW	B	20 MHz
P_m	9 dBW	$P_{n,r}$	10 dBm
P_l	10 dBm	ξ_m	1.2
$C_m^{\max} \equiv C^{\max}, \forall m$	500 b/s/Hz	$P_m^{\max} \equiv P^{\max}$	35 dBm
$R_l^{\min}$	0.5 b/s/Hz	K	8
R	8	σ^2	-104 dBm
(d_0, d_1)	(10,50) m	η	10^3

environment. The performance of Algorithm 6 is compared with three existing resource allocation schemes: *i*) CF network without RISs, *ii*) Collocated network with RISs, and *iii*) Collocated network without RISs. For collocated network, an AP is located at the center of the considered area to serve all UEs. It is equipped with MK antennas and has a maximum transmit power of $MP_m^{\max}$.

Fig. 4.3 plots the typical convergence behavior of Algorithm 6 for a random channel realization. On average, Algorithm 6 requires about 6 iterations to reach the almost optimal value of EE in all cases. As expected, increasing K results in better EE, but also

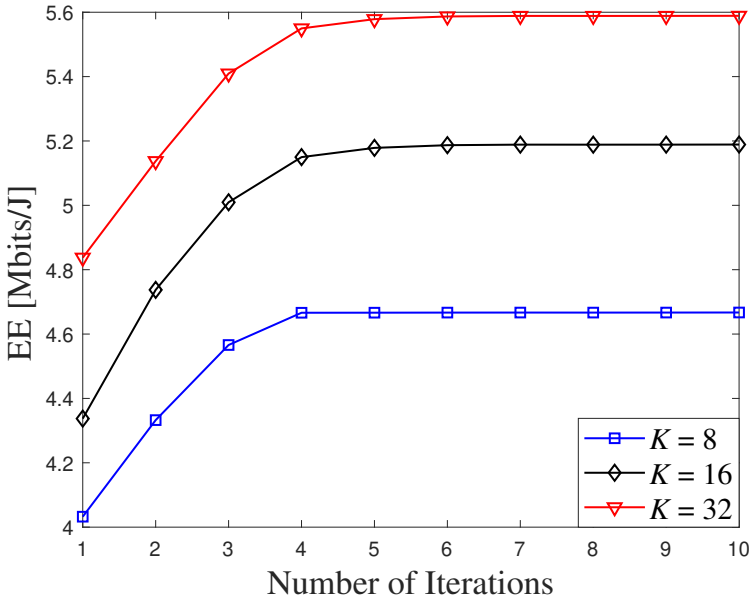

Fig. 4.3: Convergence of Algorithm 6 with different number of antennas per AP.

requires slightly more iterations.

Fig. 4.4 depicts the average EE versus the maximum transmit power per AP for different resource allocation schemes. It can be seen that the average EE of all considered schemes significantly enhances when $P^{\max}$ increases. Further, the EE of the CF network with and without RISs is much better than that of the collocated network with and without RISs, respectively. This is attributed to the fact that the CF network with distributed APs brings the service antennas closer to UEs, which not only reduces path losses but also provides higher degree of macro-diversity, compared to the collocated network. Moreover, both CF and collocated networks with RISs achieve much higher EE compared to the networks without RISs. This observation confirms that RIS boosts up the EE of CF and collocated networks. Notably, the proposed RIS-CF network provides the best EE among all considered schemes.

In Fig. 4.5, the average EE is depicted versus the maximum backhaul capacity, $C^{\max}$. As can be seen, the EE of all networks greatly increases when $C^{\max}$ increases. This is

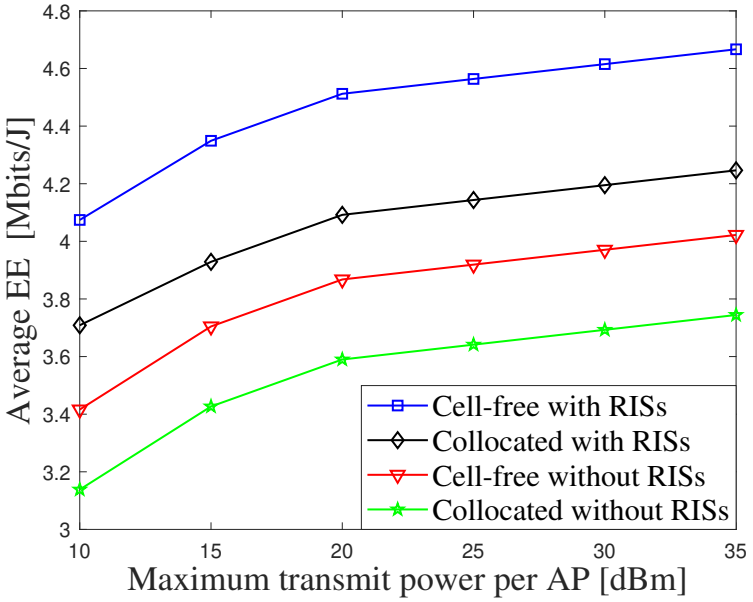

Fig. 4.4: Average EE vs. the maximum transmit power per AP, $P^{\max}$.

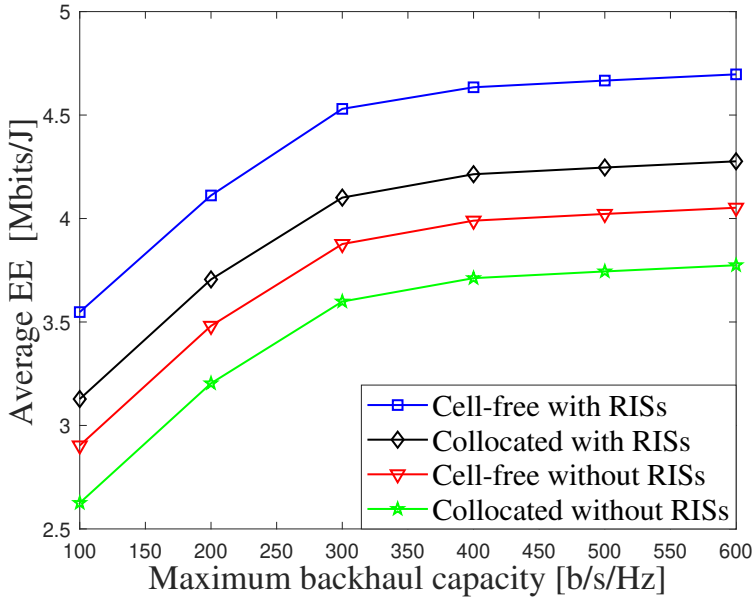

Fig. 4.5: Average EE vs. the maximum backhaul capacity, $C^{\max}$.

because the higher the maximum backhaul capacity, the more data can be conveyed over the backhaul links. Increasing $C^{\max}$ also leads to a remarkable gain in the EE by the proposed RIS-CF over other networks.

4.6 Conclusion

This chapter has considered the EE maximization problem of CF networks with the assistance of multiple RISs. The problem involves a joint optimization of transmit beamformers at APs and reflecting coefficients at RISs subject to the limited backhaul capacity constraints, which is formulated as a nonconvex problem. To address this problem, this chapter has developed a low-complexity alternating descent algorithm based on the IA framework, which converges at least to a locally optimal solution. Numerical results have confirmed the fast convergence of the proposed algorithm. Further, they have revealed the advantages of CF and RIS over collocated network.

Appendix A

Proof of Inequality (4.8)

First, it is noted that $f(t,z) \triangleq \ln(1+1/t)/z$ is a concave function on the domain ($z > 0$, $t > 0$) [15]. By the first-order Taylor approximation, it follows that

$$\begin{aligned} f(t,z) &\geq f(t^{(\kappa)},z^{(\kappa)}) - \nabla_t f(t^{(\kappa)},z^{(\kappa)})(t-t^{(\kappa)}) - \nabla_z f(t^{(\kappa)},z^{(\kappa)})(z-z^{(\kappa)}) \\ &= 2f(t^{(\kappa)},z^{(\kappa)}) + \frac{1}{z^{(\kappa)}(t^{(\kappa)}+1)} - \frac{1}{z^{(\kappa)}t^{(\kappa)}(t^{(\kappa)}+1)}t - \frac{f(t^{(\kappa)},z^{(\kappa)})}{z^{(\kappa)}}z. \end{aligned} \tag{4.21}$$

By replacing $t = y/x^2$ and $t^{(\kappa)} = y^{(\kappa)}/(x^{(\kappa)})^2$, we obtain the inequality (4.8).

References

[1] A. Yadav and O. A. Dobre, "All technologies work together for good: A glance at future mobile networks," *IEEE Wireless Commun.*, vol. 25, no. 4, pp. 10–16, Aug. 2018.

[2] Y. Teng *et al.*, "Resource allocation for ultra-dense networks: A survey, some research issues and challenges," *IEEE Commun. Surveys Tuts.*, vol. 21, no. 3, pp. 2134–2168, 3rd Quart. 2019.

[3] H. V. Nguyen *et al.*, "On the spectral and energy efficiencies of full-duplex cell-free massive MIMO," *IEEE J. Select. Areas Commun.*, vol. 38, no. 8, pp. 1698–1718, Aug. 2020.

[4] H. Q. Ngo *et al.*, "Cell-free massive MIMO versus small cells," *IEEE Trans. Wireless Commun.*, vol. 16, no. 3, pp. 1834–1850, Mar. 2017.

[5] P. Luong *et al.*, "Optimal joint remote radio head selection and beamforming design for limited fronthaul C-RAN," *IEEE Trans. Signal Process.*, vol. 65, no. 21, pp. 5605–5620, Nov. 2017.

[6] A. A. Polegre and A. G. Armada, "User-centric massive MIMO systems with hardening-based clusterization," in *Proc. 24th International ITG Workshop on Smart Antennas*, Feb. 2020, pp. 1–5.

[7] H. Q. Ngo *et al.*, "On the total energy efficiency of cell-free massive MIMO," *IEEE Trans. Green Commun. Netw.*, vol. 2, no. 1, pp. 25–39, Mar. 2018.

[8] Q. Wu and R. Zhang, "Intelligent reflecting surface enhanced wireless network via joint active and passive beamforming," *IEEE Trans. Wireless Commun.*, vol. 18, no. 11, pp. 5394–5409, Nov. 2019.

[9] Z. Zhang and L. Dai, "A joint precoding framework for wideband reconfigurable intelligent surface-aided cell-free network," *arXiv preprint arXiv:2002.03744v2*, Feb. 2020.

[10] S. Huang *et al.*, "Decentralized beamforming design for intelligent reflecting surface-enhanced cell-free networks," *arXiv preprint arXiv:2006.12238v1*, June 2020.

[11] A. Beck, A. Ben-Tal, and L. Tetruashvili, "A sequential parametric convex approximation method with applications to nonconvex truss topology design problems," *J. Global Optim.*, vol. 47, no. 1, pp. 29–51, May 2010.

[12] C. Huang *et al.*, "Reconfigurable intelligent surfaces for energy efficiency in wireless communication," *IEEE Trans. Wireless Commun.*, vol. 18, no. 8, pp. 4157–4170, Aug. 2019.

[13] D. Peaucelle, D. Henrion, and Y. Labit, "Users guide for SeDuMi interface 1.03," 2002. [Online]. Available: http://homepages.laas.fr/peaucell/software/sdmguide.pdf

[14] H. V. Nguyen *et al.*, "Joint power control and user association for NOMA-based full-duplex systems," *IEEE Trans. Commun.*, vol. 67, no. 11, pp. 8037–8055, Nov. 2019.

[15] V.-D. Nguyen *et al.*, "A new design paradigm for secure full-duplex multiuser systems," *IEEE J. Select. Areas Commun.*, vol. 36, no. 7, pp. 1480–1498, July 2018.

Chapter 5

Transmit Power Minimization of RIS-Enabled Federated Learning Networks

5.1 Abstract

Federated learning (FL) has recently emerged as a novel technique for training shared machine learning models in a distributed fashion while preserving data privacy. However, the application of FL in wireless networks poses a unique challenge on the mobile users (MUs)' battery lifetime. This chapter aims to apply RIS-aided wireless power transfer to facilitate sustainable FL-based wireless networks. The objective is to minimize the total transmit power of participating MUs by jointly optimizing the transmission time, power control, and the RIS's phase shifts. Numerical results demonstrate that the total transmit power is minimized while satisfying the requirements of both minimum harvested energy and transmission data rate.

5.2 Introduction

With the recent industrial and research activities devoted to the 6G wireless networks, the uniqueness of the future 6G networks—compared to previous wireless network generations—lies in the realization of ubiquitous intelligence. In this sense, the artificial intelligence (AI) will be exploited to orchestrate wireless networks from the core to the edge [1]. To this end, ML, which is a subfield of AI, is anticipated to be an indispensable tool in future 6G networks. ML will operate on the data collected from all network segments in order to enable smart resource management, access control, multi-layer communication, etc. The evolution of the ML paradigm was initially fueled by the huge amount of data generated from a wide range of emerging applications, including smart cities, autonomous vehicles, haptics, and augmented reality services, to name a few. Accordingly, the ML algorithms are key to leverage such data with the aim of training wireless networks, and therefore, enabling truly self-optimized and self-organized networks. Since their initial development, classical ML algorithms demonstrated a superior performance in handling complicated tasks pertaining to channel estimation, spectrum sensing, resource allocation, etc. Nevertheless, given that the underlying principle of ML is the collection of raw data generated at end-devices and stored at a centralized server for model training purposes, a number of concerning issues have been flagged. First, in cloud-based ML algorithms, users privacy is compromised due to the exchange of their local datasets, exposing participating MUs to potential security attacks. Second, the long propagation delay in centralized ML algorithms limits their applications in real-time scenarios. Finally, the centralized ML paradigm suffers from the increased network overhead, rendering it unsuitable for power-constrained MUs [2].

Recently, federated learning (FL) has been identified as an efficient decentralized learning mechanism, in which improved data privacy, reduced latency, and network overhead can be achieved [3, 4]. FL is a collaborative learning mechanism, in which the on-board

computing and storage capabilities, in addition to the local datasets of participating MUs (clients), are leveraged to perform local model training. The locally trained model updates are then shared with a cloud-based server for aggregation and global model evaluation. These steps are repeated until a desired level of accuracy is attained. Given that less information is required to be shared with the central server, compared to classical cloud-centric ML algorithms, FL features enhanced user privacy and offers a better utilization for the network resources. Inspired by its promising potentials, extensive research attempts have been initiated to investigate the advantages of the interplay of FL and other enabling technologies, including RIS, blockchain, aerial/satellite communications, and mobile edge computing [3–8].

Despite the several advantages of FL, only few attempts have explored the problem of executing energy-consuming computing and communication tasks at MUs with limited energy budget. In [9], the problem of joint delay and energy minimization in an IoT network was investigated by using a three-tier offloading scheme. The authors in [10] minimized the overall energy consumption at participating MUs using the NOMA scheme at the uplink transmission. This was accomplished by optimizing the number of iterations a client is requested to update its local model, under a particular global model accuracy threshold.

On the other hand, the work in [11–14] considered the adoption of the wireless power transfer (WPT) concept as a mean to supply power-limited MUs and enable them to participate in the training process. In particular, in [11], a hybrid radio frequency (RF)/visible light communication (VLC) scenario was considered, in which the VLC link over the downlink is leveraged for energy harvesting (EH) purposes, while the RF is used for the local model updates transmission. From a similar perspective, the authors in [12] applied the time-switching paradigm of WPT to an FL system, in which they studied the trade-off between learning and WPT, and further optimized the MU clock frequency for

improved utilization of harvested energy for model evaluation. From a similar point of view, the authors in [14] minimized the mean squared error (MSE) by optimizing the aggregation beamforming and consumed energy in a vehicular energy-limited network. The authors in [13] leveraged RIS for WPT and developed an improved local model updates transmission. In particular, they formulated an optimization problem to obtain the RIS phase shift (PS) vector that minimizes the MSE.

Unlike the works in [10–12, 14], which considered the application of WPT in FL, motivated by the intertwined benefits of RIS and FL paradigms, this chapter considers leveraging RIS for WPT purposes, to enable power-constrained MUs meet the computing and communication requirements imposed by the FL process. Instead of focusing on minimizing the MSE, as in [13], the proposed framework aims to minimize the total transmit power of the participating MUs, while satisfying particular computing and communication requirements. This is achieved by jointly optimizing the RIS and MUs operational parameters.

Notation: $\mathbf{X}^T$ denotes the transpose of a matrix $\mathbf{X}$, $\mathbb{E}[\cdot]$ represents the expectation operation, $|\cdot|$ represents the absolute value of a complex scalar, and $\Re\{\cdot\}$ returns the real part of an argument.

5.3 System Model

This chapter considers a FL model, in which the downlink transmission is utilized to recharge K EH-enabled MUs, while the uplink is dedicated for communicating the FL local model parameters to a BS, as depicted in Fig. 5.1. During the downlink transmission, a BS_1 communicates with the K MUs through the assistance of an RIS, comprising N reflecting elements (REs). This is motivated by the assumption that the direct links between BS_1 and the K devices are unavailable. Therefore, the RIS is exploited to extend

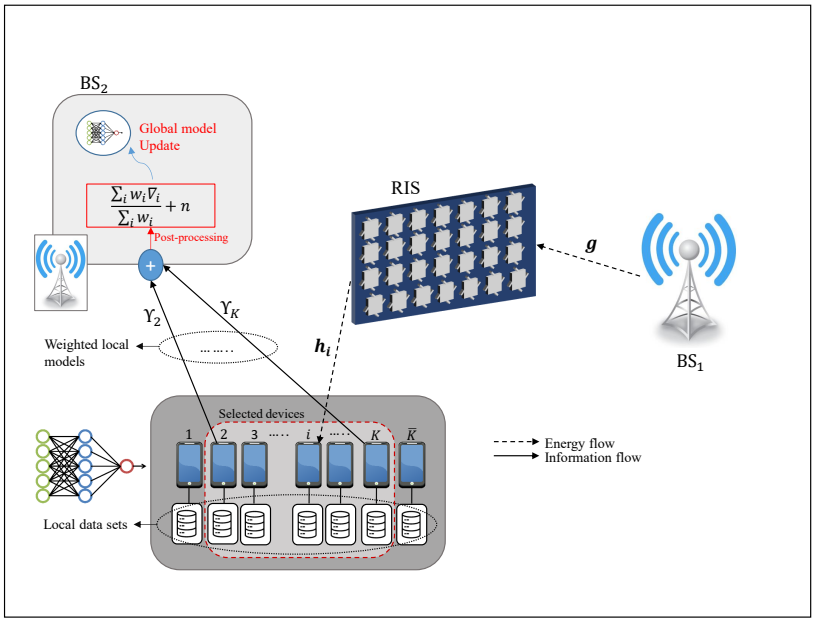

Fig. 5.1: System model.

the signal coverage and to enhance the received signal strength, and thus, to enhance the harvested energy [15]. Without loss of generality, we assume that each node in the network is equipped with a single antenna.

5.3.1 Wireless Power Transfer (WPT) Model

In the underlying system model, BS_1 sends the RF signal, x_E with $\mathbb{E}\{|x_E|^2\} = 1$, to the K MUs through the RIS. The average transmit power at BS_1 is represented by P_{BS_1}. The baseband signal received at the k-th MU can be written as

$$\begin{aligned} y_{\mathrm{BS}_1,k} &= \sqrt{P_{\mathrm{BS}_1}}\mathbf{h}_k^H \mathbf{\Phi}\mathbf{g}x_E + n_k \\ &= \sqrt{P_{\mathrm{BS}_1}}\boldsymbol{\psi}^T\left(\mathbf{g}^H\right)\mathbf{h}_k x_E + n_k \\ &= \sqrt{P_{\mathrm{BS}_1}}q_k\left(\boldsymbol{\psi}\right)x_E + n_k, \end{aligned} \tag{5.1}$$

where $\mathbf{g} \in \mathbb{C}^{N\times 1}$ and $\mathbf{h}_k^H \in \mathbb{C}^{1\times N}$ denote the channels from BS_1 to RIS, and from RIS to the k-th MU, respectively. $\mathbf{\Phi} \in \mathbb{C}^{N\times N}$ represents the PS matrix of RIS, which can be written as: $\mathbf{\Phi} \triangleq (e^{j\theta_1}, e^{j\theta_2}, \ldots, e^{j\theta_N})$, where $\theta_n \in [0, 2\pi)$ denotes the PS of the n-th RE on the RIS. Further, $\mathbf{\Phi}$ can be rewritten as $\mathbf{\Phi} = (\psi_1, \psi_2, \ldots, \psi_N)$, with $|\psi_n| = 1$, $\forall n \in \mathcal{N}$. $\boldsymbol{\psi} \triangleq \big[\psi_1, \psi_2, \ldots, \psi_N\big]^T$ and $q_k(\boldsymbol{\psi}) \triangleq \boldsymbol{\psi}^T\big(\mathbf{g}^H\big)\mathbf{h}_k$. $n_k \sim CN(0, \sigma^2)$ represents the additive white gaussian noise (AWGN) over the downlink transmission.

Assuming all K MUs are equipped with EH devices, the harvested power at the k-th MU can be written as

$$P_{EH} = \eta P_{\mathrm{BS}_1} |q_k(\boldsymbol{\psi})|^2, \tag{5.2}$$

where η accounts for the energy conversion efficiency. This chapter considers that the harvested power is the only source of power. In particular, the harvested power is divided into two parts, namely μP_{EH} and $(1-\mu)P_{EH}$, which are dedicated for local model transmission and computation, respectively, with μ denoting the power splitting factor.

5.3.2 Distributed Federated Learning (FL) Model

Consider that all K MUs are selected by BS_2 to perform a particular on-device distributed FL task, which aims at optimizing the model parameter z that minimizes the local loss function $f_k(\mathbf{z})$:

$$\underset{\mathbf{z}\in\mathbb{R}^d}{\text{minimize}} \quad f_k(\mathbf{z}) = \frac{1}{S_k}\sum_{i\in\mathfrak{D}_k} f_i(\mathbf{z}), \tag{5.3}$$

where S_k denotes the size of the local data set $\mathfrak{D}_k$ of device k and $f_i(\mathbf{z})$ represents the loss function associated with the data pair i. Without loss of generality, it is assumed that all local data sets have uniform size, i.e., $S_k = S$. To maintain higher spectral efficiency and reduce the total number of communication rounds between BS_2 and devices, a model averaging scheme [16] is utilized. In particular, BS_2 broadcasts the global model update

$\mathbf{z}$ to the selected K MUs. At each MU, a local update algorithm is executed to generate the local updated model $\bar{\mathbf{z}}_k$, relying on the local data set and the received global model. Then, the selected MUs send K weighted local models, which are aggregated at BS_2 to compute the updated global model, as $\hat{\mathbf{z}} = \xi\left(\sum_{k\in K} \phi_k\left(\bar{\mathbf{z}}_k\right)\right)$, where ξ denotes the post-processing function at BS_2, while ϕ_k represents the pre-processing function at the k-th MU. Since the harvested energy from the RF signal constitutes the only source of energy at the K MUs, it is assumed that all local model parameters at each MU are transmitted over a single transmission period. Therefore, by setting $x_k = \phi_k\left(\bar{\mathbf{z}}_k\right)$ to represent the transmitted signal at the k-th MU, the target function to be estimated at BS_2 can be written as $\chi = \sum_{k\in K} x_k$. Note that the CPU energy consumed to process all data at the k-th MU over a single local iteration can be expressed as [17]

$$E_{cp}^{(k)} = \frac{\nu_k c_k S}{2}\omega_k^2, \tag{5.4}$$

where ν_k denotes the effective capacitance coefficient of the computing chipset at the k-th MU, and c_k represents the number of CPU cycles required to process one sample data at the k-th MU. Also, ω_k accounts for the k-th MU's CPU cycle frequency. The computation time for one local iteration is $T_{cp,k} = c_k S/\omega_k$. It is worth highlighting that the energy required for model transmission at the k-th MU can be evaluated as [18]

$$E_{cm}^{(k)} = P_{T,k} T_{cm,k}, \tag{5.5}$$

where $P_{T,k}$ and $T_{cm,k}$ denote the transmission power and the transmission time at the k-th MU, respectively. Considering that the uplink channel between the k-th MU and the second BS is Υ_k, which follows the Rayleigh distribution, and based on the time division

multiple access (TDMA), the received signal at BS_2 for the k-th MU is given by

$$y_{\mathrm{BS}_2,k} = \sqrt{P_{T,k}}\Upsilon_k x_k + n_{\mathrm{BS}_2}, \tag{5.6}$$

where $n_{\mathrm{BS}_2} \sim CN(0, \sigma^2)$ represents the AWGN over the uplink transmission. At BS_2, the target function is estimated by utilizing aggregation beamforming, υ, and thus, the achievable rate of the k-th MU at BS_2 can be evaluated as

$$R_k = \log_2\left(1 + \frac{P_{T,k}|\upsilon\Upsilon_k|^2}{\sigma^2}\right). \tag{5.7}$$

5.4 Problem Formulation

Defining $\boldsymbol{P_T} \triangleq \Big[P_{T,1}, P_{T,2}, \ldots, P_{T,K}\Big]^T$, $\boldsymbol{T_{cm}} \triangleq \Big[T_{cm,1}, T_{cm,2}, \ldots, T_{cm,K}\Big]^T$, $\boldsymbol{\omega} \triangleq \Big[\omega_1, \omega_2, \ldots, \omega_N\Big]^T$, and $\delta = 1 - \mu$. Our goal is to minimize the total transmit power of MUs by jointly optimizing the transmit power of MUs $\boldsymbol{P_T}$, CPU cycle frequency of MUs $\boldsymbol{\omega}$, PS of RIS $\boldsymbol{\psi}$, the transmission time of MUs $\boldsymbol{T_{cm}}$, power splitting ratios δ and μ, and aggregation beamforming υ, stated as

$$\min_{\substack{\boldsymbol{P_T},\boldsymbol{\omega},\delta,\boldsymbol{\psi},\\ \boldsymbol{T_{cm}},\mu,\upsilon}} \quad \sum_{k\in\mathcal{K}} P_{T,k} \tag{5.8a}$$

$$\text{s. t.} \quad E_{cp}^{(k)}(\omega_k) \leq \delta P_{EH}(\boldsymbol{\psi})\tau, \forall k \in \mathcal{K}, \tag{5.8b}$$

$$E_{cm}^{(k)}(P_{T,k}, T_{cm,k}) \leq \mu P_{EH}(\boldsymbol{\psi})\tau, \forall k \in \mathcal{K}, \tag{5.8c}$$

$$T_{cm,k} BR_k(P_{T,k}, \upsilon) \geq \Theta_k, \forall k \in \mathcal{K}, \tag{5.8d}$$

$$M_k T_{cp,k}(\omega_k) + T_{cm,k} = \tau, \forall k \in \mathcal{K}, \tag{5.8e}$$

$$\omega_{\min} \leq \omega_k \leq \omega_{\max}, \forall k \in \mathcal{K}, \tag{5.8f}$$

$$\delta + \mu = 1, \tag{5.8g}$$

$$|\upsilon|^2 = 1, \tag{5.8h}$$

$$|\psi_n| = 1, \forall n \in \mathcal{N}. \tag{5.8i}$$

In the above problem, (5.8b) and (5.8c) imply that the energy consumed by local model computation and communication at the k-th MU should be less than its corresponding harvested energy. Eq. (5.8d) ensures that the transmission rate of the k-th MU is greater than or equal to the required data size Θ_k. Constraint (5.8e) ensures that each global round should be finished within the time frame τ, where M_k denotes the required number of local iterations at the k-th MU. The CPU frequency of the k-th MU is specified in (5.8f), where $\omega_{\min}$ and $\omega_{\max}$ denote the minimum and maximum CPU frequency of the k-th MU, respectively. Finally, (5.8h) and (5.8i) imply that the aggregation beamforming has unit power and unit-modulus constraint at the RIS, respectively. It is worth noting that problem (5.8) is non-convex and challenging to solve, due to the non-convexity nature of constraints (5.8c)-(5.8e), (5.8h), (5.8i) and the coupling of multiple optimization variables.

5.5 Proposed Solution

Assuming an iterative algorithm based on the inner approximation (IA) framework, let $(\boldsymbol{P_T}^{(\kappa)}, \boldsymbol{\psi}^{(\kappa)}, \boldsymbol{T_{cm}}^{(\kappa)}, \upsilon^{(\kappa)})$ be the feasible point for (5.8) that is obtained from the $(\kappa-1)$-th round. In this section, an alternating algorithm is proposed to solve (5.8), i.e., at the iteration $(\kappa+1)$ solving (5.8) to find the optimal solutions $\boldsymbol{P_T}^{\star} := \boldsymbol{P_T}^{(\kappa+1)}, \boldsymbol{\omega}^{\star} := \boldsymbol{\omega}^{(\kappa+1)}, \delta^{\star} := \delta^{(\kappa+1)}, \boldsymbol{T_{cm}}^{\star} := \boldsymbol{T_{cm}}^{(\kappa+1)}, \mu^{\star} := \mu^{(\kappa+1)}$ for given $(\boldsymbol{P_T}^{(\kappa)}, \boldsymbol{\psi}^{(\kappa)}, \boldsymbol{T_{cm}}^{(\kappa)}, \upsilon^{(\kappa)})$, then finding the optimal solution $\upsilon^{\star} := \upsilon^{(\kappa+1)}$ for given $(\boldsymbol{P_T}^{(\kappa+1)}, \boldsymbol{T_{cm}}^{(\kappa+1)}, \upsilon^{(\kappa)})$, followed by finding the optimal solution $\boldsymbol{\psi}^{\star} := \boldsymbol{\psi}^{(\kappa+1)}$ for given $(\boldsymbol{P_T}^{(\kappa+1)}, \boldsymbol{\psi}^{(\kappa)}, \boldsymbol{T_{cm}}^{(\kappa+1)}, \boldsymbol{\omega}^{(\kappa+1)}, \delta^{(\kappa+1)}, \mu^{(\kappa+1)})$.

5.5.1 Transmit Power Optimization

At iteration $(\kappa+1)$, problem (5.8) for given $(\boldsymbol{P_T}^{(\kappa)}, \boldsymbol{\psi}^{(\kappa)}, \boldsymbol{T_{cm}}^{(\kappa)}, \upsilon^{(\kappa)})$ can be expressed as

$$\min_{\boldsymbol{P_T}, \boldsymbol{\omega}, \delta, \boldsymbol{T_{cm}}, \mu} \quad \sum_{k \in \mathcal{K}} P_{T,k} \tag{5.9a}$$

$$\text{s. t.} \quad (5.8\text{b}) - (5.8\text{g}). \tag{5.9b}$$

It is noted that the constraints (5.8c), (5.8d), and (5.8e) are non-convex. In the following, (5.8c) is convexified as follows:

$$0.5 \left(\frac{T_{cm,k}^{(\kappa)}}{P_{T,k}^{(\kappa)}} P_{T,k}^2 + \frac{P_{T,k}^{(\kappa)}}{T_{cm,k}^{(\kappa)}} T_{cm,k}^2 \right) \leq \mu \eta P_{\text{BS}_1} \left| q_k \left(\boldsymbol{\psi}^{(\kappa)} \right) \right|^2 \tau, \tag{5.10}$$

where $P_{T,k} T_{cm,k} \leq 0.5 \left(\frac{T_{cm,k}^{(\kappa)}}{P_{T,k}^{(\kappa)}} P_{T,k}^2 + \frac{P_{T,k}^{(\kappa)}}{T_{cm,k}^{(\kappa)}} T_{cm,k}^2 \right)$, $\forall k \in \mathcal{K}$.

Next, (5.8d) is rewritten as follows:

$$T_{cm,k}^{(\kappa)} \ln\left(1+\frac{\left|\upsilon^{(\kappa)}\Upsilon_k\right|^2 P_{T,k}^{(\kappa)}}{\sigma^2}\right)\left(2-\frac{T_{cm,k}^{(\kappa)}}{T_{cm,k}}\right)+\frac{T_{cm,k}^{(\kappa)}\left|\upsilon^{(\kappa)}\Upsilon_k\right|^2 P_{T,k}^{(\kappa)}}{\sigma^2+\left|\upsilon^{(\kappa)}\Upsilon_k\right|^2 P_{T,k}^{(\kappa)}}\left(1-\frac{P_{T,k}^{(\kappa)}}{P_{T,k}}\right)\geq\frac{\Theta_k \ln 2}{B}, \tag{5.11}$$

$\forall k \in \mathcal{K}$, which is equivalent to

$$(5.11) \Leftrightarrow \begin{cases} T_{cm,k}^{(\kappa)} \ln\left(1+\dfrac{\left|\upsilon^{(\kappa)}\Upsilon_k\right|^2 P_{T,k}^{(\kappa)}}{\sigma^2}\right)\left(2-T_{cm,k}^{(\kappa)}\tilde{T}_{cm,k}\right)+\dfrac{T_{cm,k}^{(\kappa)}\left|\upsilon^{(\kappa)}\Upsilon_k\right|^2 P_{T,k}^{(\kappa)}}{\sigma^2+\left|\upsilon^{(\kappa)}\Upsilon_k\right|^2 P_{T,k}^{(\kappa)}} & \\ \times\left(1-P_{T,k}^{(\kappa)}\tilde{P}_{T,k}\right)\geq\dfrac{\Theta_k \ln 2}{B}, & (5.12a) \\ T_{cm,k}\tilde{T}_{cm,k}\geq 1, & (5.12b) \\ P_{T,k}\tilde{P}_{T,k}\geq 1, & (5.12c) \end{cases}$$

where $\tilde{\boldsymbol{T}}_{\boldsymbol{cm}} \triangleq\left[\tilde{T}_{cm,1},\tilde{T}_{cm,2},\ldots,\tilde{T}_{cm,K}\right]^T$ and $\tilde{\boldsymbol{P}}_{\boldsymbol{T}} \triangleq\left[\tilde{P}_{T,1},\tilde{P}_{T,2},\ldots,\tilde{P}_{T,K}\right]^T$ are new introduced variables, with $\tilde{T}_{cm,k}\geq\frac{1}{T_{cm,k}}$ and $\tilde{P}_{T,k}\geq\frac{1}{P_{T,k}}$, $\forall k\in\mathcal{K}$. Constraints (5.12b) and (5.12c) can be further expressed as the following second-order cone (SOC) constraints, for $\forall k\in\mathcal{K}$,

$$0.25\left(T_{cm,k}+\tilde{T}_{cm,k}\right)^2\geq 0.25\left(T_{cm,k}-\tilde{T}_{cm,k}\right)^2+1, \tag{5.13}$$

$$0.25\left(P_{T,k}+\tilde{P}_{T,k}\right)^2\geq 0.25\left(P_{T,k}-\tilde{P}_{T,k}\right)^2+1. \tag{5.14}$$

Similarly, constraint (5.8e) can be equivalently rewritten as

$$(5.8e) \Leftrightarrow \begin{cases} M_k c_k S\tilde{\omega}_k+T_{cm,k}=\tau, & (5.15a) \\ 0.25\left(\omega_k+\tilde{\omega}_k\right)^2\geq 0.25\left(\omega_k-\tilde{\omega}_k\right)^2+1, & (5.15b) \end{cases}$$

where $\tilde{\boldsymbol{\omega}} \triangleq \left[\tilde{\omega}_1, \tilde{\omega}_2, \ldots, \tilde{\omega}_K\right]^T$ is a new introduced variable, with $\tilde{\omega}_k \geq \frac{1}{\omega_k}$, $\forall k \in \mathcal{K}$.

The equivalent convex problem of (5.9) for iteration $(\kappa+1)$ is given by

$$\min_{\substack{\boldsymbol{P_T},\boldsymbol{\omega},\delta,\\ \boldsymbol{T_{cm}},\mu,\tilde{\boldsymbol{P}}_{\boldsymbol{T}},\\ \tilde{\boldsymbol{T}}_{\boldsymbol{cm}},\tilde{\boldsymbol{\omega}}}} \quad \sum_{k\in\mathcal{K}} P_{T,k} \tag{5.16a}$$

$$\text{s. t.} \quad \frac{\nu_k c_k S}{2}\omega_k^2 \leq \delta\eta P_{\mathrm{BS}_1}\left|q_k\left(\boldsymbol{\psi}^{(\kappa)}\right)\right|^2 \tau, \forall k \in \mathcal{K}, \tag{5.16b}$$

$$(5.8\text{f}), (5.8\text{g}), (5.10), (5.12\text{a}), (5.13), (5.14), (5.15\text{a}), (5.15\text{b}), \tag{5.16c}$$

$$0 < \delta, 0 < \mu, 0 \leq P_{T,k}, 0 \leq T_{cm,k}, \forall k \in \mathcal{K}. \tag{5.16d}$$

5.5.2 Aggregation Beamforming Optimization

Since (5.8h) is a non-convex constraint, it is relaxed as $|\upsilon|^2 \leq 1$.

At iteration $(\kappa+1)$, the following approximate convex problem is solved for given $(\boldsymbol{P_T}^{(\kappa+1)}, \boldsymbol{T_{cm}}^{(\kappa+1)}, \upsilon^{(\kappa)})$:

$$\max_{\upsilon} \quad \left(2\Re\left\{\left(\upsilon^{(\kappa)}\right)^* \upsilon\right\} - |\upsilon^{(\kappa)}|^2\right) - 1 \tag{5.17a}$$

$$\text{s. t.} \quad \frac{\left(2\Re\left\{\left(\upsilon^{(\kappa)}\right)^* \Upsilon_k\right\}\Re\left\{\upsilon^* \Upsilon_k\right\} - \left|\left(\upsilon^{(\kappa)}\right)^* \Upsilon_k\right|^2\right) P_{T,k}^{(\kappa+1)}}{\sigma^2} \geq 2^{\frac{\Theta_k}{BT_{cm,k}^{(\kappa+1)}}} - 1, \tag{5.17b}$$

$$|\upsilon|^2 \leq 1. \tag{5.17c}$$

5.5.3 Phase Shift Optimization

Since (5.8i) is a non-convex constraint, it is relaxed as $|\psi_n|^2 \leq 1, \forall n \in \mathcal{N}$.

At iteration $(\kappa+1)$, the following approximate convex problem is solved for given

$(\boldsymbol{P_T}^{(\kappa+1)}, \boldsymbol{\psi}^{(\kappa)}, \boldsymbol{T_{cm}}^{(\kappa+1)}, \boldsymbol{\omega}^{(\kappa+1)}, \delta^{(\kappa+1)}, \mu^{(\kappa+1)})$:

$$\max_{\boldsymbol{\psi}} \quad \sum_{n\in\mathcal{N}} \left(2\Re\left\{\left(\psi_n^{(\kappa)}\right)^* \psi_n\right\} - |\psi_n^{(\kappa)}|^2\right) - N \tag{5.18a}$$

$$\text{s. t.} \quad \frac{\nu_k c_k S\left(\omega_k^{(\kappa+1)}\right)^2}{2} \leq \delta^{(\kappa+1)} \eta P_{\mathrm{BS}_1} \varphi_k^{(\kappa)}(\boldsymbol{\psi})\, \tau, \forall k \in \mathcal{K}, \tag{5.18b}$$

$$P_{T,k}^{(\kappa+1)} T_{cm,k}^{(\kappa+1)} \leq \mu^{(\kappa+1)} \eta P_{\mathrm{BS}_1} \varphi_k^{(\kappa)}(\boldsymbol{\psi})\, \tau, \forall k \in \mathcal{K}, \tag{5.18c}$$

$$|\psi_n|^2 \leq 1, \forall n \in \mathcal{N}, \tag{5.18d}$$

where $\varphi_k^{(\kappa)}(\boldsymbol{\psi}) = \left(2\Re\left\{q_k^H\left(\boldsymbol{\psi}^{(\kappa)}\right) q_k(\boldsymbol{\psi})\right\} - \left|q_k\left(\boldsymbol{\psi}^{(\kappa)}\right)\right|^2\right)$.

The proposed alternating-based iterative algorithm for solving problem (5.8) is summarized in Algorithm 7.

Algorithm 7 Proposed Alternating-based Iterative Algorithm to Solve Problem (5.8)

Initialization: Set $\kappa := 0$ and generate an initial feasible point $(\boldsymbol{P_T}^{(0)}, \boldsymbol{\psi}^{(0)}, \boldsymbol{T_{cm}}^{(0)}, \upsilon^{(0)})$.
repeat
Given $(\boldsymbol{P_T}^{(\kappa)}, \boldsymbol{\psi}^{(\kappa)}, \boldsymbol{T_{cm}}^{(\kappa)}, \upsilon^{(\kappa)})$, solve the convex problem (5.16) to find the set of optimal solutions $\{\boldsymbol{P_T}^\star, \boldsymbol{\omega}^\star, \delta^\star, \boldsymbol{T_{cm}}^\star, \mu^\star\}$ and update $\boldsymbol{P_T}^{(\kappa+1)} := \boldsymbol{P_T}^\star, \boldsymbol{\omega}^{(\kappa+1)} := \boldsymbol{\omega}^\star, \delta^{(\kappa+1)} := \delta^\star, \boldsymbol{T_{cm}}^{(\kappa+1)} := \boldsymbol{T_{cm}}^\star, \mu^{(\kappa+1)} := \mu^\star$;
Given $(\boldsymbol{P_T}^{(\kappa+1)}, \boldsymbol{T_{cm}}^{(\kappa+1)}, \upsilon^{(\kappa)})$, solve the convex problem (5.17) to find the optimal solution $\upsilon^\star$ and update $\upsilon^{(\kappa+1)} := \upsilon^\star$;
Given $(\boldsymbol{P_T}^{(\kappa+1)}, \boldsymbol{\psi}^{(\kappa)}, \boldsymbol{T_{cm}}^{(\kappa+1)}, \boldsymbol{\omega}^{(\kappa+1)}, \delta^{(\kappa+1)}, \mu^{(\kappa+1)})$, solve the convex problem (5.18) to find the optimal solution $\boldsymbol{\psi}^\star$ and update $\boldsymbol{\psi}^{(\kappa+1)} := \boldsymbol{\psi}^\star$;
Set $\kappa := \kappa + 1$;
until Convergence
Ouput: $(\boldsymbol{P_T}^\star, \boldsymbol{\omega}^\star, \delta^\star, \boldsymbol{\psi}^\star, \boldsymbol{T_{cm}}^\star, \mu^\star, \upsilon^\star)$

The per-iteration computational complexity of solving (5.16), (5.17), and (5.18) is $\mathcal{O}\Big((6K+2)^2(8K+1)^{2.5} + (8K+1)^{3.5}\Big)$, $\mathcal{O}\Big((K+1)^{3.5}\Big)$, and $\mathcal{O}\Big((2K+N)^{3.5}\Big)$, respectively.

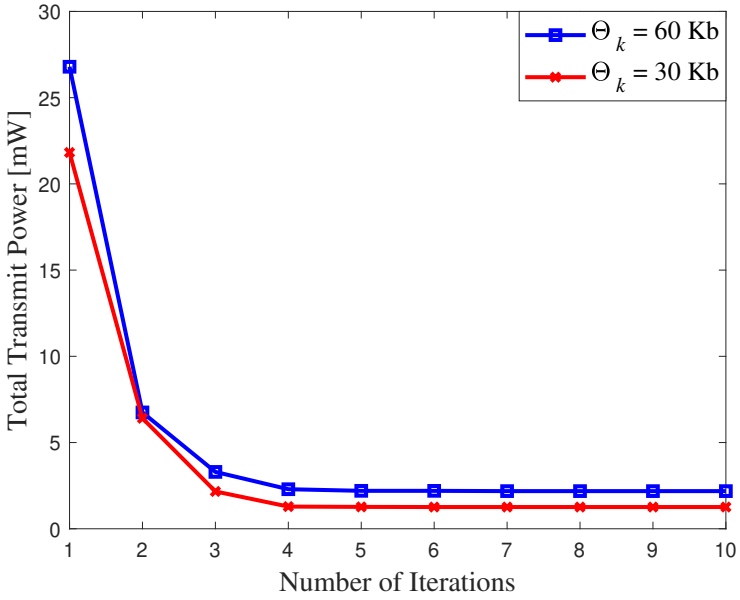

Fig. 5.2: Convergence of Algorithm 7 with different values of Θ_k.

5.6 Numerical Results

This section considers a 2-D scenario, in which two BSs and one RIS are located at (0, 20 m), (50 m, 20 m), and (20 m, 0), respectively. The total number of MUs K is 8, which are randomly distributed within a circular disc with the center (30 m, 10 m) and a radius of 1 m. Without loss of generality, it is assumed that the system bandwidth B is 20 MHz, the transmit power of BS_1 is 10 W, the energy harvesting efficiency η is 0.9, and the number of RIS REs N is 64. For local computation, the maximum and minimum CPU frequencies $\omega_{\max}$ and $\omega_{\min}$ are 1.5 GHz and 0.3 GHz, respectively, for all users [11]. The required data size Θ_k is set to 30 kbits, the coefficient of computing chip ν_k is 2×10^{-28}, and the local data S and the number of CPU cycles c_k are assumed to be 1000 bits and 10^4, respectively. The maximum number of local iterations at the k-th MU M_k is 4, and the time frame τ is set to 8 s. All simulation results are generated by averaging over 1000 different random channel realizations.

Fig. 5.2 shows the convergence behavior of Algorithm 7. It is clear that Algorithm 7

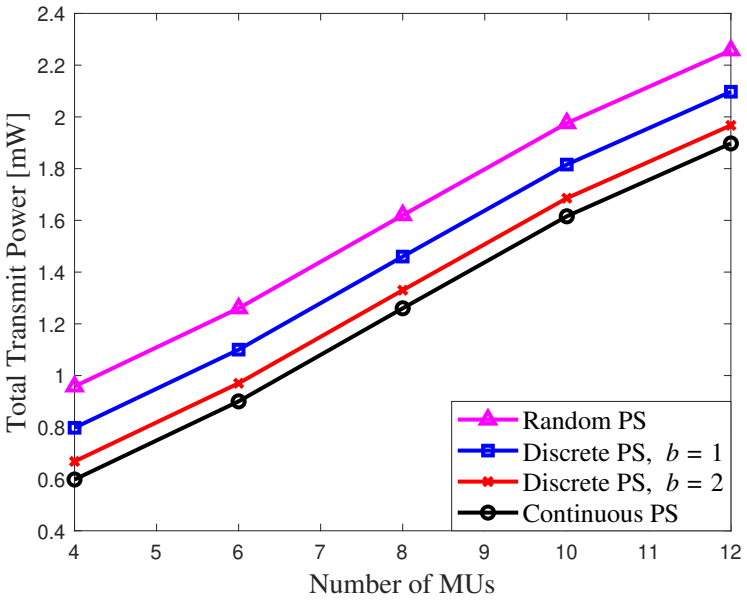

Fig. 5.3: Total transmit power of participating MUs versus the numbers of MUs.

needs around 5 iterations to reach the optimal value of the total transmit power of participating MUs. Besides, increasing Θ_k requires more total transmit power of participating MUs.

In Fig. 5.3, this power is illustrated versus the number of MUs, for different phase selection schemes, i.e., optimized, discrete, and random PS. Not surprisingly, the total transmit power of the participating MUs increases with the number of MUs. Additionally, optimized continuous PS achieves a better performance compared to the discrete and random PS cases.

Figs. 5.4 and 5.5 plot the total transmit power versus the number of RIS elements. As expected, increasing N results in lower total transmit power of all devices. This is because more power can be harvested by all devices, which increases the harvested power used for model computation and transmission. The increase in the harvested power leads to the decrease in the time required for model computation at all devices, which allows the devices have more time for model transmission. Further, increased total transmit power

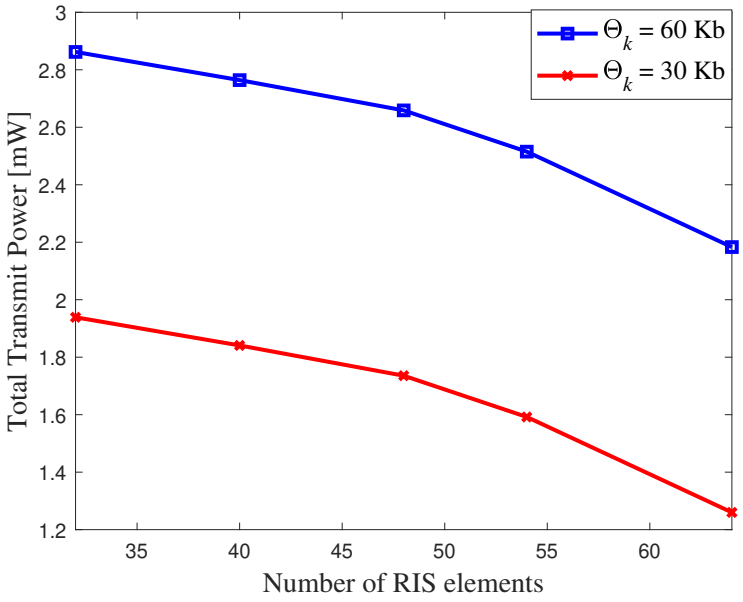

Fig. 5.4: Total transmit power of participating MUs versus the number of RIS REs with different values of Θ_k.

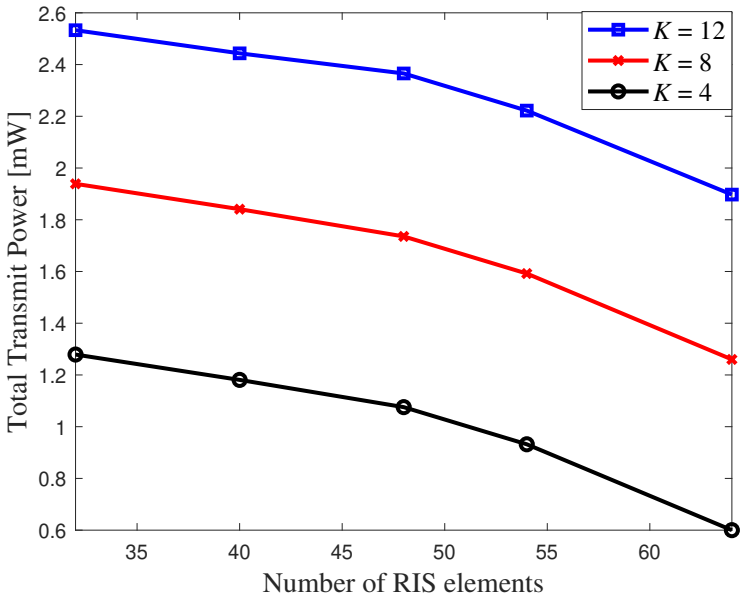

Fig. 5.5: Total transmit power of participating MUs versus the number of RIS REs with different numbers of MUs.

of participating MUs is needed for higher Θ_k.

5.7 Conclusion

This chapter has considered the total transmit power minimization problem of FL-based wireless networks with the assistance of the RIS. It involves a joint optimization of the transmission time, power control, and the RIS's phase shifts, and is formulated as a non-convex problem. To solve this problem, this chapter has developed an alternating descent algorithm based on the IA framework, which converges at least to a locally optimal solution. Numerical results have verified the quick convergence of the proposed algorithm and the benefit of using RIS.

References

[1] F. Musumeci *et al.*, "An overview on application of machine learning techniques in optical networks," *IEEE Commun. Surveys & Tuts.*, vol. 21, no. 2, pp. 1383–1408, Nov. 2018.

[2] S. Naser *et al.*, "Towards federated learning-enabled visible light communication in 6G systems," *arXiv preprint arXiv:2110.03319*, Oct. 2021.

[3] W. Y. B. Lim *et al.*, "Federated learning in mobile edge networks: A comprehensive survey," *IEEE Commun. Surveys & Tuts.*, vol. 22, no. 3, pp. 2031–2063, Apr. 2020.

[4] X. Wang, Y. Chen, and O. A. Dobre, "Federated learning for anomaly detection: A case of real-world energy storage deployment," in *Proc. IEEE Inter. Conf. Commun. (ICC)*, May 2022, pp. 1–6.

[5] H. Kim, J. Park, M. Bennis, and S.-L. Kim, "Blockchained on-device federated learning," *IEEE Commun. Lett.*, vol. 24, no. 6, pp. 1279–1283, June 2020.

[6] Y. Lu *et al.*, "Blockchain and federated learning for privacy-preserved data sharing in industrial IoT," *IEEE Trans. Industrial Informatics*, vol. 16, no. 6, pp. 4177–4186, June 2020.

[7] Y. Liu *et al.*, "Federated learning in the sky: Aerial-ground air quality sensing framework with UAV swarms," *IEEE Internet Things J.*, vol. 8, no. 12, pp. 9827–9837, June 2021.

[8] K. Li *et al.*, "Distributed network intrusion detection system in satellite-terrestrial integrated networks using federated learning," *IEEE Access*, vol. 8, pp. 214 852–214 865, Dec. 2020.

[9] S. Zarandi and H. Tabassum, "Federated double deep q-learning for joint delay and energy minimization in iot network," in *Proc. IEEE Int. Conf. Commun. Workshops (ICC Workshops)*, June 2021, pp. 1–6.

[10] X. Mo and J. Xu, "Energy-efficient federated edge learning with joint communication and computation design," *J. Communications and Information Networks*, vol. 6, no. 2, pp. 110–124, June 2021.

[11] H.-V. Tran *et al.*, "Lightwave power transfer for federated learning-based wireless networks," *IEEE Commun. Lett.*, vol. 24, no. 7, pp. 1472–1476, July 2020.

[12] Q. Zeng, Y. Du, and K. Huang, "Wirelessly powered federated edge learning: Optimal tradeoffs between convergence and power transfer," *IEEE Trans. Wireless Commun.*, vol. 21, no. 1, pp. 680–695, Jan. 2022.

[13] Z. Wang *et al.*, "Wireless-powered over-the-air computation in intelligent reflecting surface-aided IoT networks," *IEEE Internet Things J.*, vol. 8, no. 3, pp. 1585–1598, Feb. 2021.

[14] X. Li, G. Zhu, Y. Gong, and K. Huang, "Wirelessly powered data aggregation for IoT via over-the-air function computation: Beamforming and power control," *IEEE Trans. Wireless Commun.*, vol. 18, no. 7, pp. 3437–3452, July 2019.

[15] C. Pan *et al.*, "Intelligent reflecting surface aided MIMO broadcasting for simultaneous wireless information and power transfer," *IEEE J. Sel. Areas Commun.*, vol. 38, no. 8, pp. 1719–1734, Aug. 2020.

[16] B. McMahan *et al.*, "Communication-efficient learning of deep networks from decentralized data," in *Proc. 20th Int. Conf. Artificial Intelligence and Statistics*, Apr. 2017, pp. 1273–1282.

[17] N. H. Tran *et al.*, "Federated learning over wireless networks: Optimization model design and analysis," in *Proc. IEEE Conf. Comput. Commun. (INFOCOM)*, Apr. 2019, pp. 1387–1395.

[18] R. Jin, X. He, and H. Dai, "Communication efficient federated learning with energy awareness over wireless networks," *arXiv preprint arXiv:2004.07351*, Sep. 2021.

Chapter 6

Transmission Rate Maximization in RIS-Assisted FD ISAC Networks

6.1 Abstract

In this chapter, we explore the application of RIS in the ISAC network, where a FD multi-antenna BS concurrently detects a target and communicates with a UE. The objective is to maximize the UE's transmission rate by jointly optimizing the BS's transmit beamforming, UE's transmit power, and RIS's phase shifts, while satisfying the condition on the minimum required sensing power. This chapter develops a block coordinate ascend-based iterative algorithm to solve the formulated problem, which guarantees the convergence to at least a local optimum. Numerical results show the efficiency of the proposed solution as well as the trade-off between the UE's transmission rate and the required sensing power, along with the efficiency of employing RIS.

6.2 Introduction

Sensing is considered an important task of the next-generation cellular networks [1]. Many emerging mobile applications, such as smart manufacturing and industrial Internet-of-Things, not only need high-rate transmission with low latency and high reliability, but also require location information with high accuracy. In order to offer better performance and efficiently utilize spectrum, energy and hardware resources, integrating sensing and communication functions into a single network has become a favorable approach. By jointly optimizing wireless resources, waveform and signal processing flow, a significant performance gain can be achieved in ISAC networks [2].

In addition to the ISAC technology, the RIS has also received significant attention from both academia and industry [3]. By fine-tuning the phase shift matrix, RIS is able to concurrently modify communication and sensing channels, which is beneficial for ISAC networks [4, 5]. Specifically, RIS can be used to decrease the interference between the radar and communication systems [6, 7].

Incorporating FD radio into RIS-ISAC networks can provide great benefits owing to its potential to doubling the spectral efficiency by enabling transceivers to concurrently transmit and receive data in the same frequency band [4, 8]. In [8], RIS was leveraged to enhance the performance of localization and information retrieval for the FD-ISAC system, in which a FD-BS simultaneously communicates and senses the position of UE.

To reap all the above benefits, this chapter studies the joint active and passive beamforming (BF) design for a RIS-assisted ISAC system, where a FD multi-antenna BS simultaneously communicates with a single antenna UE and detects a target. The BS's transmit beamforming, UE's transmit power, and RIS's reflection coefficients are jointly optimized to maximize the UE's transmission rate subject to the minimum sensing power constraint, transmit power budgets of BS and UE, and unit modulus property of the reflecting elements. The ensuing problem is strongly non-convex and the strong coupling

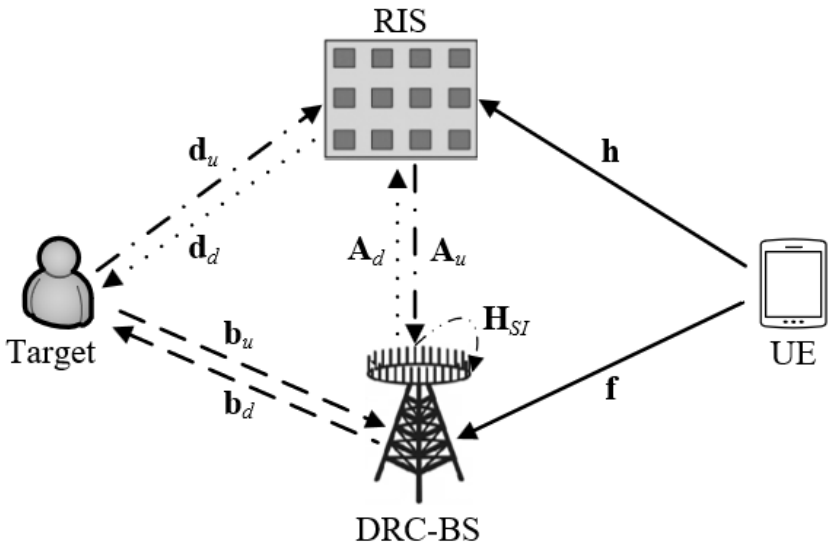

Fig. 6.1: The RIS-ISAC system.

between variables makes it NP-hard. To solve this problem more effectively, this chapter adopts a block coordinate ascend (BCA) algorithm to transform it into two tractable sub-problems and develop newly approximated functions to solve them in an iterative fashion. The proposed solution is compared with the maximum ratio transmission (MRT) case, which serves as a benchmark. Simulation results show the notable performance gain achieved with the assistance of RIS, the trade-off between the UE's transmission rate and the required sensing power, and the enhanced performance of the proposed solution compared to the MRT.

6.3 System Model and Problem Formulation

6.3.1 System Model

This chapter considers an RIS-ISAC system, as depicted in Fig. 6.1, which consists of a dual-functional radar communication (DRC)-BS equipped with M_t transmit antennas and M_r receive antennas; a single-antenna user; an RIS composed of the set $\mathcal{K} \triangleq \{1, 2, \cdots, K\}$

of K elements; and a sensing target. It is supposed that the BS and UE have the knowledge of the location of the RIS [9]. The UE's location can be either obtained by global positioning system or estimated by uplink signals [9]. Let denote by $\mathbf{f} \in \mathbb{C}^{M_r \times 1}$, $\mathbf{h} \in \mathbb{C}^{1 \times K}$, $\mathbf{A}_u \in \mathbb{C}^{M_r \times K}$, $\mathbf{b}_d \in \mathbb{C}^{M_t \times 1}$, $\mathbf{A}_d \in \mathbb{C}^{M_t \times K}$, $\mathbf{d}_d \in \mathbb{C}^{K \times 1}$, $\mathbf{b}_u \in \mathbb{C}^{M_r \times 1}$, $\mathbf{d}_u \in \mathbb{C}^{K \times 1}$, and $\mathbf{H} \in \mathbb{C}^{M_r \times M_t}$ the channels (matrix/vector) from UE to DRC-BS, from UE to RIS, from RIS to DRC-BS, from DRC-BS to target, from DRC-BS to RIS, from RIS to target, from target to DRC-BS, from target to RIS, and the self-interference link of DRC-BS, respectively. The phase shift matrix of RIS is represented by $\mathbf{\Phi} \in \mathbb{C}^{K \times K}$. $\xi \in \mathbb{R}^+$ and $\boldsymbol{v} \in \mathbb{C}^{M_t \times 1}$ are also denoted as the transmit power of the UE and the transmit beamforming of DRC-BS, respectively. The signal received at the DRC-BS can be expressed as

$$\begin{aligned}\mathbf{y}\left(\boldsymbol{\theta}, \xi, \boldsymbol{v}\right) &= \left(\mathbf{f} + \mathbf{A}_u \mathbf{\Phi} \mathbf{h}^H\right) \sqrt{\xi} x_c + \mathbf{H} \boldsymbol{v} x_s + \left(\mathbf{b}_u + \mathbf{A}_u \mathbf{\Phi} \mathbf{d}_u\right) \left(\mathbf{b}_d^H + \mathbf{d}_d^H \mathbf{\Phi} \mathbf{A}_d^H\right) \boldsymbol{v} x_s + \mathbf{n}_n \\ &= \left(\mathbf{f} + \mathbf{A}_u \left(\mathbf{h}\right) \boldsymbol{\theta}\right) \sqrt{\xi} x_c + \left(\mathbf{b}_u + \mathbf{A}_u \left(\mathbf{d}_u\right) \boldsymbol{\theta}\right) \left(\mathbf{b}_d^H + \boldsymbol{\theta}^T \left(\mathbf{d}_d\right) \mathbf{A}_d^H\right) \boldsymbol{v} x_s + \mathbf{H} \boldsymbol{v} x_s + \mathbf{n}_n,\end{aligned} \tag{6.1}$$

where x_c and x_s are the communication and sensing signals, respectively, and $\mathbf{n}_n \sim \mathcal{CN}(0, \sigma^2)$ is the additive white Gaussian noise (AWGN) with zero-mean and variance σ^2. To simplify the mathematical notations, this section denotes $\mathbf{\Phi} \triangleq (e^{j\psi_1}, e^{j\psi_2}, \ldots, e^{j\psi_K}) = (\theta_1, \theta_2, \ldots, \theta_K)$, $\boldsymbol{\theta} = \left[\theta_1, \theta_2, \ldots, \theta_K\right]^T$, $\hat{\mathbf{f}}(\boldsymbol{\theta}) = \mathbf{f} + \mathbf{A}_u \left(\mathbf{h}\right) \boldsymbol{\theta}$, and $\hat{\mathbf{b}}^H(\boldsymbol{\theta}) = \left(\mathbf{b}_u + \mathbf{A}_u \left(\mathbf{d}_u\right) \boldsymbol{\theta}\right) \times \left(\mathbf{b}_d^H + \boldsymbol{\theta}^T \left(\mathbf{d}_d\right) \mathbf{A}_d^H\right) = \hat{\mathbf{b}}_u(\boldsymbol{\theta}) \hat{\mathbf{b}}_d^H(\boldsymbol{\theta})$. As a result, (6.1) is rewritten as $\mathbf{y}\left(\boldsymbol{\theta}, \xi, \boldsymbol{v}\right) = \hat{\mathbf{f}}(\boldsymbol{\theta}) \sqrt{\xi} x_c + \hat{\mathbf{b}}^H(\boldsymbol{\theta}) \boldsymbol{v} x_s + \mathbf{H} \boldsymbol{v} x_s + \mathbf{n}_n$. The signal-to-interference-plus-noise ratio (SINR) of UE at DRC-BS is given as

$$\gamma_c\left(\boldsymbol{\theta}, \xi, \boldsymbol{v}\right) = \frac{\left\|\hat{\mathbf{f}}(\boldsymbol{\theta})\right\|^2 \xi}{\left\|\hat{\mathbf{b}}^H(\boldsymbol{\theta}) \boldsymbol{v}\right\|^2 + \left\|\mathbf{H} \boldsymbol{v}\right\|^2 + \sigma^2}. \tag{6.2}$$

6.3.2 Problem Formulation

This chapter is interested in maximizing the UE's transmission rate subject to the required sensing power at the DRC-BS by jointly optimizing the involved variables $(\xi, \boldsymbol{v}, \boldsymbol{\theta})$. The optimization problem is formulated as

$$\max_{\xi, \boldsymbol{v}, \boldsymbol{\theta}} \quad \mathcal{R}(\xi, \boldsymbol{v}, \boldsymbol{\theta}) \triangleq \ln\left(1 + \gamma_c\left(\boldsymbol{\theta}, \xi, \boldsymbol{v}\right)\right) \tag{6.3a}$$

$$\text{s. t.} \quad \xi \leq P_{UE}^{\max} \tag{6.3b}$$

$$\|\boldsymbol{v}\|^2 \leq P_{BS}^{\max} \tag{6.3c}$$

$$\left\|\hat{\mathbf{b}}^H(\boldsymbol{\theta})\boldsymbol{v}\right\|^2 \geq P_{\text{sense}} \tag{6.3d}$$

$$|\theta_k| = 1, \forall k \in \mathcal{K}, \tag{6.3e}$$

where (6.3b) and (6.3c) indicate the power constraints at the UE and DRC-BS with the maximum transmit powers $P_{UE}^{\max}$ and $P_{BS}^{\max}$, respectively. Constraint (6.3d) describes the required sensing power at the DRC-BS with P_{sense} being the minimum sensing power. Finally, (6.3e) presents the RIS phase shift constraint. From (6.3d), the target's location can be estimated by the BS as long as the received signal strength of the echo probing signal is larger than or equal to the required sensing power.

6.4 Proposed Solution

The BCA approach is adopted and decoupled (6.3) into two sub-problems corresponding to $(\xi, \boldsymbol{v})$ and $\boldsymbol{\theta}$, each of which will be solved by the inner approximation (IA) method [10]. At iteration η, let $(\xi^{(\eta)}, \boldsymbol{v}^{(\eta)}, \boldsymbol{\theta}^{(\eta)})$ be the feasible point for (6.3) that is found from the $(\eta-1)$-th round. By BCA, problem (6.3) is solved to obtain the optimal solutions $(\xi^\star, \boldsymbol{v}^\star)$ for given $\boldsymbol{\theta}^{(\eta)}$, and then update $(\xi^{(\eta+1)} := \xi^\star, \boldsymbol{v}^{(\eta+1)} := \boldsymbol{v}^\star)$ to solve (6.3) with respect to $\boldsymbol{\theta}$.

6.4.1 Transmit Power and Beamforming Iteration

For a given $\boldsymbol{\theta}^{(\eta)}$, (6.3) is rewritten at iteration $\eta+1$ as:

$$\max_{\xi,\boldsymbol{v}} \quad \mathcal{R}(\xi,\boldsymbol{v},\boldsymbol{\theta}^{(\eta)}) \triangleq \ln\left(1+\frac{\left\|\hat{\mathbf{f}}(\boldsymbol{\theta}^{(\eta)})\right\|^2\xi}{\left\|\hat{\mathbf{b}}^H(\boldsymbol{\theta}^{(\eta)})\boldsymbol{v}\right\|^2+\left\|\mathbf{H}\boldsymbol{v}\right\|^2+\sigma^2}\right) \tag{6.4a}$$

$$\text{s. t.} \quad \xi \le P_{UE}^{\max} \tag{6.4b}$$

$$\|\boldsymbol{v}\|^2 \le P_{BS}^{\max} \tag{6.4c}$$

$$\left\|\hat{\mathbf{b}}^H(\boldsymbol{\theta}^{(\eta)})\boldsymbol{v}\right\|^2 \ge P_{\text{sense}}, \tag{6.4d}$$

where the objective (6.4a) is non-concave while (6.4d) is the non-convex constraint. The concave lower bound of (6.4a) can be found as [11, Eq. (62)]:

$$\begin{aligned}\ln\left(1+\frac{\left\|\hat{\mathbf{f}}(\boldsymbol{\theta}^{(\eta)})\right\|^2\xi}{\left\|\hat{\mathbf{b}}^H(\boldsymbol{\theta}^{(\eta)})\boldsymbol{v}\right\|^2+\left\|\mathbf{H}\boldsymbol{v}\right\|^2+\sigma^2}\right) &\ge \ln\left(1+\frac{\left\|\hat{\mathbf{f}}(\boldsymbol{\theta}^{(\eta)})\right\|^2\xi^{(\eta)}}{\left\|\hat{\mathbf{b}}^H(\boldsymbol{\theta}^{(\eta)})\boldsymbol{v}^{(\eta)}\right\|^2+\left\|\mathbf{H}\boldsymbol{v}^{(\eta)}\right\|^2+\sigma^2}\right)\\ &+\frac{\left\|\hat{\mathbf{f}}(\boldsymbol{\theta}^{(\eta)})\right\|^2\xi^{(\eta)}}{\left\|\hat{\mathbf{b}}^H(\boldsymbol{\theta}^{(\eta)})\boldsymbol{v}^{(\eta)}\right\|^2+\left\|\mathbf{H}\boldsymbol{v}^{(\eta)}\right\|^2+\sigma^2+\left\|\hat{\mathbf{f}}(\boldsymbol{\theta}^{(\eta)})\right\|^2\xi^{(\eta)}}\\ &\times\left(2-\frac{\xi^{(\eta)}}{\xi}-\frac{\left\|\hat{\mathbf{b}}^H(\boldsymbol{\theta}^{(\eta)})\boldsymbol{v}\right\|^2+\left\|\mathbf{H}\boldsymbol{v}\right\|^2+\sigma^2}{\left\|\hat{\mathbf{b}}^H(\boldsymbol{\theta}^{(\eta)})\boldsymbol{v}^{(\eta)}\right\|^2+\left\|\mathbf{H}\boldsymbol{v}^{(\eta)}\right\|^2+\sigma^2}\right)\\ &:= \mathcal{R}^{(\eta)}(\xi,\boldsymbol{v}|\boldsymbol{\theta}^{(\eta)}).\end{aligned} \tag{6.5}$$

Next, the left-hand side (LHS) of (6.4d) is a quadratic function which can be innerly approximated as

$$2\Re\{(\boldsymbol{v}^{(\eta)})^H\hat{\mathbf{b}}(\boldsymbol{\theta}^{(\eta)})\hat{\mathbf{b}}^H(\boldsymbol{\theta}^{(\eta)})\boldsymbol{v}\}-\left\|\hat{\mathbf{b}}^H(\boldsymbol{\theta}^{(\eta)})\boldsymbol{v}^{(\eta)}\right\|^2 \ge P_{\text{sense}}. \tag{6.6}$$

In summary, the approximate convex program of (6.4) solved at iteration $\eta+1$ is expressed by

$$\max_{\xi,\boldsymbol{v}} \quad \mathcal{R}^{(\eta)}(\xi,\boldsymbol{v}|\boldsymbol{\theta}^{(\eta)}) \tag{6.7a}$$

$$\text{s. t.} \quad (6.4\text{b}),(6.4\text{c}),(6.6). \tag{6.7b}$$

6.4.2 Phase Shift Iteration

For given $(\xi^{(\eta+1)},\boldsymbol{v}^{(\eta+1)})$, (6.3) is rewritten at iteration $\eta+1$ as:

$$\max_{\boldsymbol{\theta}} \quad \mathcal{R}(\xi^{(\eta+1)},\boldsymbol{v}^{(\eta+1)},\boldsymbol{\theta}) \triangleq \ln\left(1+\frac{\left\|\hat{\mathbf{f}}(\boldsymbol{\theta})\right\|^2\xi^{(\eta+1)}}{\left\|\hat{\mathbf{b}}^H(\boldsymbol{\theta})\boldsymbol{v}^{(\eta+1)}\right\|^2+\left\|\mathbf{H}\boldsymbol{v}^{(\eta+1)}\right\|^2+\sigma^2}\right) \tag{6.8a}$$

$$\text{s. t.} \quad \left\|\hat{\mathbf{b}}^H(\boldsymbol{\theta})\boldsymbol{v}^{(\eta+1)}\right\|^2 \geq P_{\text{sense}} \tag{6.8b}$$

$$|\theta_k|=1,\forall k\in\mathcal{K}, \tag{6.8c}$$

where the objective (6.8a) is non-concave, while constraints (6.8b) and (6.8c) are non-convex. According to the Cauchy-Schwarz inequality, the first term in the denominator of (6.8a) can be upper bounded as

$$\begin{aligned}\left\|\hat{\mathbf{b}}^H(\boldsymbol{\theta})\boldsymbol{v}^{(\eta+1)}\right\|^2 &= \left\|\hat{\mathbf{b}}_u(\boldsymbol{\theta})\hat{\mathbf{b}}_d^H(\boldsymbol{\theta})\boldsymbol{v}^{(\eta+1)}\right\|^2\\ &\leq \left\|\hat{\mathbf{b}}_u(\boldsymbol{\theta})\right\|^2\left\|\hat{\mathbf{b}}_d^H(\boldsymbol{\theta})\boldsymbol{v}^{(\eta+1)}\right\|^2\\ &\leq t\zeta,\end{aligned} \tag{6.9}$$

where $t\in\mathbb{R}^+$ and $\zeta\in\mathbb{R}^+$ are newly introduced optimization variables, satisfying $\left\|\hat{\mathbf{b}}_u(\boldsymbol{\theta})\right\|^2\leq t$ and $\left\|\hat{\mathbf{b}}_d^H(\boldsymbol{\theta})\boldsymbol{v}^{(\eta+1)}\right\|^2\leq\zeta$. The product $t\zeta$ is convexified as $t\zeta\leq\frac{t^{(\eta)}\zeta^2}{2\zeta^{(\eta)}}+\frac{\zeta^{(\eta)}t^2}{2t^{(\eta)}}$.

Accordingly, the concave lower bound of (6.8a) is

$$\begin{aligned}\ln\left(1+\frac{\left\|\hat{\mathbf{f}}(\boldsymbol{\theta})\right\|^2\xi^{(\eta+1)}}{t\zeta+\left\|\mathbf{H}\boldsymbol{v}^{(\eta+1)}\right\|^2+\sigma^2}\right) &\geq \ln\left(1+\frac{\left\|\hat{\mathbf{f}}(\boldsymbol{\theta}^{(\eta)})\right\|^2\xi^{(\eta+1)}}{t^{(\eta)}\zeta^{(\eta)}+\left\|\mathbf{H}\boldsymbol{v}^{(\eta+1)}\right\|^2+\sigma^2}\right)\\ &+\frac{\left\|\hat{\mathbf{f}}(\boldsymbol{\theta}^{(\eta)})\right\|^2\xi^{(\eta+1)}}{t^{(\eta)}\zeta^{(\eta)}+\left\|\mathbf{H}\boldsymbol{v}^{(\eta+1)}\right\|^2+\sigma^2+\left\|\hat{\mathbf{f}}(\boldsymbol{\theta}^{(\eta)})\right\|^2\xi^{(\eta+1)}}\\ &\times\left(2-\frac{\left\|\hat{\mathbf{f}}(\boldsymbol{\theta}^{(\eta)})\right\|^2}{\left\|\hat{\mathbf{f}}(\boldsymbol{\theta})\right\|^2}-\frac{\frac{t^{(\eta)}\zeta^2}{2\zeta^{(\eta)}}+\frac{\zeta^{(\eta)}t^2}{2t^{(\eta)}}+\left\|\mathbf{H}\boldsymbol{v}^{(\eta+1)}\right\|^2+\sigma^2}{t^{(\eta)}\zeta^{(\eta)}+\left\|\mathbf{H}\boldsymbol{v}^{(\eta+1)}\right\|^2+\sigma^2}\right)\\ &\triangleq \mathcal{R}^{(\eta)}(\boldsymbol{\theta}|\xi^{(\eta+1)},\boldsymbol{v}^{(\eta+1)}).\end{aligned}\tag{6.10}$$

To convexify (6.8b), its LHS is firstly approximated as

$$\left\|\hat{\mathbf{b}}^H(\boldsymbol{\theta})\boldsymbol{v}^{(\eta+1)}\right\|^2\geq 2\Re\left\{\left(\hat{\mathbf{b}}^H(\boldsymbol{\theta}^{(\eta)})\boldsymbol{v}^{(\eta+1)}\right)^H\hat{\mathbf{b}}^H(\boldsymbol{\theta})\boldsymbol{v}^{(\eta+1)}\right\}-\left\|\hat{\mathbf{b}}^H(\boldsymbol{\theta}^{(\eta)})\boldsymbol{v}^{(\eta+1)}\right\|^2.\tag{6.11}$$

Then, the first term of the right-hand side of (6.11) is further rewritten as

$$\begin{aligned}2\Re\left\{\left(\hat{\mathbf{b}}^H(\boldsymbol{\theta}^{(\eta)})\boldsymbol{v}^{(\eta+1)}\right)^H\hat{\mathbf{b}}^H(\boldsymbol{\theta})\boldsymbol{v}^{(\eta+1)}\right\} &= 2\Re\left\{\left(\hat{\mathbf{b}}^H(\boldsymbol{\theta}^{(\eta)})\boldsymbol{v}^{(\eta+1)}\right)^H\mathbf{b}_u\mathbf{b}_d^H\boldsymbol{v}^{(\eta+1)}\right\}\\ &+2\Re\left\{\left(\hat{\mathbf{b}}^H(\boldsymbol{\theta}^{(\eta)})\boldsymbol{v}^{(\eta+1)}\right)^H\mathbf{b}_u\boldsymbol{\theta}^T(\mathbf{d}_d)\mathbf{A}_d^H\boldsymbol{v}^{(\eta+1)}\right\}\\ &+2\Re\left\{\left(\hat{\mathbf{b}}^H(\boldsymbol{\theta}^{(\eta)})\boldsymbol{v}^{(\eta+1)}\right)^H\mathbf{A}_u(\mathbf{d}_u)\boldsymbol{\theta}\mathbf{b}_d^H\boldsymbol{v}^{(\eta+1)}\right\}\\ &+2\Re\left\{\left(\hat{\mathbf{b}}^H(\boldsymbol{\theta}^{(\eta)})\boldsymbol{v}^{(\eta+1)}\right)^H\mathbf{A}_u(\mathbf{d}_u)\boldsymbol{\theta}\boldsymbol{\theta}^T(\mathbf{d}_d)\mathbf{A}_d^H\boldsymbol{v}^{(\eta+1)}\right\}\\ &\triangleq \mathcal{X}^{(\eta)}(\boldsymbol{\theta}|\boldsymbol{v}^{(\eta+1)})\\ &+2\Re\left\{\boldsymbol{\theta}^T(\mathbf{d}_d)\mathbf{A}_d^H\boldsymbol{v}^{(\eta+1)}\left(\hat{\mathbf{b}}^H(\boldsymbol{\theta}^{(\eta)})\boldsymbol{v}^{(\eta+1)}\right)^H\mathbf{A}_u(\mathbf{d}_u)\boldsymbol{\theta}\right\}\\ &=\mathcal{X}^{(\eta)}(\boldsymbol{\theta}|\boldsymbol{v}^{(\eta+1)})+2\Re\left\{\boldsymbol{\theta}^T\mathcal{Y}\boldsymbol{\theta}\right\},\end{aligned}\tag{6.12}$$

where $\mathcal{Y}\triangleq(\mathbf{d}_d)\mathbf{A}_d^H\boldsymbol{v}^{(\eta+1)}\left(\hat{\mathbf{b}}^H(\boldsymbol{\theta}^{(\eta)})\boldsymbol{v}^{(\eta+1)}\right)^H\mathbf{A}_u(\mathbf{d}_u)$. The last term of (6.12) is convexi-

fied as

$$2\Re\left\{\boldsymbol{\theta}^T\mathcal{Y}\boldsymbol{\theta}\right\} \geq 2\Re\left\{(\boldsymbol{\theta}^{(\eta)})^T\mathcal{Y}\boldsymbol{\theta} + \boldsymbol{\theta}^T\mathcal{Y}\boldsymbol{\theta}^{(\eta)} - (\boldsymbol{\theta}^{(\eta)})^T\mathcal{Y}\boldsymbol{\theta}^{(\eta)}\right\}. \tag{6.13}$$

From (6.11), (6.12) and (6.13), constraint (6.8b) is innerly approximated as follows:

$$\mathcal{X}^{(\eta)}(\boldsymbol{\theta}|\boldsymbol{v}^{(\eta+1)}) + 2\Re\Big\{(\boldsymbol{\theta}^{(\eta)})^T\mathcal{Y}\boldsymbol{\theta} + \boldsymbol{\theta}^T\mathcal{Y}\boldsymbol{\theta}^{(\eta)} - (\boldsymbol{\theta}^{(\eta)})^T\mathcal{Y}\boldsymbol{\theta}^{(\eta)}\Big\} - \left\|\hat{\mathfrak{b}}^H(\boldsymbol{\theta}^{(\eta)})\boldsymbol{v}^{(\eta+1)}\right\|^2 \geq P_{\text{sense}}. \tag{6.14}$$

Further, the unit-modulus constraint (6.8c) is relaxed by the following convex constraint:

$$|\theta_k|^2 \leq 1, \forall k \in \mathcal{K}, \tag{6.15}$$

which means that $\sum_{k\in\mathcal{K}}|\theta_k|^2 - K \leq 0$. To guarantee that constraint (6.8c) is satisfied at optimum, the following theorem is established.

Theorem 6.1. *The following penalized optimization problem is used to ensure the optimality of* (6.8)*:*

$$\max_{\boldsymbol{\theta}} \quad \mathcal{R}(\xi^{(\eta+1)}, \boldsymbol{v}^{(\eta+1)}, \boldsymbol{\theta}) + \varrho\Big(\sum_{k\in\mathcal{K}}|\theta_k|^2 - K\Big) \tag{6.16a}$$

$$\text{s. t.} \quad (6.8\text{b}), (6.15), \tag{6.16b}$$

where $\varrho > 0$ denotes a penalty parameter such that the objective and penalty terms become comparable.

Proof. Owing to constraint (6.15), the penalty term $\sum_{k\in\mathcal{K}}|\theta_k|^2 - K$ is always negative. A positive value of ϱ enables the uncertainties of the unit-modulus constraint to be penalized, which guarantees $\theta_k = 1$ at optimum. If ϱ is sufficiently large, (6.8) and (6.16) have the same optimal solution. The steps of a similar proof are found in [12, Appendix C]. □

Summing up, the approximate convex program of (6.8) solved at iteration $\eta+1$ is expressed by

$$\max_{\boldsymbol{\theta},t,\zeta} \quad \mathcal{R}^{(\eta)}(\xi^{(\eta+1)},\boldsymbol{v}^{(\eta+1)},\boldsymbol{\theta}) \triangleq \mathcal{R}^{(\eta)}(\boldsymbol{\theta}|\xi^{(\eta+1)},\boldsymbol{v}^{(\eta+1)}) + \varrho\left(\mathcal{P}^{(\eta)}(\boldsymbol{\theta}) - K\right) \tag{6.17a}$$

$$\text{s. t.} \quad \left\|\hat{\mathbf{b}}_u(\boldsymbol{\theta})\right\|^2 \leq t \tag{6.17b}$$

$$\left\|\hat{\mathbf{b}}_d^H(\boldsymbol{\theta})\boldsymbol{v}^{(\eta+1)}\right\|^2 \leq \zeta \tag{6.17c}$$

$$|\theta_k|^2 \leq 1, \forall k \in \mathcal{K} \tag{6.17d}$$

$$(6.14), \tag{6.17e}$$

where $\mathcal{P}^{(\eta)}(\boldsymbol{\theta}) \triangleq \sum_{k\in\mathcal{K}}\left(2\Re\{\left(\theta_k^{(\eta)}\right)^*\theta_k\} - |\theta_k^{(\eta)}|^2\right)$.

Algorithm 8 summarizes the BCA-based algorithm for solving (6.3).

Algorithm 8 Proposed BCA-based Iterative Algorithm to Solve (6.3)

Initialization: Set $\eta := 0$. Generate an initial feasible point $(\xi^{(0)},\boldsymbol{v}^{(0)},\boldsymbol{\theta}^{(0)},t^{(0)},\zeta^{(0)})$;
1: **repeat**
2: Given $\boldsymbol{\theta}^{(\eta)}$, solve (6.7) to obtain $(\xi^\star,\boldsymbol{v}^\star)$ and update $(\xi^{(\eta+1)},\boldsymbol{v}^{(\eta+1)}) := (\xi^\star,\boldsymbol{v}^\star)$;
3: Given $(\xi^{(\eta+1)},\boldsymbol{v}^{(\eta+1)})$, solve (6.17) to obtain $\boldsymbol{\theta}^\star$ and update $\boldsymbol{\theta}^{(\eta+1)} := \boldsymbol{\theta}^\star$;
4: Set $\eta := \eta+1$;
5: **until** Convergence
6: **Ouput**: $(\xi^\star,\boldsymbol{v}^\star,\boldsymbol{\theta}^\star)$

Complexity and convergence analysis: The computational complexity of solving (6.7) and (6.17) is $\mathcal{O}\left((M_t+1)^2 3^{2.5}+3^{3.5}\right)$ and $\mathcal{O}\left((K+2)^2(K+3)^{2.5}+(K+3)^{3.5}\right)$ for each iteration, respectively. On the other hand, from the IA principles, it is obvious from (6.7) that $\mathcal{R}(\xi^{(\eta+1)},\boldsymbol{v}^{(\eta+1)},\boldsymbol{\theta}^{(\eta)}) \geq \mathcal{R}^{(\eta)}(\xi^{(\eta+1)},\boldsymbol{v}^{(\eta+1)}|\boldsymbol{\theta}^{(\eta)}) \geq \mathcal{R}^{(\eta)}(\xi^{(\eta)},\boldsymbol{v}^{(\eta)}|\boldsymbol{\theta}^{(\eta)}) = \mathcal{R}(\xi^{(\eta)},\boldsymbol{v}^{(\eta)},\boldsymbol{\theta}^{(\eta)})$. As in (6.17), we have $\mathcal{R}(\xi^{(\eta+1)},\boldsymbol{v}^{(\eta+1)},\boldsymbol{\theta}^{(\eta+1)}) \geq \mathcal{R}^{(\eta)}(\xi^{(\eta+1)},\boldsymbol{v}^{(\eta+1)},\boldsymbol{\theta}^{(\eta+1)})$ $\geq \mathcal{R}^{(\eta)}(\xi^{(\eta+1)},\boldsymbol{v}^{(\eta+1)},\boldsymbol{\theta}^{(\eta)}) = \mathcal{R}(\xi^{(\eta+1)},\boldsymbol{v}^{(\eta+1)},\boldsymbol{\theta}^{(\eta)})$. Accordingly, it holds true that $\mathcal{R}(\xi^{(\eta+1)},\boldsymbol{v}^{(\eta+1)},\boldsymbol{\theta}^{(\eta+1)}) \geq \mathcal{R}(\xi^{(\eta)},\boldsymbol{v}^{(\eta)},\boldsymbol{\theta}^{(\eta)})$. Thus, Algorithm 8 yields a sequence $\{(\xi^{(\eta)},\boldsymbol{v}^{(\eta)},\boldsymbol{\theta}^{(\eta)})\}$ of points that converges at least to a locally optimal solution [13].

6.4.3 Sub-Optimal Design based on Maximal Ratio Transmission (MRT)

To reduce the complexity of the active beamforming, we adopt the MRT by $\boldsymbol{v} = \frac{\sqrt{\beta}\mathbf{b}_d}{\|\mathbf{b}_d\|}$, where β is the power level. The MRT-based optimization problem is re-formulated as follows

$$\max_{\xi,\beta,\boldsymbol{\theta}} \mathcal{R}(\xi,\beta,\boldsymbol{\theta}) \triangleq \ln\left(1+\frac{\left\|\hat{\mathbf{f}}(\boldsymbol{\theta})\right\|^2\xi}{\beta\left\|\hat{\mathbf{b}}^H(\boldsymbol{\theta})\frac{\mathbf{b}_d}{\left\|\mathbf{b}_d\right\|}\right\|^2+\beta\left\|\mathbf{H}\frac{\mathbf{b}_d}{\left\|\mathbf{b}_d\right\|}\right\|^2+\sigma^2}\right) \tag{6.18a}$$

$$\text{s. t.} \quad \xi \le P_{UE}^{\max} \tag{6.18b}$$

$$\beta \le P_{BS}^{\max} \tag{6.18c}$$

$$\beta\left\|\hat{\mathbf{b}}^H(\boldsymbol{\theta})\frac{\mathbf{b}_d}{\left\|\mathbf{b}_d\right\|}\right\|^2 \ge P_{\text{sense}} \tag{6.18d}$$

$$|\theta_k| = 1, \forall k \in \mathcal{K}. \tag{6.18e}$$

Based on (6.5), the convex problem of transmit power and beamforming solved at iteration $\eta+1$ is given by

$$\max_{\xi,\beta} \quad \mathcal{R}^{(\eta)}(\xi,\beta|\boldsymbol{\theta}^{(\eta)}) \tag{6.19a}$$

$$\text{s. t.} \quad (6.18\text{b}), (6.18\text{c}), (6.18\text{d}), \tag{6.19b}$$

where

$$\mathcal{R}^{(\eta)}(\xi,\beta|\boldsymbol{\theta}^{(\eta)}) \triangleq \ln\left(1+\frac{\left\|\hat{\mathbf{f}}(\boldsymbol{\theta}^{(\eta)})\right\|^2\xi^{(\eta)}}{\beta^{(\eta)}\left\|\hat{\mathbf{b}}^H(\boldsymbol{\theta}^{(\eta)})\frac{\mathbf{b}_d}{\left\|\mathbf{b}_d\right\|}\right\|^2+\beta^{(\eta)}\left\|\mathbf{H}\frac{\mathbf{b}_d}{\left\|\mathbf{b}_d\right\|}\right\|^2+\sigma^2}\right)$$
$$+\frac{\left\|\hat{\mathbf{f}}(\boldsymbol{\theta}^{(\eta)})\right\|^2\xi^{(\eta)}}{\beta^{(\eta)}\left\|\hat{\mathbf{b}}^H(\boldsymbol{\theta}^{(\eta)})\frac{\mathbf{b}_d}{\left\|\mathbf{b}_d\right\|}\right\|^2+\beta^{(\eta)}\left\|\mathbf{H}\frac{\mathbf{b}_d}{\left\|\mathbf{b}_d\right\|}\right\|^2+\sigma^2+\left\|\hat{\mathbf{f}}(\boldsymbol{\theta}^{(\eta)})\right\|^2\xi^{(\eta)}}$$
$$\times\left(2-\frac{\xi^{(\eta)}}{\xi}-\frac{\beta\left\|\hat{\mathbf{b}}^H(\boldsymbol{\theta}^{(\eta)})\frac{\mathbf{b}_d}{\left\|\mathbf{b}_d\right\|}\right\|^2+\beta\left\|\mathbf{H}\frac{\mathbf{b}_d}{\left\|\mathbf{b}_d\right\|}\right\|^2+\sigma^2}{\beta^{(\eta)}\left\|\hat{\mathbf{b}}^H(\boldsymbol{\theta}^{(\eta)})\frac{\mathbf{b}_d}{\left\|\mathbf{b}_d\right\|}\right\|^2+\beta^{(\eta)}\left\|\mathbf{H}\frac{\mathbf{b}_d}{\left\|\mathbf{b}_d\right\|}\right\|^2+\sigma^2}\right).$$

Based on (6.9), (6.10) and (6.14), the convex problem of phase shift iteration solved at iteration $\eta+1$ is expressed by

$$\max_{\boldsymbol{\theta},t,\zeta}\quad \mathcal{Q}^{(\eta)}(\xi^{(\eta+1)},\beta^{(\eta+1)},\boldsymbol{\theta}) \triangleq \mathcal{Q}^{(\eta)}(\boldsymbol{\theta}|\xi^{(\eta+1)},\beta^{(\eta+1)})+\varrho\left(\mathcal{P}^{(\eta)}(\boldsymbol{\theta})-K\right) \tag{6.20a}$$

$$\text{s. t.}\quad \left\|\hat{\mathbf{b}}_u(\boldsymbol{\theta})\right\|^2\le t \tag{6.20b}$$

$$\left\|\hat{\mathbf{b}}_d^H(\boldsymbol{\theta})\frac{\mathbf{b}_d}{\left\|\mathbf{b}_d\right\|}\right\|^2\le\zeta \tag{6.20c}$$

$$\beta^{(\eta+1)}2\Re\left\{(\boldsymbol{\theta}^{(\eta)})^T\mathcal{Y}\boldsymbol{\theta}+\boldsymbol{\theta}^T\mathcal{Y}\boldsymbol{\theta}^{(\eta)}-(\boldsymbol{\theta}^{(\eta)})^T\mathcal{Y}\boldsymbol{\theta}^{(\eta)}\right\}+\mathcal{X}^{(\eta)}(\boldsymbol{\theta}|\beta^{(\eta+1)})$$
$$-\beta^{(\eta+1)}\left\|\hat{\mathbf{b}}^H(\boldsymbol{\theta}^{(\eta)})\frac{\mathbf{b}_d}{\left\|\mathbf{b}_d\right\|}\right\|^2\ge P_{\text{sense}} \tag{6.20d}$$

$$|\theta_k|^2\le 1,\forall k\in\mathcal{K}, \tag{6.20e}$$

where

$$\mathcal{Q}^{(\eta)}(\boldsymbol{\theta}|\xi^{(\eta+1)},\beta^{(\eta+1)}) \triangleq \ln\left(1+\frac{\left\|\hat{\mathbf{f}}(\boldsymbol{\theta}^{(\eta)})\right\|^2\xi^{(\eta+1)}}{\beta^{(\eta+1)}t^{(\eta)}\zeta^{(\eta)}+\beta^{(\eta+1)}\left\|\mathbf{H}\frac{\mathbf{b}_d}{\left\|\mathbf{b}_d\right\|}\right\|^2+\sigma^2}\right)$$
$$+\frac{\left\|\hat{\mathbf{f}}(\boldsymbol{\theta}^{(\eta)})\right\|^2\xi^{(\eta+1)}}{\beta^{(\eta+1)}t^{(\eta)}\zeta^{(\eta)}+\beta^{(\eta+1)}\left\|\mathbf{H}\frac{\mathbf{b}_d}{\left\|\mathbf{b}_d\right\|}\right\|^2+\sigma^2+\left\|\hat{\mathbf{f}}(\boldsymbol{\theta}^{(\eta)})\right\|^2\xi^{(\eta+1)}}$$
$$\times\left(2-\frac{\left\|\hat{\mathbf{f}}(\boldsymbol{\theta}^{(\eta)})\right\|^2}{\left\|\hat{\mathbf{f}}(\boldsymbol{\theta})\right\|^2}-\frac{\frac{t^{(\eta)}\zeta^2}{2\zeta^{(\eta)}}+\frac{\zeta^{(\eta)}t^2}{2t^{(\eta)}}+\left\|\mathbf{H}\frac{\mathbf{b}_d}{\left\|\mathbf{b}_d\right\|}\right\|^2+\frac{\sigma^2}{\beta^{(\eta+1)}}}{t^{(\eta)}\zeta^{(\eta)}+\left\|\mathbf{H}\frac{\mathbf{b}_d}{\left\|\mathbf{b}_d\right\|}\right\|^2+\frac{\sigma^2}{\beta^{(\eta+1)}}}\right),$$

$$\mathcal{X}^{(\eta)}(\boldsymbol{\theta}|\beta^{(\eta+1)}) \triangleq \beta^{(\eta+1)}2\Re\left\{\left(\hat{\mathbf{b}}^H(\boldsymbol{\theta}^{(\eta)})\frac{\mathbf{b}_d}{\left\|\mathbf{b}_d\right\|}\right)^H\mathbf{b}_u\mathbf{b}_d^H\frac{\mathbf{b}_d}{\left\|\mathbf{b}_d\right\|}\right\}$$
$$+\beta^{(\eta+1)}2\Re\left\{\left(\hat{\mathbf{b}}^H(\boldsymbol{\theta}^{(\eta)})\frac{\mathbf{b}_d}{\left\|\mathbf{b}_d\right\|}\right)^H\mathbf{b}_u\boldsymbol{\theta}^T\left(\mathbf{d}_d\right)\mathbf{A}_d^H\frac{\mathbf{b}_d}{\left\|\mathbf{b}_d\right\|}\right\}$$
$$+\beta^{(\eta+1)}2\Re\left\{\left(\hat{\mathbf{b}}^H(\boldsymbol{\theta}^{(\eta)})\frac{\mathbf{b}_d}{\left\|\mathbf{b}_d\right\|}\right)^H\mathbf{A}_u\left(\mathbf{d}_u\right)\boldsymbol{\theta}\mathbf{b}_d^H\frac{\mathbf{b}_d}{\left\|\mathbf{b}_d\right\|}\right\}$$

and $\mathcal{Y} \triangleq \left(\mathbf{d}_d\right)\mathbf{A}_d^H\frac{\mathbf{b}_d}{\left\|\mathbf{b}_d\right\|}\left(\hat{\mathbf{b}}^H(\boldsymbol{\theta}^{(\eta)})\frac{\mathbf{b}_d}{\left\|\mathbf{b}_d\right\|}\right)^H\mathbf{A}_u\left(\mathbf{d}_u\right)$.

The computational complexity of solving (6.19) and (6.20) is $\mathcal{O}\left(2^2 3^{2.5}+3^{3.5}\right)$ and $\mathcal{O}\left((K+2)^2(K+3)^{2.5}+(K+3)^{3.5}\right)$ for each iteration, respectively.

6.5 Numerical Results

This section considers a 2-D scenario, in which the BS, target, UE, and RIS are located at (5 m, 0), (5 m, 50 m), (20 m, 10 m), and (10 m, 10 m), respectively. Unless otherwise stated, the bandwidth is 20 MHz, the BS's maximum transmit power is 1 W, and the UE's maximum transmit power is 5 mW. The number of RIS elements K is 8, the noise

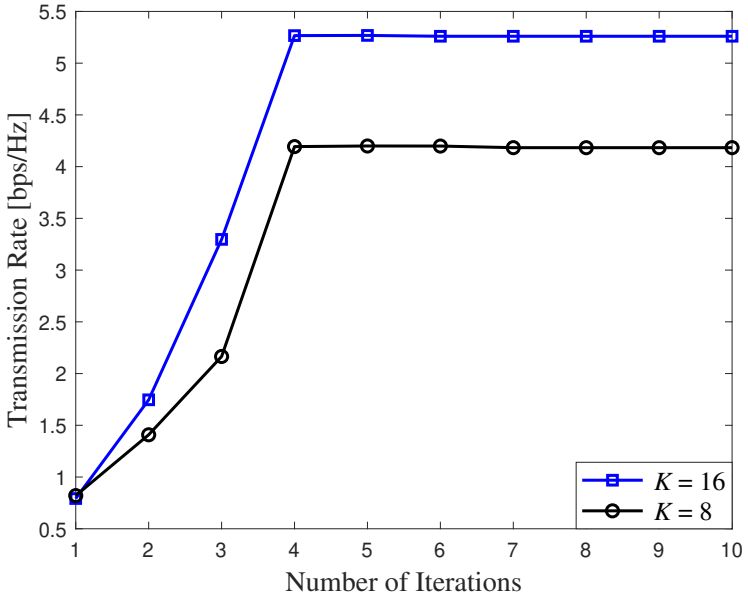

Fig. 6.2: Convergence rate of Algorithm 8 with different values of K.

power σ^2 at the BS is -80 dBm, and the BS is equipped with $M_t = M_r = 5$ antennas. We utilize the distance-dependent path-loss model [14]; the path-loss exponents of the BS-RIS, RIS-target, RIS-UE, BS-target, and BS-UE links are set to 2.5, 2.8, 2.8, 3, and 3, respectively [15,16]. All simulation results are obtained over an average of 1000 simulation runs.

Fig. 6.2 presents Algorithm 8's convergence pattern. It is clear that Algorithm 8 needs about 4 iterations to attain the optimal value of the UE's transmission rate. Also, increasing K leads to enhanced transmission rate of the UE.

Fig. 6.3 shows the transmission rate versus the UE's transmit power. Not surprisingly, the UE's transmission rate increases with the UE's transmit power. This is because increasing the UE's transmit power results in higher received signal strength at BS. Further, the transmission rate of the proposed transmit BF case is much higher than that of the MRT case regardless if the RIS is utilized or not.

Fig. 6.4 plots the UE's transmission rate versus the BS's receive antennas. As expected,

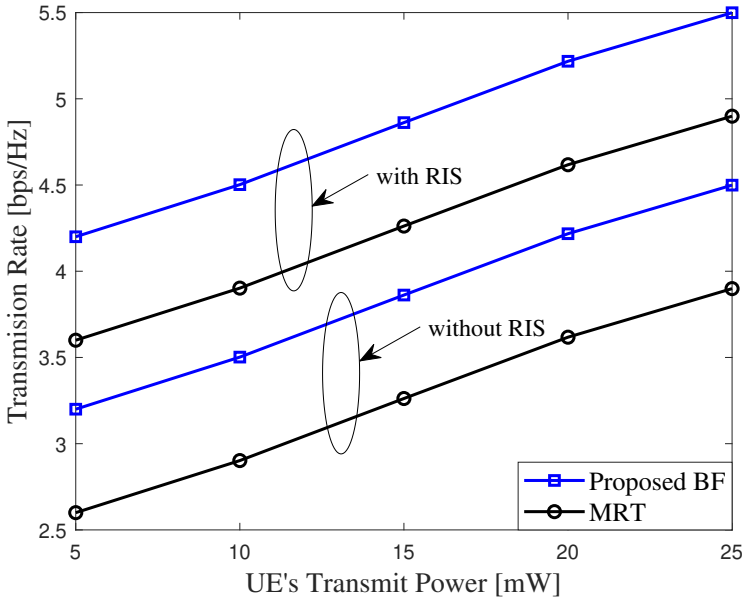

Fig. 6.3: Transmission rate of the UE versus the UE's transmit power.

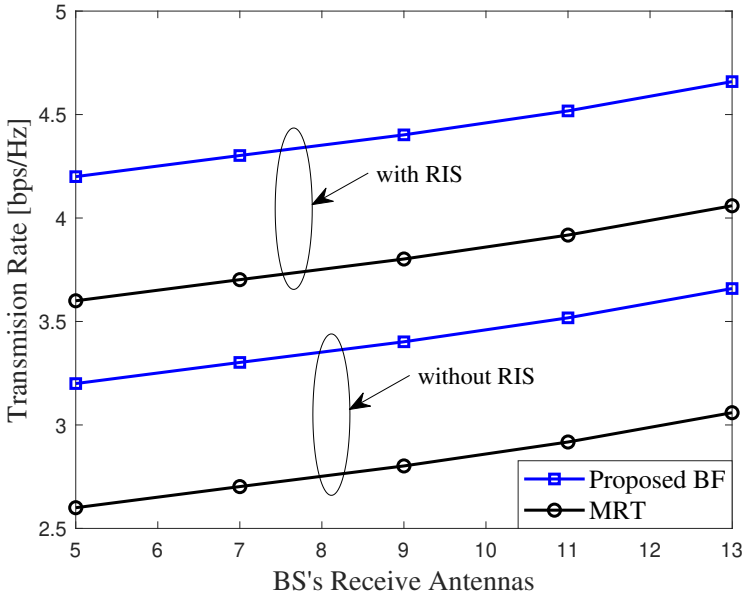

Fig. 6.4: Transmission rate of the UE versus the BS's receive antennas.

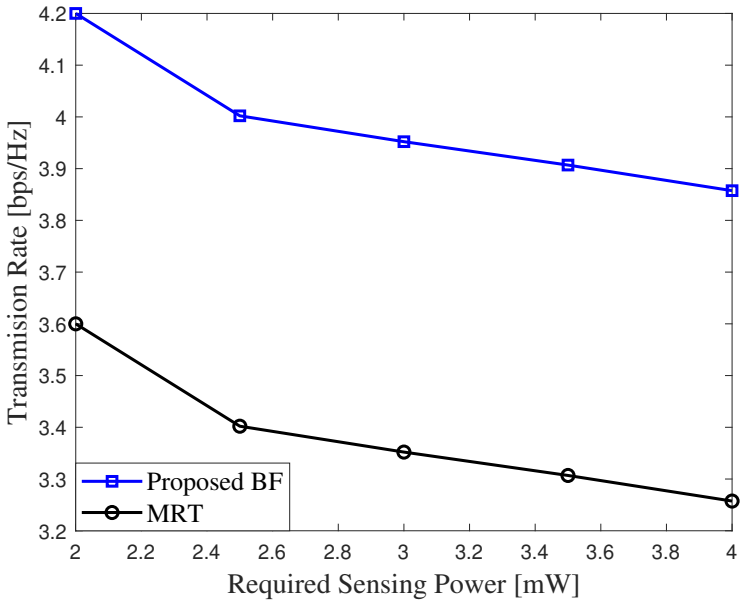

Fig. 6.5: Transmission rate of the UE versus the required sensing power.

increasing M_r results in higher transmission rate of the UE. This is attributed to the fact that the higher the value of M_r, the better the received diversity can be obtained, which in turn improves the signal reception quality at BS.

Fig. 6.5 depicts the trade-off between the UE's transmission rate and the required sensing power. As expected, increasing the required sensing power leads to a decrease in the UE's transmission rate. This is because a higher transmit power at BS is needed to enhance the received sensing signal power, but it conversely degrades the SINR of UE at BS.

6.6 Conclusion

The transmission rate maximization problem of a FD-ISAC network with the assistance of the RIS was considered in this chapter. A non-convex problem was formulated, which involved a joint optimization of the BS's transmit beamforming, UE's transmit power,

and RIS's phase shifts. It was solved with a proposed BCA algorithm that relies on the IA framework. Simulation results showed the fast convergence and effectiveness of the algorithm, the trade-off between the UE's transmission rate and the required sensing power, and the advantage of employing RIS. The extensions considering multiple targets or multiple UEs are interesting topics for our future works.

References

[1] X. Li *et al.*, "Integrated human activity sensing and communications," *IEEE Commun. Mag.*, vol. 1, no. 1, pp. 1–8, Nov. 2022.

[2] Z. Wei *et al.*, "Integrated sensing and communication signals towards 5g-a and 6g: A survey," *IEEE Internet Things J.*, vol. 1, no. 1, pp. 1–25, Jan. 2023.

[3] R. Liu *et al.*, "Integrated sensing and communication with reconfigurable intelligent surfaces: Opportunities, applications, and future directions," *arXiv preprint arXiv:2206.08518v1*, June 2022.

[4] Y. Liu *et al.*, "Deep-learning channel estimation for IRS-assisted integrated sensing and communication system," *IEEE Trans. Veh. Technol.*, vol. 1, no. 1, pp. 1–14, Dec. 2022.

[5] A. M. Elbir *et al.*, "The rise of intelligent reflecting surfaces in integrated sensing and communications paradigms," *IEEE Netw.*, vol. 1, no. 1, pp. 1–8, Dec. 2022.

[6] X. Wang *et al.*, "Joint waveform design and passive beamforming for RIS-assisted dual-functional radar-communication system," *IEEE Trans. Veh. Technol.*, vol. 70, no. 5, pp. 5131–5136, May 2021.

[7] ——, "Joint waveform and discrete phase shift design for RIS-assisted integrated sensing and communication system under cramer-rao bound constraint," *IEEE Trans. Veh. Technol.*, vol. 71, no. 1, pp. 1004–1009, Jan. 2022.

[8] Z. Shao *et al.*, "Joint localization and information transfer for RIS aided full-duplex systems," in *2022 IEEE Global Commun. Conf. (GLOBECOM)*, Dec. 2022, pp. 1–6.

[9] K. Keykhosravi *et al.*, "RIS-enabled self-localization: Leveraging controllable reflections with zero access points," in *Proc. IEEE Inter. Conf. Commun. (ICC)*, June 2022, pp. 1–6.

[10] B. R. Marks and G. P. Wright, "A general inner approximation algorithm for nonconvex mathematical programs," *Operations Research*, vol. 26, no. 4, pp. 681–683, July-Aug. 1978.

[11] A. A. Nasir *et al.*, "Hybrid beamforming for multi-user millimeter-wave networks," *IEEE Trans. Veh. Technol.*, vol. 69, no. 3, pp. 2943–2956, Mar. 2020.

[12] H. V. Nguyen *et al.*, "Joint power control and user association for NOMA-based full-duplex systems," *IEEE Trans. Commun.*, vol. 67, no. 11, pp. 8037–8055, Nov. 2019.

[13] A. Beck, A. Ben-Tal, and L. Tetruashvili, "A sequential parametric convex approximation method with applications to nonconvex truss topology design problems," *J. Global Optim.*, vol. 47, no. 1, pp. 29–51, May 2010.

[14] Q. Wu and R. Zhang, "Intelligent reflecting surface enhanced wireless network via joint active and passive beamforming," *IEEE Trans. Veh. Technol.*, vol. 18, no. 11, pp. 5394–5409, Nov. 2019.

[15] R. Liu *et al.*, "Joint transmit waveform and passive beamforming design for RIS-aided DFRC systems," *IEEE J. Sel. Top. Signal Process.*, vol. 16, no. 5, pp. 995–1010, Aug. 2022.

[16] H. Luo *et al.*, "Joint beamforming design for RIS-assisted integrated sensing and communication systems," *IEEE Trans. Veh. Technol.*, vol. 71, no. 12, pp. 13 393–13 397, Dec. 2022.

Chapter 7

Conclusions and Future Work

This chapter summarizes the main contributions of the dissertation and discusses several areas of considerable interest for future work.

7.1 Conclusions

A brief summary of the work and conclusions that can be drawn from the dissertation are presented as follows:

- Chapter 1 discussed the basics and importance of efficient resource allocation strategies in future wireless networks incorporating CFmMIMO, RIS, NOMA, ISAC, and FD technologies.
- Chapter 2 illustrated the applicability of FD, NOMA, and SWIPT in cooperative spectrum-sharing networks. Numerical results showed that the FD-NOMA system outperforms the HD-NOMA and the conventional OMA-TDMA systems in terms of the outage probability and sum transmission rate.
- Chapter 3 proposed unsupervised ML-based UC algorithms and developed a low-complexity iterative algorithm based on the IA framework for solving PA problems

in a CFmMIMO-NOMA system. Numerical results confirmed the effectiveness of the proposed UC algorithms and the superior performance of the proposed PA algorithm compared to CFmMIMO-NOMA without optimizing PA and COmMIMO-NOMA in terms of SSE.

- Chapter 4 addressed the EE maximization problem of CF networks with the help of multiple RISs and developed a low-complexity alternating descent algorithm based on the IA framework for its solution. Numerical results verified the fast convergence of the proposed algorithm and the benefits of CF and RIS over collocated networks.

- Chapter 5 focused on the total transmit power minimization problem of FL-assisted wireless networks with the help of the RIS and developed an alternating descent algorithm based on the IA framework for its solution. Numerical results confirmed the quick convergence of the proposed algorithm and the advantage of using RIS.

- Chapter 6 considered the problem of maximizing the transmission rate for an FD-ISAC network with the help of the RIS and proposed a BCA algorithm based on the IA framework for its solution. Numerical results showed the rapid convergence of the algorithm, analyzed the trade-off between the UE's transmission rate and the required sensing power, and highlighted the benefit of deploying RIS.

7.2 Possible Directions for Future Research

This section highlights other potential research problems in developing efficient resource allocation schemes for future wireless networks, which are worth of being investigated in the future.

- Sensing-assisted secure communications for FD-ISAC networks with RIS: Certainly, transmission security needs to be considered in FD-ISAC networks where designing

the waveform as dual-functional signal can be intercepted in case there exists an eavesdropper or the target is malicious, i.e., a potential eavesdropper.

- RIS-assisted unmanned aerial vehicle (UAV)-based ISAC: A virtual line-of-sight link can be set up between blocked UEs and a UAV with the help of RIS. Hence, RIS assists in extending the coverage area and offers flexibility for designing the trajectory of UAV in order to obtain higher communication and sensing performances.

- Integration of ISAC and RIS with CFmMIMO systems: The distributed essence of CFmMIMO systems can be exploited to implement ISAC, as geographically distributed APs can cooperatively conduct communication and sensing tasks concurrently. Furthermore, RIS helps to adjust the power and direction of the reflected signals and decreases the interference between communication and sensing signals, thus enhancing the overall system performance.

- Secure RIS-assisted CFmMIMO systems: Eavesdroppers pose huge challenges for CFmMIMO systems as they can conduct pilot contamination attacks to spoil the channel estimation phase at the APs. Since RIS can smartly manipulate the wireless propagation environment by reconfiguring the phase and/or amplitude of the incident signals, the reflected signals can be added constructively in the desired positions and destructively in undesired ones. On this context, RIS has the potential to improve the performance of CFmMIMO systems in terms of security and reliability.

- Orthogonal time frequency space (OTFS)-assisted ISAC systems: Recently, OTFS has emerged as a promising modulation technology for high-mobility and high frequency cases due to its potential to tackle high delay and Doppler spreads. Resource allocation, e.g., delay-Doppler resource block, power, and bandwidth, and joint optimization for communication and sensing for OTFS-assisted ISAC systems are crucial problems that are worth of being investigated to maximize the communication or

sensing performance metrics, and analyze the trade-off between communication and sensing performance.